

2012

# Computational modelling of combined storm surge and wave overtopping of embankments

Jones, David K

<http://hdl.handle.net/10026.1/920>

---

<http://dx.doi.org/10.24382/3727>

University of Plymouth

---

*All content in PEARL is protected by copyright law. Author manuscripts are made available in accordance with publisher policies. Please cite only the published version using the details provided on the item record or document. In the absence of an open licence (e.g. Creative Commons), permissions for further reuse of content should be sought from the publisher or author.*

**Computational modelling of combined  
storm surge and wave overtopping of  
embankments**

By

**David K. Jones**

A thesis submitted to the University of Plymouth  
in partial fulfilment for the degree of

**Doctor of Philosophy**

School of Marine Science and Engineering  
Faculty of Science and Technology

November 2011



This copy of the thesis has been supplied on condition that anyone who consults it is understood to recognise that its copyright rests with its author and that no quotation from the thesis and no information derived from it may be published without the author's prior consent.



**Computational modelling of combined storm surge  
and wave overtopping of embankments  
by David Kenneth Jones**

**Abstract**

The primary function of seawalls and embankments is to protect against damage and injury caused by flooding. Coastal flooding is caused by combinations of high tides, waves, wind set-up and storm surges driven by low-pressure systems. However with global warming causing sea levels to rise and with increased storminess causing more extreme waves and storm surges, the likelihood of overtopping of seawalls with zero or negative freeboard may well be expected to increase. Researchers using physical and numerical models to develop design formulae have widely investigated wave overtopping of seawalls with positive freeboard. However the design of seawalls with zero or negative freeboard has attracted much less attention, and some variation exists between overtopping discharge calculated with current design formulae. The focus of this thesis is the extreme situation when overtopping caused by storm waves is combined with surge levels above the embankment crest.

The local highly accelerative flow over the embankment crest caused by the high surge level will significantly alter the flow at the crest. This is likely to have a highly non-linear effect upon the overtopping waves. In this thesis, the flow is investigated with a 2DV numerical model based on the Reynolds averaged Navier-Stokes (RANS) equations developed by Lin and Liu (1998a). The model describes the flow characteristics of a breaking wave such as the velocities within the wave as well as the turbulence at the seabed boundary layer.

As an example of the model's ability to describe complex hydrodynamic flows, this study investigates its ability to represent the second order mass transport under progressive and standing waves. The model results are compared with available theory and experimental results. This shows that mass transport is successfully predicted, although there is some variation in the magnitude compared to the experimental and theoretical results.

To consider the model's ability to simulate storm surge wave overtopping of embankments, the RANS model has been used to simulate an experimental study conducted by Hughes and Nadal (2009). To examine the success of the model at reproducing the wave generation, transformation and overtopping processes the model results have been compared with the experimental laboratory data. This makes possible a wave-by-wave comparison of overtopping parameters such as discharge, depth and velocity for a storm surge event.

Additionally the overtopping discharge predicted by the model is compared with design formulae and the differences in the overtopping discharge calculated with current design formulae are investigated and explained. Finally, the RANS model is used to determine the effect of embankment crest width on the magnitude of the overtopping discharge. Results from RANS model tests are used to provide design guidance in the form of an equation that allows the effect of crest width to be included when evaluating combined discharge at embankments.



# LIST OF CONTENTS

<b>CHAPTER 1 INTRODUCTION</b>	
1.1. Introduction.....	1
1.2. Study aims and objectives.....	7
<b>CHAPTER 2 WAVE OVERTOPPING DESIGN FORMULAE.....</b>	<b>10</b>
2.1. Introduction.....	10
2.2. Positive freeboard.....	11
2.3. Zero freeboard.....	15
2.4. Negative freeboard.....	17
2.5. Acceptable overtopping discharge.....	22
<b>CHAPTER 3 NUMERICAL MODELLING.....</b>	<b>27</b>
3.1. Introduction.....	27
3.2. RANS model.....	31
3.2.1. Turbulence model.....	33
3.2.2. Numerical scheme.....	35
3.2.3. Initial conditions.....	37
3.2.4. Boundary conditions.....	38
3.2.5. Free surface reconstruction.....	39
3.2.6. Solid objects.....	40
3.2.7. Open boundary condition.....	40
3.2.8. Wave generation.....	41
<b>CHAPTER 4 MODEL VERIFICATION.....</b>	<b>45</b>
4.1. Introduction.....	45
4.2. Mass transport model validation.....	46
4.3. Previous work.....	46
4.4. Model testing.....	48
4.5. Progressive wave theory.....	49
4.5.1. Comparative data for progressive waves.....	55

4.5.2. Model testing for progressive waves.....	56
4.6. Standing wave theory.....	67
4.6.1. Comparative data for standing waves.....	71
4.6.2. Model testing for standing waves.....	74
<b>CHAPTER 5 COMBINED OVERTOPPING MODEL TESTING.....</b>	<b>84</b>
5.1. Introduction.....	84
5.2. Experimental data description.....	84
5.3. Description of RANS model set-up.....	90
5.4. Comparison between RANS results and physical model results.....	96
5.4.1. Wave generation.....	96
5.4.2. Discharge comparison.....	98
5.4.2.1. 1.3m surge .....	99
5.4.2.2. 0.81m surge .....	102
5.4.2.3. 0.29m surge .....	103
5.4.3. Flow depth comparison.....	105
5.4.3.1. 1.3m surge .....	105
5.4.3.2. 0.81m surge .....	106
5.4.3.3. 0.29m surge .....	106
5.4.4. Velocity comparison.....	107
5.4.4.1. 1.3m surge .....	107
5.4.4.2. 0.81m surge .....	108
5.4.4.3. 0.29m surge .....	109
5.4.5. Discussion of results.....	110
5.4.5.1. Sources of error in the numerical model.....	111
5.4.5.2. Sources of error in the physical model.....	117
<b>CHAPTER 6 MODEL COMPARISON AGAINST DESIGN FORMULAE.....</b>	<b>125</b>
6.1. Introduction.....	125
6.2. Comparison.....	125

<b>CHAPTER 7 MODEL APPLICATION.....</b>	<b>134</b>
7.1. Introduction.....	134
7.2. Effect of crest width on overtopping discharge.....	134
7.3. Model set-up.....	136
7.4. Discussion of results.....	138
7.5. Development of the design formula.....	141
<b>CHAPTER 8 CONCLUSIONS AND FUTURE WORK.....</b>	<b>150</b>
8.1 Conclusions.....	150
8.2 Further work.....	155
<b>APPENDIX A RANS model development to include sediment transport and bed morphology .....</b>	<b>157</b>
A1 Introduction.....	157
A2 Mechanics of sediment transport .....	158
A3 Bed-load sediment transport .....	163
A4 Bed morphology .....	164
A5 Modelling approach .....	165
A6 Model application .....	167
A6.1 Sediment transport and bed morphology under standing waves .....	168
A6.2 Sediment transport and bed morphology on a sloping beach .....	172
A7 Conclusion .....	180
<b>APPENDIX B Tests conducted to determine the effect of embankment crest width upon combined discharge.....</b>	<b>182</b>
<b>APPENDIX C Journal and conference papers.....</b>	<b>185</b>
<b>References.....</b>	<b>220</b>



## LIST OF SYMBOLS

$a$	Wave amplitude [m]
$b$	Weir crest length [m]
$C_d$	Coefficient [-]
$C_r$	Wave celerity [m/s]
$C_\phi$	Phase velocity [m/s]
$d$	Grain diameter [m]
$f$	Friction factor
$g$	Gravitational constant (= 9.81 m/s <sup>2</sup> )
$h$	Mean water depth measured from the bed [m]
$h_c$	Crest height of weir measured from the bed [m]
$h_b$	Wave breaking depth [m]
$h_u$	Upstream depth of flow above weir [m]
$h_w$	Depth of flow measured above weir [m]
$H$	Wave height [m]
$H_i$	Incident wave height [m]
$H_{m0}$	Energy based significant wave height [m]
$H_s$	Significant wave height, average height of the largest third of waves [m]
$H_{st}$	Standing wave height [m]
$k$	= $2\pi/\lambda$ [m <sup>-1</sup> ]
$ks$	Nikuradse bed roughness [mm]
$K$	Von Karmman constant [-]
$L_w$	Weir crest width [m]
$n$	Porosity [-]
$q$	Overtopping discharge per unit length [m <sup>3</sup> /s/m]
$q_s$	Overtopping discharge due to overflow per unit length [m <sup>3</sup> /s/m]

$q_t$	Overtopping discharge for weirs [ $\text{m}^3/\text{s}$ ]
$q_{ws}$	Overtopping discharge due to waves and surge per unit length [ $\text{m}^3/\text{s}/\text{m}$ ]
$Q$	Dimensionless discharge [-]
$Q_s$	Sediment transport rate [ $\text{m}^3/\text{s}/\text{m}$ ]
$p$	Pressure [ $\text{N}/\text{m}^2$ ]
$r$	Roughness [m]
$R$	Dimensionless freeboard defined as $R_c/H_s$ [-]
$R_c$	Crest freeboard [m]
$Re$	Grain Reynolds number
$R_i$	Any physical variable associated with the incident wave
$R_r$	Any physical variable associated with the reflected wave
$R_t$	Any physical variable associated with the total wave
$s$	$\rho_s/\rho$
$S_{om}$	Deep water wave steepness defined as $H_s/\lambda_{om}$
$S_{op}$	Deep water wave steepness defined as $H_s/\lambda_{op}$
$T$	Wave period [s]
$T_p$	Peak spectral wave period [s]
$T_{om}$	Deep water mean zero-crossing period [s]
$t$	Time [s]
$u^*$	Friction velocity $\sqrt{\tau/\rho}$ [m/s]
$u$	Horizontal velocity [m/s]
$u_b$	Near bed velocity [m/s]
$\bar{U}$	Mass transport velocity [m/s]
$v$	Vertical velocity [m/s]
$x$	Horizontal distance [m]

$z$	Vertical distance [m]
$z_b$	Elevation measured from the bed, positive upwards [m]
$z_{bed}$	Bed elevation measured above some datum, positive upwards [m]
$z_0$	Zero-intercept level of the log velocity profile [m]
$z_{sw}$	Elevation measured from still water level, positive upwards [m]
$\alpha$	Seaward embankment slope angle [-]
$\gamma$	Coefficient to take into account overtopping reduction due to slope roughness, berm detail, shallow water and angle of incidence [-]
$\delta$	Boundary layer thickness parameter $(= (2\nu/\sigma)^{1/2})$
$\varepsilon$	Turbulence dissipation [N m]
$\zeta$	Vorticity [m/s/m]
$\eta$	Water surface elevation above mean water level [m]
$\theta$	Shields parameter
$\theta_{cr}$	Critical Shields parameter
$\kappa$	Turbulent kinetic energy [N m]
$\lambda$	Wave length [m]
$\lambda_s$	Wave length based on the significant wave period at toe of structure [m]
$\lambda_m$	Wave length, based on the mean zero-crossing period [s]
$\lambda_{op}$	Deepwater wave length, based on the spectral peak period [m]
$\lambda_{om}$	Deepwater wave length, based on the mean zero-crossing period [s]
$\lambda_{om-1,0}$	Deepwater wave length, based on the mean spectral wave period [m]
$\mu$	Viscosity [kg/(ms)]
$\nu$	Kinematic viscosity [m <sup>2</sup> /s]
$\nu_t$	Eddy viscosity [m <sup>2</sup> /s]

- $\xi$  Surf similarity parameter (Iribarren number) defined as  $\xi = \frac{\tan \alpha}{\sqrt{H_s \lambda}}$
- $\xi_{om-1,0}$  Surf similarity parameter (Iribarren number) defined as  $\xi_{om-1,0} = \frac{\tan \alpha}{\sqrt{H_{m0} \lambda_{om-1,0}}}$
- $\xi_p$  Surf similarity parameter (Iribarren number) defined as  $\xi_p = \frac{\tan \alpha}{\sqrt{H_s \lambda_p}}$
- $\xi_{op}$  Surf similarity parameter (Iribarren number) defined as  $\xi_{op} = \frac{\tan \alpha}{\sqrt{H_s \lambda_{op}}}$
- $\xi_{om}$  Surf similarity parameter (Iribarren number) defined as  $\xi_{om} = \frac{\tan \alpha}{\sqrt{H_s \lambda_{om}}}$
- $\rho$  Fluid density [kg/m<sup>3</sup>]
- $\sigma = 2\pi/T$  [s<sup>-1</sup>]
- $\tau$  Shear stress [N/m<sup>2</sup>]
- $\tau_c$  Critical shear stress [N/m<sup>2</sup>]
- $\tau_{bc}$  Critical shear stress taking bed slope into consideration [N/m<sup>2</sup>]
- $\phi_i$  Sediment angle of repose
- $\beta$  Local bed slope
- $\Omega$  Specific dissipation of turbulent kinetic energy

Other symbols are defined within the text.

## LIST OF TABLES

<b>Table 2.1</b> Dimensionless discharge, dimensionless freeboard and overtopping models based partly on Hedges and Reis (1998) and Burcharth and Hughes (2002).	12
<b>Table 2.2</b> Critical values of average overtopping discharge (from Burcharth and Hughes (2002)).	24
<b>Table 4.1</b> Wave condition for tests including boundary layer velocity data from Lin and Liu (2002).	73
<b>Table 5.1</b> Test numbers, surge levels and wave conditions.	91
<b>Table 5.2</b> Average combined discharge rates for the 1.3m surge tests.	99
<b>Table 5.3</b> Average combined discharge rates for the 0.81m surge tests.	102
<b>Table 5.4</b> Average combined discharge rates for the 0.29m surge tests.	103
<b>Table 6.1.</b> Test numbers and corresponding wave conditions, freeboard and Iribarren Number.	127
<b>Table 6.2</b> Test numbers and $R_c$ calculated from $q_s$ as well as $R_c$ calculated in accordance with ISO 3846:2008	129
<b>Table. 7.1</b> Optimised coefficients for Equation 7.11.	144

## LIST OF FIGURES

<b>Fig. 1.1</b> Overtopping of embankments.	2
<b>Fig. 1.2</b> Breach in embankment at Overy Staithe Jan 1953. (Baxter (2005))	4
<b>Fig. 1.3</b> Embankment breach following Hurricane Katrina, New Orleans. August 30, 2005. (Source: FEMA) ( <a href="http://www.photolibrary.fema.gov/photodata/original/18177.jpg">http://www.photolibrary.fema.gov/photodata/original/18177.jpg</a> ).	5
<b>Fig. 3.1</b> Flow chart of RANS model key routines	36
<b>Fig. 4.1</b> Eulerian and Lagrangian velocity profiles.	47
<b>Fig. 4.2</b> Mass transport velocity profile for a progressive wave.	48
<b>Fig. 4.3</b> Circulating currents under a standing wave due to mass transport.	48
<b>Fig. 4.4</b> Vertical variations in $f(\chi)$ for a progressive wave.	50
<b>Fig. 4.5</b> Vertical mass transport profiles for values of $m$ .	51
<b>Fig. 4.6</b> Variation of $H$ with $\omega$ in turbulent (a) and laminar (b) cases, from Johns (1970).	53
<b>Fig. 4.7</b> Free surface profile calculated with the RANS model and calculated using second-order Stokes theory.	60
<b>Fig. 4.8</b> Peak horizontal velocity under a progressive wave from second-order Stokes theory and from the RANS model.	62
<b>Fig. 4.9</b> Vertical profile of mass transport for different phase averaging periods.	63
<b>Fig. 4.10</b> Vertical variation of mass transport within the boundary layer.	64
<b>Fig. 4.11</b> RANS model vertical variation of mass transport for a smooth and rough bed ( $k_s = 1.2$ mm).	65
<b>Fig. 4.12</b> Vertical variation of mass transport within the main part of the flow.	67
<b>Fig. 4.13</b> Vertical variations in $f(\chi)$ for a standing wave.	68
<b>Fig. 4.14</b> Free surface profile of generated wave calculated with the RANS model and calculated using second-order	75

Stokes theory, with reflecting wall at 14m.

<b>Fig. 4.15</b> Maximum horizontal velocity under a standing wave from the RANS model and analytical solution.	77
<b>Fig. 4.16</b> Horizontal velocity profiles for different phases in the standing wave boundary layer, experimental data (solid line) and analytical solution (dotted line).	78
<b>Fig. 4.17</b> Peak mass transport in the lower circulating cell for different phase averaging lengths.	78
<b>Fig. 4.18</b> Contours of averaged vorticity under a standing wave.	79
<b>Fig. 4.19</b> Mass transport velocity vectors showing circulation cells for standing waves.	80
<b>Fig. 4.20</b> Vertical profiles of mass transport velocity.	82
<b>Fig. 5.1</b> General set-up of flume with the model embankment.	85
<b>Fig. 5.2</b> Detail of the model embankment cross-section.	86
<b>Fig. 5.3</b> Location of pressure cells on the model embankment, dimensions in cm.	87
<b>Fig. 5.4</b> Example velocity time history from physical model.	89
<b>Fig. 5.5</b> A snap shot showing wave surface elevation, embankment detail and flow field velocity vectors plotted at every fifth node vertically and every tenth node horizontally.	90
<b>Fig. 5.6</b> A time history of discharge with a 0.4m x 0.1m mesh (T46q) and 0.2m x 0.05m mesh (T46qa).	93
<b>Fig. 5.7</b> A snap shot showing water surface elevation for mesh aspect ratio 1:4 (T46q) and 1:2 (T46qb).	94
<b>Fig. 5.8</b> Comparison of surface elevation time histories measured from mean water level at G4.	97
<b>Fig. 5.9</b> The effect of flume length on the generated waves.	98
<b>Fig. 5.10</b> Correlation between a) wave height and absolute relative error and b) Iribarren number and absolute relative error.	100
<b>Fig. 5.11</b> Comparison of discharge at P2 for 1.3m surge.	101
<b>Fig. 5.12</b> Comparison of discharge at P2 for T46q long and short flume tests.	102

<b>Fig. 5.13</b> Comparison of discharge at P2 for 0.81m surge.	103
<b>Fig. 5.14</b> Comparison of discharge at P2 for 0.29m surge.	104
<b>Fig. 5.15</b> Comparison of flow depth at P2 for 1.3m surge.	105
<b>Fig. 5.16</b> Comparison of flow depth at P2 for 0.81m surge.	106
<b>Fig. 5.17</b> Comparison of flow depth at P2 for 0.29m surge.	107
<b>Fig. 5.18</b> Comparison of flow velocities under combined discharge conditions at P2 for 1.3m surge.	108
<b>Fig. 5.19</b> Comparison of velocities under combined discharge conditions at P2 for 0.81m surge.	109
<b>Fig. 5.20</b> Comparison of velocities under combined discharge conditions at P2 for 0.29m surge.	109
<b>Fig. 5.21</b> RANS model calculated free surface profile for test T46u at 172s, showing a breaking wave at the embankment and the velocity vectors at every other point horizontally and vertically.	111
<b>Fig. 5.22</b> Depth-averaged velocity time history at P2 for Test T46u for different turbulence models.	114
<b>Fig. 5.23</b> The effect of bed roughness on dimensionless discharge.	115
<b>Fig. 5.24</b> Embankment profile (solid line), RANS calculated free surface (dotted line) and measured free surface at P1, P2, P3 and P4 (crosses) for Test T46u.	117
<b>Fig. 5.25</b> RANS model vertical profile of velocity during combined flow over the embankment crest.	118
<b>Fig. 5.26</b> Depth-averaged velocities and velocities at half the mean flow depth calculated from the RANS model results.	118
<b>Fig. 5.27</b> Depth, discharge and velocity recorded in the physical model for T47fa.	119
<b>Fig. 6.1</b> Dimensionless discharge and dimensionless negative freeboard for the RANS model test and calculated values based on $R_c$ calculated from Equation (2.15).	128
<b>Fig. 6.2</b> Embankment steady discharge, $q_{ws}$ and $R_c$ calculated with the RANS model discharge, measured in accordance with ISO 3846:2008.	131
<b>Fig. 6.3</b> Dimensionless discharge and dimensionless negative	131

freeboard for the RANS test and calculated values based on  $R_c$  evaluated in accordance with BS3846:2008 and a  $C_d$  value of 1.126.

<b>Fig. 7.1</b> Variation in embankment and seawall profiles tested by Reeve et al. (2008), left, and Hughes and Nadal (2009), right.	135
<b>Fig. 7.2</b> Variation in overflow discharge with crest width for three values of $R_c$ .	138
<b>Fig. 7.3</b> Flow patterns over rectangular broad and short-crested weirs.	139
<b>Fig. 7.4</b> Variation in combined discharge with crest width for three values of $R_c$ .	140
<b>Fig. 7.5</b> Dimensionless discharge and dimensionless negative freeboard calculated using Equations (2.17) and (2.18) and from the RANS tests at differing crest widths.	141
<b>Fig. 7.6</b> Goodness of fit of Equation (7.12) to Appendix B data.	145
<b>Fig. 7.7</b> Combined discharge predicted with Equation 7.12 and calculated with the RANS model, with line of best fit.	146
<b>Fig. 7.8</b> Variation in predicted discharge from Equation (2.12) and Equation (7.14).	147
<b>Fig. 7.9</b> Dimensionless combined discharge and dimensionless negative freeboard determined for the 74 test conditions given in Appendix B.	149
<b>Fig. A1</b> The threshold of motion of sediments under waves and/ or currents. From Soulsby (1997).	161
<b>Fig. A2</b> The threshold of motion on sloping beds.	162
<b>Fig. A3</b> Flow chart of hydrodynamic sediment transport and morphological models.	166
<b>Fig. A4</b> Circulating currents and bed profiles under a standing wave in front of a vertical wall for a) fine sediment and b) coarse sediment.	169
<b>Fig. A5</b> General set up of the numerical flume.	170
<b>Fig. A6</b> Progressive bed evolution for the wavelength nearest the reflecting boundary.	171
<b>Fig. A7</b> General set up of the numerical flume showing 1:8 beach slope and 4.7m water level.	174
<b>Fig. A8</b> Beach profile development in the physical model from López de San Roman-Blanco et al. (2006).	175

**Fig. A9** Beach profile development in the numerical model compared with the physical model.

176

## **ACKNOWLEDGEMENTS**

I would particularly like to thank my supervisor Prof Dominic Reeve for all the guidance and support given. Additionally I would like to thank my other supervisors Qingping Zou and Andrew Chadwick for good advice and helpful discussions.

I wish to kindly thank Professor Pengzhi Lin of Sichuan University, China for providing the original version of the RANS model and Dr Alec Torres-Freyermuth for providing the modified version of the wave generator subroutine. I also wish to thank Professor Steven Hughes of the US Army Corps of Engineers for providing the data from the levee overtopping study. I also wish to kindly thank Robert Uittenbogaard of Delft University who provided the data of the mass transport under progressive waves and Professor C. Lin of National Chung Hsing University, Taiwan, for providing the data for the standing wave validation part of this study.

I also wish to acknowledge the support of a scholarship provided by Britannia Royal Naval College and Plymouth University.

But most of all I would like to thank my family, Wendy, Eleanor, Megan, Hope and Miles for their continued patience.

## **AUTHOR'S DECLARATION**

At no time during the registration for the degree of Doctor of Philosophy has the author been registered for any other University award without prior agreement of the Graduate Committee.

The study was partly financed by the Britannia Royal Naval College, Plymouth University and the Institution of Civil Engineers.

Relevant scientific seminars and conferences were attended at which work was often presented; external institutions were visited for consultation purposes and in the course of this work journal and conference papers have been prepared for publication.

### **Publications**

#### **Journal paper:**

Jones, D., Zou, Q., Reeve, D. E., 2011. Computational modelling of coastal flooding caused by combined surge overflow and wave overtopping on embankments. Journal of Flood Risk Management (accepted)

#### **Conference papers:**

Jones, D., Zou, Q., Reeve, D. E., 2012. The effect of embankment crest width on overflow and wave overtopping of an embankment. 33<sup>rd</sup> International Conference on Coastal Engineering. Santander, Spain (abstract accepted)

Jones D. K., Reeve D. E. 2011. Computational modelling of combined storm surge and wave overtopping of embankments. PRIMaRE Annual Research Conference. April 2011, Plymouth UK

Jones, D., Zou, Q., Reeve, D. E., 2010. Simulation of wave overtopping with storm surge using a RANS model. 32<sup>nd</sup> International Conference on Coastal Engineering. Shanghai, China.

Word count of main body of thesis: 38,888

**Signed**.....

**Date**.....

# CHAPTER 1

## INTRODUCTION

### 1.1 Background

Low-lying areas of the world are often protected against coastal flooding by armoured earthen embankments, levees or dikes and the determination of adequate height of these structures is key to their success at protecting coastal areas. In determining the crest elevation, a balance must be met between the consequences of overtopping, against the cost of increasing crest elevation.

Coastal flooding is caused by combinations of high tides, waves, wave set-up and storm surges driven by wind set-up and low-pressure weather systems. It is expected that the likelihood of overtopping may well increase due to global warming effects such as sea level rise and increased storminess, which will cause more extreme waves and storm surges.

A storm surge is a rise in the sea level linked to low-pressure weather systems. The principal cause for the surge is the shear stress between the strong onshore wind and the water surface causing a near shore build-up of water. Other important factors that contribute to the surge are the rise in the water

height caused by the low-pressure system and the near shore bathymetry. It is the combined effect of the wind driven increase in water surface elevation and low pressure over shallower inshore waters that cause the storm surge.

However the storm surge is superimposed upon the astronomical tide and the worst case is when the surge coincides with a high tide.

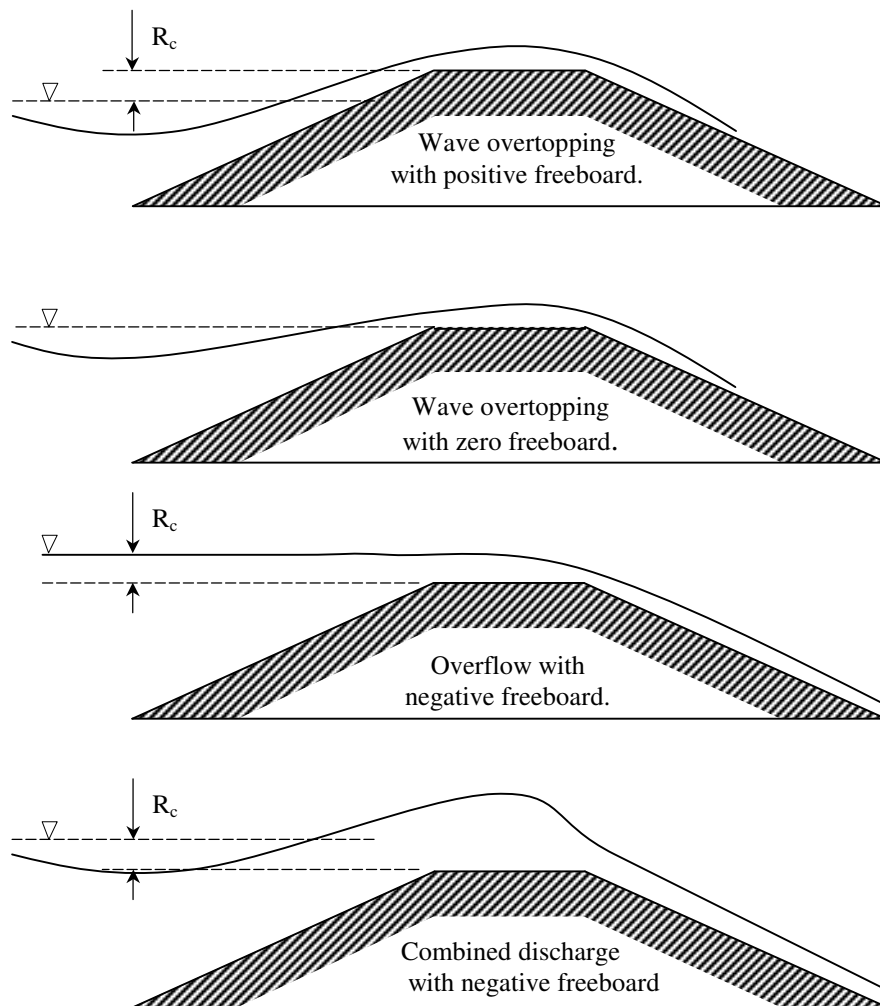


*Fig. 1.1 Overtopping of embankments*

The freeboard,  $R_c$  is the vertical distance between the mean water level and the embankment crest. This defined as positive when the mean water level is below the crest.

Embankment overtopping can result from combinations of contributing factors. An embankment with positive freeboard, can be overtopped as a result of large waves running up the front face of the structure and over the crest. This will result in intermittent overtopping. High tides combined with low-pressure weather systems can cause surge overflow where the mean water level rises above the crest elevation of the embankment, known as negative freeboard. This can cause overtopping with little or no waves. However low pressure weather systems are often associated with storms. So possibly the worst situation for overtopping will be caused by low-pressure storm surge combined with high tides causing overflow with negative freeboard combined with waves. It is this worst situation that is investigated in this thesis.

In what follows, to avoid confusion, the term 'overtopping' refers to wave overtopping a defence with positive freeboard, 'overflow' refers to the flow of water over a crest (negative freeboard) in the absence of waves and 'combined discharge' refers to the flow of water over the crest when waves are combined with negative freeboard conditions. These terms are clarified in Figure 1.1.

During extreme storm events, embankments may experience situations where the freeboard is very small or even negative, leading to a combined discharge. At these times, as well as the obvious danger presented by the volume of water flowing over the crest, there is also the potential for the overflow to remove any crest and lee side protection, erode the back face and possibly breach the embankment. Embankments are often constructed with an earthen core and clay top layer. If the overtopping rate is within permissible limits then the crest

and lee side may be protected with turf, the root system of the turf providing some modest protection from erosion during an overtopping event. If the embankment crest is expected to be subjected to periodic overtopping, the crest and the lee side are often protected by concrete mats to prevent scour, and possible embankment breach during an overtopping.



*Figure 1.2 Breach in embankment at Overy Staithe, Jan 1953. (Baxter, 2005)*

In the UK, the worst relatively recent example of an extreme water level occurred in 1953 when a storm formed south of Iceland. Strong winds and low barometric pressure caused a storm surge that funnelled down into the North Sea. The surge coincided with a spring tide and caused a storm surge of more than 2m south of the Humber estuary; and in the Netherlands the storm surge exceeded 3m (Baxter, 2005). The surge caused 1200 breaches of flood defences causing extensive flooding along the east coast of England. A breach in an embankment is shown in Fig. 1.2. The flooding caused a loss of 307 lives in the UK and over 1800 deaths in the Netherlands. Storm surges are not limited to the North Sea. Throughout much of the world, storm surges are a relatively common feature when hurricanes and tropical cyclones reach land. In

low-lying areas, protection from storm surges is often afforded by embankments. Fig 1.3 shows an embankment breach following hurricane Katrina during which the maximum surge level was between 3.4 and 4.6m. (FEMA-1605-DR-AL, 2006).

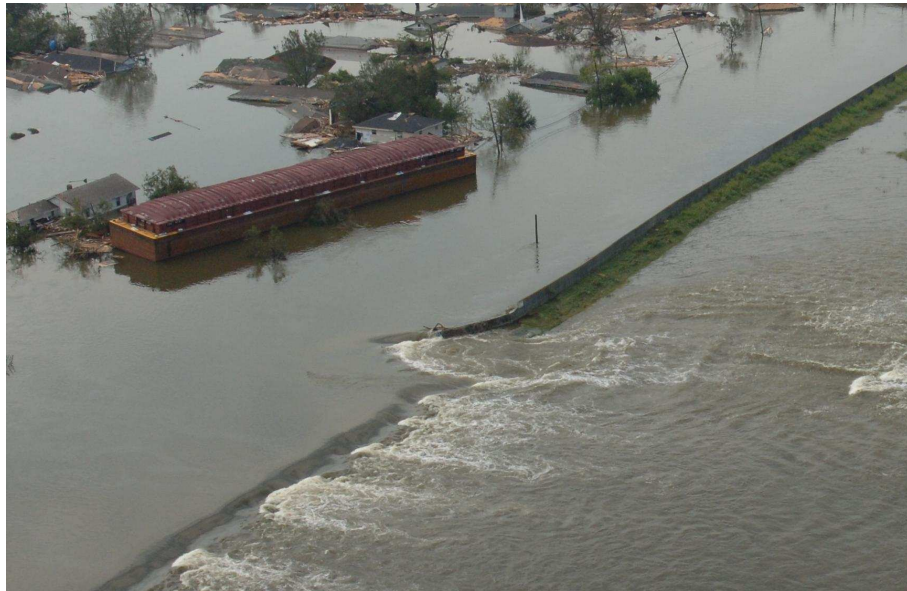


*Fig. 1.3. Embankment breach following Hurricane Katrina, New Orleans. August 30, 2005. (Source: FEMA)*

The crest elevation of embankments has historically been set by examination of local records or design formulae determined from physical models. For wave overtopping and run up on embankments with positive freeboard, the formulae for predicting wave-overtopping rates are usually based on empirical equations based on hydraulic model data. For this situation there exists extensive model data (van der Meer, 2005) against which to validate models. For surge overflow of a wide defence without waves, the situation is sometimes modelled as a broad crested weir. However, for combined discharge considerably less work has been conducted. Schuttrumpf (2001) developed equations for wave overtopping at zero freeboard based on experimental laboratory data. A method

given by Pullen (2007) to evaluate combined discharge is to sum the wave component derived for zero freeboard using the equation developed by Schuttrumpf along with the surge component calculated using weir equations. More recently, overtopping discharge formulae have been derived that allow the combined discharge to be calculated directly. This work was conducted by Reeve et al. (2008) and was carried out in a numerical wave flume using a Reynolds-averaged Navier-Stokes based wave model (RANS). The formulae produced were tested against the results predicted by Schuttrumpf combined with the weir equations. At that point, no hydraulic physical model data existed for combined wave and storm surge overtopping. More recently still, Hughes and Nadal (2009) reported the results of a laboratory study of overtopping caused by combined wave and storm surge and produced design equations that predicted more modest overtopping than Reeve et al. (2008) had predicted.

When calculating the combined discharge over embankments and seawalls, a number of parameters will be of interest to designers. These include overtopping discharge, the horizontal distribution of overtopping discharge normal to the defence alignment, flow thickness and flow velocity. In determining the overtopping discharge both the time average and maximum values are of interest. The average values may be used to determine flooding whereas the maximum values will help determine damage and injury. The horizontal distribution of the discharge may determine the location of safe distances from the crest. Flow thickness and velocities may be used to determine safe conditions and initiation of erosion of the crest. This study is principally concerned with average overtopping discharge.

## 1.2 Study objectives

The aim of this study is to assess the performance of the RANS model at describing complex hydrodynamic flow situations. Once confident that the model can adequately describe these situations, the model will be used to investigate embankment overtopping situations for which there is currently no design advice.

The study assesses the ability of a modified version of the RANS numerical model used by Reeve et al. (2008) to directly reproduce on a wave-by-wave basis the tests conducted by Hughes and Nadal (2009). This is achieved by using an alternative wave absorbing boundary condition developed by Torres-Freyermuth (2007), which allows a wave time history as input but without the usual wave absorbing sponge layer required to allow the outgoing waves to leave the computational domain without reflection.

In order to adequately describe the complex hydrodynamic flow at an embankment crest during combined overtopping, the RANS model must be able to describe the highly non-linear flow caused by the interaction between the wave overflow and weir overflow components. To demonstrate the capability of the RANS model to describe non-linear flow, an assessment of the model's ability to describe mass transport flow under standing and progressive waves is conducted. It is anticipated that the model's ability to represent mass transport will be useful for future developments of the RANS model.

The objectives of this study are to:

- Demonstrate that the RANS model can adequately describe the flow at an embankment crest during combined overtopping by comparing the flow calculated with the RANS model and experimental data.
- Assess the model's ability to describe mass transport flow under standing and progressive waves by comparing with experimental data and theoretical results.
- Compare the combined discharge rates calculated with the RANS model with those calculated with available design formulae.
- Investigate differences between the combined discharge rates found with current design formulae.
- Use the RANS model to examine the effects of embankment crest width on the overtopping discharge.

In Chapter 2, a description of current design formulae used to determine discharge over embankments is given along with the criteria used to determine safe average overtopping discharges. In Chapter 3, a description of the RANS model is given together with the main mathematical assumptions, initial conditions and boundary conditions as well as the wave generation methods. In Chapter 4, an assessment is made of the model's ability to describe mass transport flow under standing and progressive waves. In Chapter 5, the RANS model is used to simulate combined discharge over an embankment and the flow is compared to available experimental model data. A comparison between numerical and experimental flow parameters is conducted on a wave-by-wave

basis. In Chapter 6, the combined discharge calculated with the RANS model is compared with values calculated with available design formulae. In Chapter 7, the RANS model is applied to investigate the effect of embankment crest width on combined discharge. Finally, in Chapter 8, a discussion of the findings and conclusions is given.

## **CHAPTER 2**

### **WAVE OVERTOPPING DESIGN FORMULAE**

#### **2.1. Introduction**

In this section some commonly used design formulae employed to estimate discharge rates for wave overtopping of embankments are presented. The overtopping of embankments depends on environmental variables such as wave climate as well as the embankment configuration but there is no universal design formula for predicting discharge rates over embankments. Design formulae exist for particular embankment or seawall configurations and for a specified range of wave criteria. These formulae are usually empirically derived and based on small scale physical model data or numerical model data, mostly validated against available physical model tests.

In this chapter, a review of current design formulae is given for embankments with positive, zero and negative freeboard. Although overtopping of seawalls with positive freeboard is not directly part of this study, the design equations are given to provide context against which the design formulae of zero and positive freeboard were derived.

## 2.2. Positive freeboard

Most seawalls and embankments are designed so that the crest is above the water level at mean high water springs and consequently wave overtopping can only result from higher tidal levels and relatively large waves running up the seaward slope. The important parameters in determining combined discharge are the wave environment and the magnitude of the freeboard and some design equations are just a function of these variables. However, other important parameters are seaward slope,  $\alpha$ , wave angle, water depth at structure,  $h_c$ , roughness,  $r$ , permeability, berm location, berm size, revetment wall details and crest width,  $w$ . These parameters are taken into account in some of the design formulae. However, no design formula takes all of the parameters into account and design formulae represent simplified situations.

An overview of the form of available overtopping models for embankments and seawalls with positive freeboard is given in Table 2.1 from Hedges and Reis (1998) and Burcharth and Hughes (2002). The general form of the relationships between the dimensionless average discharge,  $Q$ , and the dimensionless freeboard,  $R$ , is given by Hedges and Reis (1998) as:

$$Q = a \exp(-bR) \quad (2.1)$$

or

$$Q = aR^{-b} \quad (2.2)$$

<i>Authors</i>	<i>Structure Type</i>	<i>Model</i>	<i>Dimensionless Discharge Q</i>	<i>Dimensionless Freeboard R</i>
Owen (1980,1982)	Impermeable smooth, rough, straight and bermed slopes	$Q = a \exp(-bR)$	$\frac{q}{g H_s T_{om}}$	$\frac{R_c}{H_s} \left( \frac{S_{om}}{2\pi} \right)^{0.5} \frac{1}{\gamma}$
Bradbury and Allsop (1988)	Rock armoured impermeable slopes with crown walls	$Q = aR^{-b}$	$\frac{q}{g H_s T_{om}}$	$\left( \frac{R_c}{H_s} \right)^2 \left( \frac{S_{om}}{2\pi} \right)^{0.5}$
Aminti and Franco (1988)	Rock, cube, and Tetrapod double layer armour on rather impermeable slopes with crown walls, (single sea state)	$Q = aR^{-b}$	$\frac{q}{g H_s T_{om}}$	$\left( \frac{R_c}{H_s} \right)^2 \left( \frac{S_{om}}{2\pi} \right)^{0.5}$
Ahrens and Heimbaugh (1988b)	7 different seawall /revetment designs	$Q = a \exp(-bR)$	$\frac{q}{\sqrt{g H_s^3}}$	$\frac{R_c}{(H_s^2 L_{op})^{1/3}}$
Sawaragi et al (1988)		-	$\frac{q}{g L_s H_s}$	$\frac{R_c}{H_s}$
Pedersen and Burcharth (1992)	Rock armoured rather impermeable slopes with crown walls	$Q = aR$	$\frac{q T_{om}}{L_{om}^2}$	$\frac{R_c}{H_s}$
van der Meer and Janssen (1995)	Impermeable smooth, rough straight and bermed slopes	$Q = a \exp(-bR)$	$\frac{q}{\sqrt{g H_s^3}} \sqrt{\frac{S_{op}}{\tan \alpha}}$ for $\xi_{op} < 2$ $\frac{q}{\sqrt{g H_s^3}}$ for $\xi_{op} > 2$	$\frac{R_c \sqrt{S_{op}}}{H_s \tan \alpha} \frac{1}{\gamma}$ for $\xi_{op} < 2$ $\frac{R_c}{H_s} \frac{1}{\gamma}$ for $\xi_{op} > 2$
Franco et al. (1994)	Vertical wall breakwater with and without perforated front	$Q = a \exp(-bR)$	$\frac{q}{\sqrt{g H_s^3}}$	$\frac{R_c}{H_s} \frac{1}{\gamma}$
Pedersen (1996)	Rock armoured permeable slopes with crown walls	$Q = R$	$\frac{q T_{om}}{L_{om}^2}$	$3.2 \times 10^{-5} \frac{H_s^5 \tan \alpha}{R_c^3 A_c B}$

Table 2.1 Dimensionless discharge, dimensionless freeboard and overtopping models based partly on Hedges and Reis (1998) and Burcharth and Hughes (2002).

The best fit coefficients  $a$  and  $b$  are particular to the configuration of the seawall or embankment. To be physically realistic, when the freeboard is large the overtopping discharge should be zero and when the freeboard is zero the overtopping discharge should be large but finite. However, Equations (2.1) and (2.2) predict a small dimensionless discharge when  $R$  is large and when  $R$  is

zero Equation (2.2) gives an infinite dimensionless discharge. To overcome these unrealistic scenarios Hedges and Reis (1998) suggested an equation of the form:

$$Q = a(1 - R)^b \quad (2.3)$$

The table highlights some of the current models used to determine wave overtopping with positive freeboard and indicates the considerable amount of work conducted in this area. Perhaps this is best illustrated by the CLASH database, van der Meer (2005), which contains 10532 results from 163 test series from institutions throughout the world for wave overtopping investigations with positive or zero freeboard. The purpose of the database is both as an inventory of conducted wave tests and in providing data against which numerical models can be validated.

The dataset has been recently used by Goda (2009) to derive a set of equations to predict wave overtopping,  $q_w$ , at vertical and sloping seawalls. The principal equation (2.4) is dependent upon the significant wave height at the toe of the structure,  $H_s$ , the freeboard,  $R_c$ , the gravitational constant,  $g$ , and the coefficients  $A$  and  $B$ . The formula is of the same general form as Equation (2.1). The coefficients allow the equation to be fitted to the CLASH dataset and depend upon seabed slope, seawall slope and water depth at the toe of the structure. The formula is applicable only to smooth and impermeable vertical and inclined seawalls.

$$\frac{q_w}{\sqrt{gH_s^3}} = \exp\left[-\left(A + B\frac{R_c}{H_s}\right)\right] \quad (2.4)$$

The equations given by the EurOtop Manual, (Pullen, 2007), for the deterministic design of wave overtopping of simple slopes with positive freeboard is given in Equations (2.5). The equations are for breaking and non breaking waves (Iribarren numbers,  $\xi_{om-1,0} < 5$ ) and gives the overage overtopping discharge.

$$\frac{q_w}{\sqrt{gH_{m0}^3}} = \frac{0.067}{\sqrt{\tan \alpha}} \gamma_b \xi_{om-1,0} \exp \left[ -4.3 \frac{R_c}{\xi_{om-1,0} H_{m0} \gamma_b \gamma_f \gamma_\beta \gamma_v} \right]$$

with a maximum of (2.5)

$$\frac{q_w}{\sqrt{gH_{m0}^3}} = 0.2 \exp \left[ -2.3 \frac{R_c}{H_{m0} \gamma_b \gamma_\beta} \right]$$

The symbols  $\gamma_b \gamma_f \gamma_\beta$  and  $\gamma_v$  represent the influence of berm, slope roughness, angle of attack and vertical wall on the embankment crest. The equations were compared with data from the CLASH dataset but not fully calibrated against the data. These formulae tend to overestimate large overtopping rates and underestimate the smaller overtopping rates (Goda, 2009).

The equations given by van der Meer (1995), Equations (2.6) and (2.7), are very similar to those given by Pullen (2007). However, these equations are based on the significant wave height,  $H_s$ , rather than the energy based significant wave height,  $H_{m0}$ .

$$\frac{q_w}{\sqrt{gH_s^3}} = 0.06 \frac{\xi_{op}}{\sqrt{\tan \alpha}} \exp \left[ -5.2 \frac{R_c}{\xi_{op} H_s \gamma_b \gamma_f \gamma_\beta \gamma_h} \right] \text{ for } \xi_{op} < 2 \quad (2.6)$$

with a maximum of

$$\frac{q_w}{\sqrt{gH_s^3}} = 0.2 \exp \left[ -2.6 \frac{R_c}{H_s \gamma_b \gamma_f \gamma_\beta \gamma_h} \right] \quad \text{for } \xi_{op} > 2 \quad (2.7)$$

The additional factors taken into account differ, with  $\gamma_v$  being replaced with  $\gamma_h$  which is the water depth at the toe of the structure. The equations given by van der Meer (1995) are used extensively within Europe (Reeve, 2008), along with the formulae developed by Owen (1980) and Hedges and Reis (1998).

Although a significant amount of research has been conducted into wave overtopping of embankments and seawalls with positive freeboards, an inspection of the available formulae indicates that there is still some significant inherent variability of predicted overtopping rates.

### **2.3. Zero freeboard**

Overtopping at zero freeboard is the situation when the mean water level is at the same level as the crest of the embankment. Therefore any wave crest at an embankment with zero freeboard will result in some degree of overtopping. As already stated, the CLASH data set contains 10532 results for positive and zero freeboard. However only 86 of these results, 0.8%, relate to wave overtopping of structures with zero freeboard. It is not surprising that the bulk of research has been conducted for situations with positive freeboard because this situation is most likely to occur. However, although overtopping with zero and negative freeboard is possibly rare, the consequences can be severe. Therefore understanding of the discharge relationships for these situations is important.

An investigation of wave overtopping with zero freeboard was carried out by Schuttrumpf (2001). In this study, a series of physical model tests of overtopping with zero freeboard on simple embankments was conducted so that

discharge equations could be formulated. The embankment slopes investigated were 1:3, 1:4 and 1:6 and both regular and random waves were tested.

Schuttrumpf made the assumption that a first approximation to the wave overflow can be found from the simple weir formula, Equation (2.8):

$$q = \frac{2}{3} C_d \sqrt{2g} h_u^3 \quad (2.8)$$

where the upstream head over the weir,  $h_u$ , is replaced by the wave height,  $H$ .  $C_d$  is an overtopping coefficient and is a function of embankment slope,  $\tan \alpha$  and wave steepness,  $H/\lambda$ , where  $\lambda$  is the wave length. Schuttrumpf gave the dimensionless relationship

$$Q = \frac{q}{\sqrt{2g} h_u^3} = \frac{2}{3} C_d = f(\tan \alpha, H/\lambda) = f(\xi) = d \times \xi \quad (2.9)$$

where  $Q$  is the dimensionless discharge

$$\xi \quad \text{is the Iribarren number, defined as } \xi = \frac{\tan \alpha}{\sqrt{H/\lambda}}$$

and

$d$  is a constant.

The value of the constant was found by regression analysis of physical model test data. For regular waves, the equation for the mean overtopping rate, at zero freeboard, is given in Equations (2.10).

$$\frac{q}{\sqrt{2g} H^3} = 0.063 \xi \quad \text{for } \xi < 2$$

and (2.10)

$$\frac{q}{\sqrt{2g} H^3} = 0.168 - \frac{0.336}{\xi^3} \quad \text{for } \xi > 2$$

As there was little data available for random waves, the physical model wave spectra were generated as a sum of randomly generated regular wave components assuming a Rayleigh distribution. The sequence of individual waves was generated randomly. For each wave, with wave parameters  $H_i$  and  $T_i$ , the mean wave overtopping rate  $q$  was based on Equation (2.11).

$$q = \frac{1}{N} \sum_{i=1}^N q_i(H_i, T_i) \quad (2.11)$$

$N$  = number of waves

$q_i$  = wave overtopping rate of a single wave with the wave height  $H_i$  and the wave period  $T_i$

$q$  = average overtopping rate

For random waves, the equation for the mean overtopping rate, at zero freeboard, is given by Equations (2.12).

$$\frac{q}{\sqrt{2gH_s^3}} = 0.038 \xi_{om} \quad \text{for } \xi_{om} < 2$$

and (2.12)

$$\frac{q}{\sqrt{2gH_s^3}} = 0.096 - \frac{0.160}{\xi_{om}^3} \quad \text{for } \xi_{om} > 2$$

Although wave overtopping with zero freeboard is in itself a rare occurrence, the equations given by Schuttrumpf (2001) are important because they provide a useful upper limit for the positive freeboard overtopping equations. They also provides the lower limit for overtopping with negative freeboard.

## 2.4. Negative freeboard

When the mean water level is above the crest level of the embankment, the overtopping discharge can be expected to be large and almost continuous with the discharge only stopping during the troughs of larger waves. This situation is

usually a result of high tides coinciding with a storm surge caused by strong onshore winds and low-pressure systems. This situation can also result when the crest level has been reduced as a result of embankment failure.

The consequences of embankment overtopping can clearly cause flooding on the lee side of the embankment. However, overtopping can also cause erosion and damage the embankment structure. In extreme cases, the erosion can lead to failure of the embankment.

Until recently, very little research had been conducted into wave overtopping with negative freeboard. Some research conducted by Gibson (1930) used physical model tests to investigate the effect of relatively small waves on the discharge over rectangular, v-notch and broad crested weirs and found that the presence of waves increased the overall overtopping discharge. The paper made recommendations for corrections to discharge calculations for v-notch and rectangular weirs in the presence of waves. However, for broad crested weirs the results were irregular and it was recommended that broad crested weirs should not be used for measurement in the presence of waves of significant magnitude. More recently, the analogy between overtopping of weirs and overtopping of embankments has been employed by Pullen (2007) to develop a methodology to calculate combined discharge over an embankment. This considered the overtopping of the embankment to contain two components: the component due to the surge and the component due to the waves. The part of the overflow discharge due to the storm surge was calculated by assuming the embankment would behave similarly to a broad

crested weir and can be estimated by Equation (2.13), in which  $R_c$  is the negative freeboard.

$$q_{surge} = 0.6\sqrt{g|-R_c^3|} \quad (2.13)$$

The wave component  $q_{waves}$  can be found using the equation for discharge over embankments with zero freeboard developed by Schuttrumpf (2001), Equations (2.12) for random waves. An estimate of the combined discharge is given by the superposition of the surge component and the wave component.

$$q_{ws} = q_{surge} + q_{waves} \quad (2.14)$$

Clearly this simple addition of the two components is a coarse approximation to reality and does not fully describe the complex hydrodynamic situation; it might, however, be expected to provide a reasonable first approximation to the problem.

It should be noted that flow at the crest of a broad crested weir progresses from sub-critical flow near the flooded side to critical and then supercritical flow on the lee side. Therefore, the flow depth on the embankment crest will vary with location across the crest. Consequently, the overflow discharge calculated from Equation (2.13) will vary depending where the negative freeboard was measured. An alternative equation used to determine discharge over broad crested weirs,  $q_t$ , is given in ISO 3846:2008 which is the international standard for flow over broad crested weirs. This equation is given as:

$$q_t = C_d \times 1.705bh_u^{3/2} \quad (2.15)$$

where  $b$  is the weir breadth and  $h_u$  is the upstream depth above the weir crest and  $C_d$  is 1.0 for ideal fluids. For real fluids,  $C_d$  has been derived empirically by

Ackers et al (1978). For  $0.45 < h_u/L_w < 0.8$  and  $0.35 < h_u/(h_u+h_c) < 0.6$ ,  $C_d$  has been given by Chadwick & Morfett (1998) as:

$$C_d = 0.848 \left[ 0.91 + 0.21 \frac{h_u}{L_w} + 0.24 \left( \frac{h_u}{h_u + h_c} - 0.35 \right) \right] \quad (2.16)$$

where  $L_w$  is the width of the weir crest and  $h_c$  is the height of the weir crest measured from the bed. The key difference between Equation (2.13) and Equation (2.15) is the measurement location for the depth of flow. If recorded at the weir crest, the flow depth in Equation (2.13) would be subject to the drawdown that occurs near broad crested weirs. The upstream depth used in Equation (2.15) would correspond to the surge level calculated from tide and meteorological conditions and may be better suited to this application.

Combined discharge over seawalls was also investigated by Reeve et al. (2008). A series of random waves tests using a RANS model were used to investigate combined discharge over seawalls with negative freeboard. As no full scale or physical model datasets were available to validate the model, the limiting physical constraints were used as a check. These are: when there are no waves the discharge should be well predicted by the equation for a broad crested weir, Equation (2.15); and when the level of the negative freeboard becomes zero the discharge should be well predicted by the equation for discharge at zero freeboard, Equation (2.12), for random waves. The expressions for combined wave overtopping and storm surge developed by Reeve et al. (2008) are given in Equations (2.17). The equations are based on regression analysis of the numerical flume tests for irregular breaking and non-breaking waves on seawalls with slopes 1:3, 1:4 and 1:6 and small negative dimensionless freeboards ( $R = R_c/H_s$ ) in the region  $0.0 > R \geq -1.0$ .

$$\frac{q}{\sqrt{g.H_s^3}} \cdot \frac{\sqrt{\tan \alpha}}{\xi_p} = 0.051 \exp\left(-1.98 \frac{R_c}{H_s \xi_p}\right) \quad \text{for } \xi_p < 2.0$$

(2.17)

$$\frac{q}{\sqrt{g.H_s^3}} = 0.233 \exp\left(-1.29 \frac{R_c}{H_s}\right) \quad \text{for } \xi_p \geq 2.0$$

Reeve et al. (2008) compared the combined discharge calculated from Equations (2.17) with the combined discharge calculated from the equation for zero freeboard and the broad crested weir equation. The comparison used Equation (2.15) as the equation for a broad crested weir, with  $C_d$  determined with Equation (2.16). It was noted that a comparison of combined discharge calculated with Equations (2.17) gave a higher estimate when compared to the combined discharge calculated with Equations (2.12) and (2.15).

Hughes and Nadal (2009) conducted a series of laboratory experiments of combined discharge over embankments. The experimental set-up for these tests was based on embankment configuration, surge levels and wave conditions experienced during Hurricane Katrina in America in 2005. The tests were conducted at a scale 1:25 for irregular breaking and non-breaking waves on a seawall slope of 1:4.25. The negative freeboards tested were 0.29, 0.81 and 1.3m. A regression analysis of physical model test data gave Equation (2.18).

$$\frac{q}{\sqrt{g.H_{m0}^3}} = 0.034 + 0.53 \left(\frac{-R_c}{H_{m0}}\right)^{1.58} \quad \text{for } R_c < 0 \quad (2.18)$$

The Hughes and Nadal (2009) tests were for one embankment slope only, so the result will be only applicable to that slope. It was noted that the effect of different side slopes would reduce as the surge level increases.

Wave and combined wave and surge overtopping during Hurricane Katrina was also investigated by Lynett (2010). Boussinesq model predictions of overtopping rates were used to develop empirical equations for predicting discharge based on negative freeboard. However, the derived equations were specific to the Mississippi River Gulf Outlet and cannot be generally applied.

In passing, it should be noted that, although well established, this range of predictors for combined discharge over embankments indicates some degree of uncertainty. For example, relationships inferred from computer models will be influenced by the assumptions inherent in each numerical model, while relationships derived from laboratory experiments will be subject to experimental error, scaling effects and so on. In this thesis, a comparison is made between the overtopping discharge for negative freeboard calculated with the above formulae and the RANS model.

## **2.5. Acceptable overtopping discharge**

The main function of an embankment or seawall is the prevention of flooding caused by overtopping and coastal erosion. However, these structures rarely completely prevent overtopping but reduce the level of overtopping to be within acceptable limits. The determination of these acceptable limits is the focus of this section.

The main hazards caused by overtopping of coastal structures are: injury or death of people near the structure, property damage and economic effects, damage to the defensive structure and possible breach and inconvenience caused by lower level flooding.

The function of a structure will determine the maximum permissible overtopping limits for that structure. For some situations, significant overtopping may be permissible, for example near a harbour entrance. However, further from the entrance, certain overtopping levels could cause damage if the area is used for mooring. For most structures, the overtopping limit is dependent upon the vulnerability of the area behind the seawall to damage from overtopping waves.

The overtopping limits can be specified in terms of :

- average overtopping discharge,  $q$ ;
- individual and peak overtopping volumes;
- overtopping velocities;
- overtopping flow depth;
- overtopping horizontal distribution.

The design criteria for wave overtopping can be either the limit set during normal service conditions or overtopping during extreme conditions, perhaps where some structural damage may be permissible. Most descriptions of overtopping have been in terms of  $q$  expressed as flow rate per metre run of seawall  $m^3/s/m$  or for lower flows  $l/s/m$ . However, at the peak of a storm the overtopping discharge from individual waves can be over 100 times the average overtopping discharge. The spatial and temporal variation of peak discharge

varies considerably. Some guidance on the limiting maximum overtopping volumes are given by Pullen (2007) and some information is available about the probability distribution of the overtopping volume per wave.

$q$ m <sup>3</sup> /s per m	SAFETY OF TRAFFIC		STRUCTURAL SAFETY				$q$ litres/s per m
	VEHICLES	PEDESTRIANS	BUILDINGS	EMBANKMENT SEAWALLS	GRASS EMBANKMENT	REVETMENTS	
10 <sup>0</sup>	Unsafe at any speed	Very dangerous	Structural damage	Damage even if fully protected	Damage	Damage even for paved promenade	1000
10 <sup>-1</sup>				Damage if back slope unprotected		Damage if promenade not paved	100
10 <sup>-2</sup>				Damage if crest not protected		Start of damage	10
10 <sup>-3</sup>	Dangerous on grass embankments and horizontal composite breakwaters	No damage	No damage	No damage	1		
10 <sup>-4</sup>						Unsafe parking on horizontal composite breakwaters	Dangerous on vertical wall breakwaters
10 <sup>-5</sup>	Unsafe parking on vertical wall breakwaters	Uncomfortable but not dangerous	Minor damage to fittings, sign posts, etc.	No damage	No damage	0.01	
10 <sup>-6</sup>	Unsafe driving at high speed	Wet, but not uncomfortable					No damage
10 <sup>-7</sup>	Safe driving at all speeds						

Table 2.2 Critical values of average overtopping discharge (from Burcharth and Hughes (2002)).

Recently, some destructive field tests have been conducted on grass-covered dikes using a wave overtopping simulator which determines the extent of erosion caused by large individual waves, Steendam (2010). Little data is currently available for the determination of safe overtopping velocities. Pullen et al. (2007) states that the limiting velocity for people and vehicles should be set to be below 2.5 to 5 m/s. Clearly, this is an area that requires additional work as

the flow velocity during an overtopping event may determine the level of damage. For example, the flow velocity is likely to determine if erosion will occur on an embankment.

Limits for the mean discharge have been determined for the onset of damage to pedestrians and vehicles or the structural safety of embankments, seawalls and buildings. These limits for injury to people have been determined by De Gerloni et al. (1991), Franco et al. (1994) and Endoh and Takahashi (1994) by simulating the effect of wave overtopping on people with falling water jets and full scale tests. Permissible limits for grass embankments were determined by Smith et al. (1994). Tsuruta and Goda (1968), Goda (1970) and Fukuda et al. (1974) found the overtopping limits for embankments and revetments. The critical values of average overtopping discharge from these studies were summarised by Burcharth and Hughes (2002) and is given in Table 2.2.

In determining the tolerable maximum overtopping discharge, the characteristics of the structure crest and the area immediately behind the seawall or embankment may be important. For example, if the embankment has a seaward sloping crest then the overtopping wave will be slowed, whereas if the crest slopes toward the lee side, the overtopping wave may accelerate. Clearly the characteristics of the embankment and the area behind the embankment should be taken into account alongside the critical values of overtopping discharge.

In determining the tolerable overtopping discharge, no account has been taken of the effect of wind. However, the effect of wind is likely to increase overtopping discharge particularly for lower flows; De Rouck et al. (2005).

In this chapter, current design formulae have been presented for wave overtopping of coastal structures with positive, zero and negative freeboard. Additionally the limiting acceptable overtopping discharge for various situations is also given. In the next chapter, a description is given of the numerical model used in this study.

## CHAPTER 3

### NUMERICAL MODELLING

#### 3.1. Introduction

In this chapter a review of the key numerical models used to simulate wave overtopping of coastal structures is presented. Some of the advantages and disadvantages of different models are discussed and an explanation for using the RANS-VOF model in the current study is given. A brief description of the RANS-VOF model then follows.

Many researchers have used computational models to simulate wave overtopping of coastal structures. The numerical model's success depends upon the equations and solution techniques used and how the model computes features such as turbulence and the free surface. Usually, models that offer a more complete description of the flow dynamics require greater computational effort.

A computational model often used for wave overtopping of structures uses the non-dispersive non-linear shallow water equations (NSWE). This type of model is derived by vertically integrating the Navier–Stokes equation and assumes a

hydrostatic pressure distribution, uniform vertical velocity profile and negligible vertical acceleration. With these assumptions NSWE models prove to be computationally efficient. However, in order to satisfy the shallow water limit, the seaward boundary has to be placed near the structure. Additionally, these models use a semi-empirical approach to estimate the initiation of wave breaking. These models work well from the surf zone shoreward, but do not model frequency dispersion, (Brocchini and Dodd 2008). So wave propagation in deeper water is inadequately modelled. Kobayashi and Wurjanto (1989) used an extended model of this type to investigate monochromatic wave overtopping of impermeable coastal structures on a sloping beach. The validated model proved to be capable of representing wave shoaling and reflection effects to calculate average wave overtopping rates. Also, Hu et al. (2000) used a NSWE model (Amazon) to simulate storm waves propagating in the surf zone and overtopping of vertical and near vertical structures. Good agreement was found with experimental data but further validation was required for irregular waves. Hubbard and Dodd (2002) have used NSWE models to investigate wave run up and overtopping of seawalls. These tests included random waves at off-normal incidence. Tuan and Oumeraci (2010) used a NSWE with an additional term associated with roller energy dissipation to simulate average and individual overtopping events. Whilst it was found that average overtopping rates were well modelled, the model performed less well for individual overtopping events.

An alternative model used for wave overtopping studies is based on the Boussinesq equations. These equations can be considered an extension of NSWE theory that applies to waves of shorter wavelengths and larger depths, where dispersion is significant (Madsen et al.1991). The Boussinesq equations

used in wave models were derived by Peregrine (1967), by vertically integrating the momentum and conservation of mass equations. Models based on the Boussinesq equations are limited in that they do not ‘naturally’ simulate wave breaking and, for higher order, Boussinesq models (e.g., fifth order) are more demanding to solve numerically (Brocchini and Dodd, 2008). However, Boussinesq type models have been applied to wave run up and overtopping. Stansby (2003) used a Boussinesq model for wave run up and overtopping of solitary waves. Comparison with experiments without wave breaking provided good agreement. Boussinesq type models simulate breaking wave processes with the addition of an extra term for energy dissipation due to wave breaking. This type of model was used by Chen et al. (2000) to investigate wave run up and overtopping and compared reasonably well against laboratory experiments. Also, Lynett et al. (2010) used a Boussinesq model to provide detailed predictions of wave run up and overtopping of embankments protecting New Orleans during Hurricane Katrina. However, a Boussinesq model does not readily lend itself to capturing the detail of the complex flow patterns at the embankment crest or on the leeside of the embankment.

To improve the ability of a model at describing the complexities of flow that occur during wave overtopping, a model should be used that makes no assumptions of the vertical flow structure. This is true of the Smoothed Particle Hydrodynamics (SPH) model, which is a mesh-free Lagrangian method that has been successfully applied to wave overtopping of structures. The method divides the flow into discrete elements or particles, and the fluid flow is computed as the trajectories of particles, which interact according to the Navier–Stokes equations. This has the advantage that it is possible to track

large free surface deformations, as well as fragmentation and coalescence of water. However, the accuracy of the SPH method depends on the number of particles represented, and for increased number of particles the method becomes less computationally efficient. This method has been used by a number of researchers to investigate wave overtopping. Gómez-Gesteira et al. (2005) used a two-dimensional SPH scheme to examine the overtopping of a flat plate. Gotoh et al. (2004) investigated regular wave overtopping over partially immersed breakwaters and overtopping of a vertical seawall was investigated by Gotoh et al. (2005). Dalrymple and Rogers, (2006) used SPH methods to investigate breaking waves on a beach but included some work on green water overtopping. Shao et al. (2006) used an SPH model to investigate the wave overtopping of a seawall and Lv et al. (2009) revisited this problem using a 3-D hybrid level set model coupled with the Volume of Fluid (VOF) surface-capturing scheme. To the best of the author's knowledge, the SPH model has yet to be applied to combined discharge.

An alternative to the SPH model, that also makes no assumptions of the vertical flow structure, is the fixed mesh Eulerian approach, based on the Navier–Stokes equations. This provides a more efficient alternative to the SPH model, although it remains computationally expensive in comparison with NSWE methods. It has the advantage of providing a more complete description of flow and overcomes the limitations associated with using a particular wave theory. This type of model has the ability to calculate wave breaking by including a turbulence model and by considering the Reynolds Averaged Navier-Stokes (RANS) equations. RANS models are often combined with a VOF surface-capturing scheme that allows the model to treat large free surface deformations.

Numerous researchers have been working with this type of model, with applications that include wave breaking and overtopping. Lin and Liu (1998a) developed a two-dimensional RANS model based on a previous model called RIPPLE, Kothe et al. (1991). Numerous researchers have subsequently used this model or its variants to investigate surf zone dynamics. For example, Hsiao and Lin (2009) used this model to investigate solitary waves overtopping of trapezoidal seawalls. However, there are a number of other RANS based models. For example, Lara et al. (2008) and Losada et al. (2008) used an alternative RANS model to investigate wave run-up, transmission, wave overtopping and breaking on low-mound breakwaters.

In this study the RANS-VOF model developed by Lin and Liu (1998a) is used. This offers the advantage of being a depth resolved model and so describes the vertical variation in velocities and turbulence that is not offered in models such as the NSWE or the Boussinesq models. Additionally, during wave overtopping and breaking, the RANS-VOF model can consider large deformations with the Volume of Fluid surface-capturing scheme. Models such as the Boussinesq model can only accommodate relatively mild free surface curvatures and so are not fully capable of describing breaking waves. A description of the RANS-VOF model is given below.

### **3.2. RANS model**

The two-dimensional breaking wave numerical model used in this study was developed by Lin and Liu (1998a) and is described here. The model is based on an earlier Navier-Stokes equation solver called RIPPLE, which was developed at Los Alamos Laboratory (Kothe et al. 1991). In this chapter, a brief description

of the main features of the RANS model is presented. Descriptions of the main mathematical assumptions, initial conditions and boundary conditions as well as the wave generation methods are given. A more complete description of the RANS model is given in Lin and Liu (1998a,b).

The RANS model is able to calculate the free surface and general turbulent flow by decomposing the flow in the model into the mean flow and turbulent fluctuations. This results in a set of equations for the mean flow containing contributions from the fluctuating turbulence flow. This requires the introduction of a turbulence model to describe the effects of these fluctuations on the mean.

The model solves the RANS equations by splitting the turbulent velocity and pressure into two parts, the mean velocity and pressure  $\langle u_i \rangle$  and  $\langle p \rangle$  and the turbulent fluctuation components of velocity and pressure  $u_i'$  and  $p'$  so that

$$u_i = \langle u_i \rangle + u_i' \quad \text{and}$$

$$p = \langle p \rangle + p'$$

where  $i, j = 1, 2$  for two dimensional flow. If these are substituted into the Navier-Stokes equations:

$$\frac{\partial u_i}{\partial x_i} = 0 \tag{3.1}$$

$$\frac{\partial u_i}{\partial t} + u_j \frac{\partial u_i}{\partial x_j} = -\frac{1}{\rho} \frac{\partial p}{\partial x_i} + g_i + \frac{1}{\rho} \frac{\partial \tau_{ij}}{\partial x_j} \tag{3.2}$$

and if the fluid is assumed to be incompressible then the Reynolds Averaged Navier-Stokes equations become:

$$\frac{\partial \langle u_i \rangle}{\partial x_i} = 0 \quad (3.3)$$

$$\frac{\partial \langle u_i \rangle}{\partial t} + \langle u_j \rangle \frac{\partial \langle u_i \rangle}{\partial x_j} = -\frac{1}{\rho} \frac{\partial \langle p \rangle}{\partial x_i} + g_i + \frac{1}{\rho} \frac{\partial \langle \tau_{ij} \rangle}{\partial x_j} - \frac{\partial \langle u_i' u_j' \rangle}{\partial x_j} \quad (3.4)$$

where the Reynolds stress is the product of the density and the correlation of the velocity fluctuation,  $\rho \langle u_i' u_j' \rangle$ ,  $\rho$  is the density,  $g$  is the acceleration due to gravity and  $\tau_{ij}$  is the viscous stress. The mean viscous stress,  $\langle \tau_{ij} \rangle$  is given as:

$$\langle \tau_{ij} \rangle = \mu \frac{\partial \langle u_i \rangle}{\partial x_j} + \mu \frac{\partial \langle u_j \rangle}{\partial x_i} \quad (3.5)$$

### 3.2.1. Turbulence model

In the model, the Reynolds stress is assumed to be related to the mean flow strain rate and the characteristic scales of turbulence by a non-linear algebraic stress model, called the  $\kappa$ - $\varepsilon$  model, (Shih et al., 1996):

$$\rho \langle u_i' u_j' \rangle = \frac{2}{3} \rho \kappa \delta_{ij} - C_\mu \rho \frac{\kappa^2}{\varepsilon} \left( \frac{\partial \langle u_i \rangle}{\partial x_j} + \frac{\partial \langle u_j \rangle}{\partial x_i} \right) - \rho \frac{\kappa^3}{\varepsilon^2} \left( C_1 \left( \frac{\partial \langle u_i \rangle}{\partial x_l} \frac{\partial \langle u_l \rangle}{\partial x_j} + \frac{\partial \langle u_j \rangle}{\partial x_l} \frac{\partial \langle u_l \rangle}{\partial x_i} - \frac{2}{3} \frac{\partial \langle u_k \rangle}{\partial x_l} \frac{\partial \langle u_l \rangle}{\partial x_k} \delta_{ij} \right) + C_2 \left( \frac{\partial \langle u_i \rangle}{\partial x_k} \frac{\partial \langle u_j \rangle}{\partial x_k} - \frac{1}{3} \frac{\partial \langle u_l \rangle}{\partial x_k} \frac{\partial \langle u_l \rangle}{\partial x_k} \delta_{ij} \right) + C_3 \left( \frac{\partial \langle u_k \rangle}{\partial x_i} \frac{\partial \langle u_k \rangle}{\partial x_j} - \frac{1}{3} \frac{\partial \langle u_l \rangle}{\partial x_k} \frac{\partial \langle u_l \rangle}{\partial x_k} \delta_{ij} \right) \right) \quad (3.6)$$

$C_\mu$ ,  $C_1$ ,  $C_2$  and  $C_3$  are empirical coefficients and  $\delta_{ij}$  is the Kronecker delta (equals 1 if  $i = j$ , and 0 if  $i \neq j$ ).  $\kappa$  is the turbulent kinetic energy,  $\varepsilon$  is the

turbulent kinetic energy dissipation rate and  $\nu$  is the kinematic viscosity,  $\nu = \frac{\mu}{\rho}$ .

Where:

$$\kappa = \frac{1}{2} \langle u_i' u_j' \rangle \quad \text{and} \quad \varepsilon = \nu \langle (\partial u_i' / \partial x_j)^2 \rangle \quad (3.7)$$

Lin and Liu (1998a) found the value of the coefficients from:

$$C_\mu = \frac{2}{3} \left( \frac{1}{7.4 + S_{\max}} \right), \quad C_1 = \frac{1}{185.2 + D_{\max}^2} \quad (3.8)$$

$$C_2 = -\frac{1}{58.5 + D_{\max}^2}, \quad C_3 = \frac{1}{370.4 + D_{\max}^2}$$

where

$$S_{\max} = \kappa / \varepsilon \max \left( \left| \frac{\partial u_i}{\partial x_i} \right| \right) \quad \text{and} \quad D_{\max} = \kappa / \varepsilon \max \left( \left| \frac{\partial u_i}{\partial x_j} \right| \right)$$

The conventional eddy viscosity model is found when  $C_1 = C_2 = C_3 = 0$  giving:

$$\langle u_i' u_j' \rangle = \frac{2}{3} \kappa \delta_{ij} - 2\nu_t \langle \sigma_{ij} \rangle \quad (3.9)$$

where  $\sigma_{ij}$  is the strain rate tensor and  $\nu_t$  is the eddy viscosity given by Lin and

Losada (2002) as:

$$\nu_t = C_\mu \kappa^2 / \varepsilon \quad (3.10)$$

and  $C_\mu = 0.09$

The value of the turbulent kinetic energy,  $\kappa$ , and the turbulence dissipation,  $\varepsilon$ , are found by solving the transport equations for turbulent kinetic energy and turbulence dissipation:

$$\frac{\partial \kappa}{\partial t} + \langle u_j \rangle \frac{\partial \kappa}{\partial x_j} = \frac{\partial}{\partial x_j} \left[ \left( \frac{\nu_t}{\sigma_\kappa} + \nu \right) \frac{\partial \kappa}{\partial x_j} \right] - \langle u_i' u_j' \rangle \frac{\partial \langle u_i \rangle}{\partial x_j} - \varepsilon \quad (3.11)$$

$$\frac{\partial \varepsilon}{\partial t} + \langle u_j \rangle \frac{\partial \varepsilon}{\partial x_j} = \frac{\partial}{\partial x_j} \left[ \left( \frac{\nu_t}{\sigma_\varepsilon} + \nu \right) \frac{\partial \varepsilon}{\partial x_j} \right] + C_{1\varepsilon} \frac{\varepsilon}{\kappa} \nu_t \left( \frac{\partial \langle u_i \rangle}{\partial x_j} + \frac{\partial \langle u_j \rangle}{\partial x_i} \right) \frac{\partial \langle u_i \rangle}{\partial x_j} - C_{2\varepsilon} \frac{\varepsilon^2}{\kappa} \quad (3.12)$$

$\sigma_k$ ,  $\sigma_\varepsilon$ ,  $C_{1\varepsilon}$ ,  $C_{2\varepsilon}$  are coefficients.

The values for the coefficients have been found experimentally by Rodi (1980)

and are:  $\sigma_k = 1.0$ ,  $\sigma_\varepsilon = 1.3$ ,  $C_{1\varepsilon} = 1.44$ ,  $C_{2\varepsilon} = 1.92$

### 3.2.2. Numerical scheme

The RANS model uses the two-step projection finite difference method (Chorin, 1968) to solve the Reynolds Averaged Navier-Stokes equations. The two step method is used to split the finite difference approximation to the momentum equation into two steps. The finite difference approximation to the momentum equation is:

$$\frac{u_i^{n+1} - u_i^n}{\Delta t} + u_j^n \frac{\partial u_j^n}{\partial x_j} = \frac{1}{\rho^n} \frac{\partial p^{n+1}}{\partial x_i} + g_i + \frac{\partial \tau_{ij}^n}{\partial x_j} \quad (3.13)$$

The initial step used to obtain a tentative velocity,  $\tilde{u}$ , without the term for the pressure gradient:

$$\frac{\tilde{u}_i^{n+1} - u_i^n}{\Delta t} = -u_j^n \frac{\partial u_j^n}{\partial x_j} + g_i + \frac{\partial \tau_{ij}^n}{\partial x_j} \quad (3.14)$$

The second step is to update the velocity using the new pressure information:

$$\frac{u_i^{n+1} - \tilde{u}_i^{n+1}}{\Delta t} = -\frac{1}{\rho^n} \frac{\partial p^{n+1}}{\partial x_i} \quad (3.15)$$

The new pressure information is obtained by solving the Poisson Pressure Equation:

$$\frac{\partial}{\partial x_i} \left( \frac{1}{\rho^n} \frac{\partial p^{n+1}}{\partial x_i} \right) = \frac{1}{\Delta t} \frac{\partial \tilde{u}_i^{n+1}}{\partial x_i} \quad (3.16)$$

The Poisson Pressure Equation is derived from the finite difference approximation to the continuity equation and Equation (3.15).

A flow chart showing the RANS model key routines is shown in Fig. 3.1.

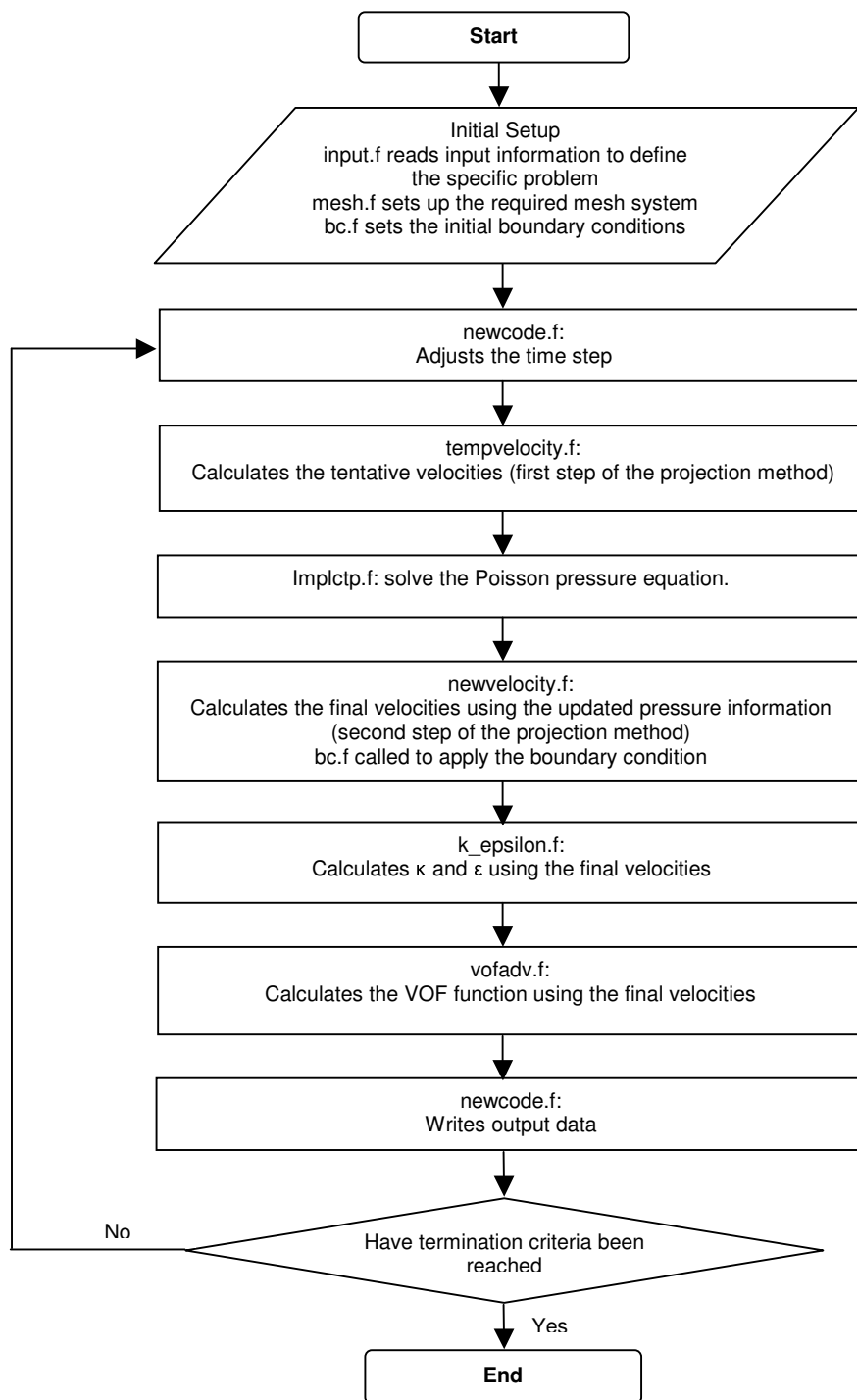


Fig. 3.1 Flow chart of RANS model key routines.

The time derivative is discretized with the forward time difference method. The pressure gradient terms are discretized using the central difference method and other convective terms are discretized by a combination of the central difference and upwind method.

The computational domain is discretized as an  $m \times n$  mesh system. The scalar quantities are given at the cell centres i.e. pressure, turbulence intensity, and eddy viscosity, and the vector quantities, i.e. velocities, are specified at the cell nodes. The model is able to utilise both a uniform and non-uniform mesh. Although a uniform mesh can produce more accurate results, often a non-uniform mesh is used to reduce computational cost. Additionally, a non-uniform mesh can be used to increase resolution in regions of greater flux, such as near regions where waves may break.

### 3.2.3. Initial Conditions

The model requires initial conditions for the mean flow and pressure distribution across the whole computational domain. These are often taken from initial stationary flow at the start of a test with zero mean velocity and hydrostatic pressure. However, the velocity field can be specified along with initial free-surface displacements from laboratory measurements or analytical solutions.

An inspection of the transport equations shows that if  $\kappa$  is zero then the production and dissipation term for  $\varepsilon$  becomes singular. Additionally, if  $\kappa$  is zero the model will produce no turbulence energy if there is no initial turbulent kinetic energy. Consequently, it is necessary to initially set  $\kappa$  to a small non-zero figure. This is given in Lin and Liu (1998a) as:

$$\kappa = \frac{1}{2} u_t^2 \quad (3.17)$$

with  $u_t = \delta_c C_r$  where  $C_r$  is the wave celerity at the inflow boundary and

$\delta_c = 2.5 \times 10^{-3}$ . Experiments conducted by Lin and Liu (1998a) found that

numerical results in the surf zone were insensitive to small changes in  $\delta_c$ .

However, near the breaker point, results became sensitive to changes in  $\delta_c$ .

Lower values of  $\delta_c$  have been found to delay the initiation of breaking.

The value of  $\varepsilon$  in the model is estimated from:

$$\varepsilon = C_\mu \frac{\kappa^2}{v_t} \quad (3.18)$$

with  $v_t = 0.1v$ .

### 3.2.4. Boundary Conditions

The usual boundary conditions are applied within the model. That is the zero stress term is applied at the surface and the no-slip boundary and free-slip boundary condition can be applied at any solid boundary. The no-slip conditions are defined as,

$$\langle u_n \rangle = 0, \langle u_{\tau_k} \rangle = 0 \quad (3.19)$$

with  $n$  and  $\tau_k$  denoting the normal and tangential components. However, the application of the no-slip condition at the boundary is only applied if the viscous boundary layer is resolved. If the viscous boundary layer is not resolved then a free-slip condition is more appropriate at a solid boundary.

$$\langle u_n \rangle = 0 \quad \frac{\partial \langle u_{\tau_k} \rangle}{\partial n} = 0 \quad (3.20)$$

In this case, the turbulent field near the solid boundary is described using the log-law to find the distribution of mean tangential velocities within the boundary layer. This is given as:

$$\frac{\langle u \rangle}{u^*} = \frac{1}{K} \ln \left( E \frac{u^* z_b}{\nu} \right) \quad (3.21)$$

where  $K = 0.41$  is the Von Karman constant,  $u^*$  is the friction velocity,  $z_b$  is the vertical coordinate from the bed and  $E = 9.0$  for smooth walls. This equation allows values of  $\kappa$  and  $\varepsilon$  to be expressed as a function of distance from the solid boundary:

$$\kappa = \frac{u^{*2}}{\sqrt{C_\mu}} \quad (3.22)$$

$$\varepsilon = \frac{u^{*3}}{K z_b} \quad (3.23)$$

On the free surface it is assumed that the turbulence does not diffuse across the free-surface boundary. So, at the surface, the gradients for  $\kappa$  and  $\varepsilon$  are set to zero;

$$\partial\kappa/\partial n = 0, \quad \partial\varepsilon/\partial n = 0 \quad (3.24)$$

### 3.2.5. Free surface reconstruction

The wave surface profile is tracked using the volume of fluid method (VOF).

The method was originally developed by Hirt and Nichols (1981) and later modified by Kothe et al. (1991). This method defines a function  $F(x,y,t)$  that represents the fraction of fluid in a cell. When  $F$  is 1 the cell is completely filled with fluid and there is no water surface. When  $F$  is 0 the cell is empty and again there is no water surface. At values of  $F$  between 0 and 1 a free surface exists.

The free surface is reconstructed by tracking the derivative of  $F$ . The normal direction to the boundary lies in the direction in which  $F$  is changing most rapidly. The VOF function is governed by:

$$\frac{\partial F}{\partial t} + u \frac{\partial F}{\partial x} + v \frac{\partial F}{\partial z_b} = 0 \quad (3.25)$$

A benefit of the VOF method is that it requires the minimum of computational storage, i.e. one per cell, which is consistent with the storage requirements of other dependent variables. Also, as the VOF method follows regions rather than boundaries, it avoids problems with intersecting surfaces.

### 3.2.6. Solid objects

The definition of solid objects within the computational domain is treated in a similar way to the VOF function. An openness function is calculated for each cell and represents the proportion of the cell open to flow. The openness function differs from the VOF function in that it is time invariant. Both the VOF and openness function allow the shape of the free surface and structures to be viewed using contour plots.

### 3.2.7. Open boundary condition

The open boundary condition is used at the inlet and outlet open boundaries use the radiation boundary condition and the sponge layer. This allows the outgoing waves to exit the computational domain whilst minimising wave reflection.

The radiation boundary condition is:

$$\frac{\partial \varphi}{\partial t} + C_r \frac{\partial \varphi}{\partial x} = 0 \quad (3.26)$$

where  $\varphi$  is any physical variable associated with the wave, such as velocity or surface elevation and  $C_r$  is the wave celerity. The wave celerity is calculated using:

$$C_r = \sqrt{\frac{g\lambda}{2\pi} \tanh\left(\frac{2\pi}{\lambda}(\eta + h)\right)} \quad \text{for short waves} \quad (3.27)$$

$$C_r = \sqrt{g(\eta + h)} \quad \text{for long waves} \quad (3.28)$$

Lin and Liu (1998a) showed that this boundary condition works well for waves up to intermediate non-linear waves,  $H/h < 0.3$ .

The sponge layer is placed in front of an absorbing boundary to prevent waves reflecting back into the computational domain. This is achieved in the RANS model by including an extra damping term in the original momentum equation (Equation (3.4)). Wei and Kirby (1995) gave the form of the damping factor  $d(x)$  as:

$$d(x) = \frac{\exp\left[\left(\frac{x_s - x}{x_s}\right)^n - 1.0\right]}{\exp(1.0) - 1.0} \quad (3.29)$$

in which  $x_s$  is the length of the sponge layer and  $x$  is the distance between the point on the sponge layer and the boundary,  $n$  is equal to 10 in the current model. The sponge layer method of absorbing reflected waves has the disadvantage of considerably increasing the computational domain.

### 3.2.8. Wave generation

The wave generation used within the RANS model developed by Lin et al. (1999) can use two different methods to generate waves: the conventional method that sends waves from the boundary and the source function method generates waves within the domain.

The conventional wave boundary specifies an absorbing-generating boundary condition for the RANS model. For depth-averaged models only the surface elevations are needed at the inlet boundary. Kobayashi et al. (1987) used an absorbing-generating boundary based on linear superposition of incident and reflected waves. However, this can only be applied to small amplitude waves and can lead to cumulative errors. The RANS model requires the specification of both the velocity and surface information at the boundary. Petit et al. (1994) used Equation (3.30) to determine the incident wave whilst simultaneously absorbing the weakly reflected wave.

$$\frac{\partial R_t}{\partial t} + C_r \frac{\partial R_t}{\partial x} = 0 \quad (3.30)$$

$R_t$  is any physical variable associated with the total wave and is found from  $R_t = R_i + R_r$ . The variable  $R_i$  is associated with the incident wave and  $R_r$  is the variable associated with the reflected wave. As this method uses linear wave assumptions, this approach can only be used for small amplitude waves.

An alternative method uses a mass source function in a specific region inside the computational domain. This method removes the difficulty of specifying the incident waves through an inflow boundary whilst absorbing reflected waves. To generate waves using the source function, Equation (3.1) is modified to give:

$$\frac{\partial u}{\partial x} + \frac{\partial v}{\partial z} = s(x, z, t) \quad (3.31)$$

where  $s(x, z, t)$  is a non zero mass source function within the region,  $\Delta$ . The source function causes the free surface to respond to the mass change and the gravitational restoring force generates a train of surface gravity waves. In the RANS model the source function is a rectangular region. If it is assumed that all the mass increase and decrease in the source region contribute to generating

the target wave, then:

$$\int_0^t \int_{\Delta} s(x, z, t) d\Delta dt = 2 \int_0^t C_{\phi} \eta(t) d(t) \quad (3.32)$$

where  $C_{\phi}$  is the phase velocity and the factor 2 on the right side of the above equation is due to waves being generated on both sides of the source region.

For this study linear waves and 2<sup>nd</sup> order Stokes waves are used. For linear waves,  $\eta(t) = H \sin(\sigma t)$  the source function  $s(x, z, t)$  is:

$$s(t) = \frac{C_{\phi} H}{A} \sin(\sigma t) \quad (3.33)$$

where  $A$  is the area of the source region.

For 2<sup>nd</sup> order Stokes wave:

$$s(t) = \frac{C_{\phi} H}{A} \cos(\sigma t + p_s) + \frac{C_{\phi} k H^2}{8A} \frac{\cosh(kh)}{\sinh^3(kh)} (2 + \cosh(2kh)) \cos(2\sigma t + 2p_s) \quad (3.34)$$

where  $p_s$  is a phase shift constant used to ensure the source function starts from zero; where  $p_s$  is given as:

$$p_s = \arcsin\left(\frac{-a_s + \sqrt{a_s^2 + 8b_s^2}}{4b_s}\right) \quad (3.35)$$

where,  $a_s = H/2$  and:

$$b_s = H^2 k \cosh(kh) \frac{(2 + \cosh(2kh))}{16 \sinh^3(kh)} \quad (3.36)$$

It has been found that the positioning of the internal mass source is important.

For example, if the source is placed too close to the water surface the generated wave is too steep and if it placed too deep the wave is too small. It has been found that the optimum position for the internal mass source region should be specified as follows:

- The width of the source region should be less than 5% of the wavelength.
- The height of the region should be between  $\frac{1}{4}$  and  $\frac{1}{3}$  of the water depth, with the top the region always below the trough.
- The region should be at least  $\frac{1}{2}$  wavelength from the open boundary to avoid false reflections.

In a further development of the model by Torres-Freyermuth (2007), the wave generation uses a wave time history defined at the seaward boundary. This is sometimes used in preference to the mass source function (Lin et al. 1999) because the absorbing sponge layer is not required at absorbing boundaries and leads to a more efficient reduction in computational domain. However, the main feature of this adaptation is the ability of the boundary condition to absorb long-waves. This is important in modelling mild slope beaches. The assumptions used within this wave generating procedure are that high frequency energy is dissipated by the breaking waves at the beach and long wave components reflected from the shore propagate as non-dispersive waves according to linear shallow water wave theory. So that, at the boundary, linear superposition between incident and reflected waves is valid.

In this study, the two-dimensional breaking wave numerical model described in this chapter is used to model mass transport under progressive and standing waves and combined discharge over embankment crests. In the following chapter, a validation procedure is carried out to assess the model ability to describe mass transport.

## **CHAPTER 4**

### **MODEL VERIFICATION**

#### **4.1. Introduction**

For the RANS model to adequately describe the complex hydrodynamic flow at an embankment crest during combined overtopping, it must be capable of describing the highly non-linear flow caused by the interaction between the wave overflow and weir overflow components. As an example of the RANS model's ability to describe non-linear flow, this chapter assesses the model's ability to describe the second order mass transport flow under standing and progressive waves. The model's ability to represent mass transport will be useful for future anticipated developments of the RANS model.

The RANS model provides a description of velocities within the surf zone and it is possible to provide a detailed description of velocities near the bed in this region. An improved prediction of bed velocities will allow the parameters important for sediment transport to be more accurately calculated and it is planned that the author will incorporate sediment transport within the RANS model at a later date. Initial development of the RANS model in this area is included in Appendix A. The mass transport is of particular interest for sediment

transport because these drift velocities appear to be important for predicting bar formation.

## **4.2. Mass transport model validation**

Although wave motions are often thought to be purely oscillatory, measurements of velocities under waves show the existence of time-averaged currents. Although these currents are usually small compared with the oscillatory components of velocity, their effect is cumulative and so over time they are thought to have a significant effect on transport of sediments. As a validation exercise for the RANS model, the ability of the model to reproduce the mass transport velocities has been investigated. The ability of the model to reproduce mass transport, which is at second order to the wave induced velocity, is a significant challenge for a wave model. A brief description of the development of mass transport theory is now given.

## **4.3. Previous work**

Stokes (1847) showed that for a perfect non-viscous fluid, individual particles in an irrotational progressive wave do not describe a closed path. The particles have a second-order mean Lagrangian and Eulerian velocity in the direction of the progressive wave. The Eulerian velocity is obtained by examining the flow from a fixed point and the Lagrangian velocity is obtained by the frame of reference moving with the particle as it changes location. The Lagrangian velocity results from a fluid particle in a sine wave moving forward with a larger velocity at the top of its orbit than the backwards velocities at the bottom. The particles move with the wave during the forward part of the motion and against it during the backward part of the motion. Consequently it will travel forwards

more than it travels backwards, Nielsen (1992). The Eulerian velocity is as a result of the forward velocity near the water surface as a result of the waveform. Near beaches this forward net transport of water at the surface will result in a uniform return velocity in the seaward direction. Both Lagrangian and Eulerian velocities are purely based on continuity considerations. The general form of the Eulerian and Lagrangian drift velocities is shown in Fig. 4.1.

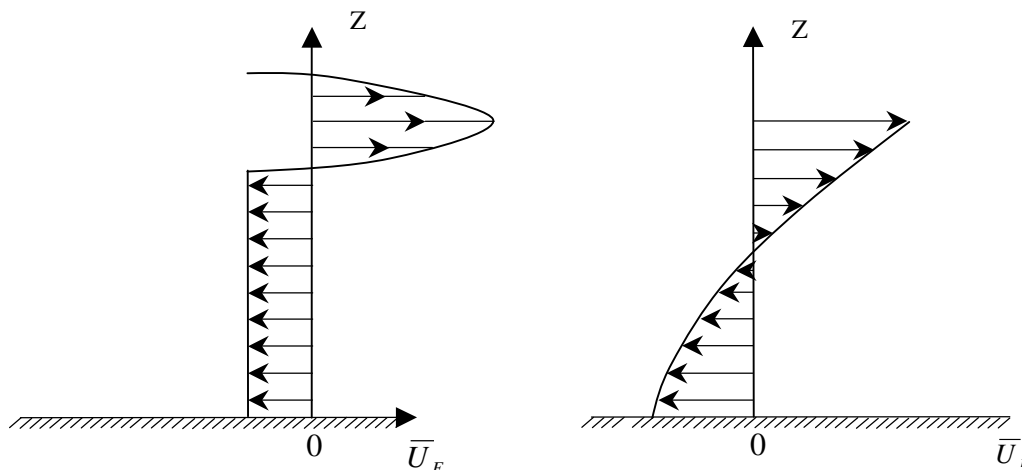


Fig. 4.1 Eulerian and Lagrangian velocity profiles.

The velocity distribution for both the Lagrangian and Eulerian drift discussed above would lead to a seaward net velocity near the bed for a progressive wave. In fact, most measurements under non-breaking waves actually show a shoreward drift near the bed. The Lagrangian and Eulerian drifts are based on the idea of a perfect, non-viscous fluid. Longuet-Higgins (1953) developed a general theory of a time-averaged mass transport that takes into account viscous effects for progressive waves of finite amplitude for laminar flow. The vertical distribution of mass transport velocity for a progressive wave is shown in Fig. 4.2. The wave induced streaming in the boundary layer is always in an onshore direction.

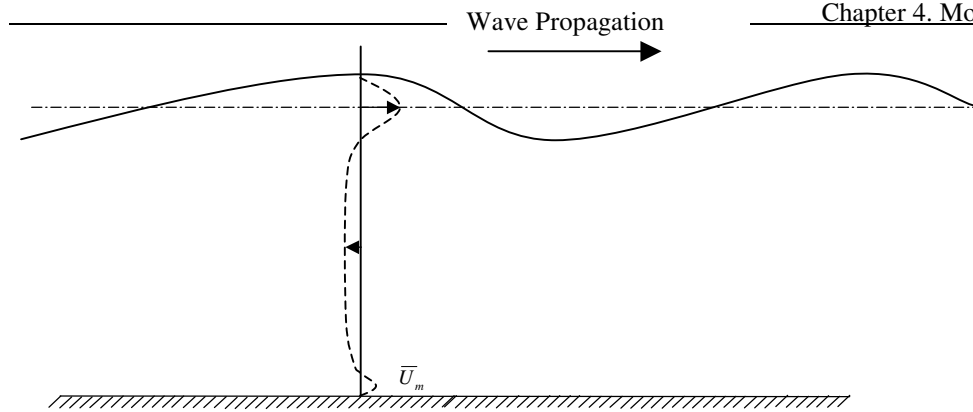


Fig. 4.2 Mass transport velocity profile for a progressive wave.

Within the same paper, Longuet-Higgins (1953) applied the general theory developed for a progressive wave to regular standing waves. In this case, the steady mass transport within the lower boundary layer developed as a circulating current from anti-node to node. Further circulating currents developed above this layer but in the opposite direction. In fact, Longuet-Higgins solutions suggest that the number of circulating cells in the vertical direction could be infinite but the lower cell is always from anti-node to node. These currents are shown in Fig. 4.3 for two vertical cells.

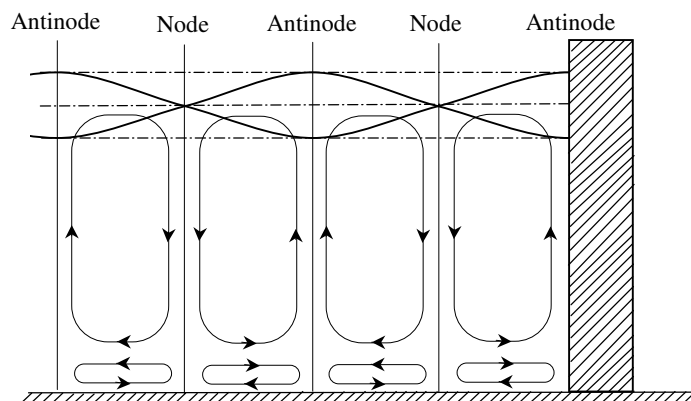


Fig. 4.3 Circulating currents under a standing wave due to mass transport.

#### 4.4. Model testing

In order to evaluate the model performance at reproducing these wave-induced currents, two main cases are to be tested. The first case looks at the ability of the model to predict the steady streaming due to progressive waves. The

second case considers the performance of the model in calculating the steady streaming under standing waves. In both cases, the RANS results are compared with available theoretical and experimental data.

#### 4.5. Progressive wave theory

In this section, the development of mass transport theory for progressive waves is described, followed by an account of the available comparative data. Finally, an assessment is made of the ability of the RANS model to represent mass transport under progressive waves.

Longuet –Higgins (1953) showed that the nature of mass-transport within the interior of the fluid depends on the ratio  $a^2/\delta^2$ , where  $a$  is the amplitude of the first order wave and the thickness of the boundary layer is of order  $\delta$ , where  $\delta = (2\nu/\sigma)^{1/2}$  and  $\sigma = 2\pi/T$ . When the ratio  $a^2/\delta^2$  is small, the nature of mass transport is different to when  $a^2/\delta^2$  is large. These correspond to the ‘conduction solution’ and ‘convection solution’ respectively. In nearly all practical cases  $a^2/\delta^2 \gg 1$  and so for the situations studied here the convection solution should be the most applicable.

The magnitude of the mass transport within the boundary layer does not depend on the ratio  $a^2/\delta^2$  but depends on the boundary conditions and the first order motions. The equation for mass transport within the bottom boundary layer at a stationary boundary is given by:

$$\bar{U} = \frac{a^2 \sigma k}{4 \sinh^2 kh} f(\chi) \quad (4.1)$$

where  $f(\chi) = (5 - 8e^{-\chi} \cos \chi + 3e^{-2\chi})$  and  $\chi = \frac{h - z_b}{\delta}$

The vertical profile of mass transport varies with the function  $f(\chi)$ . This function is plotted against  $\chi$  in Fig. 4.4.

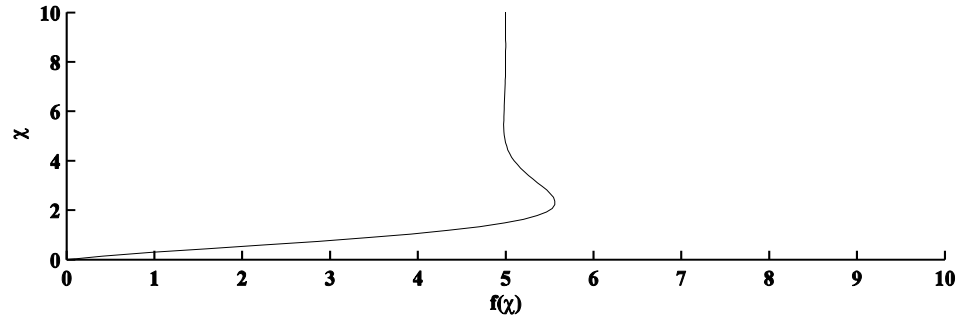


Fig. 4.4 Vertical variations in  $f(\chi)$  for a progressive wave.

It can be seen that the transport is always positive and as  $\chi$  tends to infinity, the value of  $f(\chi)$  tends to 5. So, just beyond the boundary layer, the equation for mass transport (4.1) becomes:

$$\bar{U} = \frac{5a^2 \sigma k}{4 \sinh^2 kh} \quad (4.2)$$

It can also be seen that the peak value of mass transport within the boundary layer will be when  $f(\chi) = 5.5$ , i.e. when:

$$\bar{U} = \frac{5.5a^2 \sigma k}{4 \sinh^2 kh} \quad (4.3)$$

In the interior of the fluid, the mass transport is given by:

$$\bar{U} = \frac{a^2 \sigma}{4 \sinh^2 kh} \left( \frac{8k^3}{4k^2 + d^2} \cosh 2k(z-h) + \frac{k(12k^2 + 5d^2) \cos dz}{(4k^2 + d^2) \cos dh} - \frac{8k^2(2k^2 + d^2)}{d(4k^2 + d^2)} \sinh(2kh) \frac{\sin d(z-h)}{\cos dh} \right) \quad (4.4)$$

where:

$$d^2 = 4k^2 + \frac{m^2 \pi^2}{h^2} \quad \text{and } m \text{ is a integer}$$

There exists an infinite number of solutions to this mass transport equation depending on the value chosen for  $m$ . The solution for mass transport within the boundary layer is not dependent on  $m$  and so only one solution exists. Fig. 4.5 shows how the mass transport varies through the water column for values of  $m$  from 1 to 3. Clearly all of these cannot be true simultaneously. When the wave amplitude is large compared to  $\delta$  it is not possible to predict the mass transport above the boundary layer. Longuet-Higgins suggested that this was because when  $\frac{a^2}{\delta^2}$  is large the diffusion of vorticity by convection along the streamlines will be much greater than the diffusion by viscous conduction.

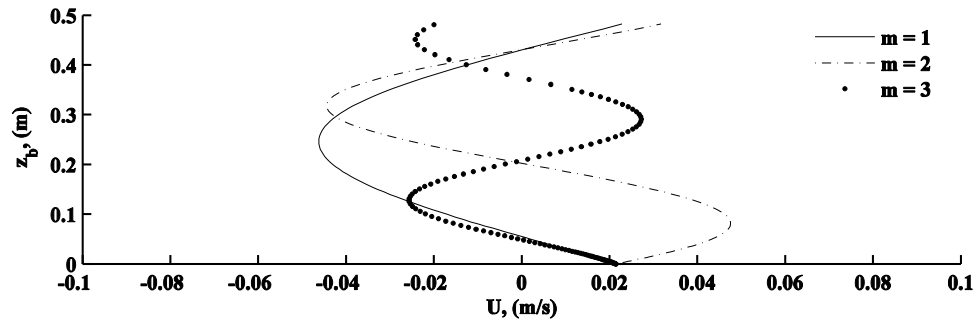


Fig. 4.5 Vertical mass transport profiles for values of  $m$ .

Although the convection solution does not have a unique value, the conduction solution for flow in the interior is unique. This situation applies when  $\frac{a^2}{\delta^2}$  is small. If the thickness of the boundary layer is of the order 0.5mm, then this situation will apply in only very limited circumstances. In the interior, the conduction solution is given by:

$$\bar{U} = \frac{a^2 \sigma k}{4 \sinh^2 kh} \left[ \cosh 2kh(\chi - 1) + 3 + kh \sinh 2kh (3\chi^2 - 4\chi + 1) + 3 \left( \frac{\sinh 2kh}{2kh} + \frac{3}{2} \right) (\chi^2 - 1) \right] \quad (4.5)$$

where  $\chi = \frac{z_b}{h}$

In an annex to a paper by Russell and Osorio (1958), Longuet-Higgins extended the previous work on laminar flow to include the effect of turbulence. He showed that the mass transport velocity outside the boundary layer is independent of viscosity provided flow is laminar. Inside the boundary layer the velocity distribution is dependant on the viscosity. For turbulent flows he showed that the flow may be well approximated by the laminar profile for the outer part of the layer, if the viscosity is replaced by an eddy viscosity that is independent of time and height. This tells us that drift at the edge of the boundary layer would be the same in both the turbulent and laminar situation. However, the distribution of velocity within the boundary layer will differ for the laminar and turbulent situations. In particular the maximum drift velocity would not be predicted by Equation (4.3).

Johns (1970) modelled the turbulent boundary layer using an eddy viscosity that was time independent but varied with distance from a fixed boundary. He showed that for progressive waves the mass transport could be found using:

$$\bar{U} = -\frac{a^2 k \sigma}{\sinh^2 kh} \text{Im} H(\omega) \quad (4.6)$$

$$\text{and } \omega = \left( \frac{\sigma}{2\nu} \right)^{1/2} z$$

where values of function  $\text{Im} H(\omega)$  are shown in Fig. 4.6.

It can be seen in both the laminar and turbulent cases that  $\text{Im} H(\omega)$  is approximately 1.25 for sufficiently large values of  $\omega$ . Therefore, the mass transport for progressive waves, just outside the boundary layer, is shown to be very close to the laminar case. In fact, the maximum drift velocity within the

boundary layer is slightly greater for the laminar case. Fig. 4.6 also shows that the thickness of the turbulent layer is much greater than the laminar layer.

Mass transport in a turbulent boundary layer over a rough flat bed was investigated by Trowbridge and Madsen (1984). The eddy viscosity was assumed to be a function of both distance above the bed and bed shear stress. The authors found for long waves that the direction of the mass transport near the bed is in the opposite direction to the direction of wave propagation. It was noted that the availability of validation data was very limited but the measurements of mass transport by van Doorn (1981) were used for validating the analysis. This dataset is for a rippled bed, with measurements of mass transport recorded under the wave troughs and the crests. For the purpose of comparison the rippled bed was considered as a bed with a large relative roughness. The agreement was not particularly good.

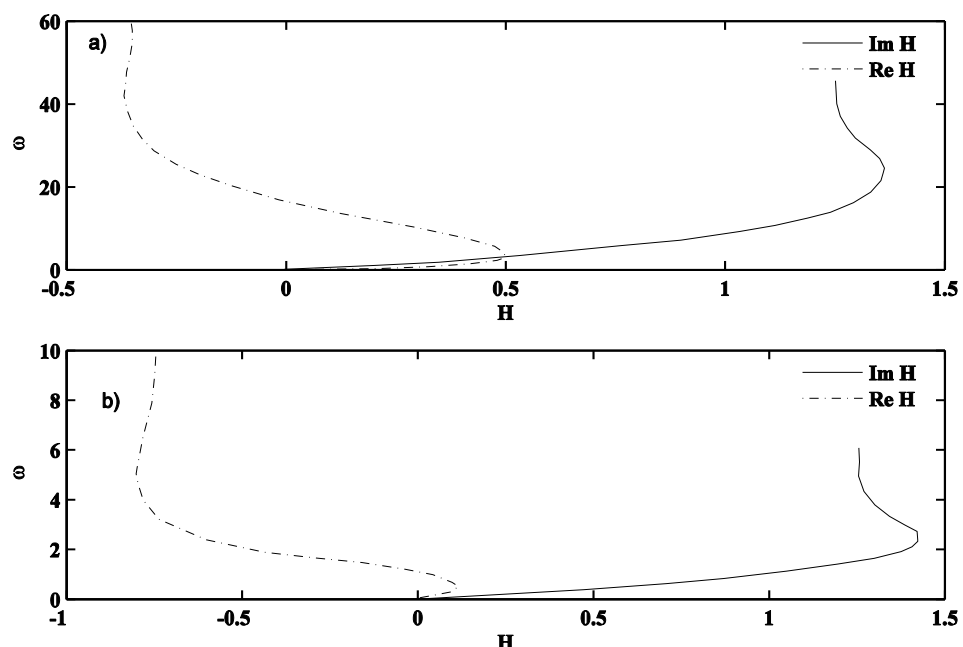


Fig. 4.6 Variation of  $H$  with  $\omega$  in turbulent (a) and laminar (b) cases, from Johns (1970).

An analytical model of mass transport induced by progressive waves over rippled and very rough beds in turbulent flows was developed by Davies and

Villaret (1999). In this case, the momentum transfer is dominated by organised vortices which are shed for the bed roughness elements rather than by random turbulence. In the analysis, the authors used a time-varying eddy viscosity. The result from this analysis are characterised by a near-bed jet in the direction of wave propagation which is much greater than that shown by Longuet-Higgins. Again the data in van Doorn (1981) was used for validation. Marin (2004) made some accurate measurements of Eulerian drift over rippled beds using laser-Doppler anemometry and compared the prediction from Davies and Villaret (1999) with those from Longuet-Higgins (1953). The Longuet-Higgins result gave better agreement with the measured data for both transitional and fully turbulent conditions.

The influence of bottom slope on the mass transport by progressive waves was investigated by Bijker et al. (1974). They showed experimentally the value of mass transport on slopes of 1:10, 1:25 and 1:40 when calculated at the outer edge of the boundary layer is smaller by a factor of two than predicted by Longuet-Higgins for a horizontal bottom. The difference between theory and experimental data increases with decreasing depth and increasing relative wave height. By considering the first harmonic of the local waveform, they found good agreement with the experimental work.

A second approximation to the mass transport velocity within the bottom boundary layer was found by Dore (1982). Comparison with the first approximation for progressive waves given by Longuet-Higgins (1953) showed only a very small decrease in mass transport.

#### 4.5.1. Comparative data for progressive waves

The lack of available laboratory data on mass transport found by Trowbridge and Madsen (1984) is still largely true today. However, the instrumentation available to researchers has improved significantly and some studies conducted since then include detailed data on mass transport within the boundary layer.

The earliest recorded observations of mass transport were conducted by Caligny (1878). These flume tests looked at progressive waves driven by a steam-driven plunger and dissipating on a beach. The movements of resin particles observed through glass windows allowed simple measurements to be taken. Longuet-Higgins demonstrated that the velocity recorded closest to the bed is in broad agreement with that predicted at the edge of the boundary layer.

More detailed experimental work was conducted by Russell and Osorio (1958) using a 56m long flume with a width of 1.2m and maximum depth of 0.56m. Waves were generated with a simple oscillatory hinged paddle and waves were dissipated on a 1/10 shingle beach and wave filters. Drift velocities were measured by observing neutrally buoyant particles and dye streaks. The results showed that drift near the bed was always in the direction of wave propagation and the magnitude of the drift was in quantitative agreement with Longuet-Higgins. For values of  $kh$  between 0.7 and 1.5, it was found the mass transport above the boundary layer was in agreement with the conduction solution as given by Longuet-Higgins. Although, for the waves tested, the ratio  $a^2/\delta^2$  would have meant that the convection solution would be more appropriate than the conduction solution. The test conducted by Russell and Osorio provides no information about the profile of mass transport within the boundary layer.

More recently, Klopman (1994) conducted a detailed experimental study of the vertical structure of flow due to progressive waves and currents in order to provide data for the verification of mathematical and numerical models. A 46m long flume was used with active wave absorption to avoid reflections. The horizontal bed was roughened using coarse sand with a grain size of approximately 2mm; this resulted in a Nikuradse roughness of 1.2mm. Flow velocities were measured at one vertical cross-section of the flume using LDV systems. These provided an extremely detailed picture of the vertical variation of velocities down to within 0.2mm of the bed.

The series of tests conducted by Klopman (1994) included monochromatic, bi-chromatic and random waves. These included tests with waves following the currents, opposing the currents and without currents. For the purpose of this investigation, only monochromatic waves without currents are studied. The monochromatic wave height was 0.12m, with a wave period of 1.44s. All tests were performed with a still-water depth of 0.500m.

#### **4.5.2. Model testing for progressive waves**

The RANS model has the option of either a constant mesh or an automatic mesh generator that can produce a variable mesh. Although it is more accurate to use a constant mesh size, frequently a variable mesh is used for computational efficiency. Usually the variable mesh function is used with a smaller grid at the free surface and a coarser mesh near the bottom. This allows greater accuracy in the definition of the free surface. However, for this investigation, the mesh near the bottom boundary must be small enough to

resolve the boundary layer. Further away from the bed a coarser mesh is used for computational efficiency.

Another consideration is the aspect ratio of the horizontal mesh spacing  $\Delta x$  to the vertical mesh spacing  $\Delta y$  near the free surface. Ideally, the ratio of  $\Delta x / \Delta y$  should be 1 but this would not be computationally efficient. For investigations where the horizontal scale is much larger than the vertical scale, such as small amplitude long waves,  $\Delta x$  may need to be an order of magnitude greater than  $\Delta y$ . However, when investigating breaking waves, Lin and Liu (2002) found that an aspect ratio greater than 2.5 may create false breaking. The aspect ratio is less important for the waves considered in the mass transport part of this study, because no breaking waves are being considered.

The mesh used in these series of tests had a constant horizontal step,  $\Delta x$  of 0.025m. To define flow within the boundary layer, a variable mesh was used in the vertical direction. For tests where the flow within the boundary layer was to be resolved, a step size of 0.0003m was used at the bed and increased linearly to 0.01m, after which a constant mesh size was used. The maximum rate of mesh divergence  $\left( \frac{\Delta x_{i+1}}{\Delta x_i} \right)$  was limited to 105% to avoid false internal reflections.

The maximum divergence rate limitation was found to have a large impact on the overall number of nodes used in the mesh and, as a consequence, the array sizes used within the code. The larger array sizes increased the length of computation and this often made the length of time for a test unduly long. For a computer running with a 2.8 GHz processor, a typical test with the above mesh

would run for a number days. For comparison, the same test run on the same PC with a fixed vertical mesh  $\Delta y$  of 0.01m would have a cpu time of a few hours. Therefore, due care was taken, where possible, to reduce the length of tests. However, it should be noted that increasing mesh size might not directly correlate with shorter test run-time. This is because a course mesh may result in the RANS model taking longer to converge to a solution, and may possibly fail to converge.

The RANS model defines the location of vector and scalar quantities in a staggered fashion. Scalar quantities such as the VOF function  $F$ , the turbulence intensity and eddy viscosity are defined at the cell centres, whereas the vector quantities such as velocities are defined at the cell boundaries. It should also be noted the vector quantity, vorticity is defined at the top right corner of a cell. So that free surface information and velocities can be plotted together, the velocities are redefined at the mesh centres using interpolation. The implication of a staggered mesh system is that great care must be taken when interpreting numerical results.

The flume length used for the computational model was 20m. Although this is significantly shorter than the experimental flume used by Klopman (1994), the waves generated by the external wave maker had fully settled within this length flume. Using a shorter model flume length reduced the time taken for each model run. Although the model generates data at all the mesh nodes, for this test series the dataset was also analysed at a location 18m from the left hand boundary. In the model, it is possible to output more detailed data at a particular

location in the form of a wave gauge and to generate a time history of various parameters at that location.

The RANS model allows for the wave maker to be positioned either internally or externally. Lin et al. (1999) developed the internal source function for wave generation within the RANS model to overcome the difficulty of a boundary both absorbing and generating waves at the same time. One of the requirements of the internal source function is that it should be placed at least  $\frac{1}{2}$  wavelength from the open boundary to avoid false reflections. However, the placing of the source region at  $\frac{1}{2}$  wavelength from the left hand boundary is a disadvantage because the length of flume to the right of the wave maker then has to be sufficiently long for waves to fully develop. This effectively requires a longer flume and consequently is more computationally expensive. In this series of tests, waves have been generated at the left hand boundary of the flume. The right hand edge of the flume was set to be wave absorbing, so that no waves should reflect back into the region of interest. To assess the wave absorption, a test was conducted with a sufficiently long flume so that no waves could be reflected from the right hand end of the flume and re-enter the test section. This indicated that wave absorption worked well for monochromatic waves within the model and, consequently, the more computationally efficient shorter flume length of 20m was adopted.

The duration of the physical model tests was set to 600s, which is approximately 420 wave periods. This duration was not feasible for the numerical model because the computational time required for such a test would

be prohibitive. The time taken for both the surface waves and the mass transport to establish is clearly an important parameter for these tests.

The time taken for the surface wave to establish was found by considering the wave speed, length of flume and by checking the wave profile. Fig. 4.7 shows the model test results 20s after the test was initiated from a condition of rest. It shows that the waves have become fully established when reaching the 18m test section. Consequently 20s after the start of the test was considered to be the starting point for mass transport investigations.

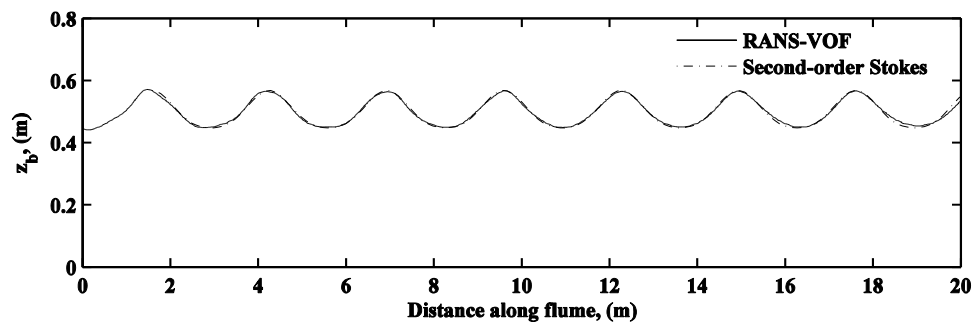


Fig. 4.7 Free surface profile calculated with the RANS model and calculated using second order Stokes theory.

It has been previously shown, Lin et al. (1999), that the wave generation within the model performs better when the ratio of  $H/h$  is less than 0.15. For  $H/h$  greater than 0.15, it takes longer for the generated waves to take a stable form. For this series of tests, with a wave height of 0.12m and a water depth of 0.5m, this ratio is 0.24. Fig. 4.7 shows the free surface profile calculated with the RANS model, shown as a solid line, after a period of 20s from the start of the test. For comparison with theory, the free surface profile calculated using Stokes second order approximation (Dean and Dalrymple, 1991) is superimposed. This equation is given by:

$$\eta = \frac{H}{2} \cos(kx - \sigma) + \frac{\pi H^2}{8 \lambda} \frac{\cosh(kh)[2 + \cosh(2kh)]}{[\sinh(kh)]^3} \cos[2(kx - \sigma)] \quad (4.7)$$

Komar (1976) give the region of application of several wave theories as a function of the ratios  $H/h$  and  $h/\lambda$ . The second order approximation to Stokes theory has been selected because, for the ratios of  $H/h$  and  $h/\lambda$  determined for these tests, the accuracy of the linear wave theory starts to degenerate and non-linear wave theory is required.

The figure shows very good agreement between the second-order Stokes waves and those predicted with the model. However, some phase shift can be seen to develop through the test. This is consistent with the validation exercise carried out by Lin and Liu (1998a) who suggested that this might be partly caused by the model requiring further time to reach the quasi-steady state.

In the model, the wave maker at the left boundary of the flume will cause a steady mass transport into the computational domain. Under some conditions, this could lead to a long-term net accumulation of mass within the model so that the program could eventually fail. To ensure that there is a conservation of mass within the model, an option is available to provide a compensating return flow averaged over both period and water depth, which is subtracted from the calculated horizontal velocity. The return flow for Stokes waves is calculated based on a depth averaged, time mean mass transport of  $U = gH^2 T / 8h\lambda$ .

Before investigating mass transport, a comparison of the vertical profile of horizontal velocities between theory and the model is made. A second

approximation to Stokes for horizontal velocities under a progressive wave is given in Dean and Dalrymple (1991) as:

$$u = \frac{H}{2} \frac{gk}{\sigma} \frac{\cosh k(h+z)}{\cosh(kh)} \cos(kx - \sigma t) + \frac{3}{16} \frac{H^2 \sigma k \cosh 2k(h+z)}{\sinh^4 kh} \cos 2(kx - \sigma t) \quad (4.8)$$

A comparison between the model and the analytical solution is shown in Fig. 4.8. When making the comparison, it should be remembered that the analytical solution does not include the effects of viscosity and turbulence, whilst these factors are represented within the RANS model. The model also enforces the no-slip condition at the boundary. The magnitudes of the peak velocities within the boundary layer show good agreement, but away from the bed the model produces a lower velocity compared with the analytical solution.

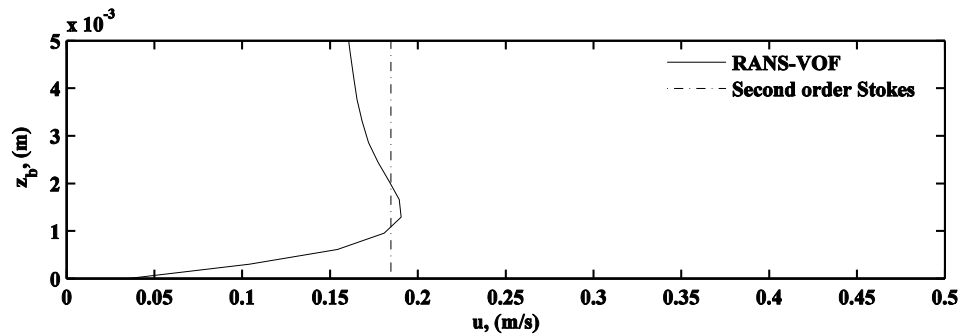


Fig. 4.8 Peak horizontal velocity under a progressive wave from second-order Stokes theory and from the RANS model.

When investigating mass transport, the length of time over which the phase averaging was taken must be sufficiently long without being computationally infeasible. Fig. 4.9 shows the effect of different phase averaging periods on the vertical profile of mass transport. A logarithmic vertical axis is used so both the boundary layer and the near surface variations can be seen. This shows that the mass transport profile outside the boundary layer establishes very quickly. Phase averaging over two cycles or more produces very little variation.

However, within the boundary layer the mass transport takes a little longer to converge. The variation between phase averaging over eight and ten cycles is very small and consequently mass transport was calculated by phase averaging over ten cycles. Therefore, for this test series, the RANS model tests were run for 20s to establish the waves and the mass transport was evaluated over the following 14.4s.

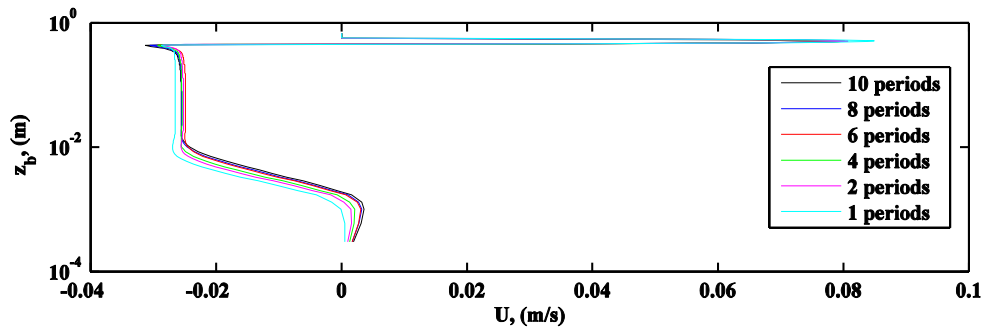


Fig. 4.9 Vertical profile of mass transport for different phase averaging periods.

Fig. 4.10 shows the vertical variation of mass transport within the boundary layer, as predicted by the RANS model, by Longuet-Higgins (1953) and as measured by Klopman (1994). The Longuet-Higgins values were calculated using Equation (4.1), which is the appropriate equation for mass transport within the boundary layer. The three sets of data show the wave-induced streaming within the boundary layer as predicted by Longuet-Higgins. However, the magnitudes of the mass transport vary. The peak streaming velocity for the Longuet-Higgins curve is shown to be approximately twice that recorded by Klopman, whilst the peak streaming velocity predicted by the RANS model is approximately half the value recorded by Klopman. In experimental studies Collins (1963) and Brebner et al. (1966) observed that the mass transport near the bottom is less than that predicted by laminar theory as the boundary layer becomes turbulent. This is in agreement with both the RANS model and Klopman's experimental data.

The three sets of data deal with turbulence in different ways. Klopman (1994) ensured that flow near the boundary was fully turbulent by using a rough bed. The predictions based on Longuet-Higgins (1953) are based on laminar conditions. However, Longuet-Higgins (1958) showed that at the edge of the boundary layer the mass transport for laminar and turbulent conditions should be similar. The peak values within the turbulent flow are not predicted by Longuet-Higgins. The RANS model used a no-slip boundary condition, which is the appropriate boundary condition when the viscous boundary layer is resolved.

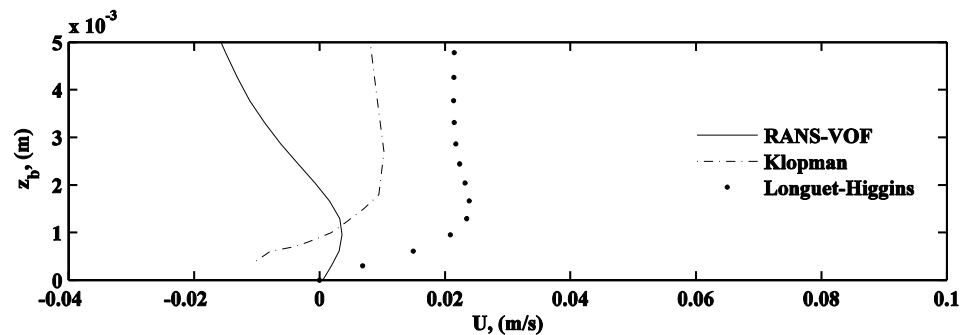


Fig. 4.10 Vertical variation of mass transport within the boundary layer.

The measured data show a flow reversal very close to the bed, at  $z_b$  below 1 mm. This is thought to be due to local effects of individual sand grains at this level. Spatial averaging in the horizontal direction would be necessary to overcome the local variations due to roughness. For this study the vertical profile at one location was studied.

For comparison, the RANS model was also run with a finely resolved boundary layer with a Nikuradse bed roughness,  $ks$  of 1.2 mm, which is the equivalent bed roughness of the Klopman (1994) data. The results are shown in Fig. 4.11.

The magnitudes of the onshore wave-induced streaming near the bed remain very similar, but the turbulence induced by the bed roughness has resulted in an increased vertical spread of the streaming layer. Beyond the boundary layer there is good agreement between the results from the rough and smooth bed tests.

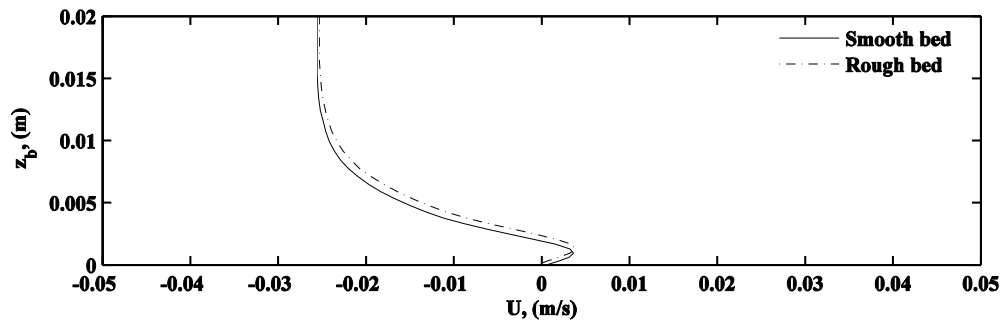


Fig. 4.11 RANS model vertical variation of mass transport for a smooth and rough bed ( $k_s = 1.2$  mm).

A comparison between the theoretical, experimental and model data for the main part of the flow is shown in Fig. 4.12. All sets of data show, at mid depth, the mass transport develops in the direction opposite to the wave propagation direction. The Klopman (1994) data varies almost linearly with distance from the bed, whereas the RANS model mass transport is almost constant between the boundary layer and the wave trough. The peak negative magnitudes of the mass transport measured by Klopman and the mass transport predicted by the model agree to within 0.5%, although the model predicts greater mass transport in the region above the boundary layer. Both the Longuet-Higgins (1953) convection and conduction solutions are shown. These were calculated using Equations (4.4) and (4.5) respectively. As there is no unique convection solution, the curve shown is for the convection solution evaluated when  $m$  takes a value of 1. As shown in Fig. 4.5, both the magnitude of the peak and the

vertical profile depend on the value of  $m$  selected. So the convection solution gives little information about flow in the interior.

The near uniform variation in the mass transport calculated within the model is thought to be due to the way the model ensures conservation of mass within the computational domain. The mass flux into the model, caused by incoming waves, is compensated for within the model. This is achieved by subtracting from the calculated velocities a small return flow, which is averaged over depth and period. Whilst this compensation does ensure that there is a conservation of mass within the model it is likely to distort the mass transport profile shown in Fig.4.12. It would have the effect of producing a uniform negative offset to the phase averaged mass transport and would account for the uniform shape seen within the interior of the flow. It is also likely that the peak mass transport predicted by the model in the lower boundary layer will be reduced by this effect.

Although the conduction solution is not strictly applicable for waves of these amplitudes, it does show reasonable agreement with the measured data at mid depth. However, the conduction solution does not accurately predict the vertical profile of mass transport.

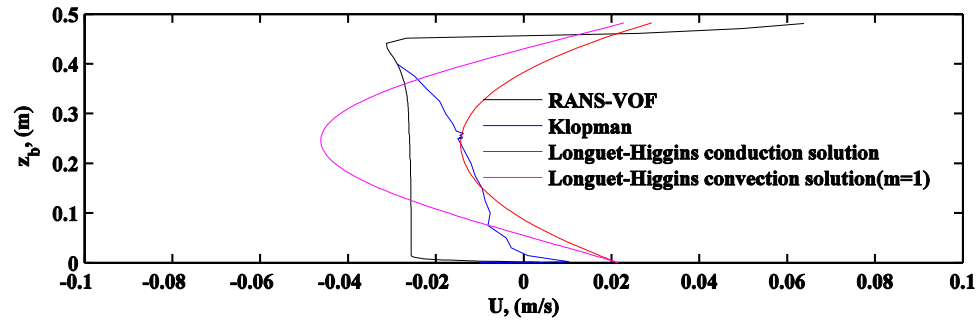


Fig. 4.12 Vertical variation of mass transport within the main part of the flow.

## 4.6. Standing wave theory

In this section, the development of mass transport theory for standing waves is described, followed by an account of the available comparative data and finally a comparison is made with RANS results.

Longuet-Higgins (1953) gave the equation for mass transport within the bottom boundary layer for a standing wave as:

$$\bar{U} = \frac{1}{2} \frac{a^2 \sigma k}{\sinh^2 kh} \sin 2kx f(\chi) \quad (4.9)$$

$$\text{where } f(\chi) = (-3 + 8e^{-\chi} \sin \chi + 3e^{-2\chi}) \quad \text{and} \quad \chi = \frac{h-z}{\delta}$$

This shows that the horizontal variation of mass transport varies as  $\sin 2kx$  and is zero at  $x=0, \pm 1/4\lambda, \pm 1/2\lambda, \dots$  and is a maximum at  $\pm 1/8\lambda, \pm 3/8\lambda, \dots$ . The vertical profile of mass transport in the standing wave varies with the function  $f(\chi)$ . This function is plotted against  $\chi$  in Fig. 4.13.

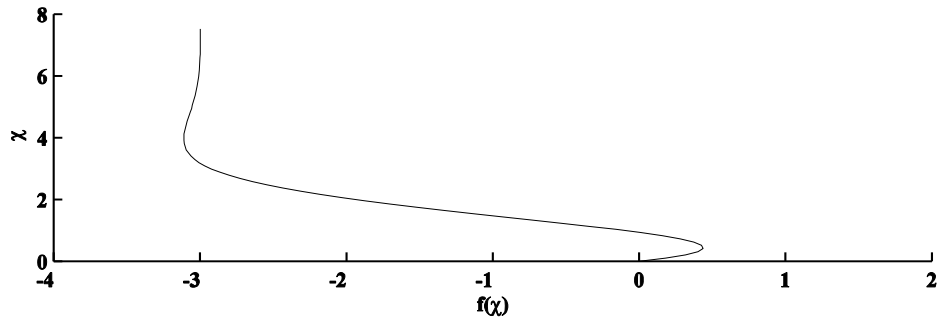


Fig. 4.13 Vertical variations in  $f(\chi)$  for a standing wave.

The main feature of Fig. 4.13 and Equation (4.9) is that the transport in the lower boundary layer ( $\chi < 0.9$ ) is always in the direction from the antinode to the node of the standing wave. Above this ( $\chi > 0.9$ ), the transport is in the opposite direction. Therefore, a circulation cell is generated within the boundary layer. This is the lower cell shown in Fig. 4.3.

Considering the maximum magnitude of the mass transport, it can be seen that as  $\chi$  tends to infinity the value of  $f(\chi)$  tends to  $-3$  and so the mass transport beyond the boundary layer is given by:

$$\bar{U} = \frac{-3}{2} \frac{a^2 \sigma k}{\sinh^2 kh} \sin 2kx \quad (4.10)$$

It can also be seen that the peak value of mass transport within the lower boundary layer will be at its maximum when  $f(\chi) = 0.44$ , i.e. when:

$$\bar{U} = 0.22 \frac{a^2 \sigma k}{\sinh^2 kh} \sin 2kx \quad (4.11)$$

In the main body of flow, the mass transport when the ratio  $a^2/\delta^2$  is large is given by the convection solution as:

$$\bar{U} = (-1)^{m+1} \frac{3}{2} \frac{\sigma k a^2}{\sinh^2 kh} \sin 2kx \cos\left(\frac{m\pi z}{h}\right) \quad (4.12)$$

where  $m$  is an integer.

Again, this function varies with  $\sin 2kx$  in the horizontal direction, so the mass transport is zero at the nodes and antinodes and at a maximum between nodes and antinodes. In the vertical direction there are  $m$  cells and the circulation in adjacent cells is in opposite directions. The direction of flow in all the cells is dependent on the direction of flow in the cell within the boundary layer. Fig. 4.3 shows the cell pattern when  $m = 1$ . As with the progressive wave theory, for the convection solution there are an infinite number of solutions. However, the conduction solution for standing waves does have a unique solution, which is expressed as:

$$\bar{U} = \frac{3a^2\sigma}{2\sinh^2 kh} \frac{\sin 2kx}{(\sinh 4kh - 4kh)} \quad (4.13)$$

$$\times [4k^2 h \cos 2kx \cosh 2kz - 2k \cosh 2kz \sin 2kx + 4k^2 z \sinh 2kz \sin 2kx]$$

The conduction solution therefore gives only one cell in the vertical direction above the boundary layer, so it has a similar pattern to the convection solution when  $m = 1$ , as shown in Fig. 4.3. It will be seen that it is this pattern that seems to develop within the RANS model and has been observed in experimental studies, Noda (1968).

The Longuet-Higgins (1953) laminar theory for standing waves was extended by Johns (1970) to include a model of eddy viscosity, which varies with distance from the boundary. He showed that for standing waves the mass transport could be found using:

$$\bar{U} = \frac{a^2 k \sigma}{2 \sinh^2 kh} \sin 2kx \operatorname{Re} H(\omega) \quad (4.14)$$

where values of function  $\operatorname{Re} H(\omega)$  are shown in Fig. 4.6.

Although the profiles of  $\operatorname{Re} H(\omega)$  are similar for the laminar and turbulent cases, the magnitudes vary. The limiting value of the function at the edge of the laminar boundary layer is approximately  $-0.75$  and  $-0.35$  for the turbulent case. So the predicted mass transport for a turbulent boundary layer gave a value that is only 45% of the figure given for the laminar case. Within the bottom boundary layer, the peak value of  $\operatorname{Re} H(\omega)$  is approximately 0.15 for the laminar case and 0.5 for the turbulent case. Therefore, within the turbulent boundary layer, Johns predicted the peak velocity to be about three times greater than for the laminar case. Fig. 4.6 also shows the thickness of the turbulent layer is much greater than the laminar layer.

In a further development of mass transport theory, Carter et al. (1973) considered the effect of the magnitude of the reflection coefficient on the mass transport profile. It was observed that, for progressive waves, mass transport within the boundary layer is always in the direction of wave propagation and for

standing waves the mass transport within the boundary layer changes sign.

Carter et al. (1973) investigated what happens to the profile of mass transport within the boundary layer for reflection coefficients between 1 and 0. It was found there exists a critical reflection coefficient of 0.414. Below this figure the wave is essentially a progressive wave and mass transport is the direction of wave progression. For a reflection coefficient above this figure there is a region near  $\lambda/8$  where the flow in the lower boundary layer is backwards but elsewhere the mass transport is always in the flow direction. This critical reflection coefficient determines the mode of mass transport and we shall later see this directly determines the type of bed forms that are likely to develop.

#### **4.6.1. Comparative data for standing waves**

Noda (1968) conducted some experimental measurements of standing waves. This work used a number of techniques to measure mass transport velocity. The first method involved photographing dye-streaks obtained by dropping potassium permanganate crystals that sank and left a vertical dye streak in the water column. By examining photographs of the movement of the dye streaks, the horizontal velocities could be calculated. Also neutrally buoyant pellets in the water column were photographed, using strobe lighting, to determine phase-averaged velocities. The techniques provided some quantitative data outside the boundary layer that were then compared with Longuet-Higgins theory. The data are in broad agreement with theory but the magnitudes are less. To investigate mass transport within the boundary layer, small particles with a density greater than water were spread evenly over the bed. The photographic record of the displacement of these particles demonstrated qualitatively the

direction of mass transport within the boundary layer but the technique was unable to provide quantitative data for this region.

A number of researchers, including de Best et al. (1971), Xie (1985), Hsu et al. (1989) and Sumer and Fredsøe (2000), have considered waves reflecting from a vertical wall and investigated the resulting scour patterns that result from mass transport. This work has focused on predicting final bed profiles from given wave parameters and for given sediments. Whilst mass transport has been discussed as a driver for the equilibrium bed profiles, no direct recordings of phase-averaged velocities were taken. Although this work is not of use in validating the capabilities of the wave model, it may be of interest later for validation purposes when the model has been extended to include sediment transport and bed morphology. Initial work is presented in Appendix A.

Gislason et al. (2009) used a Navier-Stokes based solver with a  $\kappa - \Omega$  turbulence model to investigate the mechanism of the energy exchange between the outer wave motion and the oscillatory near-bed boundary layer. The  $\kappa - \Omega$  turbulence model used is described in Wilcox (1998) and Menter (1993). The study found the mean velocity and shear stress distribution to be identical to that found by Longuet-Higgins (1958). Standing waves in front of sloping walls were modelled and agreed well with experimental results. The experimental results described flow within the main body of fluid but did not record information within the boundary layer.

Although mass transport under standing waves has been widely discussed and its significance for sediment transport is generally acknowledged, no recent

detailed experimental data exist beyond the work of Noda, and that discussed above. However, Lin et al. (2002) conducted some measurements of velocities under a standing wave using a fibre-optic laser Doppler velocimeter (FLDV). The study was primarily interested in the apparent movement of the antinodes in a standing wave. However, the study recorded the vertical variation in horizontal velocity at a discrete location and throughout the wave period. In particular, the measurements contained flow velocities within the boundary layer. In order to determine the mass transport in these experiments, the phase average of the velocities needs to be found. The data set in the Lin et al. (2002) paper presented the vertical variation in horizontal velocities at various phases. However, the particular phase information was not shown. On request, the author made available the phase data from this study. The data provided contained the vertical variation of horizontal velocity at 400 points through the wave period. The sampling time of each test run was 8-15 s, depending on the case tested. The table below shows the test conditions for which measurements of the boundary layer flow were conducted.

<i>Case</i>	<i>T (s)</i>	<i>h (cm)</i>	<i>Hi (cm)</i>	<i>Hst (cm)</i>	<i>λ (cm)</i>	<i>Hi/λ</i>	<i>Hi/h</i>
B	1.012	27	4.94	9.3	133	0.037	0.18
D	1.255	27	7.2	13.78	184	0.039	0.27
E	1.495	27	9.7	19.7	224	0.043	0.36
H	2.1	27	9.2	17.72	329	0.027	0.34

*Table 4.1 Wave condition for tests including boundary layer velocity data from Lin and Liu (2002).*

The FLDV recorded velocities to within 0.08 mm of the boundary and to a maximum distance of 6mm from the boundary. In total there are 23 data points

in the vertical direction. This set of data should give a good picture of flow within and at the edge of the boundary layer, but will not give information about flow in the interior.

#### **4.6.2. Model testing for standing waves**

The mesh used for this series of tests employed the automatic mesh generator within the model. The smallest vertical mesh step was used near the bed in order to resolve the boundary layer. Over the lowest 0.005 m the vertical mesh size was 0.0005 m and the maximum mesh size near the water surface was 0.005 m. In the horizontal direction a constant mesh size of 0.025m was used.

The wave parameters for the computational study were the same as for case B given in Table 4.1. This was selected because the ratio  $H/h$  for this test is the lowest. This ratio is important because wave generation within the model has been shown by Lin and Liu (2002), to perform better when this ratio is below 0.15. The value for case B is slightly above this figure and this means that it may take longer for the generated wave to take a stable form. The other cases for which data are available had  $H/h$  values well above 0.15 and so these were not modelled.

To ensure the waves generated within the model were as expected, a comparison was made between waves recorded in the RANS model and theory. Fig. 4.14 shows the free surface profile calculated with the RANS model, shown as a solid line, after a period of 10s from the start of the test. This shows the situation before the wave has reached the reflecting wall and before the standing wave has established. For comparison with theory the free surface

profile, calculated using the second order approximation of Stokes, Equation (4.7), is superimposed.

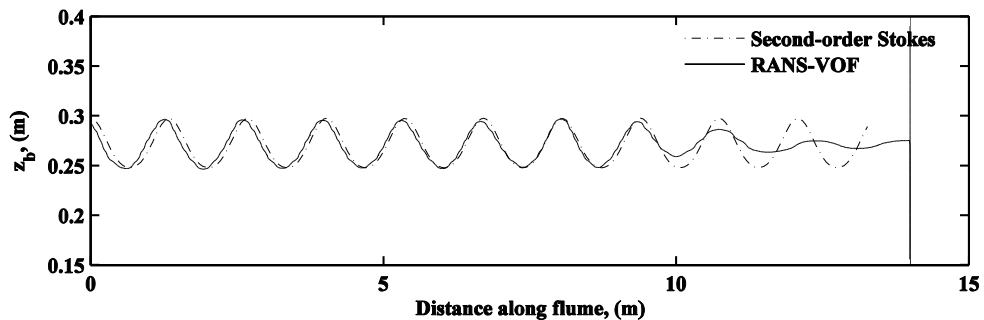


Fig. 4.14 Free surface profile of generated wave calculated with the RANS model and calculated using second order Stokes theory, with reflecting wall at 14m.

The figure shows good agreement between the second order Stokes wave and that predicted with the model. The model again shows some phase shift. This is consistent with both the progressive wave tests and the validation tests conducted by Lin and Liu (1998a) and, in this case, may well indicate that the waves have not settled. The figure confirms that the external wave generator is producing the specified wave conditions.

The mass transport experiments were carried out with a flume length between wave maker and reflective wall of 14m. This was the same in both the experimental study and the computational model. Velocity data were output from the model at all mesh nodes at 0.01s intervals, which gave 101 samples per wave period. Additionally, wave data at 0.001s intervals were output at a location of  $\lambda/8$  from the reflecting wall. This location corresponds to a point midway between node and anti node. This gave a time history of various parameters at that location. This location was chosen because horizontal velocities within the circulating cells will be at a maximum at distances  $\lambda/8$ ,  $3\lambda/8$ ,  $5\lambda/8$  etc from the reflecting wall. This can be seen in Fig. 4.3.

Before making a comparison of mass transport, a comparison is made between the horizontal velocities calculated with the RANS model and those calculated with second order wave theory, as shown in Fig. 4.15. The horizontal velocity in the boundary layer given by the second order solution of potential flow theory for standing waves is given in Noda (1968) as:

$$\begin{aligned}
 u = & -\sin kx \frac{\sigma H_{st}}{2 \sinh kh} \left[ \cos \sigma - e^{-z_b/2\delta} \cos \left( \sigma - \frac{z_b}{2\delta} \right) \right] + \\
 & \frac{\sigma H_{st}^2}{2\lambda \sinh kh} \left\{ \begin{aligned}
 & -\frac{3\pi}{8 \sinh^3 kh} \cos 2kx \left[ \sin 2\sigma - e^{-\sqrt{2}z_b/2\delta} \sin \left( 2\sigma - \sqrt{2} \frac{z_b}{2\delta} \right) \right] + \\
 & \frac{\pi}{4 \sinh kh} \sin 2kx \left[ e^{-\sqrt{2}z_b/2\delta} \cos \left( \sqrt{2} \frac{z_b}{2\delta} \right) - e^{-z_b/2\delta} \cos \frac{z_b}{2\delta} + \sqrt{2} \frac{z_b}{2\delta} e^{-z_b/2\delta} \sin \left( \frac{z_b}{2\delta} + \frac{\pi}{4} \right) \right] \sin 2\sigma + \\
 & \frac{\pi}{4 \sinh kh} \sin 2kx \left[ -e^{-\sqrt{2}z_b/2\delta} \sin \left( \sqrt{2} \frac{z_b}{2\delta} \right) + e^{-z_b/2\delta} \sin \frac{z_b}{2\delta} + \sqrt{2} \frac{z_b}{2\delta} e^{-z_b/2\delta} \cos \left( \frac{z_b}{2\delta} + \frac{\pi}{4} \right) \right] \cos 2\sigma + \\
 & \frac{\pi}{8 \sinh kh} \sin 2kx \left[ -3 + e^{-2z_b/2\delta} + 8e^{-z_b/2\delta} \sin \frac{z_b}{2\delta} + 2e^{-z_b/2\delta} \cos \frac{z_b}{2\delta} - 2\sqrt{2} \frac{z_b}{2\delta} e^{-z_b/2\delta} \cos \left( \frac{z_b}{2\delta} + \frac{\pi}{4} \right) \right]
 \end{aligned} \right\}
 \end{aligned}
 \tag{4.15}$$

Noda uses Equation (4.15) to derive the mass transport within the boundary layer for a standing wave, which is in agreement with Equation (4.9).

The agreement near the boundary layer between the velocities calculated with the RANS model and those calculated with theory is very promising. The agreement is also very good outside of the boundary layer. The analytical solution is a second order approximation based on laminar theory and includes the effects of viscous damping.

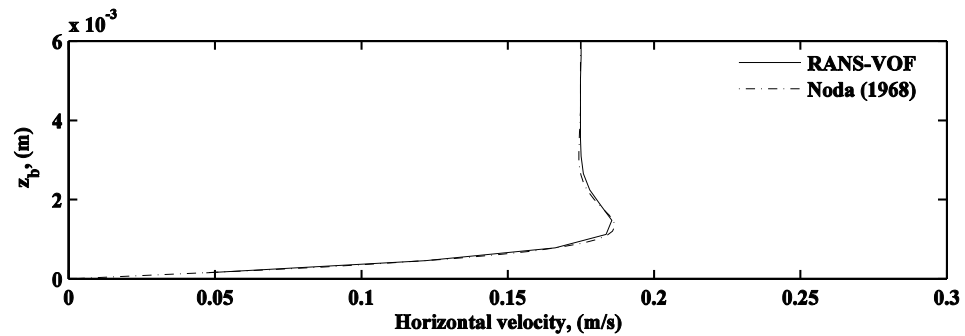


Fig. 4.15 Maximum horizontal velocity under a standing wave from the RANS model and analytical solution.

The phase variations of the horizontal velocities for case B are shown in Fig. 4.16. This shows the profiles of the vertical variations of both the experimental data and the analytical solutions. The analytical solutions were calculated using Equation (4.15). The phases shown are for values of  $t/T$  of 0, 0.1, 0.2 ....0.9. This is equivalent to Fig. 8b as given by Lin and Liu (2002), although at different phase steps. It can be seen from Fig. 4.16 that the experimental results only agree well with theoretical results for certain phases. In particular, good agreement is found at phases  $t/T = 0.7, 0.8$  and  $0.9$ . Phases  $t/T = 0.2, 0.3$  and  $0.4$  show less good agreement. It appears, at some phases, that the experimental data have had a phase shift when compared to the analytical solution. The cause of the phase shift in the experimental data is not known. However, the experimental data were resolved to 400 points per phase and so should be capable of accurately describing the velocities at these phase intervals.

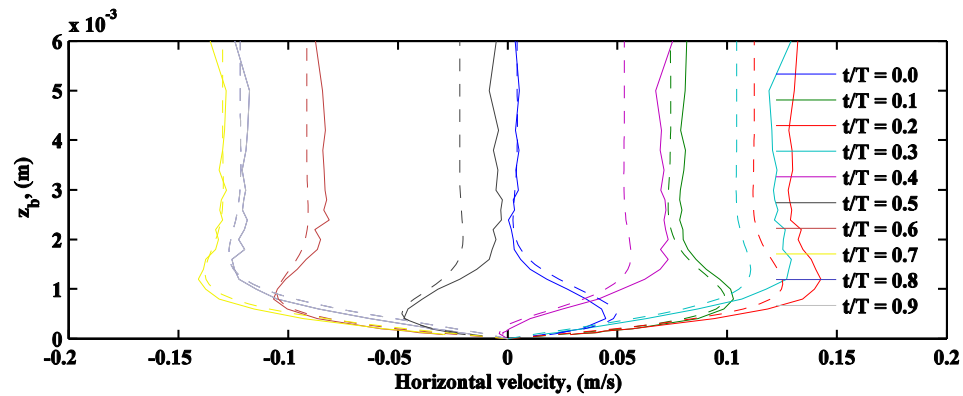


Fig. 4.16 Horizontal velocity profiles for different phases in the standing wave boundary layer, experimental data (solid line) and analytical solution (dotted line).

When determining the mass transport, the phase averaging time for the RANS model tests must be defined. This must be sufficiently long to allow a settled condition but without being too computationally expensive. Fig. 4.17 shows a graph of the peak value of mass transport within the lower circulating cell, plotted against the phase averaging length. The graph shows that averaging over more than 10 wave periods is unlikely to significantly alter the predicted values of maximum mass transport. Consequently, tests were phase averaged over 10 wave periods.

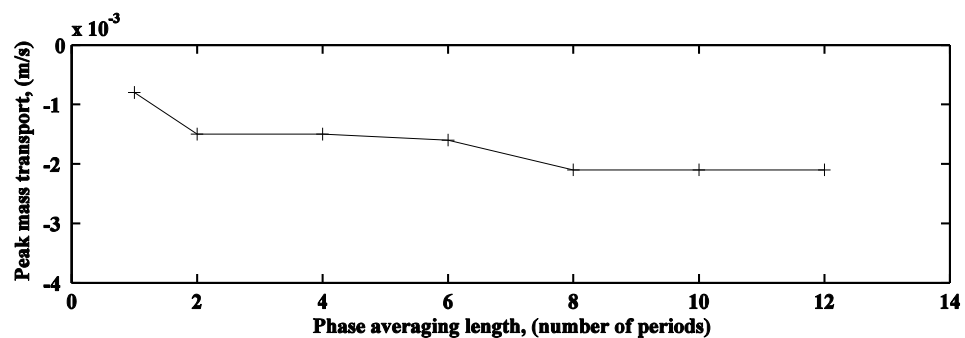


Fig. 4.17 Peak mass transport in the lower circulating cell for different phase averaging lengths.

The length of time taken for the standing wave pattern to establish before initiating the RANS model tests was determined by careful inspection of the free surface. After 20s, a consistent standing wave pattern had established near the

reflecting wall. Consequently, a 20s settling period was used for subsequent model tests and the mass transport investigations were carried out between 20s and 30.12s.

The mass transport predicted with the model was compared against both theory and experimental findings. As the experimental data were recorded at the location where the maximum mass transport was expected, this was useful for comparing the magnitudes of mass transport at that location. In order to check the ability of the model to reproduce the general circulation patterns, the model is compared to theory.

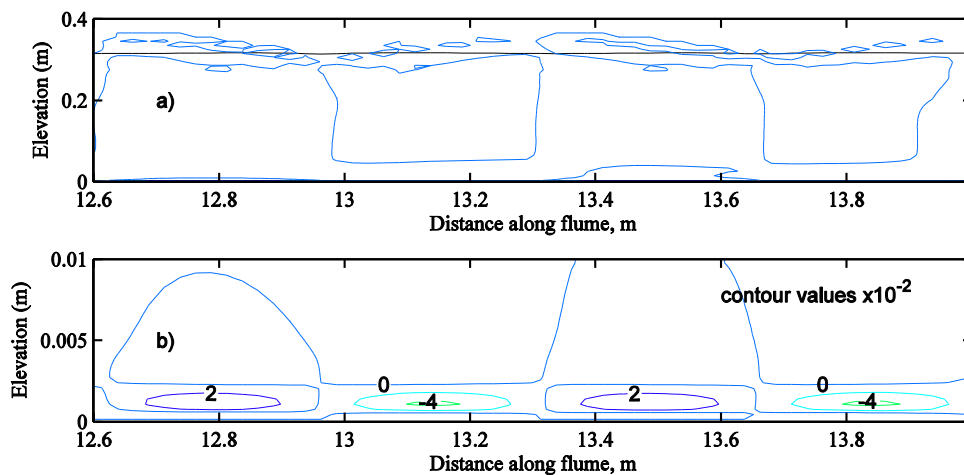


Fig. 4.18 Contours of averaged vorticity under a standing wave.

In order to examine the pattern of circulation generated by the mass transport, the contours of averaged vorticity,  $\zeta$ , are shown in Fig. 4.18. The vorticity can be found using:

$$\zeta = \frac{\partial v}{\partial x} - \frac{\partial u}{\partial y} \quad (4.16)$$

Fig. 4.18 shows the contour plots of vorticity for the wavelength closest to the reflecting wall. Fig. 4.18a shows the circulation in the interior of the fluid whilst Fig. 4.18b shows the circulation in the cell within the boundary layer. The

circulation cell patterns are clearly similar to those shown in Fig. 4.3. With a wavelength of 1.33m and with the reflecting wall at 14m, the nodes will be at 13.7 and 13.0m and the antinodes at 12.7, 13.3 and 14.0m. Fig. 4.18 shows the boundaries of the cells coincide with the locations of the nodes and antinodes. The four cells within the boundary layer show stronger vorticity than the cells in the interior of the fluid. The direction of flow within these cells is not clear from these plots.

In order to visualise the direction of flow within the cells, the mass transport velocities can be represented by velocity vectors. Fig. 4.19 shows mass transport velocity vectors for each cell. The flow for the 10mm nearest the bottom boundary is shown and for the half wavelength nearest the reflecting wall. Arrows indicating the general direction of the flow are also superimposed on the diagram. The diagram shows that the direction of the mass transport within the lower cells is always towards the nodes at the bed and away from the antinodes. The direction of flow in the upper cells is in the opposite direction. The velocities at the node and antinodes are shown to be only in the vertical direction. The general pattern of the flow is consistent with that predicted by Longuet-Higgins (1953) and shown in Fig. 4.3.

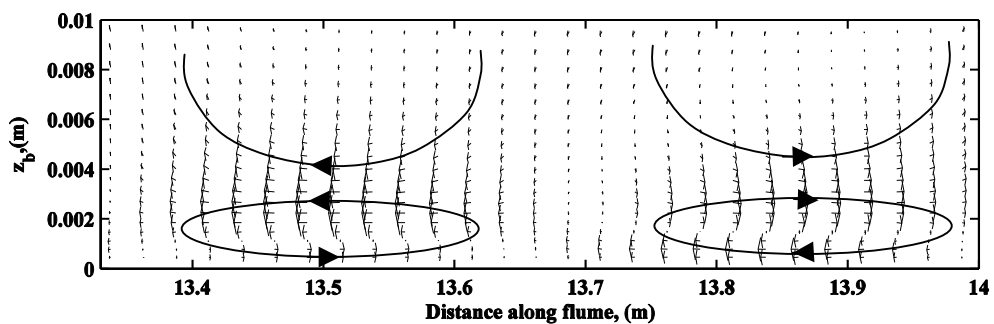


Fig. 4.19 Mass transport velocity vectors showing circulation cells for standing waves.

In order to assess the magnitudes of the mass transport predicted by the model, the vertical profile of mass transport velocities is compared with experimental and analytical results. The comparison is made at a location that is  $\lambda/8$  from the reflecting wall i.e. at 13.83m from the left-hand wall of the flume. This corresponds to midway between nodes and antinodes and should give peak values of mass transport. Fig.4.20 shows the comparisons for flow near the boundary layer. From first inspection, it can be seen that the results from the RANS model and from Longuet-Higgins (1953) theory show similar trends but the phase averaged experimental data shows poor agreement. The key difference is that the experimental data do not show the flow reversal within the boundary layer. However, Noda (1968) demonstrated qualitatively that this flow reversal does take place. It is thought that the experimental data showed poor agreement because of the apparent phase shift in the velocities shown in Fig. 4.16. The shift observed occurs at some phases and not at others and this will then affect the phase-averaged velocities. Unfortunately, this means the data cannot be used to validate the mass transport calculated by the model. However, the model can still be compared with theory.

The peak value of mass transport predicted by Longuet-Higgins (1953) near the edge of the boundary layer is approximately 0.01m/s, which compares with a value of 0.0035m/s from the RANS model. The Longuet-Higgins prediction is based on laminar theory whilst the RANS model includes turbulence. However, it has been suggested by Johns (1970), and shown in Fig. 4.6, that the peak value of mass transport near the edge of the turbulent boundary layer would be only 45% of the value within a laminar boundary layer. This is broadly in line with the figure calculated with the RANS model.

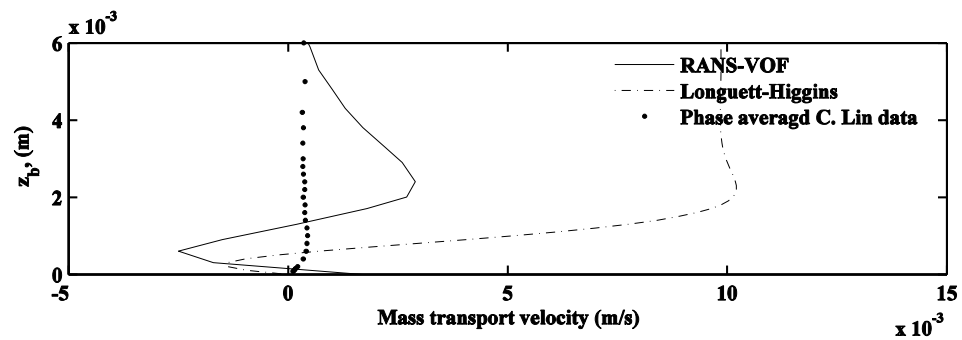


Fig. 4.20 Vertical profiles of mass transport velocity.

Johns (1970) also suggested that the drift in the lower layer would be in the opposite direction and would be larger than predicted by Longuet-Higgins (1953). Inspection of Fig. 4.6 shows that for turbulent flow, the peak mass transport in the lower layer should be approximately three times the equivalent laminar value. The value calculated with the RANS model is approximately twice that calculated by Longuet-Higgins (1953) theory.

In this chapter, a comparison has been made between the RANS model and available experimental and theoretical data for mass transport under progressive and standing waves. For progressive waves, the model has been compared to Longuet-Higgins (1953) theory and available experimental data. The wave-induced streaming within the boundary layer, as predicted by Longuet-Higgins was seen in the experimental and computational modelling results. The experimental data recorded half the peak streaming velocity predicted by Longuet-Higgins (1953) and the RANS model predicted half the velocity found within the experimental data. Outside the boundary layer, all data sets show that the mass transport develops in the direction opposite to the direction of wave propagation. However, each vertical profile of mass transport is different.

For mass transport under standing waves, currently there are no experimental data against which the RANS model can be validated for flow within the boundary layer. The model validation against theory shows that the flow under a standing wave contains the circulation cell predicted by theory both in the boundary layer and in the fluid interior. Additionally, the RANS model correctly identified the flow direction within these circulation cells. The peak magnitude of the mass transport outside the boundary layer was found to be a little less than the turbulent mass transport theory and within the boundary layer the peak was found to be approximately 30% less than turbulent theory.

It has been shown that the RANS model is capable of describing the non-linear mass transport flow under standing and progressive waves. A comparison has shown that the model results are comparable with available theoretical and experimental results. This has been done as a demonstration of the model's ability to describe complex hydrodynamic flows. For flow over an embankment crest during combined discharge, the model must be capable of describing the highly non-linear flow caused by the interaction between wave overtopping and weir overflow components. The ability of the model to describe mass transport adds confidence that the model will also be able to describe combined discharge. However, this must be assessed independently and will be the focus of the following chapters.

## **CHAPTER 5**

### **COMBINED OVERTOPPING MODEL TESTING**

#### **5.1. Introduction**

In this chapter, the RANS model previously described is used to determine combined wave overtopping discharge over embankments subjected to a negative freeboard. To assess the ability of the model at reproducing the wave transformation and overtopping processes, the model is compared with experimental data conducted by Hughes and Nadal (2009). Initially, a description is given of the experimental data against which the model is compared. This is followed by details of how the RANS model is set-up to reproduce the experimental data. A wave-by-wave comparison of physical and model data is performed for overtopping parameters such as discharge, flow depth and velocity. Finally, a discussion of the results is conducted with a view to explaining any differences. In the following chapter, the combined discharge calculated with the model is compared to current design formulae.

#### **5.2. Experimental data description**

In this chapter, a description is given of the experimental study used to validate the RANS model for combined wave-surge overtopping and the model set-up

for the RANS model. In the following section, the validation of the RANS model is described.

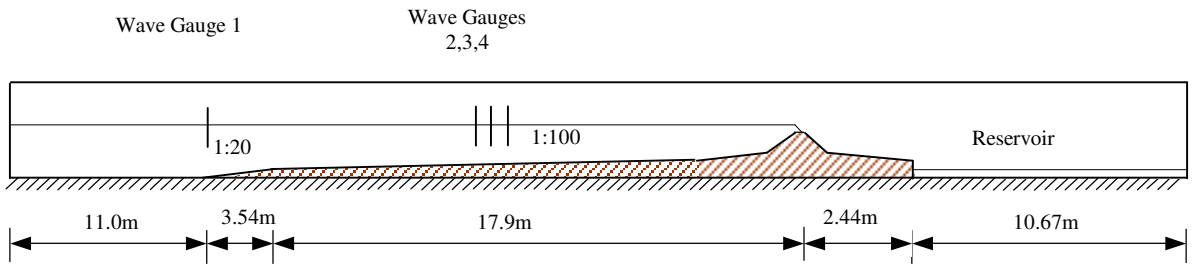


*Fig. 5.1 General set-up of flume with the model embankment.*

The model validation data for the combined discharge aspect of this study was obtained from an experimental study by Hughes and Nadal (2009). This study was conducted to provide design guidance following Hurricane Katrina. The model embankment used is typical of the cross sections used in the Mississippi River Gulf Outlet and is of standard cross section as defined by Burcharth and Hughes (2002). Full details of the physical model can be found in Hughes and Nadal (2009) but a summary of the data description is give here.

Hughes and Nadal (2009) conducted the series of physical model flume tests of combined discharge over an embankment at a scale of 1:25. The general flume set-up is shown in Fig. 5.1; and Fig. 5.2 gives details of the embankment geometry. Fig. 5.1 shows the location of the four resistance type wave gauges, one near the wave generator and a three-gauge array on the 1:100 slope. Flow depths over the embankment were recorded with Druck PDCR-200 pressure cells. Details of the locations of the pressure cells are given in Fig. 5.3. The horizontal flow velocity was recorded with a fibre-optic laser Doppler velocimeter (LDV) at a location directly above the pressure cell at P2. The

vertical height of the LDV was adjusted for each test so that the velocity was always recorded at half of the flow depth.

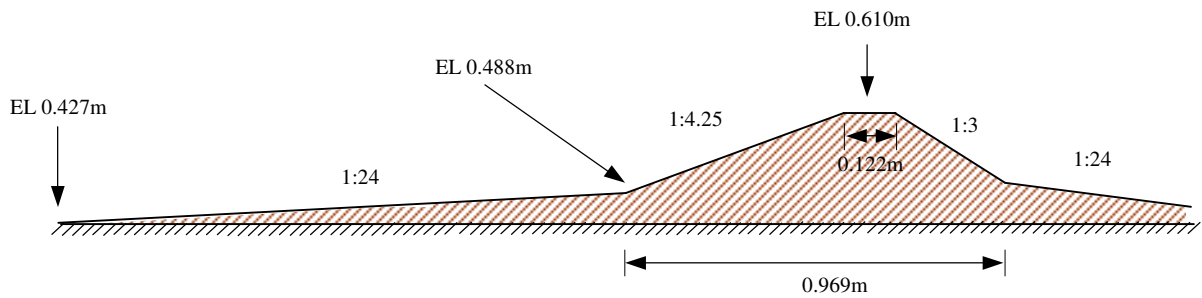


Fig. 5.2 Detail of the model embankment cross-section.

The test programme investigated storm surge levels of 0.29, 0.81 and 1.3m above the embankment crest. Each storm surge level was tested for three wave heights and three wave periods. This gave a total of 27 tests.

Recirculation of the discharge over the crest was achieved in the physical model by pumping the water from the reservoir to near the wave generator. Adjusting the flow rate in the pump set the surge level tested in the model. This could introduce a laboratory effect by creating a slope on the water surface over the length of the flume. For each surge level, the water surface elevations were recorded at regular intervals along the flume. The measurement showed that the water level was reasonably horizontal away from the embankment. The draw down near the embankment began close to the toe of the 1:24 slope for the 0.29 and 0.81m surge levels and near the toe of the 1:4.25 slope for the 1.3m surge level.

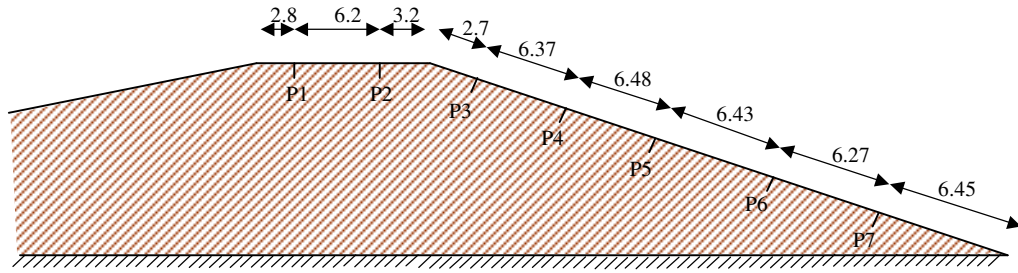


Fig. 5.3 Location of pressure cells on the model embankment, dimensions in cm.

Flood protection embankments are often built with wide crests to provide road access for maintenance and inspection. However, an embankment with a wide crest acts similarly to a broad crested weir when subjected to surge overflow, with flow at the crest progressing from sub critical near the seaward boundary to critical and then to supercritical on the lee side. Therefore, the flow depth on the embankment crest will vary with location across the crest. In order to determine an appropriate surge level, the model was run without waves for an initial period at the start of each test. The steady overflow discharge for this period was determined from the flow depth and velocity information at P2. Hughes and Nadal (2009) then used the average discharge over this period to determine the surge level from the equation for flow over a broad crested weir, Equation (2.15), with a  $C_d$  value of 1.0. This estimate of the upstream surge level would correspond to the surge level calculated from tide and meteorological conditions. It would be more useful to designers than a depth at the weir because it would not be subject to the drawdown that occurs near weirs.

The pressure cells on the embankment were calibrated prior to placing in the model but calibration checks were also conducted by flooding the model to known static levels. The pressure and velocity data for the tests were collected

at 50Hz and a total of 15000 data points were collected for each channel, giving an equivalent of 300s of model scale data or 1500s at the prototype scale. The data from the first 50 seconds at prototype scale were used to determine the steady overflow conditions, with waves beginning to reach the embankment shortly after this. The discharge average over the prototype time period 100 to 1500 seconds was used to determine the combined discharge when the embankment was subject to waves.

The LDV was located outside the flume with the laser beam crossing point located approximately 7.6 cm from the inside face of the flume. The instrument height was adjusted for each test so that the velocity at half depth for each of the tests was recorded. This measurement was used to give an estimate of the depth-averaged horizontal velocity. However, when the embankment was subjected to waves, the water level would periodically drop below the level of the LDV. The LDV was set so that when this occurred the velocity recorded would remain at the last measured value. A typical example is shown in Fig. 5.4. The water level falling below the LDV was more likely to occur in the tests with the lower surge levels or during troughs of large waves. The consequence was that average calculated discharges would be higher than the true value. To determine the range of this error, a second calculation was done with the LDV set to zero when the water level dropped below the laser level. These two sets of readings effectively gave the maximum range of the error. Hughes and Nadal (2009) determined that the maximum difference in the combined discharge caused by this problem was 13% for a test at the lower surge level. On average, it caused a 4% error. For tests at the highest surge level the LDV mostly remained submerged and so the problem was less apparent.

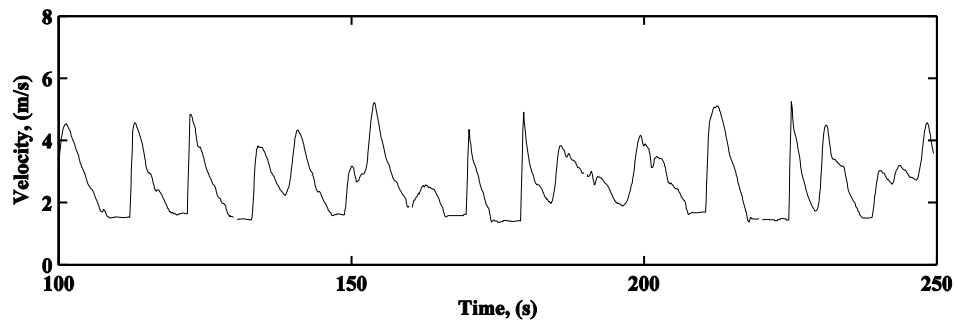


Fig. 5.4 Example velocity time history from physical model.

The wave generation in the model used a paddle that did not have the ability to absorb reflected waves. There was a possibility that waves reflected from the embankment then reflected again from the paddle, back towards the model. Output from the three wave gauge array near the embankment was analysed to determine the incident and reflected energy using the frequency-domain method of Goda and Suzuki (1976). The calculated reflection coefficients varied between 0.095 for the smaller shorter period waves to a maximum of 0.344 for the larger longer period waves. As the physical model used a non-absorbing wave paddle, the reflected waves became re-reflected from the paddle and the recorded waves include this component and became part of the wave spectrum statistics.

In the physical model, the surface of the embankment was covered in articulated mats to simulate the articulated concrete mats used to armour embankments and levees in the Mississippi River Gulf Outlet area. The model articulated mats were manufactured from firebrick in order to correctly scale the density of the prototype concrete mats. The roughness of the cut firebrick encouraged turbulent flow and was thought to help avoid scale effects associated with laminar flow in wave overtopping models.

### 5.3. Description of RANS model set-up

This section describes how the RANS model has been configured in order to reproduce the physical model tests described in the previous section. In the next section, a comparison is made between the physical and computational model results to assess the performance of the RANS model at simulating combined discharge.

In this part of the study, the wave generation method development by Torres-Freyermuth (2007) is used. The method uses a wave time history to generate waves at the seaward boundary and is used to directly simulate the physical model tests. The wave gauge data from the physical model provides the required time history of water surface elevation. However, in order to reproduce the required waves at the boundary, as well as wave height data, the model also required the velocity components at the boundary, which were derived from the wave data using linear theory.

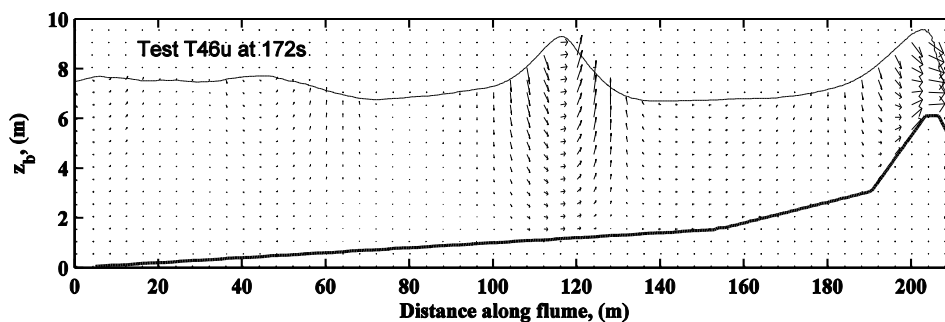


*Fig. 5.5 A snapshot showing wave surface elevation, embankment detail and flow field velocity vectors plotted at every fifth node vertically and every tenth node horizontally.*

The embankment crest in the physical model was approximately 810m from the wave paddle. In the computational model, for most tests, only part of the physical model flume was represented for computational efficiency. The extent of the computational model was approximately 210m. The wave input signal for

the RANS model was taken from wave gauge 2, G2, in the physical model and so the seaward boundary of the computational model was the G2 location in the physical model. This allowed waves generated with the RANS model to be compared with those measured at wave gauge positions G3 and G4. The landward boundary of the RANS model was located on the 1:3 slope on the lee side of the embankment. This boundary was defined as being an open boundary, so allowing waves to exit the flume without reflection. The surge level and the largest wave determined the vertical extent of the computational mesh, so that the wave peaks did not reach the top of the flume. Reducing the height where possible ensured computational efficiency and reduced run time. Fig. 5.5 shows the model set-up along with a snapshot of the wave surface elevation and flow field velocity vectors.

<i>Test Number</i>	<i>Nominal Surge , m</i>	$H_{m0}$	$T_p$
T46lh	0.29	0.27	5.71
T46x	0.29	1.73	6.06
T47b	0.29	2.46	6.51
T47e	0.29	0.88	10.60
T46pa	0.29	1.66	10.60
T47fa	0.29	2.49	10.60
T47k	0.29	0.76	12.07
T47la	0.29	1.74	13.86
T47m	0.29	2.26	14.00
T46na	0.81	0.81	5.71
T47a	0.81	1.53	5.83
T46v	0.81	2.33	5.83
T47c	0.81	0.79	9.86
T47g	0.81	2.36	9.65
T47h	0.81	0.71	14.58
T47i	0.81	1.57	14.58
T47j	0.81	2.32	14.58
T46ms	1.3	0.67	5.83
T46q	1.3	1.21	5.83
T46ra	1.3	2.24	6.09
T46s	1.3	0.78	9.86
T46t	1.3	1.59	10.14
T46u	1.3	2.45	9.65
T46w	1.3	0.75	14.58
T46y	1.3	1.53	14.58
T46z	1.3	2.37	14.58

Table 5.1 Test numbers, surge and wave conditions.

The computational model has been used to simulate the tests conducted at each of the flow depths tested in the physical model. Table 5.1 gives a full list of wave conditions tested. It should be noted that one of the physical model tests at the 0.81m surge level was not repeated in the computational model because the physical model depth time history at P2 was approximately 0.1m higher than other tests at this surge level. As the discrepancy could not be accounted for, the data were not used.

The defining criterion for the mesh size was that the mesh had to be small enough to resolve the supercritical flow on the landward side of the embankment and define flow during wave breaking. To achieve this, a mesh size for all 1.3m surge tests was 0.4m in the horizontal direction and 0.1m in the vertical direction. This gave a total of up to 58600 node points. To ensure that this mesh size was small enough to adequately define the flow at the embankment crest, a test was conducted to check if the calculated flow was dependent upon the mesh size. T46qa is a repeat of test T46q but with a mesh size set to be 0.2m horizontally and 0.05m vertically, which is a 50% reduction in mesh size in both directions. This caused a four-fold increase in the number of node points and the cpu time increased from 10hours for test T46q to 53 hours for test T46qa. A time history of combined discharge measured at the embankment crest with the coarser mesh (T46q) and the finer mesh (T46qa) is shown in Fig. 5.6. The average combined discharge recorded for the finer mesh was 3.4% lower than with the coarse mesh. The coarser mesh was accepted to give sufficient resolution whilst providing satisfactory computational efficiency.

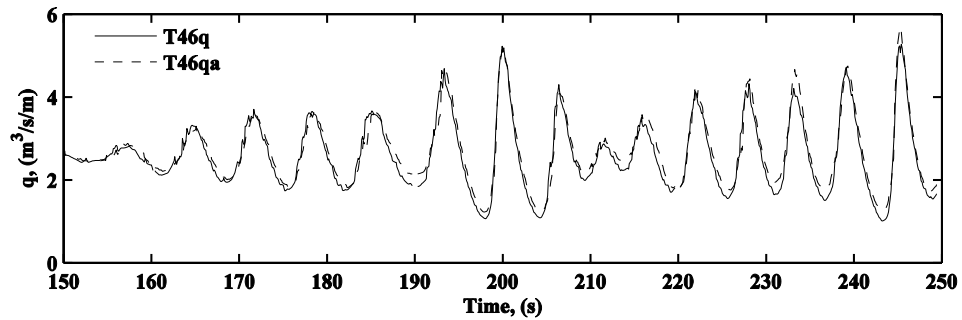


Fig. 5.6 Time history of discharge with a  $0.4\text{m} \times 0.1\text{m}$  mesh (T46q) and  $0.2\text{m} \times 0.05\text{m}$  mesh (T46qa).

As well as the mesh size, the aspect ratio of the mesh, defined as  $\Delta y/\Delta x$ , also needs to be considered. Lin and Liu (2002) recommended a mesh aspect ratio of 1:1 but acknowledged that for some situations a larger aspect ratio is acceptable. For breaking waves, the maximum recommended mesh aspect ratio is 1:2.5 to avoid false breaking. As some of the wave conditions to be tested included plunging breakers, it was important that the model was capable of representing breaking waves. However, for the 1.3m surge tests the aspect ratio with a  $0.4 \times 0.1\text{m}$  mesh was 1:4. To ensure that this did not introduce unacceptable errors, a comparative test was conducted with an aspect ratio of 1:2 i.e. a mesh size of  $0.2 \times 0.1\text{m}$ . A comparison of flow was made between Test T46q, which had a 1:4 mesh aspect ratio, and T46qb, which had a 1:2 aspect ratio. The wave conditions for these tests included plunging breakers. Fig.5.7 shows a snapshot of the water surface at the end of the test,  $t = 250\text{s}$ , for the two aspect ratios and shows very little difference between the two tests. A comparison between the average combined discharge calculated for the two tests at the differing aspect ratios showed that the average combined discharge was 2.0% higher with the larger mesh aspect ratio. It was considered that the larger aspect ratio provided sufficient resolution to define the breakers whilst remaining computationally efficient.

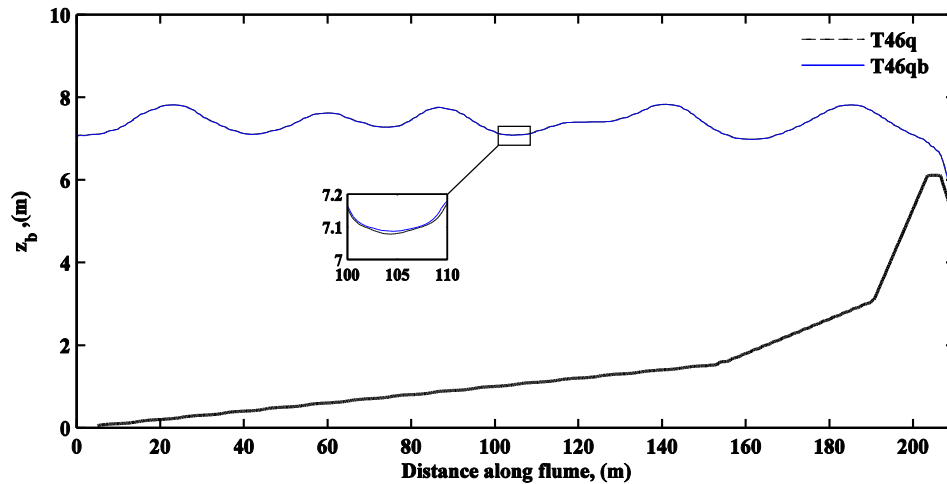


Fig.5.7 A snapshot and magnified view of water surface elevation for mesh aspect ratio 1:4 (T46q) and 1:2 (T46qb).

For other surge levels, the embankment crest periodically dried during wave troughs. For these tests, it was necessary to reduce the mesh size to resolve the layer thickness when waves ran down the seaward side of the embankments as well as the reduced layer thickness on the lee side of the embankment. For some tests, a variable mesh was used so that a more refined grid could resolve the flow near the embankment crest. The smallest mesh size used in this region was 0.05m in both the horizontal and vertical directions.

The duration of the RANS model tests was 250s. This allowed approximately 50s of steady overflow with no waves followed by a period in which the waves began to establish at the embankment and then approximately 150s of combined discharge. The initial period allowed the surge level in the physical model to be calculated by using Equation (2.15) and, for consistency, the discharge with the RANS model was also calculated at the location of P2. However, unlike the physical model that only recorded the velocity at half of the

average depth at P2, with the RANS model the velocities were evaluated at each node, allowing a depth-integrated discharge to be calculated.

With a wave overtopping model, a system has to be devised to ensure that the overtopping discharge is recycled back into the flume. This ensures the conservation of mass. Failure to do this would result in a lowering of water level within the flume over time. This was achieved in the physical model with a pump recirculating water from the reservoir back to the wave paddle. To implement this within the RANS model, the depth and velocity information at the crest of the embankment was used to determine the discharge. The discharge was used as an input back into the model as a depth-averaged velocity at the seaward boundary. This velocity was combined with the velocity determined for wave generation. If the instantaneous discharge was directly fed back into the wave-generating boundary, it effectively generated a false wave at the boundary. To overcome this problem, whilst still maintaining conservation of mass, a running average discharge was used to feed the seaward boundary. It was found that a running mean over a twenty second period successfully produced the required wave profiles whilst maintaining the required surge level. It will later be shown that the degree of success of the wave generating procedure is quite satisfactory.

The RANS model used a rigid free slip boundary condition at the bed and at the embankment. This condition is used when the mesh size is thicker than the viscous boundary layer and the  $k-\varepsilon$  turbulence model is used. However, the use of an alternative turbulence model is also discussed later.

In this section, a description has been given of how the RANS model has been set-up for the combined overtopping tests. In the next, section a comparison is made between the physical and computational model results.

## **5.4. Comparison between RANS model and physical model results**

### **5.4.1. Wave generation**

Waves generated within the RANS model used the waves recorded at wave gauge 2 in the physical model for most of the tests. For verification purposes, it was useful to compare waves recorded at wave gauge 4 in the physical model with those at the equivalent position in the RANS model. As the wave gauge is only 14.922m away from the wave-generating boundary and little wave transformation will have occurred, this is a good test of the wave-generating boundary condition. This comparison is shown in Fig. 5.8 for a representative sample of tests conducted at a surge depth of 1.3m. The difference between the recorded physical and numerical model wave peaks was 0.053m. The good agreement seen in the time histories demonstrates that both the wave generating method is good and the assumption that breaking waves dissipated high frequency energy is valid and there is no build-up of unwanted long wave reflections. As mentioned previously, this assumption is an important condition for wave generation. It was noted that the tests with the best agreement were those with the smallest wave heights. This was true for each of the surge levels tested. The general level of agreement between the physical model waves and those recorded with the RANS model at this location does not appear to be dependent upon the surge level.

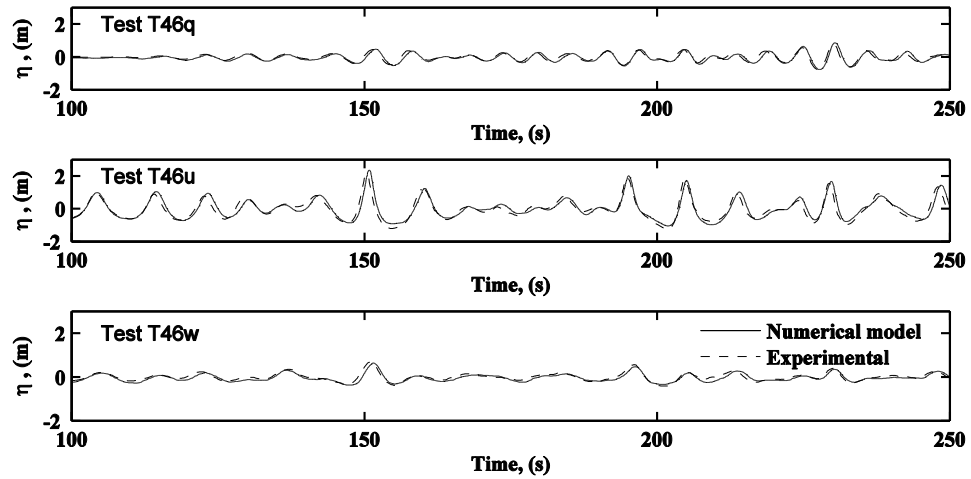


Fig. 5.8 Comparison of surface elevation time histories measured from mean water level at G4.

For computational efficiency, the wave gauge at G2 was selected as the wave input condition to the numerical model. This located the seaward edge of the embankment crest 203.5m from the wave-generating boundary and the embankment crest was 6.1m above the base of the numerical flume. This gave a representation of about a quarter of the physical model flume.

In order to check that the results were similar when a larger proportion of the flume was represented, test T46q was repeated with a wave-generating boundary at the location of wave gauge G1. This test was named T46qlong. The test resulted in a considerable increase in the computational domain. The wave-generating boundary was located 812.8m from the seaward edge of the embankment and the embankment crest was 15.2m above the base of the numerical flume. This increased the number of mesh nodes being represented by a factor of almost eight, resulting in a considerable increase in computation time. Fig. 5.9 shows a time history of wave height at the location of G4 for both the shorter and longer flume tests. The agreement is generally good, but the

wave generation in the longer flume did not agree with the physical model record as well as the wave generation in the shorter flume. A regression analysis gives a coefficient of determination of 0.76 for the long flume test and 0.96 for the short flume equivalent test. The differences between the two plots may be due to waves in the shorter flume not being fully developed because of the close proximity of the wave gauge to the wave maker.

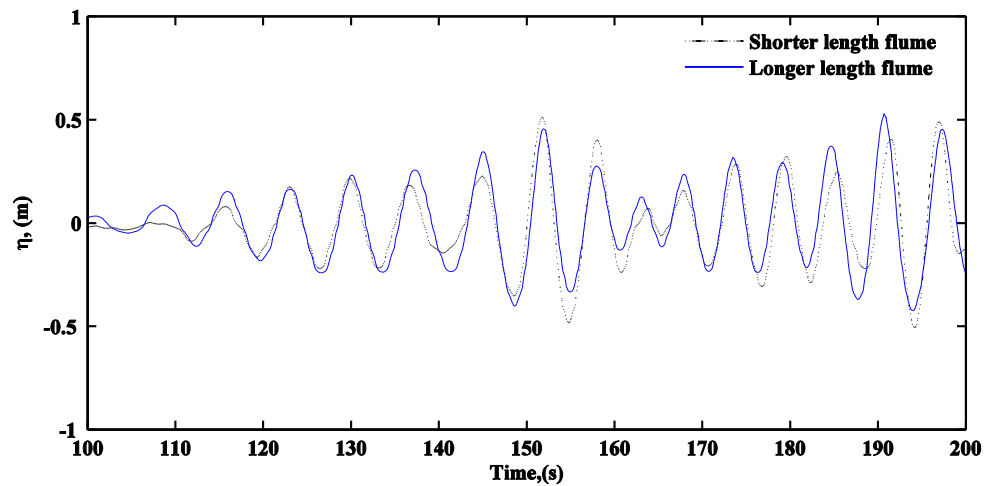


Fig. 5.9 The effect of flume length on the generated waves.

#### 5.4.2. Discharge comparison

The flow depth and velocity information at P2 was used to calculate the discharge in both the physical model and the RANS model at the crest of the embankment. The discharge through partially filled cells in the RANS model was calculated using the VOF function. The calculated discharge with steady overflow and no waves ( $q_s$ ) and the discharge with combined wave overtopping and overflow ( $q_{ws}$ ) were averaged over the same time period in the physical model and the RANS test to ensure equivalence. The start time for the averaging period for  $q_{ws}$  began when the waves had reached the embankment and were established. This was defined as being after the crest of the second wave had arrived at the embankment crest.

### 5.4.2.1. 1.3m surge

Table 5.2 gives, for each of the 1.3m surge tests, wave parameters, Iribarren number, discharge rates and the relative error. The relative error is the difference between the discharge determined from the RANS model and laboratory result, divided by the laboratory result. The table also presents the same data for the long flume test (T46qlong).

Test	Physical Model					RANS		$q_{ws}$ error %
	$H_{m0}$ (m)	$T_p$ (s)	$\xi_p$	$q_s$ ( $m^3/s/m$ )	$q_{ws}$ ave ( $m^3/s/m$ )	$q_s$ ( $m^3/s/m$ )	$q_{ws}$ ave ( $m^3/s/m$ )	
T46ms	0.67	5.83	2.1	2.495	2.654	2.593	2.685	+1.2
T46q	1.21	5.83	1.6	2.456	2.587	2.487	2.634	+1.8
T46ra	2.24	6.09	1.2	2.404	2.716	2.427	2.940	+8.2
T46s	0.78	9.86	3.3	2.634	2.675	2.529	2.618	-2.1
T46t	1.59	10.14	2.4	2.534	2.666	2.528	2.778	+4.2
T46u	2.45	9.65	1.8	2.700	2.712	2.563	2.982	+10.0
T46w	0.75	14.58	5.0	2.567	2.664	2.543	2.626	-1.4
T46y	1.53	14.58	3.5	2.506	2.565	2.400	2.730	+6.4
T46z	2.37	14.58	2.8	5.534	2.752	2.501	2.940	+6.8
T46qlong	1.21	5.83	1.6	2.456	2.587	2.391	2.588	+4.7

Table 5.2 Average combined discharge rates for the 1.3m surge tests.

The average of the relative errors for all the 1.3m surge tests is 4.7%. This varies between a minimum of 1.2% and a maximum of 10.0% for these tests. It was found that the average relative error has a dependence on wave height. For each wave period, three wave heights were tested. For the lower wave heights, with a height less than 1m, the average relative error is 1.6% and increases to 8.3% for the larger waves, over 2m. However, the relative error does not show any obvious dependency on wave period, with each of the wave periods tested showing that the average relative error is broadly similar.

It might also be thought that the relative error would depend on the nature of the wave breaking. The average relative error for Iribarren numbers less than two, indicating plunging waves, was 6.7% and for Iribarren numbers greater than two, surging waves, the average relative error was 3.7%. However, for this surge level the strongest trend was shown to be between wave height and relative error. This can be seen in Fig. 5.10, which shows the correlation between wave height and relative error and Iribarren number and relative error. The correlation coefficient between the wave height and relative error is 0.94 and between Iribarren number and relative error it is  $-0.4$ . This confirms a strong positive correlation between wave height and relative error and that Iribarren number is poorly correlated with relative error.

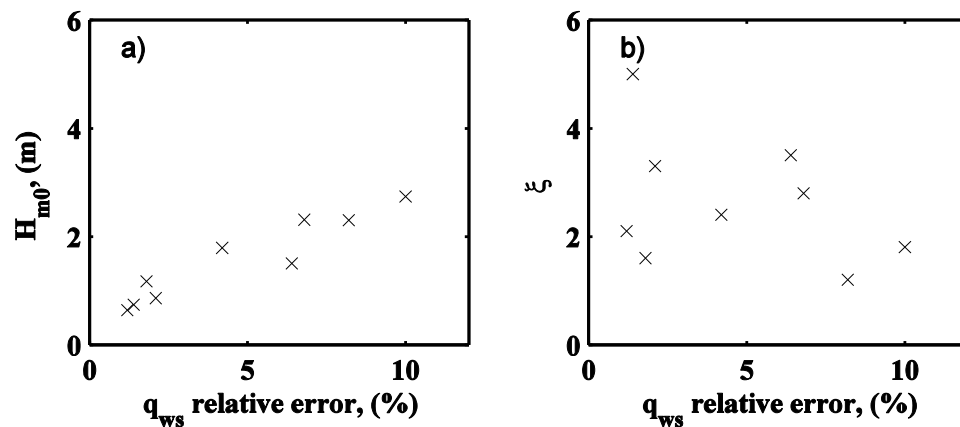


Fig. 5.10 Correlation between a) wave height and absolute relative error and b) Iribarren number and absolute relative error.

In order to determine why the tests with larger wave heights have a higher relative error, it is useful to plot the time histories of discharge for different wave heights. These are shown in Fig. 5.11 for three tests.

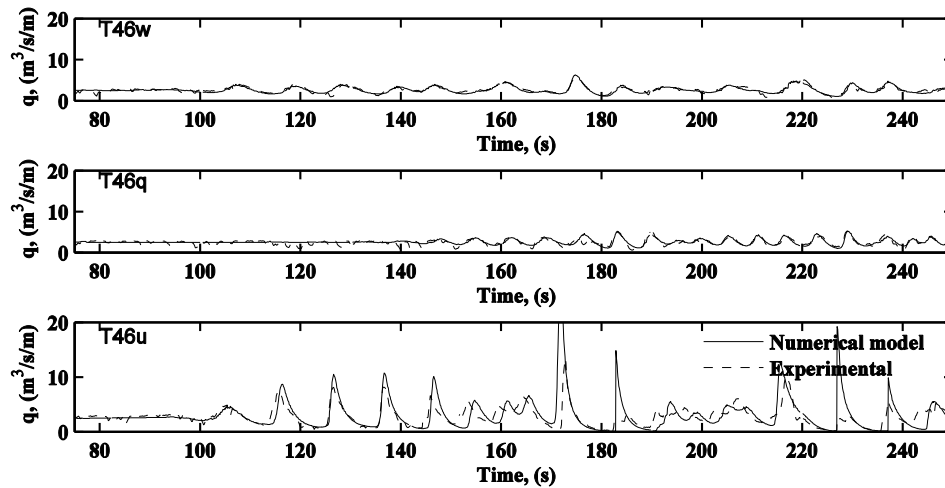


Fig. 5.11 Comparison of discharge at P2 for 1.3m surge.

The time histories indicate a good level of agreement, particularly for the smaller wave heights. However, T46u, which is the test with the larger wave heights, does show that the RANS model has higher peaks, particularly at the larger wave heights.

A comparison between the discharge recorded at P2 during test T46q for the long and short flume tests is shown in Fig. 5.12. The useful part of the wave record for the longer flume test is quite short because of the longer time taken for the waves to propagate from the wave-maker to the embankment crest. Nevertheless, the comparison does show a good visual agreement between the long and short flume tests. The values of  $q_{ws}$  calculated over the shorter time frame for both the long and short tests are 2.588 and 2.585  $m^3/s/m$  respectively. This gives a 0.1% relative error when comparing the long flume test to the short flume test over the same shorter time frame. As the degree of agreement in discharge for these tests is good, it is accepted that using the shorter representation of flume for the remaining tests has not had a significant effect on the results.

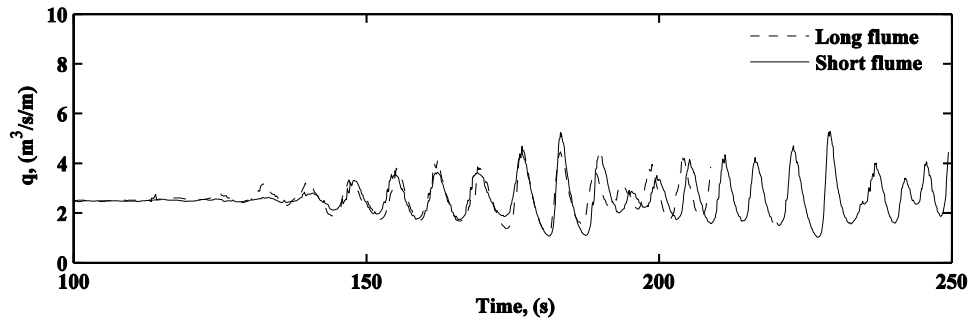


Fig.5.12 Comparison of discharge at P2 for T46q long and short flume tests.

#### 5.4.2.2. 0.81m surge

The discharge rates and the relative errors between the laboratory and numerical models for each of the 0.81m surge tests is given in Table 5.3. As previously mentioned, one of the tests conducted in the physical model was not simulated with the RANS model because the physical model data showed some inconsistencies between the water level at the embankment crest when compared with other tests at this surge level. The average relative error for all tests conducted at this surge depth was 21.8%. Again, this was lower for the smaller wave heights (5.4%) and increased for the larger wave heights (44.2%). The average relative error was worse for plunging waves (29.4%) than for surging waves (14.3%).

Test	$H_{m0}$ (m)	$T_p$ (s)	$\xi_p$	Physical Model		RANS		$q_{ws}$ error %
				$q_s$ (m <sup>3</sup> /s/m)	$q_{ws}$ ave m <sup>3</sup> /s/m)	$q_s$ (m <sup>3</sup> /s/m)	$q_{ws}$ ave (m <sup>3</sup> /s/m)	
T46na	0.81	5.71	1.9	1.203	1.221	1.095	1.209	+1.0
T47a	1.53	5.83	1.4	1.207	1.194	1.110	1.372	+14.8
T46vb	2.33	5.83	1.1	1.207	1.143	1.056	1.796	+57.1
T47c	0.79	9.86	3.3	1.107	1.151	1.052	1.236	+7.4
T47g	2.36	9.65	1.8	1.215	1.431	1.100	2.070	+44.5
T47h	0.71	14.58	5.1	1.153	1.225	1.063	1.215	-7.9
T47i	1.57	14.58	3.3	1.225	1.450	1.076	1.605	+10.7
T47j	2.32	14.58	2.7	1.268	1.491	1.075	1.956	+31.1

Table 5.3 Average combined discharge rates for the 0.81m surge tests.

Fig. 5.13 shows the time histories of combined discharge for three of the tests. The agreement for smaller waves is again shown to be better than for larger waves. There is a reduced level of agreement for the largest waves when compared to the 1.3m surge tests.

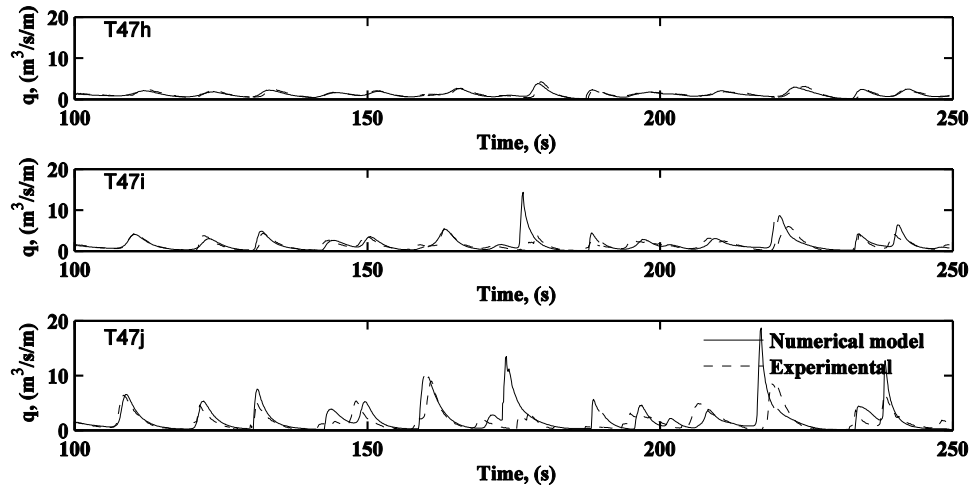


Fig. 5.13 Comparison of discharge at P2 for 0.81m surge.

#### 5.4.2.3. 0.29m surge

Test	$H_{m0}$ (m)	$T_p$ (s)	$\xi_p$	Physical Model		RANS		$q_{ws}$ error %
				$q_s$ (m <sup>3</sup> /s/m)	$q_{ws}$ ave m <sup>3</sup> /s/m)	$q_s$ (m <sup>3</sup> /s/m)	$q_{ws}$ ave (m <sup>3</sup> /s/m)	
T46lh	0.27	5.71	3.3	0.266	0.317	0.271	0.347	+9.3
T46x	1.73	6.06	1.4	0.311	0.446	0.284	0.620	+39.1
T47b	2.46	6.51	1.2	0.310	0.489	0.291	1.03	+111.3
T47e	0.88	10.60	3.3	0.259	0.324	0.258	0.484	+49.5
T46pa	1.66	10.60	2.4	0.245	0.545	0.239	0.732	+34.3
T47fa	2.49	10.60	1.9	0.270	0.704	0.281	1.309	+86.0
T47k	0.76	12.07	4.0	0.244	0.327	0.246	0.427	+30.8
T47la	1.74	13.86	3.1	0.259	0.552	0.261	0.673	+22.1
T47m	2.26	14.00	2.5	0.256	0.678	0.262	1.254	+85.1

Table 5.4 Average combined discharge rates for the 0.29m surge tests.

The combined discharge rates and the relative errors for the 0.29m surge tests are given in Table 5.4. The average combined discharge relative error for all tests at this surge depth was 59.1%. This is significantly larger than the 0.81m

and the 1.3m surge tests. The relative error was lower for the smaller wave heights (29.9%) and increased for the larger wave heights (94.1%). The average relative error was worse for plunging waves (78.8%) than for surging waves (38.5%).

Fig. 5.14 shows the time histories of combined discharge for three of the tests and demonstrates that, for the lowest surge level, the agreement for smaller waves is shown to be better than for larger waves. The level of agreement for the largest waves is shown to be lower when compared to both the 0.81m and 1.3m surge tests.

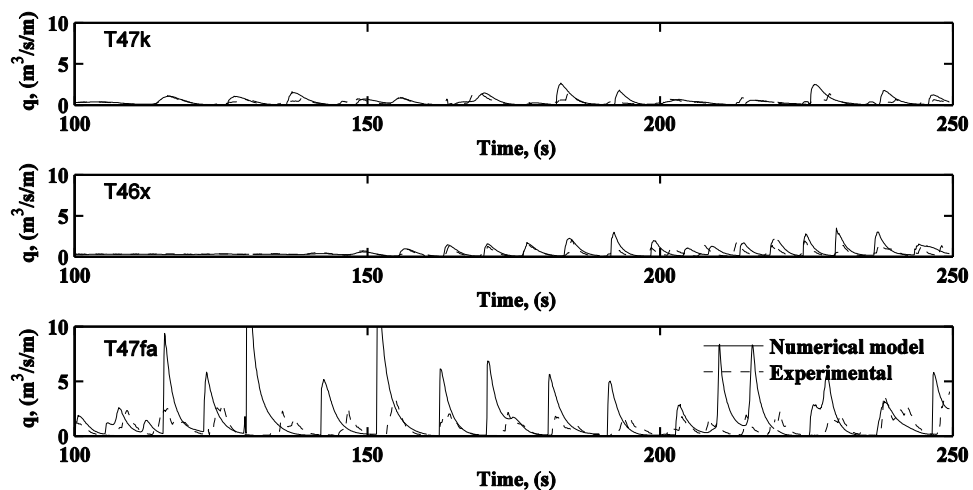


Fig. 5.14 Comparison of discharge at P2 for 0.29m surge.

Having made a comparison between the physical and computational model in terms of the discharge at each of the surge levels, the differences between the models could be a result of differences between the calculation/measurement of either the surge depth or velocity or both. To investigate this further, a comparison of time histories of surge depth and velocity in each model has been performed.

### 5.4.3. Flow depth comparison

The water depth at the embankment crest in the physical model was recorded with a pressure cell (Druck PDCR-200) that was regularly calibrated by flooding the model to known static levels. The water depth in the computational model was determined with reference to the VOF function.

#### 5.4.3.1. 1.3m surge

The time histories of water depth at the embankment crest for the same three tests presented for the discharge comparison at a surge depth of 1.3m are shown in Fig. 5.15. Again, the agreement is very good for the smaller wave heights but, for some of the waves in the larger wave test (T46u), the crests calculated with the RANS model are high compared with the physical model. The phase shift is limited to just two of the larger discharge peaks at about 185 and 230s in Fig. 5.11. Fig. 5.15 shows a more favourable agreement for water depth, but with the RANS model peaks still being higher than those from the laboratory.

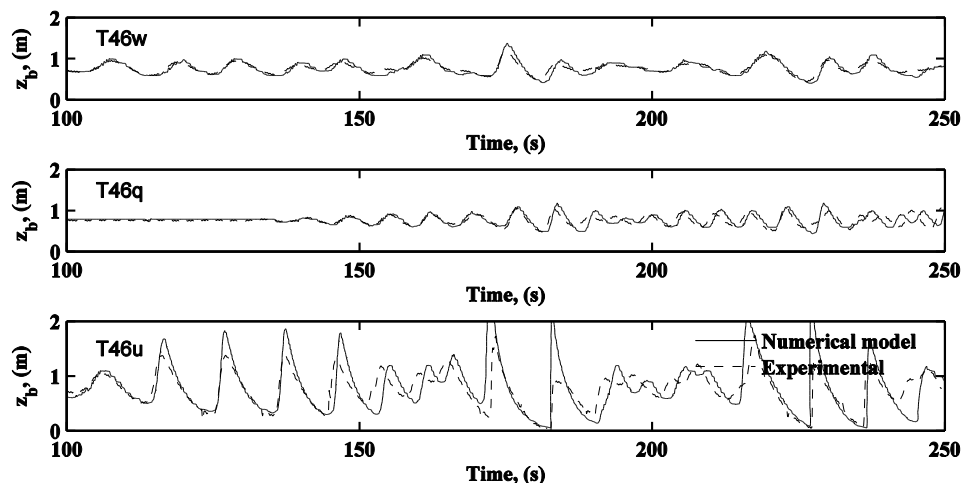


Fig. 5.15 Comparison of flow depth at P2 for 1.3m surge.

### 5.4.3.2. 0.81m surge

The time history of flow depths at the embankment crest for three tests with a flow depth of 0.81m are shown in Fig. 5.16. The test with the lowest significant wave height shows the best agreement (T47h). T47i shows a time history for an intermediate size significant wave height and generally shows good agreement, but the largest wave in the record shows a lower peak in the physical model, with some phase shift. The time history with the largest waves (T47j) shows two large peaks having substantially lower elevations in the physical model and, again, the phase shift is apparent.

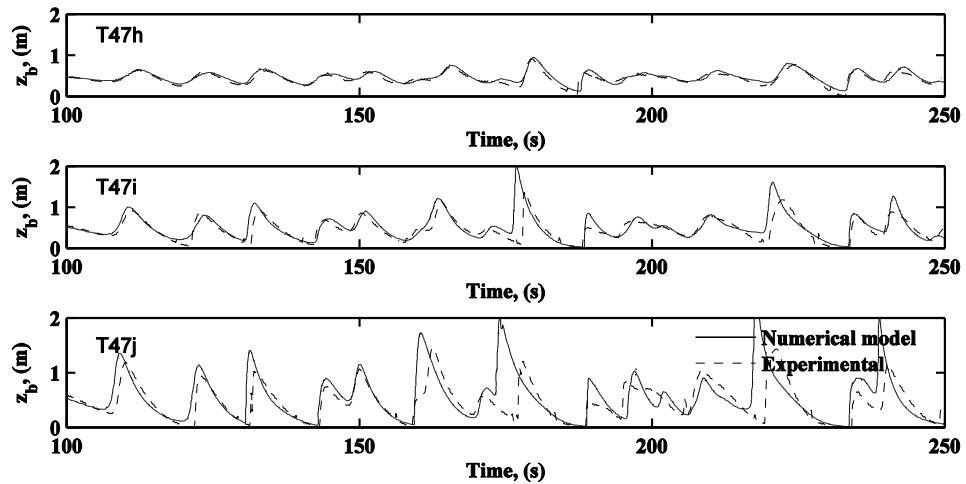


Fig. 5.16 Comparison of flow depth at P2 for 0.81m surge

### 5.4.3.3. 0.29m surge

Time histories of flow depth at the surge depth of 0.29m are shown in Fig. 5.17 for three tests. T47k generally has good agreement between the numerical and physical model. However, the physical model has a number of short period wave spikes that do not appear in the numerical model time history. The time history for the highest significant wave (T47fa) shows that the two largest waves have phase shifts and lower crest elevations in the physical model. Other large

waves in the time history also are shown to have lower crest elevations in the physical model.

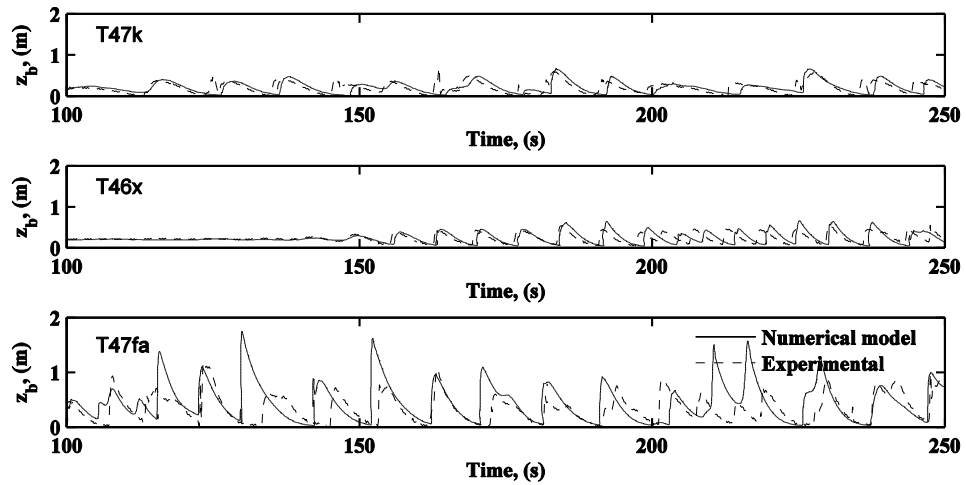


Fig. 5.17 Comparison of flow depth at P2 for 0.29m surge.

#### 5.4.4. Velocity comparison

As already stated, the flow velocity measurements on the embankment crest were taken with an LDV recording the flow velocity at half depth. The RANS model calculates velocities at each cell node. The velocities used in this comparison are an average of the node velocities.

##### 5.4.4.1. 1.3m surge

The time histories of flow velocities at the crest of the embankment at a 1.3m surge for both the RANS model and the physical model are shown in Fig. 5.18. It is evident that the velocity time history from the physical model has some high frequency noise. This is true for all tests but is particularly true of the velocities recorded during the steady surge period of T46q. The variation in the physical model discharges shown for T46q result from the variable nature of the velocity signal for this period.

For all tests, the peak velocities recorded in the physical model are generally larger than those recorded with the RANS model. In Test T46u, it can be seen that when the water level fell below the level of the LDV in the physical model, the recorded velocities remained uniform during this period. This has affected the two largest velocity peaks at approximately 185s and 230s in the record. Each of these results has flat periods that extend onto the next peak and appear to have significantly reduced the following peaks. These under-predictions of velocities correspond to an under-prediction of discharge and are the two peaks that appear as over-predictions with the RANS model in Fig. 5.11.

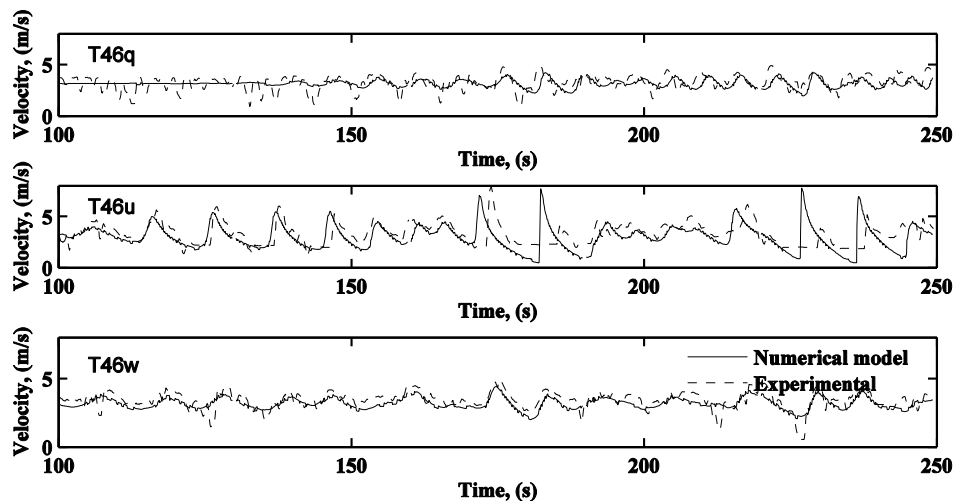


Fig. 5.18 Comparison of flow velocities under combined discharge conditions at P2 for 1.3m surge.

#### 5.4.4.2. 0.81m surge

Although the LDV height was adjusted to half the steady flow depth for each surge level tested, for lower surge levels this means that the instrument was exposed during wave troughs more frequently. Fig. 5.19 shows that at this surge level the velocities recorded in the physical model are all showing periods

when the wave trough fell below the LDV level. This is particularly striking in test T47j where the LDV is not recording velocities for a substantial period of time.

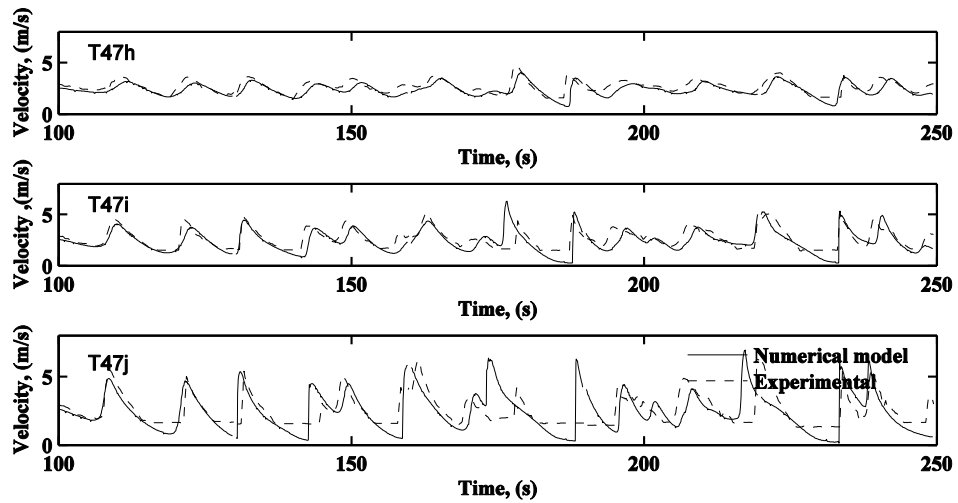


Fig. 5.19 Comparison of velocities under combined discharge conditions at P2 for 0.81m surge.

#### 5.4.4.3. 0.29m surge

Fig. 5.20 clearly shows that for a 0.29m surge the LDV is frequently exposed during troughs and often not recording even during the smaller wave heights. Test T47fa also shows a significant time lag between the velocities calculated with the RANS model and those measured in the physical model.

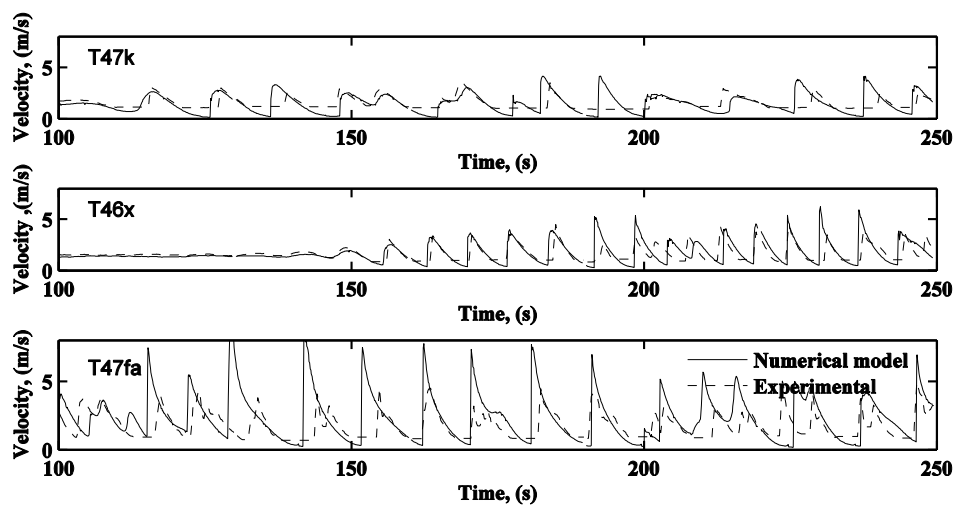


Fig. 5.20 Comparison of velocities under combined discharge conditions at P2 for 0.29m surge.

#### 5.4.5. Discussion of results

It has been shown that the average relative error during the steady surge part of the tests shows no general trend and the relative error is similar for both large and small surges. On the other hand, the average relative error for the combined discharge has been shown to increase as the surge depth decreases. This indicates that the physical and numerical model have better agreement at the larger surge depths. It has also been shown that there is an increase in relative error as the wave heights increase and some of the larger peaks are much higher in the RANS model than in the physical model. The tests have also shown that there is little correlation between Iribarren number and relative error. The time histories for each of the surge depths show that, for some waves, a phase shift sometimes exists between the numerical and physical model results. This has occurred for each of the surge levels but only occurs for the larger wave heights.

The flow regime at each of the flow depths varies considerably with the different wave heights. For the higher surge level, the embankment crest remains mostly fully submerged. However, at the intermediate and lower surge levels the embankment is frequently exposed during wave troughs. This poses some significantly increased modelling challenges for both the physical and computational model and is discussed later.

The prediction of discharge using the RANS model is generally acceptable. However, for larger wave heights the discrepancy between the predictions made by the RANS model and the physical model tend to increase. These

discrepancies could be due to the assumptions made within the RANS model or could be due to scale effects or modelling methodology within the physical model or possibly a combination of both. In this section, the differences between the computational and physical model results are considered.

#### 5.4.5.1. Sources of errors in the numerical model

The differences between the computational model and the physical model results could be due to the RANS model not correctly describing the flow conditions during wave peaks at the embankment crest. The free surface profile of a typical wave on the embankment is shown in Fig. 5.21 and shows that, for some tests, the wave is clearly breaking.

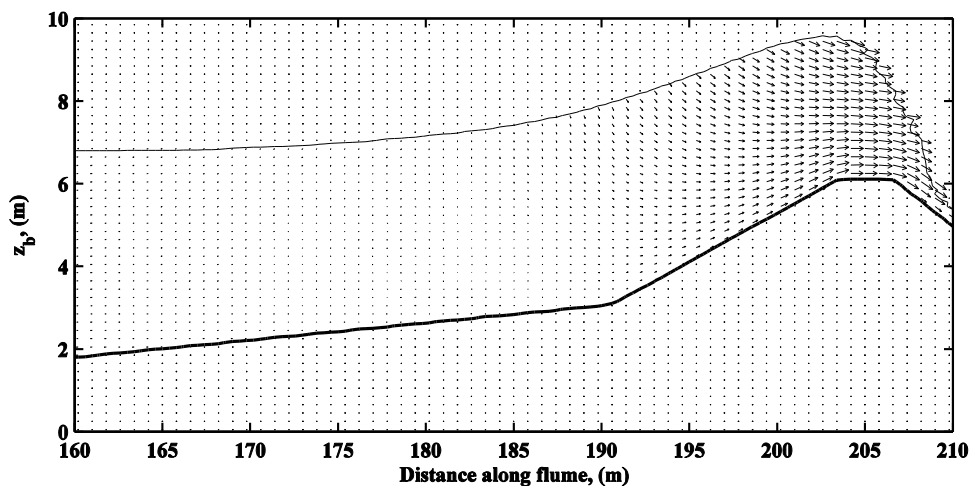


Fig. 5.21 RANS model calculated free surface profile for test T46u at 172s, showing a breaking wave at the embankment and the velocity vectors at every other point horizontally and vertically.

Lin and Liu (1998a) validated the RANS model for a cnoidal wave breaking on a sloping beach against numerical and laboratory data. Although the hydrodynamics of a wave breaking on a sloping beach will be different from a wave breaking on the top of an embankment with combined overflow, it is useful to consider how the RANS model performs with regard to a breaking wave. In

the tests performed by Lin and Liu (1998a), a comparison was made for mean quantities such as wave elevation, velocities and turbulence at points in a breaking wave. The mean quantities were obtained by phase averaging after waves had reached a quasi-steady state. Four locations were investigated on the landward side of the breaking point, with the nearest point being about a quarter of a wavelength from the breaker point. For these tests, it was found that, at the point nearest to the breaking point, the crests measured in the model were lower than in the laboratory data and the velocities were higher. This is the opposite of that found in the current study. In the Lin and Liu study, it was found that near to the breaking point turbulence intensity was overestimated and was quite different from the measurements. The lower crest elevations were a result of the excessive estimated turbulence intensity. Further from the breaker point, the RANS model more accurately represented the turbulence intensity and, consequently, the water surface elevation was also better represented. The poorer representation of the turbulence intensity near the breaker point was caused by the model not accurately predicting the initiation of turbulence in the initial stages of wave breaking where a rapidly distorted shear flow region exists. These uncertainties in the initial turbulent conditions at the initiation of breaking generate difficulties in predicting the location of the breaking point. As stated above, the turbulence closure model used in the RANS model describes the velocity profile in a steady, uniform, turbulent boundary layer, which is not the situation in a breaking wave although, as Lin and Liu have demonstrated, the model can still provide a good approximation.

The comparison between calculated and measured values in the current series of tests differs from the study by Lin and Liu (1998a) in that it is not the phase-averaged quantities being compared but the instantaneous measurements. Also, the instantaneous measurements at P2 are at or near the breaking point, whereas the phase-averaged measurements were at about a quarter of a wavelength from the breaking point.

To determine the type of wave at the crest of the embankment, the Iribarren number,  $\xi_p$ , has been calculated for each test. These values are shown in Tables 5.2, 5.3 and 5.4. Where  $\xi_p$  is less than two, indicating plunging breakers, generally a worse agreement was found for combined discharge at all surge depths. For tests where  $\xi_p$  is greater than two, surging waves, the RANS model generally provided a better representation of wave overtopping discharge. This is because the turbulence regime under a wave depends on the nature of the wave and whether it is breaking. The results from the current study indicate that the present RANS model is not fully able to reproduce the surface profile and breaking point for a plunging wave. A breaking wave is a two-phase flow problem, whereas the RANS model is based on single-phase assumptions that assume zero shear stress at the water-air interface. To fully represent a breaking wave, a two-phase representation of the situation must be included so that the air-water interactions can be included. A study by Wang et al. (2009) extended the current RANS model to include two-phase flow and repeated the validation exercise conducted by Lin et al. (1999) and described above. When comparing phase-averaged measurements near the breaker, the two-phase model showed some improvement compared to the present RANS model.

However, it was suggested that the model could be improved by including a two-phase turbulence model.

To test the sensitivity of the RANS model output to different turbulence models, some tests were conducted where the non-linear eddy viscosity model that is used to calculate the mean tangential velocities within the boundary layer was replaced with both a linear eddy viscosity model and then a laminar model. Fig. 5.22 shows the depth-averaged velocity time history for the tests with the different turbulence models for the largest wave within test T46u. The Iribarren number for this test is 1.8, suggesting a plunging breaker type. The tests resulted in near identical velocities and flow depths at the embankment crest, indicating that the results are not particularly sensitive to the type of turbulence model available as options within the RANS model. However, it should be remembered that the  $k-\varepsilon$  turbulence closure model describes the velocity profile in a steady, uniform, turbulent boundary layer which is unlikely to be true in a breaking wave. So, it is probable that none of the available options correctly describe the situation at the embankment crest. To fully represent the situation near the breaking point, an improved turbulence closure model is required, along with a two-phase flow representation.

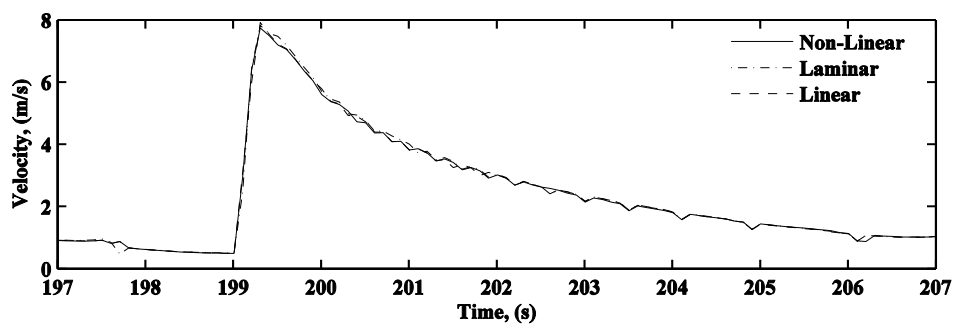


Fig. 5.22 Depth-averaged velocity time history at P2 for Test T46u for different turbulence models.

Although the energy dissipation at the crest of the embankment is dependent on the turbulence level, it is also dependent on the roughness of the bed. The log law turbulence Equation (3.18), used in the RANS model, describes the velocity profile in a steady, uniform, turbulent boundary layer. Nikuradse (1933) related the zero intercept in the log velocity profile,  $z_0$ , and the bed roughness,  $r$ , with  $z_0 = r/30$ . Clearly, the bed roughness has potential to alter the energy dissipation and the free surface profile. A number of tests were conducted with varying levels of bed roughness in the RANS model. To determine the effect on discharge, the discharge at the embankment crest was examined for a range of reasonable values of roughness from smooth,  $r = 0.0001$  mm, to 20 mm. For all the tests conducted, varying the roughness had a negligible effect on the discharge, as shown in Fig. 5.23.

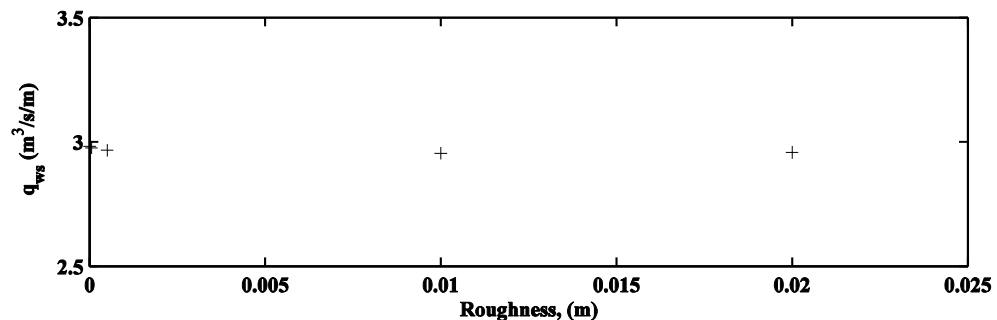


Fig. 5.23 The effect of bed roughness on dimensionless discharge.

As already discussed, Fig. 5.21 shows that location of the breaking point occurs at the crest of the embankment. The criteria used to define when a wave will break are usually based on Stokes' waves, with the assumption that waves break when the horizontal velocity at the crest of the wave becomes equal to the wave celerity. This leads to two criteria that determine when a wave will break, a limiting wave steepness and a limiting wave height to water depth ratio. Pullen and She (2002) found that a minimum vertical acceleration and maximum horizontal acceleration in the wave were good universal criteria to

determine when breaking will occur. In the present study it was observed that waves broke at the crest of the embankment and usually nearer the rear edge of the crest. This is near P2, which is the point at which the velocities and depths were recorded in the physical model. This is clearly a region of great flux and small changes in the computed location of the breaker point will significantly alter the calculated depth at this point. Although it is not possible to compare discharges at locations other than P2, it is possible to compare the flow depths. The measured and calculated free surface profiles are shown in Fig. 5.24 for various stages during wave breaking, at locations P1, P2, P3 and P4. This is for one of the larger waves in T46u and demonstrates that the embankment crest dries for short periods. The figure shows good agreement between the RANS model results and the physical model data. However, at the point when the wave breaks the agreement is not as good. This is in agreement with the depth time histories shown in Fig.5.15, 5.16 and 5.17, with the depths for the highest waves being over-predicted within the RANS model. Fig. 5.24 confirms that the over-prediction is not localised to P2. However, with the RANS model, the wave is breaking very near P2 and small errors in the calculation of the breaker location have a large effect on the depth of flow at this point.

In tests where drying occurred, it was important to ensure that the mesh size was chosen to provide an adequate representation of flow in these conditions. This was achieved by reducing the mesh size. For some tests, a variable mesh was used, so that a smaller mesh could be defined near the embankment. The smallest mesh size was 0.05 x 0.05m.

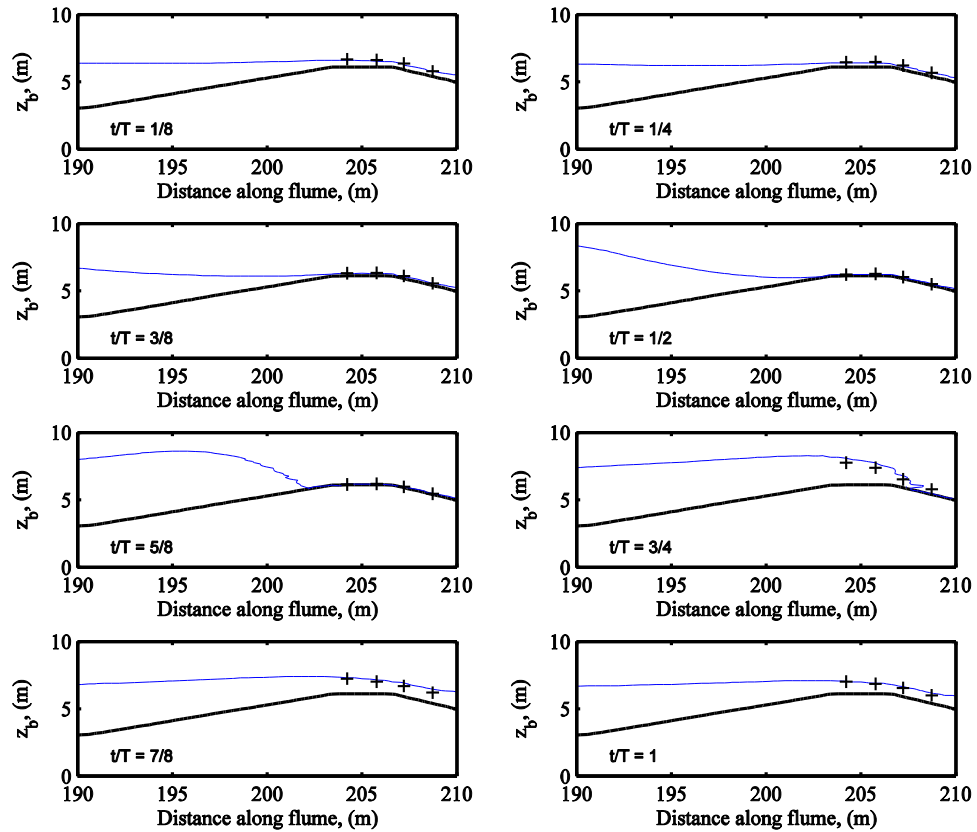


Fig. 5.24 Embankment profile(solid line), RANS calculated free surface (blue line) and measured free surface at P1, P2, P3 and P4 (crosses) for Test T46u.

#### 5.4.5.2. Sources of error in the physical model

A possible cause for the lower velocities recorded in the physical model during wave peaks was using the velocities recorded at half the mean flow depth. To understand this, it is useful to look at a vertical profile of velocity through the water column at the crest of the embankment. Fig. 5.25 shows a RANS model velocity profile and corresponds to the peak at 172s in test T46u. It can be seen that a velocity recorded at half depth of 0.65m will record a higher value than a depth-averaged velocity.

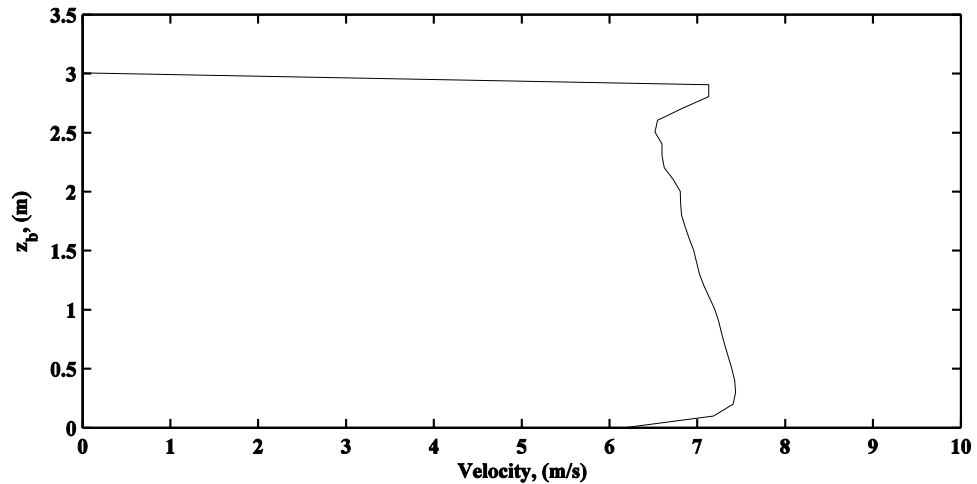


Fig. 5.25 RANS model vertical profile of velocity during combined flow over the embankment crest.

To demonstrate this effect, the RANS model velocities were reanalysed. Fig. 5.26 shows the instantaneous depth-averaged velocity calculated by averaging the velocity at each node and, for comparison, the corresponding velocity calculated at half-depth is also shown. The half-depth velocity clearly shows larger peaks, similar to those shown in the physical model data. The half-depth velocity drops to zero when the water level is below half-depth. This demonstrates that recording the velocity at half-depth will give higher peaks than if a depth-averaged velocity is used.

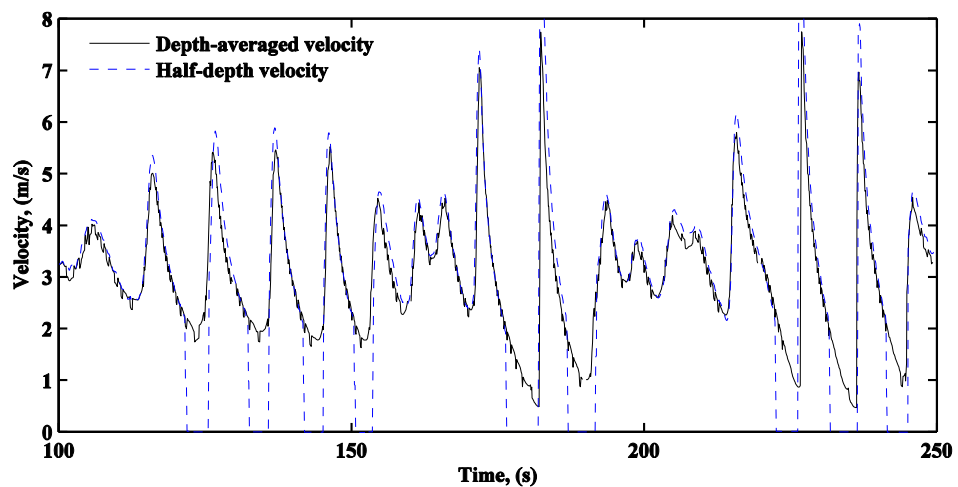


Fig. 5.26 Depth-averaged velocities and velocities at half the mean flow depth calculated from the RANS model results.

As previously mentioned, an inspection of the depth and velocity record shows an apparent time delay between the water level rising above the LDV and the LDV beginning to record data. This has occasionally resulted in the next peak not being recorded and consequently, the next discharge peak being underestimated. As the water level drops below the LDV more frequently during the tests with a lower surge level, the delayed restarting of the LDV recording is more evident in the 0.29 and 0.81m surge conditions. To clarify this, the physical model discharge, velocity and depth in test T47fa are plotted in Fig. 5.27. This shows that following a wave trough when the LDV has been exposed, there is sometimes a delay between the water level rising above the LDV and the LDV recording velocities. The depth at which the instrument begins to record is not constant and so it is not possible to apply a correcting time step to the whole record. This appears to cause an under-estimation of the velocities at the peak of the wave.

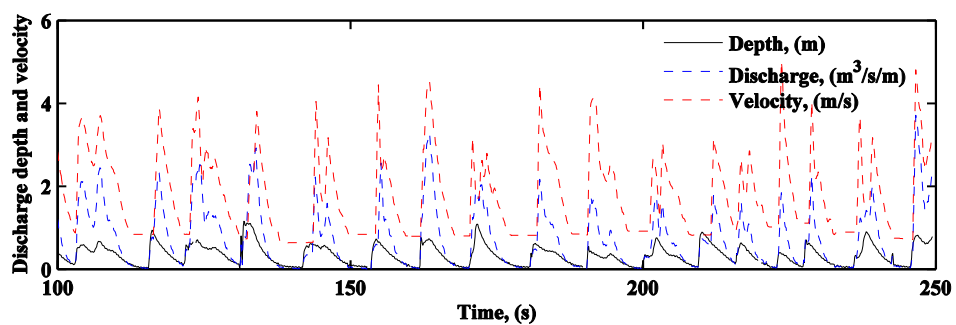


Fig. 5.27 Depth, discharge and velocity recorded in the physical model for T47fa.

A comparison of flow depth at the embankment crest shows good agreement between the RANS model and physical model for all but the peaks of the largest waves. However, the peaks are larger with the RANS model than in the physical model. A possible cause for the underestimation of the flow depth in the physical model might be the method used to determine the depth.

The depth of flow was recorded using bottom-mounted pressure gauges. These gauges are frequently used to measure wave parameters in coastal waters such as wave heights. Water surface elevation above mean water level,  $\eta$ , can be calculated from the pressure records using linear wave theory for progressive waves, Equation (5.1). The first term in this equation is just the hydrostatic pressure and the second term is dynamic pressure. The dynamic pressure results from two contributions. The first is the increase in pressure due to the free surface displacement, and the second is the component from the vertical acceleration under the wave. This is  $180^\circ$  out of phase with the free surface displacement.

$$p = -\rho g z_{sw} + \rho g \eta \frac{\cosh k(h + z_{sw})}{\cosh kh} \quad (5.1)$$

In the physical model the pressure gauges on the embankment were situated in regions of high local velocity caused by the overflow. This altered both the wave speed and the wavelength. Hedges (1987) showed that Equation (5.1) is valid in the presence of currents, but only if the effect of the current on the wavelength and therefore the wave number,  $k$ , is taken into consideration. However, for flow at the crest of the embankment, flow is unlikely to be well described by linear theory, particularly when waves are breaking. This makes it difficult to account for the effects of currents within the physical model. If the effect of the velocities caused by the overflow on the pressure gauges were not taken into account, then this may account for some variation between the depths recorded in the physical model and calculated using the RANS model. In a study comparing wave buoy data against wave height calculated from bottom-mounted pressure, McKee Smith (2002), estimated that overestimates of up to 20% occur if currents were neglected.

The physical model tests were conducted using Froude's Model Law, which ensures that inertia, pressure and gravity forces are reproduced correctly to scale. Froude similarity means that the turbulent Reynolds shear stress terms are scaled, so macro features of turbulent dissipative processes are also scaled correctly. However, viscous and surface tension influences are not modelled and these have the potential to introduce significant scale effects. Certainly, viscous features such as micro turbulence dissipative processes will not be modelled. Generally, building models at a large enough scale ensures that the Reynolds number is sufficiently large to maintain turbulent flow and ensure that viscous effects are not significant. The effect of viscous damping in non-breaking waves propagating over a short distance such as the embankment crest can be considered to be negligible for flow depths greater than 20 –30 mm (Tirindelli et al., 2000). When scaled at 1:25, these values correspond to 0.5 – 0.75 mm and an inspection of the time histories shown in Fig. 5.15, 5.16 and 5.17 shows that all tests have wave troughs that fall below these values. For the lower surge tests, the flow depth reduces to zero during the largest wave troughs, as shown in Fig. 5.24. Viscous scale effects can be expected to be negligible for depths above say 0.5mm but become progressively more significant as depths reduce. Viscous and surface tension effects may also affect the shape of a breaking wave. As the wave steepness increases so the radius of curvature of the breaker crest will decrease. If breaking waves are scaled, the surface tension effect can be expected to alter the radius of curvature. Tirindelli et al., (2000) expected breaker shape to be affected by scale if the waves had a wavelength less than 0.5m and period less than 0.5s. The waves in this study should not be affected by this scale effect. With regard

to wave run-up and downwash, surface tension forces can usually be ignored if the flow depth is greater than 6mm in the model (Hamill, 1995). However, for tests where a large degree of drying of the embankment occurs, then surface tension effects may play an increasing role. Viscous and surface tension scale effects may be expected to affect both depths and velocities at low flow depths. However, a comparison of depths between the physical and RANS model during wave troughs generally show better agreement at low flow depths. A comparison of velocities at low flow depths is not possible because the velocities in the physical model were not recorded below approximately half the surge depth.

The scaling of the surface roughness of the articulated concrete mats is also a potential for scale effect within the physical model. The mats were made to be smooth because it is difficult to scale the roughness according to the model scale length. This gave less frictional resistance and is expected to have slightly increased the flow velocities adjacent to the mats.

In this section, a comparison has been made between the RANS and physical model results. The relatively good wave generation results demonstrate that the wave generating procedure used in the numerical model adequately reproduces the waves recorded in the physical model. A wave-by-wave analysis of combined discharge over the embankment crest shows the average relative error increases as the surge depth decreases. Furthermore, there is an increase in relative error as the wave height increases and some of the larger wave peaks are much smaller in the physical model than found using the RANS model. The flow depths were generally found to be higher with the RANS model

than the physical model, particularly for larger waves. This was in part because the larger waves were breaking at the crest of the embankment. Previous studies have shown that the RANS model does not adequately predict the initiation of turbulence near the breaking point and this could cause an error in calculating the location of the breaking point. Small changes in the breaker location at the embankment crest would cause differences in flow depth at the measurement point.

Additionally, some errors may exist in the physical model because the pressure gauges used to determine flow depth at the embankment required a correction for the effect of overflow velocity and any vertical acceleration. However, for the highly non-linear flow at the crest of the embankment, it is difficult to account for the effects of currents within the physical model. This may account for some variation between the depths recorded in the physical model and calculated using the RANS model.

The velocities recorded with the RANS model were generally higher than in the physical model. The recording procedure in the physical model when the water level dropped below the LDV caused some errors. The LDV was shown on occasion to have a time delay between the water level rising above the LDV and velocities beginning to record again. This caused some velocity and discharge peaks to be missed within the physical model. The flow velocities and discharges calculated with the RANS model were shown to be insensitive to both the different turbulence models and the different bed roughnesses tested. Viscous and surface tension scale effects could well affect both velocities and flow depths for tests where the flow depths are shallow, i.e. when the

embankment crest dries between waves. However, overall the comparison between the computational model and physical model showed that the RANS model performed well. In the next chapter, the validated RANS model is used to investigate the effect of crest width on overtopping discharge.

## Chapter 6

# MODEL COMPARISON AGAINST DESIGN FORMULAE

### 6.1. Introduction

In this section, the discharge calculated with the RANS model is compared with the available design formulae for combined overtopping. In Chapter 2, three available design formulae for combined overtopping were presented. Firstly, the equation developed by Schuttrumpf (2001) for overtopping with zero freeboard, combined with an equation for flow over a weir. Secondly, the equation developed by Reeve et al. (2008), which is based on a series of RANS model tests. Finally, the equation by Hughes and Nadal (2009) that is based on the same experimental data used for the model validation in this study.

### 6.2. Comparison

To compare the RANS results with the equation presented by Schuttrumpf (2001) summed with a broad crested weir equation, the most appropriate weir equation must be selected. Pullen et al. (2007) suggested Equation (2.13) could be used to calculate the weir discharge, which can be evaluated directly from the depth of flow over the weir. This is equivalent to the negative freeboard  $R_c$ . However, the flow over a broad crested weir can vary from sub-critical to critical

and then super-critical so the flow depth will vary with location. Consequently, the value of  $q$  calculated in Equation (2.13) is dependent on where  $R_c$  is recorded. For broad crested weirs, it is usual to use the upstream head measured at a distance sufficiently upstream to be relatively free from the draw down in water surface elevation near the weir. In terms of water level above a seawall, this is the tidal level plus the surge component. Equation (2.15) uses the upstream head and is based on ideal flow conditions with the value of  $C_d$  found from empirical formulae and is 1.0 for ideal flow. Reeve et al. (2008) used Equation (2.15) with the value of  $C_d$  given by Equation (2.16), which has a range of validity given in Chadwick and Morfett (1998) as  $0.45 < h_u/L_w < 0.8$  and  $0.35 < h_u/(h_u+h_c) < 0.6$ . For the tests conducted in this study  $h_u/L_w$  had a range from 0.1 to 0.44 and  $h_u/(h_u+h_c)$  had a range of 0.09 to 0.30. Therefore, the value of  $C_d$  calculated with Equation (2.16) was outside the acceptable range for the formula. The approach adopted by Hughes and Nadal was to calculate the equivalent upstream head above the weir crest from the measured steady discharge at the start of each test using Equation (2.15) with a  $C_d$  value of 1.0. For the purposes of comparison, the value of  $R_c$  calculated from the steady discharge part of the RANS tests, using the same procedure as adopted by Hughes and Nadal, was used to predict the dimensionless discharge from each of the design formulae. The values used to calculate the discharge are given in Table 6.1. The discharge calculated with each of the design equations and the RANS model is shown in Fig. 6.1 and this figure is comparable with Fig. 7 in Hughes and Nadal (2009).

	$H_s$	$H_{m0}$	$R_c$	$\xi_p$
T46lh	0.26	0.27	-0.29	3.26
T46x	1.73	1.73	-0.30	1.35
T47b	2.50	2.46	-0.31	1.21
T47e	0.87	0.88	-0.28	3.34
T46pa	1.70	1.66	-0.27	2.39
T47f	2.69	2.49	-0.30	1.90
T47k	0.79	0.76	-0.28	3.99
T47l/T47la	1.78	1.74	-0.29	3.05
T47m	2.71	2.26	-0.29	2.50
T46na	0.82	0.81	-0.74	1.86
T47a	1.56	1.53	-0.75	1.37
T46v	2.40	2.33	-0.73	1.11
T47c	0.78	0.79	-0.72	3.28
T47g	2.45	2.36	-0.75	1.81
T47h	0.71	0.71	-0.73	5.10
T47i	1.71	1.57	-0.74	3.28
T47j	2.48	2.32	-0.74	2.72
T46ms	0.65	0.67	-1.31	2.12
T46q	1.20	1.21	-1.29	1.56
T46ra	2.26	2.24	-1.27	1.19
T46s	0.76	0.78	-1.30	3.33
T46t	1.57	1.59	-1.30	2.38
T46u	2.49	2.45	-1.31	1.80
T46w	0.74	0.75	-1.31	4.98
T46y	1.53	1.53	-1.26	3.46
T46z	2.41	2.37	-1.29	2.76

Table 6.1 Test numbers and corresponding wave conditions, freeboard and Iribarren Number.

The dimensionless combined discharge calculated with the RANS model generally agrees well with that predicted by Equations (2.12) and (2.15) and Equation (2.18). The dimensionless combined discharge calculated using Equations (2.12) and (2.15) is generally slightly larger than that found with the RANS model, whilst that found with Equation (2.18) is generally slightly less. It is noted that better agreement is found for more negative values of  $R_c / H_{m0}$ . The range of applicability of Equations (2.17) is for negative freeboards in the region  $0 > R_c / H_s > -1.0$ . A number of the tests conducted in this series were outside of this range of applicability and these results have been excluded from Fig. 6.1. The remainder show an overestimation of the dimensionless discharge when compared with the other results.

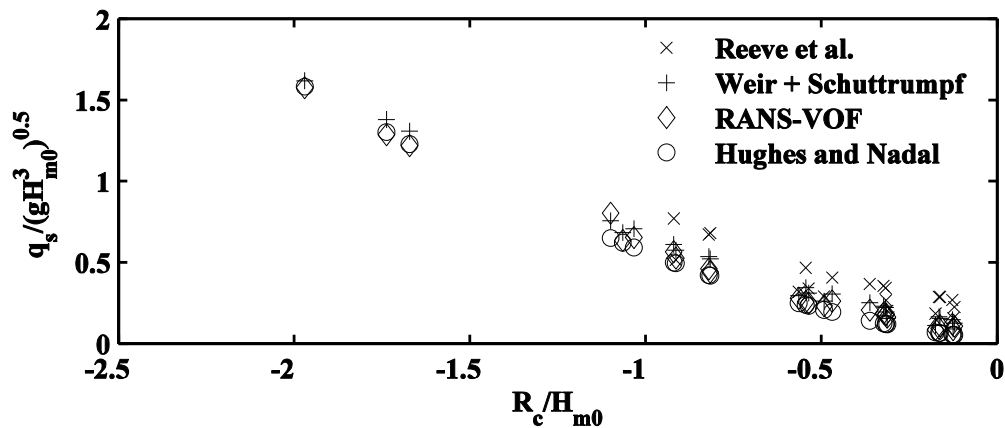


Fig. 6.1 Dimensionless combined discharge and dimensionless negative freeboard for the RANS model test and calculated values based on  $R_c$  calculated from Equation (2.15).

A problem with this analysis is that the steady discharge at the start of the test has been used to calculate  $R_c$  rather than a direct measurement. Also, using Equation (2.15) for this calculation, with a value of  $C_d$  set to 1.0, assumes ideal flow. This method of calculating  $R_c$  values may well produce different values to  $R_c$  determined from a direct measurement recorded at an upstream location.

ISO 3846:2008 is the international standard for flow over broad crested weirs. It recommends that the upstream head readings should be recorded at a distance of between 3 and 4 times the value of the head on the weir. This allows a measurement of head that is a sufficient distance upstream to avoid the drawdown near the weir and is close enough to the weir for the energy loss between the measurement location and the weir to be negligible. The equation given in the standard is equivalent to Equation (2.15), with tables and graphs that allow  $C_d$  to be evaluated and  $C_d$  being dependent on the ratios of the upstream head to crest width and upstream head to height of weir. To determine the value of  $R_c$  for the RANS tests in accordance with ISO

3846:2008, the average depth was determined during the steady surge part of the test for the period 30-80 seconds at a location approximately 3.5 times the nominal upstream head from the seaward edge of the embankment. The value of  $R_c$  found using this method was on average 6.0% less than that using the steady discharge and Equation (2.15) to calculate  $R_c$ . The values of  $R_c$  calculated using both methods are shown in Table 6.2.

<i>Test Number</i>	<i><math>R_c</math> calculated from <math>q_s</math></i>	<i><math>R_c</math> calculated using ISO 3846:2008</i>
T46lh	-0.293	-0.287
T46x	-0.303	-0.297
T47b	-0.308	-0.297
T47e	-0.284	-0.277
T46pa	-0.270	-0.267
T47f	-0.301	-0.297
T47k	-0.275	-0.272
T47l/T47la	-0.286	-0.227
T47m	-0.287	-0.237
T46na	-0.744	-0.707
T47a	-0.751	-0.727
T46v	-0.727	-0.657
T47c	-0.725	-0.707
T47g	-0.747	-0.707
T47h	-0.730	-0.702
T47i	-0.736	-0.727
T47j	-0.735	-0.717
T46ms	-1.311	-1.247
T46q	-1.286	-1.197
T46ra	-1.265	-1.197
T46s	-1.301	-1.207
T46t	-1.300	-1.197
T46u	-1.312	-1.197
T46w	-1.305	-1.197
T46y	-1.256	-1.197
T46z	-1.291	-1.177

Table 6.2 Test numbers and  $R_c$  calculated from  $q_s$  as well as  $R_c$  calculated in accordance with ISO 3846:2008.

The geometry of the broad crested weir for which Equation (2.15) is applicable is a rectangular weir where the upstream face forms a sharp right angle corner at its intersection with the crest. The embankment used in this study is significantly different to this design and this difference is a likely source of error. ISO 3846:2008 states that if this edge is slightly rounded the discharge

coefficient may increase significantly. For the embankment used in this study, the upstream face has a 1:4.25 slope, which is likely to increase discharge in a similar way to having a rounded edge.

To demonstrate this effect the values of  $R_c$  determined from the RANS results were used to calculate the discharge over the embankment using Equation (2.15) and values of  $C_d$  given in ISO 3846:2008. This gave an average discharge that was 21% lower than the RANS calculated discharge. A cause of the higher discharge found with the RANS model is the upstream face of the embankment not being perpendicular to the crest. When a non-standard broad crested weir is used in the field, a calibration exercise is usually carried out either in the field or a scale model study is used to determine the characteristics of the weir. As no discharge characteristics exist for this type of weir, the characteristics could be derived from the physical model study data. Unfortunately, the depth of flow information at the required location is not available. However, this information is available for all the combined overtopping tests conducted with the RANS model. To determine the weir characteristics, a graph of measured values of  $q_s$  and  $R_c^{3/2}$  is given in Figure 6.2. The data are well correlated and the linear regression line has a coefficient of determination of 0.9987. The slope of the regression line is 1.9197 when the y intercept is zero. Therefore, the equation of the regression line is identical to Equation (2.15) with a  $C_d$  value of 1.126.

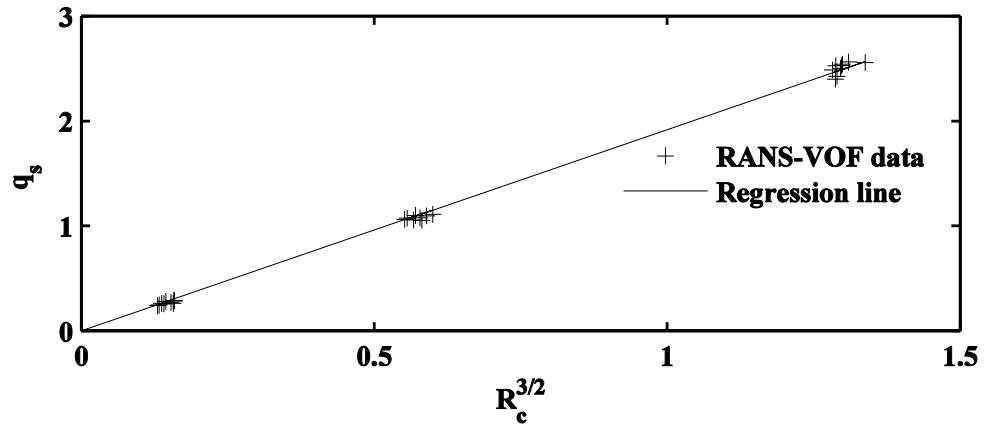


Fig. 6.2 Embankment steady discharge,  $q_s$  and  $R_c$  calculated with the RANS model discharge,  $R_c$  measured in accordance with ISO 3846:2008.

Equations (2.17) and (2.18) were used to recalculate the combined overtopping discharge over the embankment with  $R_c$  measured in accordance with ISO 3846:2008, as shown in Table 6.2. The combined overtopping discharge was also calculated using the expression developed by Schuttrumpf (2001), combined with Equation (2.15) with the value of  $C_d$  of 1.126. Figure 6.3 shows the dimensionless discharge and dimensionless freeboard for these equations along with the RANS measured values.

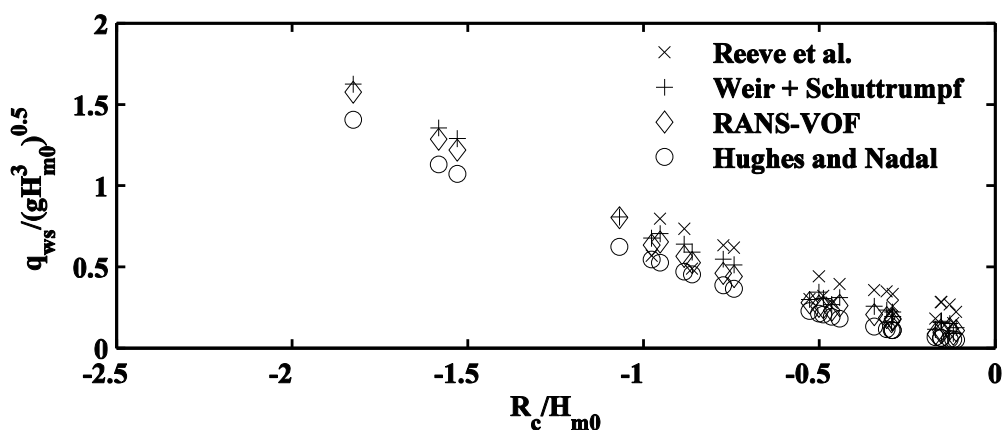


Fig. 6.3 Dimensionless combined discharge and dimensionless negative freeboard for the RANS test and calculated values based on  $R_c$  evaluated in accordance with ISO 3846:2008 and a  $C_d$  value of 1.126.

Comparing Fig. 6.1 and Fig.6.3 shows that the dimensionless discharge is sensitive to the method of evaluating  $R_c$ . Although the dimensionless discharge calculated with the RANS model has not changed, the measured value of  $R_c$  has reduced. This has caused the data points calculated with the RANS model shown on Figure 6.3 to move to the right. The dimensionless discharge calculated from Hughes et al., Equation (2.18), gives lower values than computed with the RANS model. This is because a value of  $R_c$  measured in this way is 6.0% lower on average. As the only parameters in Equation (2.18) are  $R_c$  and  $H_{m0}$ , and  $H_{m0}$  remains the same, a lower value of  $R_c$  results in a lower dimensionless discharge. Similarly, the lower dimensionless discharge found with Equations (2.17), is also a result of the lower value of  $R_c$ . Although the wave component of the overtopping discharge calculated with Equations (2.12) has remained the same, the weir flow component calculated with Equation (2.15) has increased significantly. This has increased the combined total and given a combined total marginally above the RANS results. Overall, the results calculated with the RANS model fall somewhere between the results from the equations provided by Reeve et al. and Hughes and Nadal and are marginally lower than the dimensionless discharge found by combining the modified weir equation and the equation provided by Schuttrumpf.

Perhaps one of the key differences between the combined wave overtopping study reported by Reeve et al. (2008) and the other studies on combined wave overtopping is the model set up. Reeve et al. used a sloping embankment seaward face retained by a thin wall of approximately 0.5m thickness. The crest of this wall would act more like a thin plate weir than a broad crested weir. The

discharge over a sharp edged rectangular weir is given by Douglas et al. (1979) as;

$$q_t = \frac{2}{3} b \sqrt{(2g)} h_w^{3/2} \quad (6.1)$$

A comparison between Equation (2.15) and Equation (6.1) shows that a thin wall would be expected to show an increase in measured discharge. This may explain why the dimensionless discharge predicted by Equation (2.17) is greater than recorded in the current study.

It should be noted that as the ratio  $R_c / H_{m0}$  increases, i.e. as the wave height reduces, the predicted discharge should tend towards that given by the equation for a broad crested weir. Clearly, this will be true for the Schuttrumpf model combined with the weir equation, but it is also true for both the RANS model results, but Figure 6.3 shows this is less so for the formula derived by Hughes and Nadal.

## Chapter 7

### MODEL APPLICATION

#### 7.1. Introduction

In the previous chapters, it has been shown that the RANS model can calculate the complex hydrodynamic flow for combined discharge over embankments and mass transport under progressive and standing waves. For these situations, the model has been validated against available experimental data and theoretical results. In this chapter, the model is used to determine how embankment crest width alters the combined discharge rates. Design guidance is provided, so the effect of crest width can be included when evaluating combined discharge at embankments.

#### 7.2. Effect of crest width on overtopping discharge

Often the crest width of embankments is determined by criteria such as the ability to use the embankment crest for vehicular access for maintenance and repair or, in coastal towns, wide-crested embankments are built for both coastal protection and to provide promenades. The effect of the crest width on wave overtopping discharge for negative freeboard has yet to be defined. However, some recent physical model tests (Verwaest et al. 2010) have been conducted

to investigate wave overtopping of wide-crested dikes with positive freeboard and intermittent wave overtopping. A provisional formula has been derived based on the energy balance consideration of a single overtopping wave. Currently, there is no design advice on the effect of crest width on embankments and dikes with negative freeboard. In this chapter, the validated RANS model is used to investigate this situation and a design formula is presented.

During the RANS model comparison against design formulae, conducted in Chapter 6, it has been found that the key difference between the design formulae given by Hughes and Nadal (2009), Equation (2.18), and Reeve et al. (2008), Equation (2.17), was the configuration of the embankment and seawall, as shown in Fig. 7.1. The embankment used by Hughes and Nadal is detailed in Fig. 5.1 and 5.2 and has a 3.05m crest width, a 1:4.25 seaward slope and a 1:3 lee side slope. In comparison, the seawall configuration used by Reeve et al. had a similar slope on the seaward side but the crest was only approximately 0.5m wide and the lee side of the crest had a vertical wall. It was found that the flow over the structures, when subjected to overflow, behaved like a broad crested weir over the 3.05m embankment, but the flow over the relatively thin crest of the seawall showed an increase in discharge. The crest of the thinner seawall was thought to act more like a thin plate weir than a broad crested weir and this could possibly account for the increase in discharge.



Fig. 7.1 Variation in embankment and seawall profiles tested by Reeve et al. (2008), left, and Hughes and Nadal (2009), right.

### 7.3. Model set-up

For this part of the study, the general embankment configuration was the same as shown in Figs. 5.1 and 5.2, used in the Hughes and Nadal (2009) physical model tests. However, this test series used six different crest widths, varying from 0.5m to 3.0m in 0.5m increments. Overall seventy-four tests were conducted. The tests contained thirty differing random wave conditions, with a range of significant wave heights tested between 0.265m and 2.71m and for peak periods in the range 5.7 to 14.6s. This included wavelengths in the range 38.8m to 111.4m and for both plunging and surging waves. Negative freeboards were tested between 0.26m and 1.21m. A complete list of tests included in the analysis is given in Appendix B.

The procedure used to determine the negative freeboard for the tests was similar to that described in Chapter 6. For an initial period, the embankment was subjected to overflow with no waves and the value of  $R_c$  for each test was evaluated at a location near 3.5 times the nominal negative freeboard from the seaward edge of the embankment. This was in accordance with ISO 3846:2008. In the tests, the depth at this location was determined and averaged over the initial 30-80 seconds of the test. The values of negative freeboard found for each test are presented in Appendix B.

For these tests the waves began to reach the embankment after 80s and had established by 100s. The average combine discharge ( $q_{ws}$ ) was determined between 100 and 250s and values for each test are given in Appendix B.

Generally, the model used a mesh size of 0.4m in the horizontal direction and 0.1m in the vertical direction. However, for the tests with lower negative freeboards, the flow running down the leeside of the embankment would be intermittent and shallow and required a greater level of mesh refinement to adequately define this flow. For computational efficiency a variable mesh was used. In the horizontal direction this began at 0.4m node spacing and at a distance of 190m from the wave-generating boundary, it gradually decreased until, at the embankment crest, the node spacing was 0.1m. In the vertical direction, again a variable mesh was used, with 0.1m node spacing near the bed and in the region of embankment crest this was reduced to 0.05m.

The time step used with the RANS model ranged between 0.01s for tests with larger negative freeboards to 0.002s for the lower surge level. The time step was selected to provide adequate definition near the embankment crest. For all tests, the roughness of the bed and embankment was set to be smooth and the  $k-\varepsilon$  turbulence closure model was used.

It is possible to output the flow depth and velocity information at each node of the model mesh. Additionally, it is possible to output time histories of particular parameters at specified gauge locations. To analyse the flow depth and velocity at the embankment crest, a gauge location was defined at 204.000m from the wave generating boundary. This equates to a location on the crest of 0.484m landward of the seaward edge. The same gauge location was used for each test.

## 7.4. Discussion of results

The first 30 tests in Appendix B were carried out with the same wave conditions but with six different crest widths and at five different negative freeboards.

These tests show how discharge varies with crest width and negative freeboard, with other parameters remaining the same.

The effect of crest width on steady overflow discharge for five different surge levels is shown in Fig. 7.2. The value of  $R_c$  given is the mean value for that particular nominal surge level. The figure shows that as the crest width is reduced the overflow discharge increases. The average increase in  $q_s$  is 15% for a 0.5m crest width compared to a 3.0m crest width. This would be as expected, because generally as the weir crest width reduces, the nature of the weir changes from being broad crested to, in the extreme case, sharp edged. For the same flow depth, the equation for a sharp edge weir, Equation (6.1), predicts greater discharge than the equation for a broad crested weir, Equation (2.15).

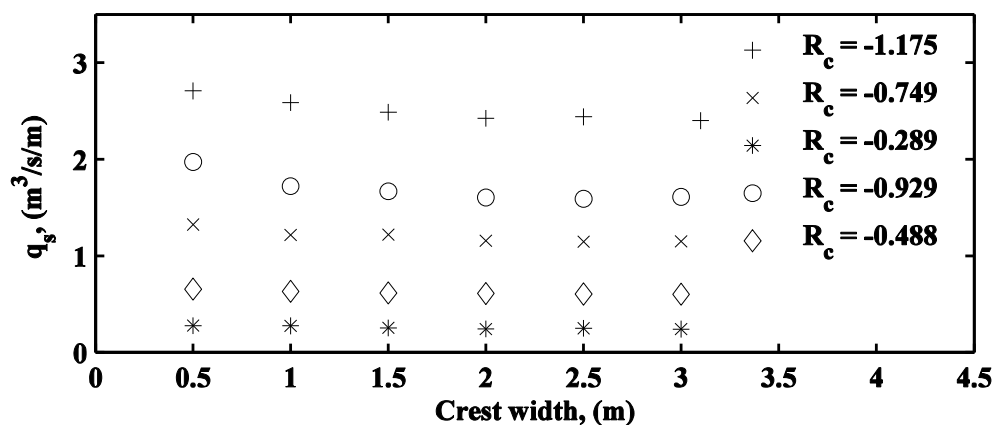


Fig. 7.2 Variation in overflow discharge with crest width for five values of  $R_c$ .

As the weir crest width,  $L_w$ , is reduced, the flow pattern changes as shown in Fig. 7.3. ISO 3846:2008 notes that for  $0.1 < R_c / L_w < 0.4$  the flow will be similar to

a broad crested weir and for  $0.4 < R_c / L_w < 1.6$  flow will be as for a short crested weir. For broad crested weirs, the flow is parallel to the crest for a portion of the flow over the crest and for short crested weirs flow is curvilinear, as shown in Fig. 7.3. For the tests in this series, at the highest surge level the embankment acts as a broad crested weir only when its crest is 3m wide. For the -0.749m surge level, the weir is broad crested above 2.0m wide and for the -0.287m surge level it is broad crested above 1.0m wide. Although the transition from short to broad crested weir occurs at each of the surge levels, Fig. 7.2 shows that for steady overflow there is no abrupt change in discharge during this transition.

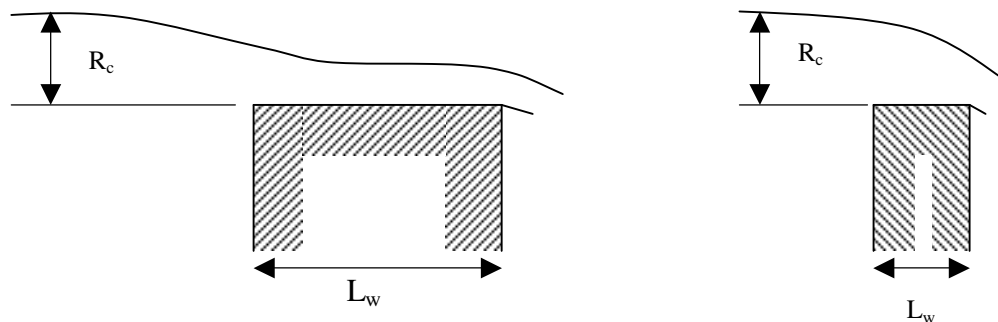


Fig. 7.3 Flow patterns over rectangular broad and short-crested weirs.

For combined discharge, the effect of crest width for five surge levels is shown in Fig. 7.4. The figure again shows that with the shorter crest widths there is an increase in discharge. The average increase in  $q_{ws}$  is 21% for a 0.5m crest width compared to a 3.0m crest width.

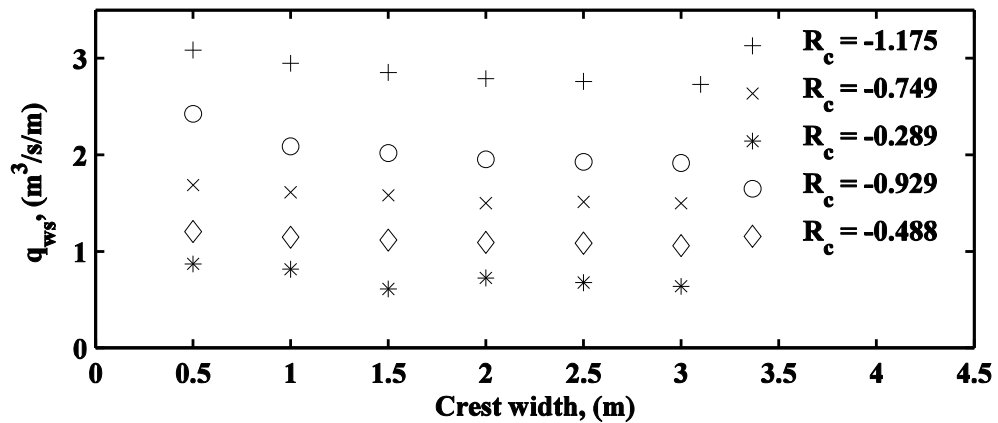


Fig. 7.4 Variation in combined discharge with crest width for five values of  $R_c$ .

It was anticipated that the effect of reducing the embankment crest width may explain the difference in discharge calculated with Equations (2.17) and Equation (2.18). However, the results here cannot fully account for these differences. This is shown in Fig. 7.5, which is a plot of dimensionless discharge and dimensionless negative freeboard calculated for each of the crest widths and wave conditions tested using Equations (2.17) and (2.18) and the RANS model. It should be noted that the range of applicability of Equation (2.17) is for negative freeboards within the region  $0 > R_o/H_s > -1.0$ . Tests outside this range of applicability have been excluded from the plot. The vertical spread of the RANS model results at each of the surge levels is caused by the increase in discharge at the shorter crest widths. As Equations (2.17) were derived from tests with a 0.5m crest width, while Equation (2.18) was derived from tests with a 3.05m crest width and the RANS model results are for crests widths ranging from 0.5m to 3.05m, the RANS model results should range between the Equations (2.17) and (2.18) results. Fig. 7.5 demonstrates that this is not quite the case and although the crest width difference certainly accounts for some of the variation between the equations, other factors must also be important. One of the other differences between the configurations used to derive Equations

(2.17) and (2.18) was that for Equations (2.17), as well as having a shorter crest width the landward side of the crest had a vertical wall. For Equation (2.18), the landward side of the crest had a 1:3 slope. It would be expected that the configuration with the vertical wall on the landward side of the crest would have a greater discharge and this explanation is consistent with the results.

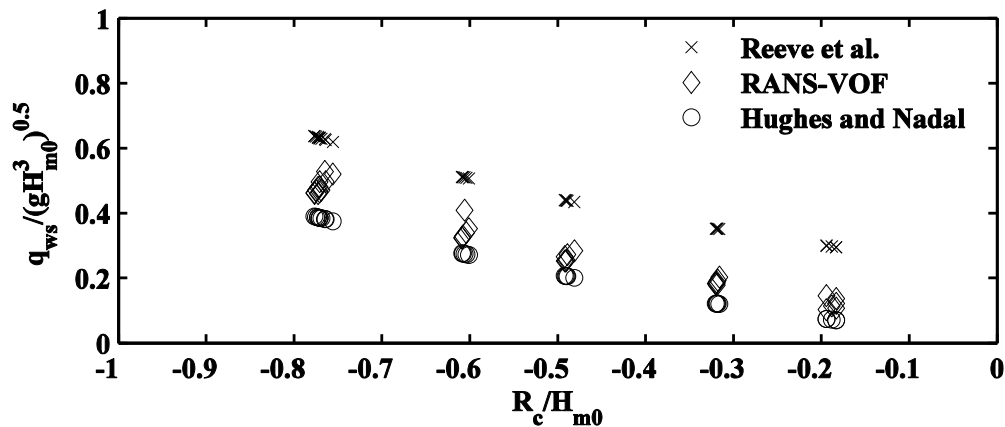


Fig. 7.5 Dimensionless discharge and dimensionless negative freeboard calculated using Equations (2.17) and (2.18) and from the RANS tests at differing crest widths.

In this section, the effect of crest width on combined discharge has been considered. The combined discharge has been found to increase as the crest width is reduced. It was also found that the differences between the predicted combined discharge calculated using Equations (2.17) and (2.18) can be partially explained by the differences in the crest width used in the test configurations used to derive the equations.

## 7.5. Development of the design formula

In this section the development of a design equation for combined discharge over embankments with negative freeboards, that includes the effect of crest width, is described.

To develop a design equation for combined discharge the key variables need to be determined. These were considered to be:  $q_{ws}$ ,  $g$ ,  $H_s$ ,  $R_c$ ,  $L_w$ , and  $\lambda_p$  or  $T_p$ .

The general form of a relationship can be found using Buckingham  $\pi$  Theorem.

A good description of Buckingham  $\pi$  Theorem can be found in Hamill (1995),

but is not given here. With the variables  $q_{ws}$ ,  $g$ ,  $H_s$ ,  $R_c$ ,  $L_w$ , and  $T_p$ , the general

form of the equation can be found to be Equation 7.1 or 7.2 depending on the

repeating variables chosen. In the following equations  $C_1$ ,  $C_2$ ,  $C_3$ ,  $C_4$  and  $C_5$  are

constants to be determined from tests.

$$\frac{q_{ws}}{\sqrt{g|R_c|^3}} = C_1 \left( \frac{H_s}{|R_c|} \right)^{C_2} \left( \frac{L_w}{|R_c|} \right)^{C_3} \left( \sqrt{\frac{gT_p^2}{|R_c|}} \right)^{C_4} \quad (7.1)$$

$$\frac{q_{ws}}{\sqrt{gH_s^3}} = C_1 \left( \frac{|R_c|}{H_s} \right)^{C_2} \left( \frac{L_w}{H_s} \right)^{C_3} \left( \sqrt{\frac{gT_p^2}{H_s}} \right)^{C_4} \quad (7.2)$$

With the variables  $g$ ,  $H_s$ ,  $R_c$ ,  $L_w$ , and  $\lambda_p$  the general form is given as:

$$\frac{q_{ws}}{\sqrt{gL_w^3}} = C_1 \left( \frac{|R_c|}{L_w} \right)^{C_2} \left( \frac{H_s}{L_w} \right)^{C_3} \left( \frac{\lambda_p}{L_w} \right)^{C_4} \quad (7.3)$$

However, a suitable design equation for combined discharge has to correctly

take into account that when  $H_s$  becomes zero  $q_{ws}$  will be non zero with a

negative freeboard, and when  $R_c$  is zero  $q_{ws}$  is again non zero if  $H_s$  is non zero.

Unfortunately, none of these equations can correctly account for this and

another approach needs to be adopted.

An alternative method is to form an equation that fits the data and conforms to

the limiting conditions. That is, the equation should tend towards the form of the

weir equation when  $H_s$  becomes small and should tend toward Equations (2.12)

as  $R_c$  becomes zero. The approach taken was to combine these two equations

whilst incorporating additional terms to take into consideration embankment crest width, as shown below.

From the weir equation (2.15),

$$q = C_1 \sqrt{|R_c|^3} \quad (7.4)$$

which for dimensionless discharge gives:

$$\frac{q_{ws}}{\sqrt{gH_s^3}} = C_1 \left( \frac{-R_c}{H_s} \right)^{3/2} \quad (7.5)$$

From Equation (2.12) for  $\xi_p < 2$  gives

$$\frac{q_{ws}}{\sqrt{gH_s^3}} = C_1 \left( \frac{H_s}{\lambda_p} \right)^{-1/2} \quad (7.6)$$

From Equation (2.12) for  $\xi_p > 2$  gives

$$\frac{q_{ws}}{\sqrt{gH_s^3}} = C_1 - C_2 \left( \frac{H_s}{\lambda_p} \right)^{3/2} \quad (7.7)$$

The form of the combined discharge equation was found by combining Equation (7.5) and Equations (7.6) and (7.7) whilst including an additional dimensionless term to account for crest width. This gave;

$$\frac{q_{ws}}{\sqrt{gH_s^3}} = C_1 \left( \frac{-R_c}{H_s} \right)^{3/2} \left( \frac{L_w}{\lambda_p} \right)^{C_2} + C_3 \left( \frac{\lambda_p}{H_s} \right)^{1/2} \left( \frac{L_w}{\lambda_p} \right)^{C_4} \quad \text{for } \xi_p < 2 \quad (7.8)$$

$$\frac{q_{ws}}{\sqrt{gH_s^3}} = C_1 \left( \frac{-R_c}{H_s} \right)^{3/2} \left( \frac{L_w}{\lambda_p} \right)^{C_2} + C_3 - C_4 \left( \frac{H_s}{\lambda_p} \right)^{3/2} \left( \frac{L_w}{\lambda_p} \right)^{C_5} \quad \text{or } \xi_p > 2 \quad (7.9)$$

The next stage is to find the value of these constants such that the sum of the absolute value of  $X$ , calculated for each of the seventy-four tests, is a minimum, where:

$$X = \frac{q_{ws}}{\sqrt{gH_s^3}} - C_1 \left( \frac{-R_c}{H_s} \right)^{3/2} \left( \frac{L_w}{\lambda_p} \right)^{C_2} - C_3 \left( \frac{\lambda_p}{H_s} \right)^{1/2} \left( \frac{L_w}{\lambda_p} \right)^{C_4} \quad \text{for } \xi_p < 2 \quad (7.10)$$

and

$$X = \frac{q_{ws}}{\sqrt{gH_s^3}} - C_1 \left( \frac{-R_c}{H_s} \right)^{3/2} \left( \frac{L_w}{\lambda_p} \right)^{C_2} - C_3 + C_4 \left( \frac{H_s}{\lambda_p} \right)^{3/2} \left( \frac{L_w}{\lambda_p} \right)^{C_5} \quad \text{for } \xi_p > 2 \quad (7.11)$$

This was achieved using the pattern search method developed by Hooke and Jeeves (1961). This uses a pattern search process to find the minimum of a multidimensional surface. Using this method, an initial estimate was made for each of the constants and the sum of  $|X|$  was obtained by summing  $|X|$  calculated for each of the tests. This was followed by exploratory moves, increasing and decreasing each of the values in turn. This allows an optimum direction of travel to be obtained and the value giving the minimum sum of  $|X|$  was updated. This search was continually repeated and each time the value that gave the optimal direction of travel was updated. When the exploratory moves showed an improvement that was lower than a tolerance limit then the size of the search step was reduced and the iterations continued until convergence was achieved.

<i>Coefficient</i>	<i>Optimal value</i>
C <sub>1</sub>	0.4740
C <sub>2</sub>	-0.0845
C <sub>3</sub>	0.0499
C <sub>4</sub>	-0.0056
C <sub>5</sub>	0.2045

Table. 7.1 Optimised coefficients for Equation (7.11).

The optimum values for the coefficients in Equation (7.11) are given in Table (7.1). It was found that a better fit was found for the data with Equation (7.11) than Equation (7.10) and it was also found that Equation (7.11) was insensitive to differing Iribarren numbers. The value of the dimensionless discharge in Equation (7.11) was found to be only very weakly dependent upon the last term. The last term contributed only a maximum of 0.06% to the total dimensionless discharge in any of the 74 tests. Consequently, the last term was dropped from the equation and the optimal equation for combined discharge is given in Equation (7.12), for a range of applicability between  $0.1 < -R_c/H_s < 1.9$  and  $13 < \lambda_p/L_w < 220$ .

$$\frac{q_{ws}}{\sqrt{gH_s^3}} = 0.050 + 0.474 \left( \frac{-R_c}{H_s} \right)^{3/2} \left( \frac{\lambda_p}{L_w} \right)^{0.085} \quad (7.12)$$

Fig. 7.6 shows how well the data from the 74 tests fits Equation (7.12). The data points for  $\xi_p < 2$  and  $\xi_p > 2$  are shown separately to demonstrate that the equation fits well for both. The coefficient of determination for  $\xi_p < 2$  is 0.9956 and for  $\xi_p > 2$  it is 0.9959, indicating that Equation (7.12) provides a similar level of goodness of fit to both data sets.

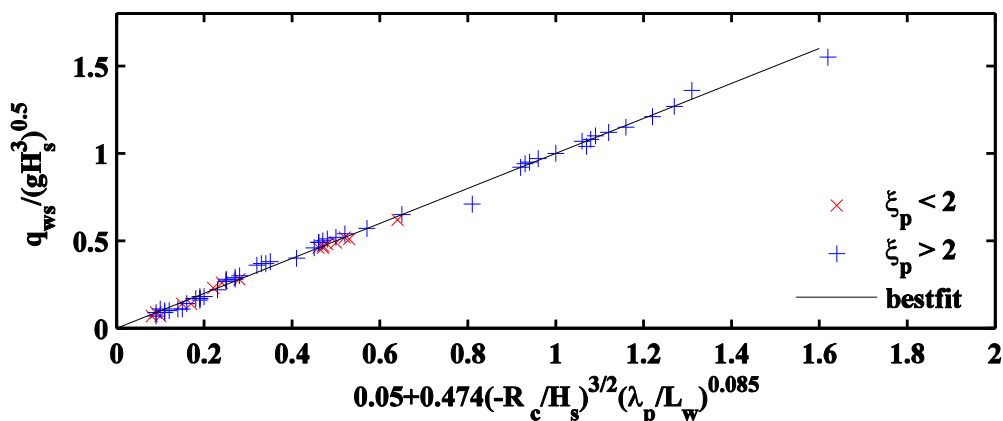


Fig. 7.6 Goodness of fit of Equation (7.12) to Appendix B data.

An additional indication of the success of Equation (7.12) at predicting  $q_{ws}$  may be found by plotting the combined discharge calculated in the RANS model

tests against that predicted with Equation (7.12). This is shown in Fig. 7.7 along with the least squares line of best fit. The coefficient of determination is 0.979, indicating that the predicted discharge is in good agreement with that found with the RANS model.

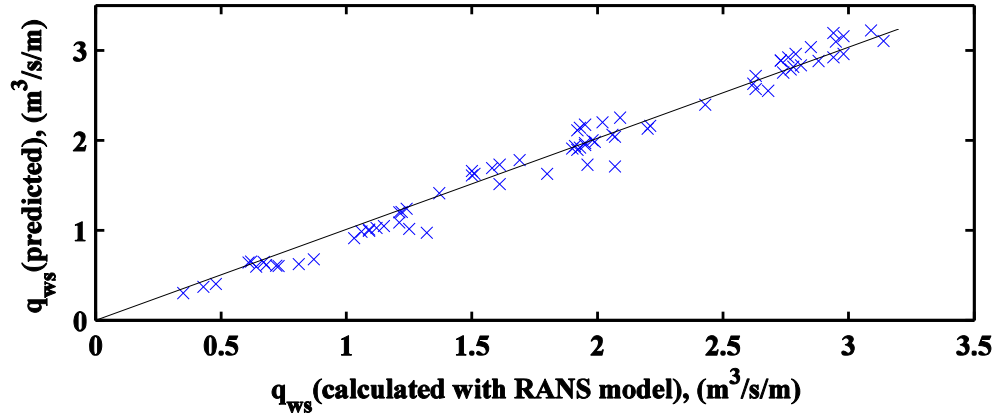


Fig. 7.7 Combined discharge predicted with Equation 7.12 and calculated with the RANS model, with line of best fit.

It is interesting to note how Equation (7.12) behaves when  $H_s$  becomes small and to see if the equation tends towards the form of the equation for a broad crested weir. As the significant wave height becomes zero in Equation (7.12) the equation for  $q_s$  becomes;

$$q_s = 1.485 |R_c|^{3/2} \left( \frac{\lambda_p}{L_w} \right)^{0.085} \quad (7.13)$$

As the wavelengths tested range from 39 to 111m, and with a 3.05m crest width, the term  $(\lambda_p/L_w)^{0.085}$  has values between 1.24 and 1.36. This gives  $q_s$  a range between  $1.84|R_c|^{3/2}$  and  $2.02|R_c|^{3/2}$ . This can be compared with the equation determined for  $q_s$  for an embankment with a 1:4.25 sloping face and 3.05m crest width, found in Chapter 6. This found that the discharge was  $1.9197|R_c|^{3/2}$ , which is equivalent to Equation (2.15) with a  $C_d$  value of 1.126. The comparison shows that Equation (7.12) is in good agreement with the equation

for discharge over an embankment when the significant wave height reduces to zero.

It is also interesting to consider how Equation (7.12) behaves when  $R_c$  becomes small and to see if the equation tends to the form of the Equations (2.12) given by Schuttrumpf (2001). As the negative freeboard becomes zero, Equation (7.12) becomes;

$$q = 0.050\sqrt{gH_s^3} \quad (7.14)$$

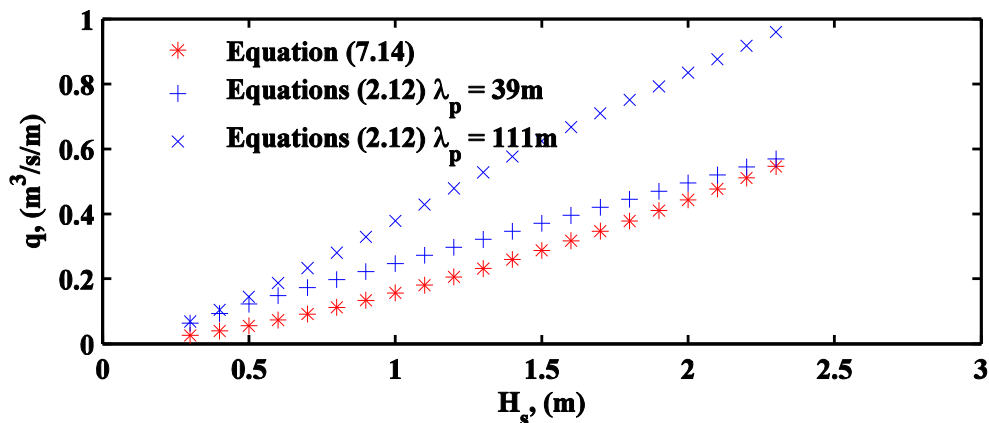


Fig. 7.8 Variation in predicted discharge from Equation (2.12) and Equation (7.14).

A comparison between the discharge calculated using Equation (7.14) and Equations (2.12) is shown in Fig. 7.8, evaluated for a range of wave heights. The discharges calculated with Equations (2.12) were evaluated for a 1:4.25 slope and for wavelengths of 39 and 111 m to indicate the effect of differing wavelengths upon the discharge. Equations (7.14) and (2.12) show reasonable agreement for the shorter wavelength but for the longer wavelength, Equation (7.14) predicts a significantly lower discharge. To some extent this is consistent with Fig. 6.3 which shows that the dimensionless discharge predicted with the Equations (2.12) plus the weir equation is greater than that predicted by both the RANS model and by the equation given by Hughes and Nadal. However, it

should be remembered that the lowest negative freeboard tested with the RANS model when deriving Equation (7.12) was 0.29m. So applying Equation (7.12) to situations with zero freeboard will be outside the range of applicability.

Equations (2.12) remain the most appropriate equation for situations with zero freeboard.

Finally, the combined discharge found with Equation (7.12) is compared with that found with the existing equations for this situation. Fig 7.9 shows the dimensionless combined discharge and dimensionless negative freeboard determined for each of the 74 test conditions given in Appendix B. It shows that the dimensionless discharges determined with the equation given by Hughes and Nadal have on average a 24% lower value than that determined with Equation (7.12). Also, the dimensionless discharge determined with the equation given by Reeve et al. is on average 27% higher than the values calculated using Equation (7.12). It should be noted that only the values within the range of applicability of the equations given by Reeve et al. were used. The method given by Pullen (2007) to evaluate combined discharge sums the wave component for zero freeboard given by Schuttrumpf and the surge component calculated using weir equations. Fig. 7.9 shows that the combined discharge determined with this method is on average 30% greater than that found with Equation (7.12). Although, agreement is better for higher values of dimensionless freeboard. Fig. 7.9 shows a similar pattern to Fig. 6.3, but includes a greater range of test conditions, particularly for the situations with differing embankment crest width. However, using Equation (7.12) shows that the dimensionless discharge will vary for similar tests if the crest width differs.

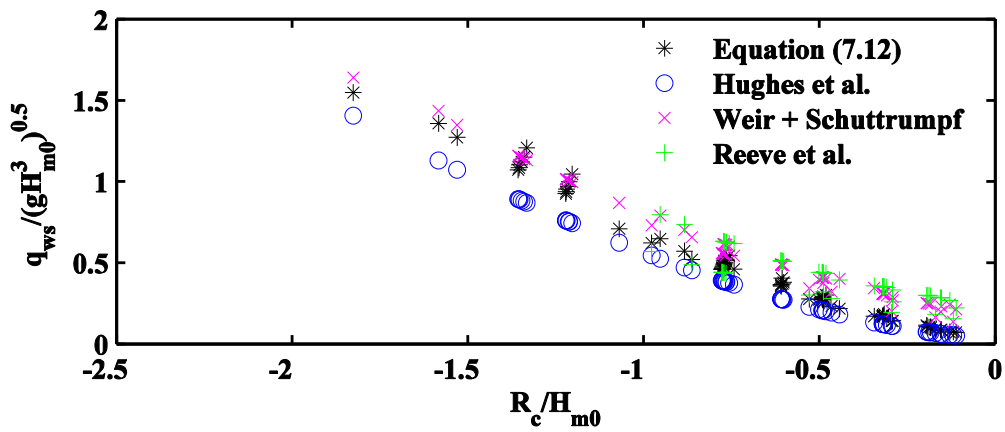


Fig. 7.9 Dimensionless combined discharge and dimensionless negative freeboard determined for the 74 tests conditions given in Appendix B.

In this chapter the RANS model has been used to determine how crest width affects the discharge over embankments that are subjected to extreme surge levels with negative freeboards. For this situation, a reduction in combined discharge has been observed as the crest width is increased. For a seawall subjected to intermittent overtopping and occasionally subjected to negative freeboards, the reduction in combined discharge as a result of increased crest width may be important. Therefore, a design equation has been derived, so that the effect of embankment crest width can be included when evaluating combined discharge.

## **CHAPTER 8**

### **CONCLUSIONS AND FUTURE WORK**

#### **8.1. Conclusions**

In this study the RANS model has been used to describe the highly non-linear flow at the crest of an embankment during combined discharge. Initially the performance of the model has been assessed at describing complex hydrodynamic flow for two situations. Firstly, the performance of the model was assessed for its ability to predict the second order mass transport under progressive and standing waves by comparing predictions against available theory and experimental data. Secondly, the ability of the model to represent combined discharge over embankments was assessed by comparing the model with recent physical model data. The combined discharge rates calculated with the verified RANS model were compared with those calculated with design formulae. Also the RANS model was used to investigate differences in discharge rates found with the different design formulae. Finally, the model was used to investigate the effects of embankment crest width on the combined discharge and to provide design advice. Results from a series of RANS model tests were used to develop a design formula that allows the combined

discharge to be determined and allows for the effect of the embankment crest width.

The study has demonstrated that the RANS model is capable of describing second order effects such as mass transport under both progressive and standing waves. For progressive waves, the model was compared to theory given by Longuet-Higgins (1953) and available experimental data given in Klopman (1994). This demonstrated that the model is capable of predicting the wave-induced streaming within the boundary layer. The magnitude of the streaming found using the RANS model is shown to be about half that found in the experimental data and about a quarter of that predicted by theory. Outside the boundary layer, the mass transport calculated with the RANS model develops in the opposite direction to the direction of wave propagation. This is in agreement with the experimental data and theory. The peak magnitude of the mass transport found with the RANS model agreed with the experimental data, although the shape of the vertical profiles differed. Unfortunately, flow outside the boundary layer is not uniquely defined by theory and could not be used for comparison. For standing waves, there are currently only limited qualitative experimental data against which to compare the model, so it was only possible to compare the model to theory. Longuet-Higgins' theory predicts that under standing waves there is a pattern of circulating cells that direct flow toward the standing wave nodes near the bed, and towards the antinodes above the boundary layer. The RANS model correctly predicted the flow within these cells, although the magnitude of the mass transport was less than laminar theory but in general agreement with mass transport theory for a turbulent boundary layer (Johns, 1970).

For combined discharge over an embankment, the RANS model used a wave generation procedure that allowed a direct simulation of waves recorded within a physical model, therefore allowing a wave-by-wave comparison of parameters such as discharge, flow depth and velocity. Comparison against the experimental data of combined discharge over an embankment crest, by Hughes and Nadal (2009), shows good overall agreement. However, better agreement is found for higher surge levels and smaller wave heights. The differences for larger waves were partly because the larger waves were breaking at the embankment crest. It has been shown that the RANS model does not correctly predict the initiation of turbulence near the break point (Lin and Liu, 1998a). This caused some errors in calculating the location of the breaker and, as a consequence, incorrect flow depths at the point where flow depths were compared. In the physical model, there is potential for errors in the recorded flow depth if the depth calculated from the pressure gauges did not account for the vertical acceleration within the flow conditions. For all surge levels tested, the embankment crest periodically dried during wave troughs, especially at low surge levels. This required increased mesh refinement within the RANS model so that the low flow levels could be adequately defined. In the physical model, the low flows will be subject to scale effects, as shallow flow tends to become laminar. Velocities recorded within the RANS model tended to be higher than in the physical model. This is partly due to comparing the RANS model depth-integrated velocity with the physical model velocity recorded at half the still water level. For larger waves, the velocity recorded at half depth is larger than the depth-integrated velocity. Also the velocities in the physical model were not recorded when the water level dropped below the LDV, and on occasion there was sometimes a delay between the water level rising above the

LDV and the LDV beginning to record. This caused some peaks to be missed. Overall, the average relative error for discharge over the embankment crest ranged from 4.7% for the larger surge level to 59.1% at the lower surge level.

The discharge rates for combined discharge over an embankment calculated with the RANS model were compared with three available design formulae. The dimensionless discharge calculated with the model was very similar to that calculated with the equation given by Hughes and Nadal (2009), less than that found with the method suggested by Pullen (2007), and the highest values were found with the equation given by Reeve et al. (2008). However, the discharge calculated with these design formulae is dependent upon the method used to determine the freeboard. Direct measurement of the freeboard at the embankment crest is reliant on the measurement location, because flow varies from sub critical to supercritical at a broad crested weir. Hughes and Nadal used the measured discharge during a period of steady overflow at the start of a test to calculate the freeboard using the broad-crested weir equation. For the comparisons of combined discharge with design equations, a similar method was used to determine the freeboard within the RANS model calculations. However, it was found that the embankment tested differs from a broad-crested weir because it does not have vertical sides. The RANS model test dataset was used to determine a better estimate of the coefficient in the broad-crested weir equation. The modified equation was used to recalculate the freeboard. This was found to be 6.0% lower on average. A comparison of the dimensionless discharge evaluated using the recalculated freeboard found that the equation given by Hughes and Nadal gave the lowest values, the method given by Pullen gave values slightly higher than the RANS model, and the equation given by

Reeve et al. gave the highest values. It was noted that the experimental set-up used by Reeve et al. to derive the equation was based on a seawall configuration with a sloping front face retained by a thin wall. The other design equations were based on tests with embankment set-ups with broad crests but with sloping front face and lee sides. The thin wall would be expected to behave more like a short-crested weir than a broad-crested weir and would be expected to have an increased discharge. This partly explained why the equation derived by Reeve et al. predicted greater discharge.

The study has also used the RANS model to investigate the effect of crest width on the rate of combined discharge over embankments. The same embankment configuration was used for each test but with crest widths increasing from 0.5m to 3.05m. Three surge levels were tested. The combined discharge was found to decrease as the embankment crest increased. Reducing the embankment crest width from 3.05m to 0.5m resulted in an average 21% increase in combined discharge. It was found that the effect of a narrower crest width did not fully account for the differences between the equation given by Reeve et al. (2008) and that given by Hughes and Nadal (2009) and may be accounted for by other factors such as the details of the lee slope.

Of the current equations used to determine combined discharge, given by Hughes and Nadal (2009), Reeve et al. (2008) and Pullen (2007), none considers the effect of crest width on reducing the overall combined discharge. As the effect of embankment crest width was found to have a significant impact on the overall overtopping discharge, the RANS model was used to develop a

new empirical equation, which quantifies the effect of embankment crest width on combined discharge.

In all, 74 random wave tests were conducted with embankment crests width varying from 0.5m to 3.05m in 0.5m increments. The tests included  $R_c$  between -0.1m and -1.6m and  $H_s$  between 0.7 and 2.5m and  $T_p$  between 6.1 and 14.4s. The new equation was developed so that it successfully conforms to the limiting conditions. That is, it should approximate to the equation for a broad crested weir when  $H_s$  becomes zero and when  $R_c$  becomes zero the new equation should tend towards Equation (2.12). The goodness of fit of the test data to the new equation was found to be quite satisfactory with a coefficient of determination of 0.996. Additionally, the new equation was shown to have a very similar coefficient of determination for both  $\xi_p < 2$  and  $\xi_p > 2$ . This shows a similar level of goodness of fit for both plunging and surging waves. The new equation is given in Equation (7.12) and has a range of applicability between  $0.1 < -R_c / H_s < 1.9$  and  $13 < \lambda_p / L_w < 220$ .

The study has demonstrated the RANS model is a useful tool for efficiently investigating situations subjected to highly non-linear flow such as mass transport and combined discharge over embankments. It has proved to be a useful tool that has facilitated the development of a new equation that allows embankment crest width to be taken into account when determining combined discharge over embankments.

## 8.2. Further work

Although the mass transport under standing waves described by Longuet - Higgins (1953) is often cited, it is surprising that there are still no quantitative validating physical model data. The instrumentation is now available to measure velocities within the boundary layer and would allow this work to be done.

The validation of the RANS model has been conducted against available experimental data for combined discharge over embankments. However, the study has demonstrated a continued need for further physical model tests with more detailed descriptions of flow parameters at the embankments crest.

Further work on the RANS model should consider the effect of commonly used embankment configurations on the combined discharge, such as seaward slope, berm, and water depth at the toe of the structure. These should be tested for a range of wave conditions and the results should then be formulated into design advice.

Finally, work has begun on coupling the RANS model to sediment transport and morphological models, presented in Appendix A. When complete it will provide a sophisticated 2D cross-shore morphodynamic model. The RANS model's ability to describe the flow characteristics of a breaking wave, as well as describing the turbulence at the seabed boundary layer will provide an increased level of sophistication compared with existing sediment transport models. As the RANS model can represent the second order effects, such as the mass transport circulating cells under standing waves, it should be able to describe the development of the bar formation seen under standing waves.

## **APPENDIX A**

### **RANS MODEL DEVELOPMENT TO INCLUDE SEDIMENT TRANSPORT AND BED MORPHOLOGY**

#### **A1 Introduction**

The RANS model has been shown to provide satisfactory prediction of the flow field near breaking waves and the mass transport under standing waves. The aim of this aspect of the study was to determine if this flow description could be coupled to sediment transport equations so that cross-shore bed morphological evolution could be described. In particular, it was hoped that a modified RANS model would be able to predict the offshore bar formation that are associated with mass transport, as well as swash zone beach evolution.

Although the RANS model provides a good description of flow, it is relatively computationally expensive. Typically, for wave induced bed morphology, equilibrium bed profiles take in the order of 1500 waves to be reached. For the RANS model, when run on a typical 2.8Ghz computer, the long-term beach profile evolution may prove to be excessively computationally expensive. However, it was hoped that the RANS model could assess the performance of sediment transport models at a shorter time scale. So, the objective of these

---

tests was to determine if the detailed hydrodynamic description of the flow, demonstrated in Chapters 4 and 5, can be utilised to determine short term bed evolution.

However, hydrodynamic sediment transport processes are highly complex and there is currently no generally accepted model that can be applied to a wide range of conditions. This appendix describes the preliminary work conducted to extend the RANS model to include the ability to calculate sediment transport rates and hence describe bed morphology. However, the validation of this modelling work proved to be problematic and was deferred.

## **A2 Mechanics of sediment transport**

The theory for coastal sediment transport has been derived from results obtained for sediment transport in rivers. The existing formulas have been adapted and extended to account for the conditions met at the coast. Coastal sediment transport is likely to result from wave motion, which can induce both longshore and cross-shore transport. This study used a 2D version of the RANS model, which offers the potential to determine cross-shore sediment transport.

Sediment transport, for a non-cohesive bed, is commonly divided into bed load and suspended load transport. Bed load transport is defined by Fredsoe and Deigaard (1992) as part of the total load that is in more or less continuous contact with the bed during transport. This can include individual grains rolling, sliding or hopping along the bed, saltation. The weight of the grain is partially borne by the contact with the bed. Bed load transport can be determined by the effective shear stress. In contrast, suspended load transport is defined as

---

having particles fully entrained within the flow and individual particles are moving without continuous contact with the bed. In this study only bed load transport has been considered, so that this portion of the total load can be validated separately. At a later date it may be possible to include suspended load transport.

Recording sediment transport rates in the field is notoriously difficult, and the distinction between bed load and suspended load transport is very difficult to verify. Some researchers have overcome this problem by attempting to model sediment transport as a total load transport without distinguishing the transport mode. In this analysis, the distinction between bed load and suspended load is maintained in order to utilize the different physical mechanisms that are dominant for the respective transport modes.

The movement of sediment depends on many factors, both deterministic and random. Einstein (1950) approached this problem using stochastic methods. He argued that the number of particles available to be deposited depends on both the number of particles in motion and on the probability of the dynamic forces allowing deposition. He developed a formula for calculating sediment transport under unidirectional flow based on stochastic concepts.

An alternative, deterministic approach was taken by Bagnold (1954) who experimentally determined the shear stress on particles at the bed. Bagnold (1963, 1966) derived a stream based sediment transport model dependent upon: the energy dissipation within the boundary layer, the sediment fall

velocity, bottom slope and particle friction angle. He found the energy dissipation to be related to the bed shear stress.

In his study of unidirectional flow, Shields (1936) considered the balance of the mobilising shear force and stabilising gravitational force. The threshold of motion can be determined for bed load transport by considering the bed shear stress. The Shields parameter is given as:

$$\theta = \frac{\tau}{\rho(s-1)gd} = \frac{u_*^2}{(s-1)gd} \quad (\text{A1})$$

where  $s = \rho_s / \rho$

Here  $\tau$  is the shear stress,  $g$  is the acceleration due to gravity,  $\rho_s$  is the grain density,  $\rho$  is the water density,  $d$  is the grain diameter, and  $u_*$  is the friction velocity,  $\sqrt{\tau/\rho}$ . The shear stress can be found from

$$\tau = 0.5\rho f u_b^2 \quad (\text{A2})$$

where  $u_b$  is the near bed velocity and  $f$  is a friction factor. The threshold of motion can be determined by the critical Shields parameter,  $\theta_{cr}$ , which is defined as:

$$\theta_{cr} = \frac{\tau_{cr}}{\rho(s-1)gd} \quad (\text{A3})$$

in which  $\tau_{cr}$  is the threshold shear stress. The critical Shields parameter is a weak function of the grain Reynolds number,  $R_e$ , defined as

$$R_e = \frac{u_b d}{\nu} \quad (\text{A4})$$

where  $\nu$  is the kinematic viscosity of water.

Typical values of  $R_e$  are of the order of 0.05.

In the original analysis, Shields plotted  $\theta_{cr}$  against  $R_e$ . However,  $u_b$  is required to determine both  $R_e$  and the shear stress in  $\theta_{cr}$ . This made the graph problematic to use. More usefully, Shields plotted  $\theta_{cr}$  against  $D_*$ , which is given by

$$D_* = \left[ \frac{g(s-1)}{v^2} \right]^{1/3} d \quad (\text{A5})$$

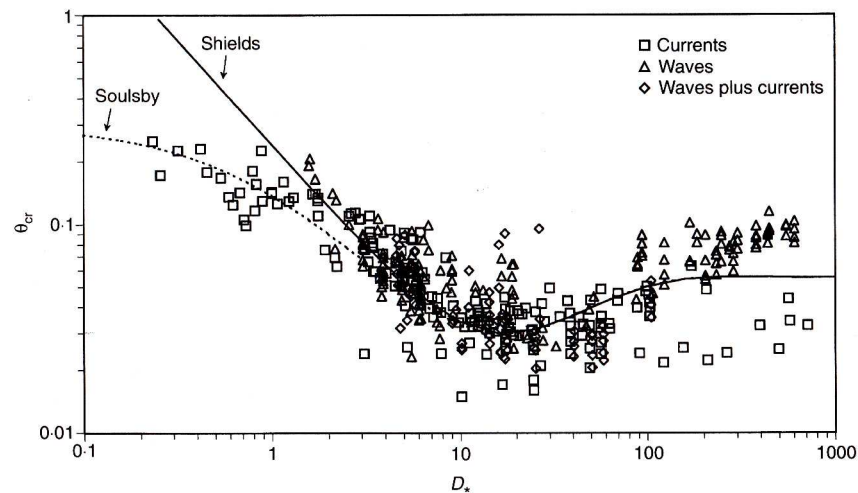


Fig. A1 The threshold of motion of sediments under waves and/ or currents. From Soulsby (1997).

Fig. A1 has become known as the Shields diagram and allows the critical Shields parameter to be determined for a particular sediment type. Soulsby and Whitehouse (1997) extended the original work for unidirectional flow derived by Shields. An updated Shields diagram was produced to include tests for waves and combined waves and currents, and these data are also shown on Fig. A1. The results for currents, waves and combined currents and waves all show similar behaviour. For gravel sized grains the experimental values of  $\theta_{cr}$  for waves are seen to be larger than for currents. Soulsby (1997) speculated that this might partly be because an average shear stress may be more appropriate than the peak, when calculating  $\theta_{cr}$ .

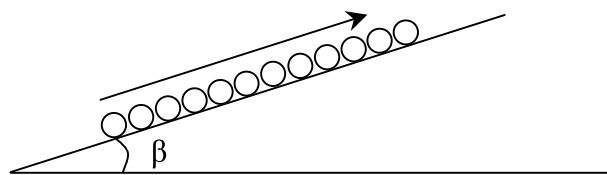


Fig. A2 The threshold of motion on sloping beds.

Shields plotted a curve through the original limited data set, shown on Fig. A1. Soulsby and Whitehouse fitted a further curve that passes through the additional data for currents, waves and the combined currents and waves. This curve differs from the original Shields curve for very fine sands. The Soulsby and Whitehouse curve gives the following threshold bed shear-stress formula.

$$\theta_{cr} = \frac{0.30}{1+1.2D_*} + 0.055[1 - \exp(-0.020D_*)] \quad (\text{A6})$$

The threshold shear stress required for a grain to move may increase or decrease due to bed slope because of the gravity component. Soulsby (1997) related the critical shear stress to the local bed slope,  $\beta$ , and the angle of repose,  $\phi_i$ , see Fig. A2. This is defined as the smallest angle to the horizontal that grains will begin to roll in zero flow. In zero flow, when  $\beta$  is greater than  $\phi_i$ , the grains begin to move. If the bed slope is uphill relative to the flow then Soulsby (1997) gives the critical shear-stress that includes the effect of bed slope as

$$\frac{\tau_{bc}}{\tau_c} = \frac{\sin(\phi_i + \beta)}{\sin(\phi_i)} \quad (\text{A7})$$

and if the bed slope is down hill then

$$\frac{\tau_{bc}}{\tau_c} = \frac{\sin(\phi_i - \beta)}{\sin(\phi_i)} \quad (\text{A8})$$

$\tau_{bc}$  is the critical shear-stress taking into consideration the bed slope.

In this section the method used to determine the initiation of motion has been described, in the next section the method used to quantify the sediment transport is given.

### A3 Bed-load sediment transport

There have been many attempts at deriving empirical and conceptual models for bed-load sediment transport. The basis of many formulae derive from the empirically derived equation presented by Meyer-Peter and Muller (1948)

$$\Phi_b = \begin{cases} 8(\theta - \theta_{cr})^{3/2} & \text{for } \theta \geq \theta_{cr} \\ 0 & \text{for } \theta < \theta_{cr} \end{cases} \quad (\text{A9})$$

where

$$\Phi_b = \frac{Q_s}{\sqrt{(s-1)gd^3}} \quad (\text{A10})$$

$Q_s$  is the sediment transport rate.

Equation (A11) was developed by Madsen (1991) based upon the Equation (A9) but extended to include the effect of bed slope.

$$\Phi_b = \begin{cases} \frac{C}{1 + \frac{\tan \beta}{\tan \phi_i}} (\psi - \psi_{bc})^{3/2} \frac{u_b}{|u_b|} & \text{for } \theta \geq \theta_{cr} \\ 0 & \text{for } \theta < \theta_{cr} \end{cases} \quad (\text{A11})$$

where  $C = 8$ , and

$$\psi_{bc} = \frac{\tau_{bc}}{\rho(s-1)gd} \quad (\text{A12})$$

$$\psi = \frac{0.5\rho f u_b^2}{\rho(s-1)gd} \quad (\text{A13})$$

where  $f$  is a friction coefficient. For the mass transport aspect of this study  $f = 0.03$  was used. For swash zone sediment transport  $f = 0.04$  was used during wave uprush and 0.02 for down wash.

## A4 Bed Morphology

To update the bathymetry, an equation for the conservation of sediment is used.

$$\frac{\partial z_{bed}}{\partial t} = -\frac{1}{1-n} \frac{\partial Q_s}{\delta x} \quad (\text{A14})$$

Here,  $z_{bed}$  is the bed level above some datum,  $Q_s$  is the volume of sediment transport per unit width of bed per unit of time, and  $n$  is the porosity of the

sediment, which is assumed to be 0.4. When  $\frac{\partial z_{bed}}{\partial t} > 0$  then sediment accretion

will result and when  $\frac{\partial z_{bed}}{\partial t} < 0$  the bed will erode.

Rakha et al. (1997) presented a finite difference scheme for the above based on a modified Lax scheme. This is given by:

$$\frac{z_j^{t+1} - z_{j^*}^t}{\Delta t} = -\frac{Q_{s,j+1}^t - Q_{s,j-1}^t}{2\Delta x} \quad (\text{A15})$$

where

$$z_{j^*} = \alpha_d z_{j+1} + (1 - 2\alpha_d) z_j + \alpha_d z_{j-1} \quad (\text{A16})$$

where the index  $j$  is for the spatial grid and  $t$  for the time and  $\alpha_d$  is a coefficient given by Rakha et al.(1997) to be 0.25.

The application of the above equations without further qualification can lead to situations where the bed slope may exceed the angle of repose of the sediment. This situation was dealt with by allowing the quantity of sediment above the angle of repose to slump. This can, in turn, cause the bed slope within the next cell to exceed the angle of repose, so a cascading slump may occur. Following a slump, the morphological module then recalculates the parameters required to define the bed for use within the next hydrodynamic time step.

### **A5 Modelling approach**

The implementation of the sediment transport routine and the morphological routine within the RANS hydrodynamic model is shown schematically in Fig. A3. In the sediment transport module, the critical Shields parameter is determined using Equations (A5) and (A6). The instantaneous sediment transport rate was calculated using Equations (A10), (A11), (A12) and (A13). The near bed velocity, used for the sediment transport calculations, was determined at the nearest cell node above the bed.

The sediment transport models imply that bed load transport responds instantaneously to time varying near bottom flow conditions. In particular, the initiation of bed load transport is determined by the instantaneous value of the Shields parameter. If the instantaneous near bed shear stress is high enough to raise the Shields parameter above the critical value then bed load transport is initiated.

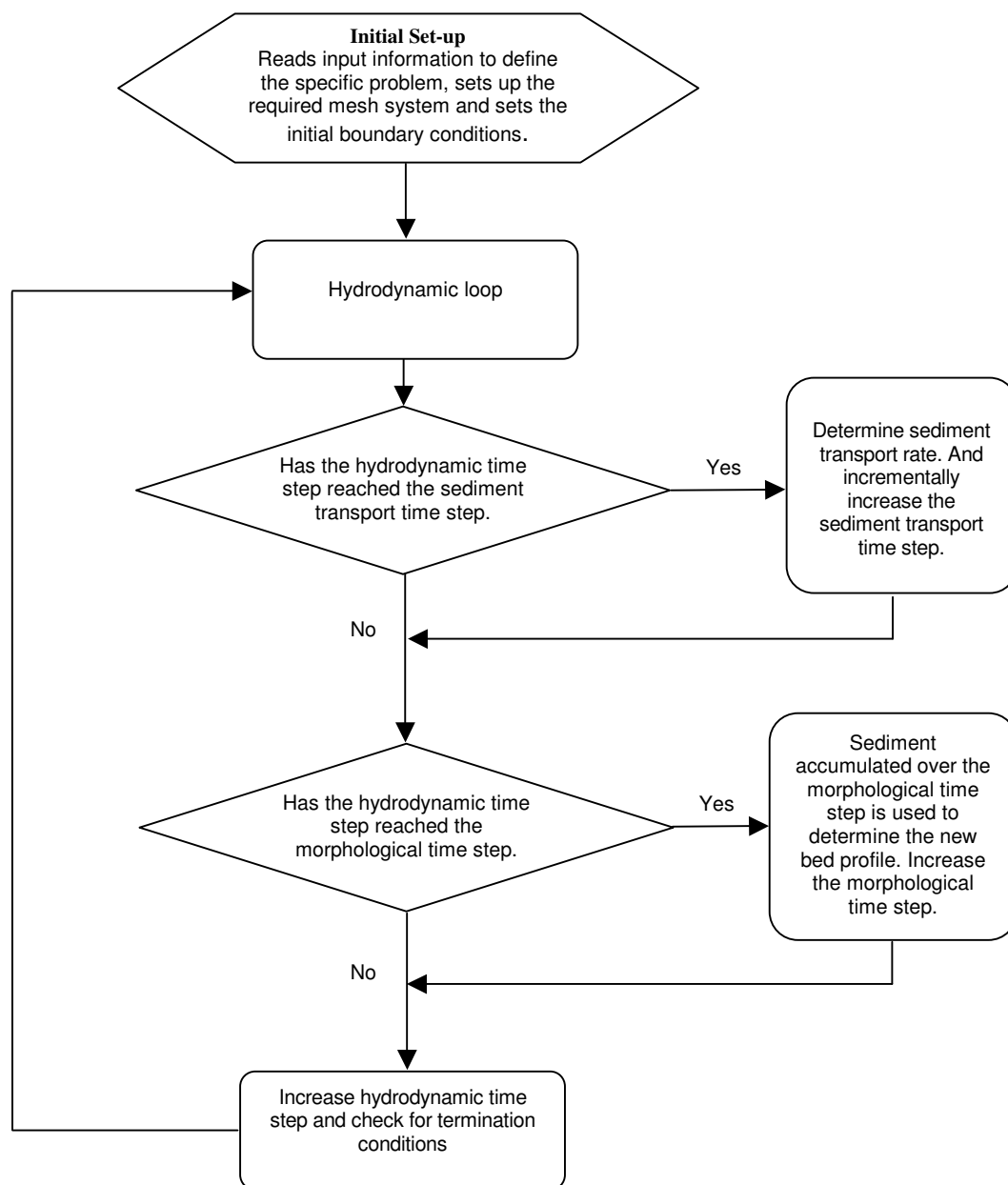


Fig. A3 Flow chart of hydrodynamic sediment transport and morphological models.

Under a sinusoidal wave, the net bed load transport will be zero because of symmetry. In asymmetrical waves, such as steep waves in shallow water, net sediment transport results from velocities being greater under the crest of the wave than under the trough. To determine the overall net sediment transport it is necessary to separately evaluate the sediment transport at each half-wave

---

period. The net sediment transport is the difference between the transport found for the two half wave periods.

In the current study it is possible to evaluate the sediment transport rate at a time step which is somewhat less than the wave period. In fact, it is possible to set the sediment transport time step to be the same as the hydrodynamic time step. However, the hydrodynamic time step may be required to be quite fine to adequately define the flow, for example to define a wave breaking. The sediment transport does not need to be so finely defined. The model allows a sediment transport time step to be set at a value that is somewhat larger than the hydrodynamic time step but is a fraction of the wave period. Similarly, the morphodynamic time step can afford to be larger than the sediment transport time step, as the bed evolution at a time step significantly smaller than the wave period is likely to be small. The morphodynamic time step needs to be chosen so that bed evolves gradually, as clearly the bed evolution will then influence future hydrodynamic calculations. This provides some improved computational efficiency and avoids accumulating errors with the very small rates of sediment transport that may occur at the hydrodynamic time step.

## **A6 Model application**

A modified version of the RANS model that includes the sediment transport and morphological modules has been applied to two situations. Firstly, the model has been applied to bed morphology resulting from a standing wave in front of a vertical wall. Secondly the model has been applied to swash zone beach morphology. Whilst these situations are quite different, they were selected to

determine if the sediment transport and bed morphology formulae given above could be applied to such varying conditions.

### **A6.1 Sediment transport and bed morphology under standing waves**

The mass transport generated under standing waves, discussed in Chapter 4, leads to a system of recirculating cells. In the lower boundary layer, these cells produce circulating currents that act from anti-node to node. The directions of the circulating currents for the half wavelength nearest to the reflecting wall are shown in Fig. A4. De Best et al. (1971) showed that the scour profile resulting from these currents is different for coarse and fine material. If the sediment size is small, the sediment is stirred up by the waves, is brought into suspension, and will be carried to a higher elevation. The fine sediments are then transported by the top-circulating cell and were found to move from the nodes towards the antinodes. For fine sediments, it is the first order velocities that lift the sediment into suspension and the mass transport within the interior that transfers the sediment to the nodes where it settles. The resulting bed profile for fine sediments is shown in Fig. A4 a). For relatively coarse sediments, the bed shear, caused by the lower part of the lower circulating cell, moves the sediment from the antinodes towards the nodes. The resulting bed profile is shown in Fig. A4 b). Carter et al. (1973) were the first to relate the mass transport under standing waves to the formation of offshore sand bars. Xie (1981) conducted experimental studies to determine the scour pattern in front of vertical breakwaters. The study gives a method for determining the maximum scour depth, but it is noted that this equilibrium profile occurs at between 6500

and 10000 waves. This work was extended to scour patterns in front of vertical and sloping walls by Sumer and Fredsøe (2000).

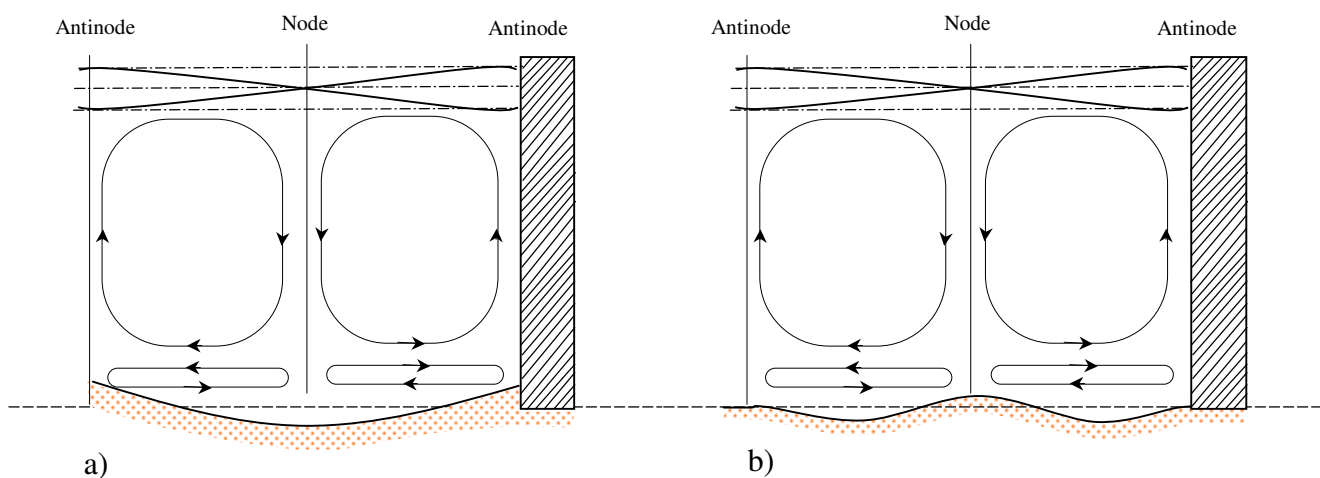
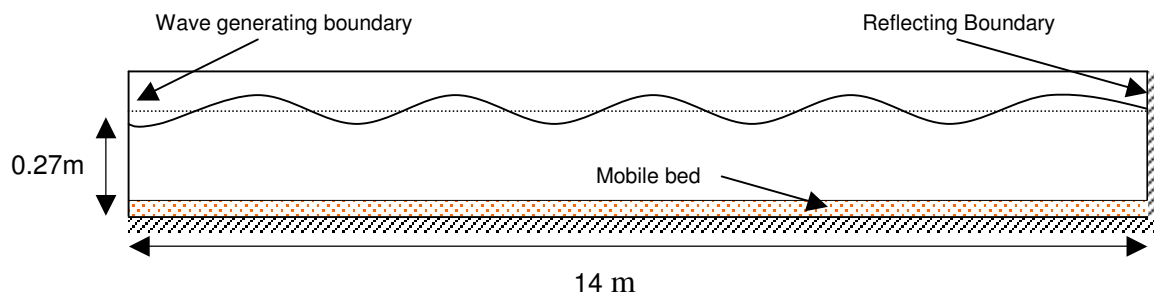


Fig. A4 Circulating currents and bed profiles under a standing wave in front of a vertical wall for a) fine sediment and b) coarse sediment.

In this study, sediment transport under standing waves has been investigated in a 14m numerical flume, with waves generated from the left boundary and a vertical reflecting wall at the right boundary. The flume set up is shown in Fig. A5. The still water level was 0.27m above the bottom of the flume and the bed material covered the flume uniformly to a depth of 0.006m. The sediment had  $d_{50}$  sediment size of 1.0 mm, with a density of  $2580 \text{ kg m}^{-3}$ . This sediment size is classified as coarse sand, Soulsby (1997). The regular waves generated in the flume had an incident wave height of 0.0494m, a wavelength of 1.33m and a wave period of 1.012s. The wave condition and general flume set up is the same as that discussed in section 4.6.2. In section 4.6.2 the incident wave profile generated in the model was compared against theory and was found to be satisfactory. Additionally, it was previously demonstrated that the RANS model is capable of reproducing the mass transport circulation cells, which is consistent with that predicted by Longuet-Higgins, (1953).



*Fig. A5 General set up of the numerical flume.*

The mesh spacing in the horizontal direction was 0.025m and in the vertical direction variable mesh spacing was used. This was so that the mesh near the bed provided enough resolution to define the mass transport in the lower circulation cell. The mesh spacing was constant at 0.0003m for the first 0.01m and then increased at a rate of 5% to a maximum spacing of 0.005m. For this test, the time step used with the RANS model was 0.01s.

As the aim of this test was to establish if the RANS model could determine short-term bed evolution, a relatively short test was conducted. An initial 20 wave periods allowed the standing wave pattern in front of the reflecting wall to establish. During this period, there was no sediment transport and the bed was immovable. For the following 40 wave periods, sediment transport and bed evolution was recorded. The resulting pattern of progressive bed evolution under standing waves is shown in Fig. A6. This shows that, whilst the magnitude of the changes to the bed is very small, the resulting pattern is consistent with that shown in Fig. A4b. The circulating mass transport cells, observed in section 4.6.2, generate a current near the bed, which is always towards the standing wave node. This caused bed erosion mid way between the nodes and the antinodes and deposition at the nodes. The observed RANS

model sediment response is consistent with that expected for bed load sediment transport.

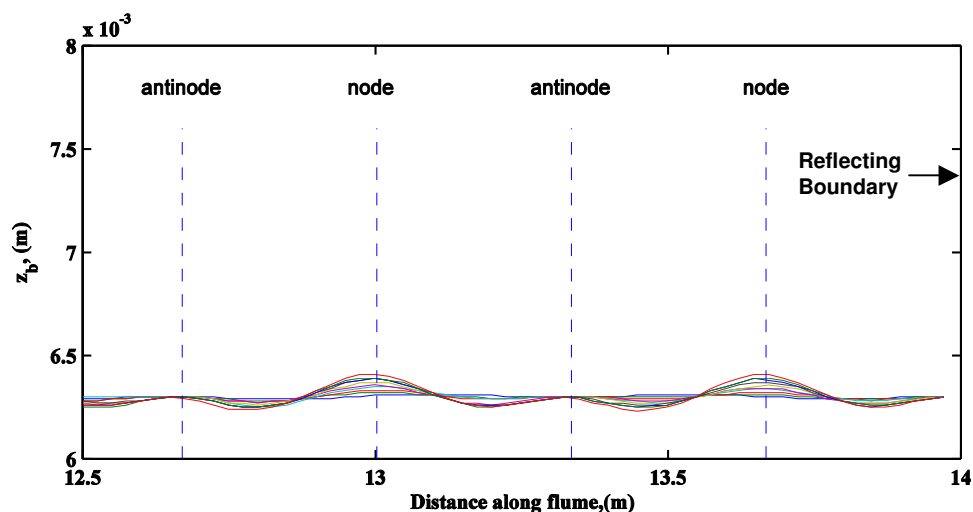


Fig. A6 Progressive bed evolution for the wavelength nearest the reflecting boundary.

The scour patterns determined by Xie (1981) and Sumer and Fredsøe (2000) are for equilibrium conditions, and can be expected after 6500 to 10000 waves. Unfortunately, to the author's knowledge, no data exists of progressive bed evolution under standing waves. So it is not possible to validate the magnitude to the bed evolution except for the equilibrium conditions. It should be made clear that no attempt was made to run the model for the number of wave periods required for an equilibrium profile to be reached. Tests of this duration with the RANS model would be excessively computationally expensive. However, the test duration of 40 wave cycles was sufficient to meet the aims of the test, which was to demonstrate that the hydrodynamic description of the flow could be utilised to successfully determine short-term bed evolution trend.

## **A6.2 Sediment transport and morphology on a sloping beach.**

In this section, the RANS model has been applied to swash zone beach morphology on gravel beaches. This situation has been selected as a further example of bed load sediment transport against which the sediment transport and morphology routines incorporated into the RANS model could be validated.

Gravel beaches have sediment that vary in size between 2 to 64mm and have a larger pore size compared to sand beaches allowing flow between the grains. This allows significant infiltration and absorption of incoming waves and a much-reduced backwash. This results in a much steeper beach profile, which is typically within the range 1:12 to 1:2. Because the beach is relatively steep, the surf zone for gravel beaches is narrow, as waves break almost at the shoreline. Consequently, the dominant location for beach morphology on gravel beaches is within the swash zone. Quantitative understanding of sediment transport is important for estimating coastal erosion and accretion and, in the UK, gravel beaches represent 20% of the total shoreline.

Present understanding of sediment transport within the swash zone is fairly limited. Consequently, current methods used to determine beach profile response use empirical methods such as that given by Powell (1990) or van de Meer (1988). In order to develop process based models that allow feedback between wave hydrodynamics and sediment transport and beach morphology, the key mechanisms need to be identified. This will facilitate improvements in current understanding of sediment transport and beach morphology.

To assess the ability of the model at reproducing bed load sediment transport and bed evolution on a coarse grained beach, the model is compared with

large-scale laboratory tests. The physical model study was carried out by López de San Roman-Blanco et al. (2006) in a 309m long, 5m wide and 7m deep facility at the Large Wave Flume (GWK) at the Coastal Research Centre in Hanover, Germany. The physical model study investigated cross-shore processes on gravel and mixed beaches, with the objective of providing validation data for numerical models. The physical model had a 1:8 mobile beach placed over a 1:6 impermeable slope. Tests covered a range of regular and random wave conditions. Measurements included a series of beach profiles so that progressive beach profile development could be observed.

This study attempted to reproduce Test 1 from the physical model tests, so that beach evolution calculated with the numerical model could be compared with that measured in the physical model. In this test, the sediment was gravel between 16 and 32mm, with a median diameter,  $d_{50}$ , of 21mm and the beach porosity was assessed to be 0.4. The sediment density was of  $2580 \text{ kg m}^{-3}$  and the still water level was 4.7m above the flume bed. The tests began with a 1:8 slope and after 50 waves the beach profile was measured. The beach profile was not reshaped and further tests with 100, 500, 1000, 1500, and 3000 waves were conducted, the beach profile was recorded after each test.

For computational efficiency, the numerical flume represented the 55m of the physical model flume nearest to the beach. The wave record from a wave gauge, located 220m from the wave paddle in the physical model, was used to generate waves at the left boundary in the numerical model. The wave record at this location had a significant wave height,  $H_s$  of 0.49m and a peak period,  $T_p$  of 3.01s. The water level and beach material in the numerical model matched that in the physical model. The numerical model used a mesh spacing of 0.1m and

0.05 in the horizontal and vertical directions respectively. The hydrodynamic time step was 0.01s, the sediment transport time step was 0.2s and the morphological time step was 2.5s. The numerical model flume set-up is shown in Fig. A7.

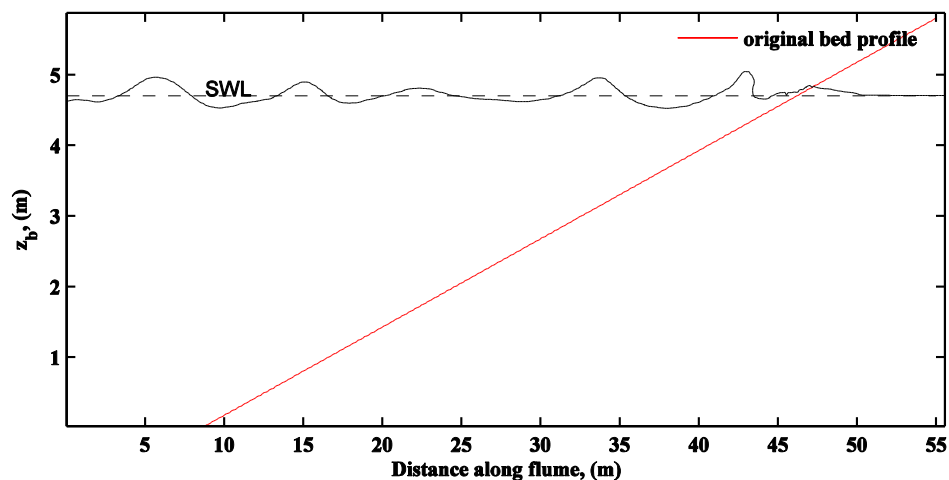


Fig. A7 General set up of the numerical flume showing 1:8 beach slope and 4.7m water level.

Fig. A8 shows a plot of the progressive morphological change in the physical model, found by López de San Roman-Blanco et al. (2006). This figure shows swash zone morphological change from the flattened original profile at a 1:8 slope to the profile after 50, 100, 500, 1500 and 3000 waves. This shows that there is a net transport from below to above the still water level, (SWL). This has resulted in a build up of material above the SWL and a step has formed below the SWL.

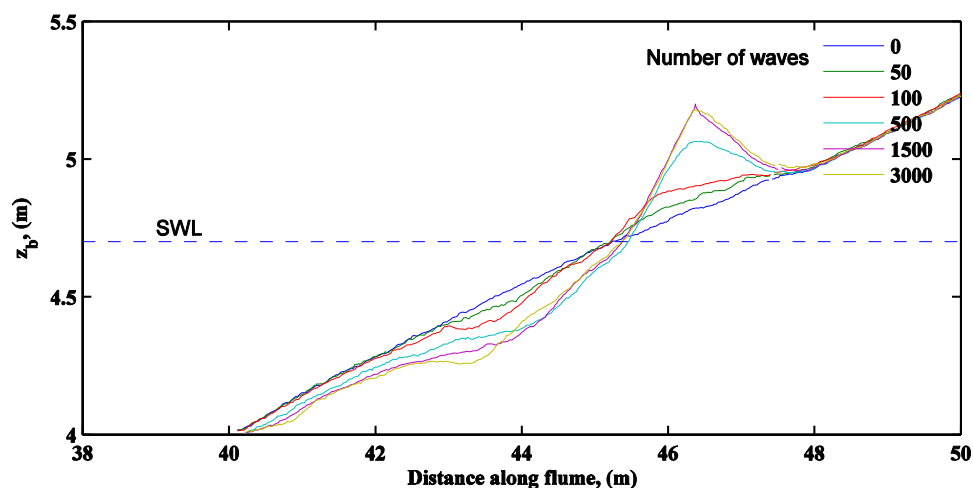


Fig. A8 Beach profile development in the physical model from López de San Roman-Blanco et al. (2006).

The numerical model was run for a total of 50 waves, which corresponds to the first part of Test 1 in the physical model. Fig. A9 shows the beach profile evolution calculated with the numerical model. The initial uniform 1:8 slope and the beach profile after 50 waves are shown. Comparing the beach profiles after 50 waves in Fig. A8 and Fig. A9 show some discrepancy. The numerical model shows a deposition of material above SWL, but the magnitude and location of the crest differs from the physical model. In the numerical model, the deposited crest has developed further up the beach and is volumetrically smaller than in the physical model. Additionally, the numerical model does show a small step at the SWL but this is located further up the beach than in the physical model and is less well defined.

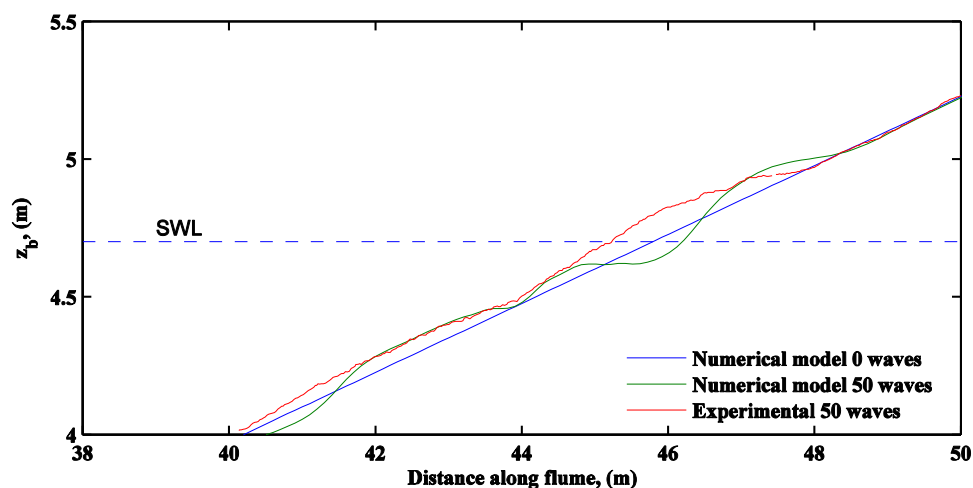


Fig. A9 Beach profile development in the numerical model compared to the physical model.

The discrepancy between the physical and numerical model results has yet to be resolved. However, some possible explanations for the differences are discussed below.

The discrepancy in the beach evolution may be due to the methodology used to represent porosity within the model. For gravel beaches, the porosity of the beach contributes significantly to the hydrodynamics at the beach face, and consequently affects sediment transport. As a wave breaks, the turbulent bore is accelerated up the beach face. As the bore rises above the SWL during the wave uprush, there is a significant hydraulic gradient between the bore front and the SWL. As a result, flow infiltrates the beach and the beach face absorbs some of the swash lens. In the downwash, the raised water level within the beach begins to percolate down. This means that during the uprush a thicker lens of fast moving water moves up the beach face compared to the relatively thin layer of slower moving water moving down the beach face during back wash. This inequality of flow in the uprush and downwash is thought to cause the deposition of the crest above the SWL. In the RANS model, there is an option that allows the porosity of the beach to be modeled. This can be seen in

Fig. A7, which shows a breaking wave and the raised water level within the beach face. This process will impact upon the sediment transport because it affects the local velocities at the bed and bed shear stress, which in turn determine bed mobilization. A possible explanation for the discrepancy in bed evolution may be that the porosity of the beach material is not modeled well for this situation. In particular, if the porosity is underestimated within the RANS model, then this would result in the turbulent bore propagating further up the beach and may result in the deposition of material at a higher level. However, the RANS model has been successfully validated against experimental data for flow in porous structures and in low crested permeable breakwaters; see Liu, et al. (1999) and Garcia et al. (2004). Additionally, Pedrozo-Acuña et al. (2010) used the RANS model to simulate the impact pressures in the same physical model tests conducted by López de San Roman-Blanco et al. (2006). This study demonstrates that the RANS model can determine the variation in pressure due to plunging waves deep within the porous media, suggesting that flow within the media is modelled to an acceptable degree of accuracy.

Also, differences in the sediment transport rates and beach morphology may be subject to the value of friction coefficient,  $f$ , used in Equation (A13). Suitable values of  $f$  have been presented by a number of researchers. Puleo and Holland (2001) found the mean uprush value of  $f$  to be 0.007 and for the backwash the coefficient varied between 0.01 and 0.07. However, Masselink and Hughes (1998) found the uprush value to be approximately twice that of the downwash. This is consistent with Cox et al. (2000) who also found that  $f$  is higher during uprush. Raubenheimer et al. (2004) and Nielsen (2002) found  $f$  to be similar during uprush and downwash. Additionally, Barnes and Baldock

(2010) found that the friction factors may even vary within the uprush period, with the calculated shear-stress at the leading edge being twice the steady flow figure. Pedrozo-Acuña (2005) conducted sensitivity tests of varying friction coefficients upon the Madsen sediment transport model, coupled to a Boussinesq hydrodynamic model. Results from the test show better general agreement between the calculated bed evolution and measurements when uprush coefficients were larger than downwash. The suggested values for the friction coefficient from these tests were 0.04 for uprush and 0.02 for the backwash. These were the values used within the test for this study. However, the sensitivity tests conducted with the Boussinesq model used a depth-averaged velocity, whilst the model used in this study used a near bed velocity. Differences in the location of velocity calculation will result in significant differences in velocity values particularly near a breaking wave. Consequently, this is expected to alter friction factors and by varying the friction factor for uprush and down wash will impact upon the numerical model beach evolution.

The equation used for sediment transport in the current model considers the balance between the mobilizing shear force and the stabilizing gravitational force. However, there has been some research that suggests that sediment may respond to fluid acceleration. Puleo et al. (2003) found that including an acceleration term in the sediment transport model reduced the error in predicting sediment transport for suspended sediments. It was considered that the extra term might account for additional sediment transport mechanisms that occur in the swash zone, such as bore turbulence. Also, Pedrozo-Acuña et al. (2007) investigated the role of acceleration in bed load sediment transport under plunging waves. A Boussinesq model was coupled with a sediment transport model with an additional acceleration term. The results were

---

compared with large-scale laboratory tests, López de San Roman-Blanco et al. (2006). However, differences between the predicted beach profile and that determined in the laboratory suggest key processes were not included in the numerical simulation.

The equation used for sediment transport has assumed that bed mobility has been caused primarily by bed load transport. However, under plunging waves the vertical velocity was, on occasion, observed to be in excess of the settling velocity for this gravel. This has potential to mobilize the sediment vertically up into the wave column and the sediment may then be transported partially as suspended load transport for short distances. If this were the case, this may account for the observed differences in bed evolution.

As well as the equations used to determine sediment transport, the differences in bed evolution could be as a result of the inaccuracies in determining flow conditions under plunging wave conditions. In the RANS model, the representation of the turbulence intensity near the breaker point has been demonstrated to be less well modelled, Lin and Liu (1998a). In particular, the poorer representation of the turbulence intensity near the breaker point was caused by the model not accurately predicting the initiation of turbulence in the initial stages of wave breaking. Uncertainties in determining the initial turbulent conditions during the initiation of breaking create uncertainties in determining the breaking point. Uncertainties in determining flow conditions during wave breaking have potential to impact upon the sediment transport and beach evolution calculations.

## A7 Conclusion

In this part of the study, the RANS model has been coupled to sediment transport and bed morphology routines. The extended model has been applied to two situations where wave action causes sediment transport and bed evolution: bed morphology under standing waves and bed evolution on a gravel beach.

In section 4.6.2, the RANS model was demonstrated to be capable of reproducing the mass transport circulation cells under standing waves. The calculated bed profile found with the extended model was found to be consistent with that expected for bed load transport. That is, the sediment was found to respond to the lower mass transport circulation cell, with bed erosion taking place between nodes and antinodes and deposition occurring at the nodes. The new model successfully determined the predicted bar formation. However, it was not possible to validate the magnitude of the bed evolution because, currently, validation data for short-term bed evolution for this situation do not exist. In addition, validation of the extended model against equilibrium bed profiles was judged to be too computationally expensive to be practical.

The extended model was also applied to short-term beach evolution on a 1:8 gravel beach due to plunging waves. For this situation, the bed evolution determined with the extended model was compared against large-scale physical model data. The test for this situation demonstrated that the numerical model predicts sediment deposition above the SWL and a step formation below the SWL. This is in agreement with the physical model data. However, the magnitude and location of the crest and step were not well predicted. In the numerical model, the crest above the SWL and the step below SWL are further

---

up the beach when compared the experimental study. The beach profile evolution for this test is not presently adequately modelled. Some possible explanations for the differences have been discussed but further development in this area will be required.

Further improvements to the extended model require additional validation data. This is true for both the study of bed morphology under standing waves and beach evolution on a gravel beach. However, detailed measurements of parameters on steep gravel beaches subjected to plunging waves are extremely difficult. Additionally, difficulties are presented for instrumentation because of the hostile environment presented by gravel under plunging waves and because the flow can be highly aerated. Consequently, it is anticipated that additional validation data will remain problematic to obtain. For this reason, further development work in this area was postponed.

## **APPENDIX B**

### **TESTS CONDUCTED TO DETERMINE THE EFFECT OF EMBANKMENT CREST WIDTH UPON COMBINED DISCHARGE.**

<i>Test No</i>	<i>Significant</i>					
	<i>Combined Discharge, <math>q_{ws}</math> (<math>m^3/s/m</math>)</i>	<i>wave Height, <math>H_s</math> (m)</i>	<i>Negative Freeboard, <math>R_{C_r}</math> (m)</i>	<i>Crest Width (m) <math>L_w</math></i>	<i>Peak Period, <math>T_p</math></i>	<i>Wavelength <math>\lambda_p</math></i>
T46y	2.73	1.532	-1.183	3.05	14.4	109.7
T46ya	3.09	1.532	-1.158	0.5	14.4	109.7
T46yb	2.95	1.532	-1.171	1	14.4	109.7
T46yc	2.85	1.532	-1.181	1.5	14.4	109.7
T46yd	2.79	1.532	-1.178	2	14.4	109.7
T46ye	2.76	1.532	-1.181	2.5	14.4	109.7
T46yf	1.69	1.532	-0.737	0.5	14.4	109.7
T46yg	1.61	1.532	-0.749	1	14.4	109.7
T46yh	1.58	1.532	-0.753	1.5	14.4	109.7
T46yi	1.50	1.532	-0.754	2	14.4	109.7
T46yj	1.51	1.532	-0.751	2.5	14.4	109.7
T46yk	1.50	1.532	-0.751	3	14.4	109.7
T46yl	0.61	1.532	-0.297	1.5	14.4	109.7
T46ym	0.72	1.532	-0.280	2	14.4	109.7
T46yn	0.68	1.532	-0.288	2.5	14.4	109.7
T46yo	0.64	1.532	-0.280	3	14.4	109.7
T46yp	0.81	1.532	-0.280	1	14.4	109.7
T46yq	0.87	1.532	-0.297	0.5	14.4	109.7
T46yr	2.43	1.532	-0.929	0.5	14.4	109.7
T46yra	2.09	1.532	-0.921	1	14.4	109.7
T46yrb	2.02	1.532	-0.926	1.5	14.4	109.7
T46yrc	1.95	1.532	-0.932	2	14.4	109.7
T46yrd	1.93	1.532	-0.933	2.5	14.4	109.7
T46yre	1.92	1.532	-0.932	3	14.4	109.7
T46ys	1.21	1.532	-0.484	0.5	14.4	109.7
T46ysarerun	1.15	1.532	-0.487	1	14.4	109.7
T46ysbrerun	1.12	1.532	-0.489	1.5	14.4	109.7
T46yscrerun	1.09	1.532	-0.489	2	14.4	109.7
T46ysdrerun	1.09	1.532	-0.490	2.5	14.4	109.7
T46ysererun	1.06	1.532	-0.488	3	14.4	109.7
T46yt	2.20	1.205	-0.925	0.5	6.1	41.9
T46ytarerun	2.07	1.205	-0.932	1	6.1	41.9
T46ytbrerun	1.99	1.205	-0.934	1.5	6.1	41.9
T46ytcrerun	1.95	1.205	-0.937	2	6.1	41.9
T46ytdrerun	1.93	1.205	-0.939	2.5	6.1	41.9
T46ytererun	1.92	1.205	-0.939	3	6.1	41.9
T46yu	2.21	0.758	-0.936	0.5	10.1	75.8
T46yua	2.06	0.758	-0.942	1	10.1	75.8
T46yub	1.98	0.758	-0.944	1.5	10.1	75.8
T46yuc	1.95	0.758	-0.948	2	10.1	75.8
T46yud	1.91	0.758	-0.949	2.5	10.1	75.8
T46yue	1.90	0.758	-0.950	3	10.1	75.8
T46yv	3.14	0.877	-1.192	0.5	10.8	81.1
T46yva	2.98	0.877	-1.199	1	10.8	81.1
T46yvb	2.88	0.877	-1.205	1.5	10.8	81.1
T46yvc	2.81	0.877	-1.210	2	10.8	81.1
T46yvd	2.77	0.877	-1.212	2.5	10.8	81.1
T46yve	2.74	0.877	-1.214	3	10.8	81.1

<i>Test No</i>	<i>Combined Discharge, <math>q_{ws}</math> (<math>m^3/s/m</math>)</i>	<i>Significant wave Height, <math>H_s</math> (m)</i>	<i>Negative Freeboard, <math>R_c</math> (m)</i>	<i>Crest Width (m) <math>L_w</math></i>	<i>Peak Period, <math>T_p</math></i>	<i>Wavelength <math>\lambda_p</math></i>
T46x	0.62	1.735	-0.294	3.05	6.1	41.8
T47b	1.03	2.497	-0.292	3.05	6.5	45.8
T47e	0.48	0.873	-0.270	3.05	10.6	79.7
T46pa	0.73	1.700	-0.257	3.05	10.6	79.7
T47f	1.32	2.686	-0.275	3.05	10.6	79.7
T47k	0.43	0.789	-0.261	3.05	12.1	91.5
T47l/T47la	0.67	1.781	-0.265	3.05	13.9	105.7
T47m	1.25	2.711	-0.291	3.05	14.0	106.8
T46na	1.21	0.816	-0.702	3.05	5.7	38.8
T47a	1.37	1.559	-0.711	3.05	5.8	39.8
T46v	1.80	2.401	-0.685	3.05	5.8	39.8
T47c	1.24	0.783	-0.696	3.05	9.9	73.7
T47g	2.07	2.453	-0.688	3.05	9.7	72.0
T47h	1.22	0.707	-0.673	3.05	14.6	111.4
T47i	1.61	1.708	-0.694	3.05	14.6	111.4
T47j	1.96	2.478	-0.676	3.05	14.6	111.4
T46ms	2.68	0.652	-1.214	3.05	5.8	39.8
T46q	2.63	1.205	-1.180	3.05	5.8	39.8
T46ra	2.94	2.255	-1.185	3.05	6.1	42.1
T46s	2.62	0.758	-1.190	3.05	9.9	73.7
T46t	2.78	1.567	-1.184	3.05	10.1	76.0
T46u	2.98	2.487	-1.197	3.05	9.7	72.0
T46w	2.63	0.742	-1.190	3.05	14.6	111.4
T46y	2.73	1.532	-1.183	3.05	14.6	111.4
T46z	2.94	2.409	-1.189	3.05	14.6	111.4

## MODELLING STORM SURGE WAVE OVERTOPPING OF SEAWALLS WITH NEGATIVE FREEBOARD

David K. Jones<sup>1</sup>, Qingping Zou<sup>2</sup>, Dominic E. Reeve<sup>3</sup>

A Reynolds-averaged Navier-Stokes based wave model (RANS) is used to simulate storm surge wave overtopping of embankments. The model uses a wave generating boundary condition that accepts a wave time history as an input and reproduces the time history in the model. This allows a direct wave by wave simulation of recorded data. To investigate the success of the model at reproducing the wave generation, transformation and overtopping processes the model is compared with experimental laboratory data. A wave-by-wave comparison is performed for overtopping parameters such as discharge, depth and velocity. Finally the overtopping discharge predicted by the model is compared against design formulae.

*Keywords: overtopping, embankment, storm surge*

### Introduction

Coastal flooding is caused by combinations of high tides, waves, wind set-up and storm surges driven by low-pressure systems. With global warming causing sea levels to rise and the potential of increased storminess to cause more extreme waves and storm surges, the likelihood of overtopping may well be expected to increase.

Protection of low-lying areas of the world against coastal flooding is often in the form of armoured earthen embankments or levees and the determination of adequate height of these structures is key to their success at protecting coastal areas. In determining the crest elevation a balance must be met between the cost of increasing crest elevation against the consequences of overtopping or breach. The difference in the level between the defence crest and the undisturbed water depth is known as the freeboard.

During extreme storm events, embankments may experience situations where the freeboard is very small or even negative, leading to a combination of pure overflow (weir flow) and wave overtopping. At these times, as well as the obvious danger presented by the volume of water flowing over the crest there is also the potential for the overflow to remove lee side protection, erode the back face and possibly breach the embankment.

Overtopping of embankments can be caused by various situations. Overtopping occurs in the form of wave overtopping which is a result of large waves running up the front face of the structure that has positive freeboard, resulting in intermittent overtopping. High tides combined with low pressure surge levels can cause surge overflow with negative freeboard and little or no waves. Low pressure systems are often associated with storms, so possibly the worst situation for overtopping will be caused by low pressure storm surge causing over flow with negative freeboard combined with waves. It is this worst situation that is investigated in this paper.

In what follows, to avoid confusion, we use 'overtopping' to refer to wave overtopping a defence with positive freeboard, 'overflow' to refer to the flow of water over a crest (negative freeboard) in the absence of waves and 'combined discharge' to refer to the flow of water over the crest when waves are combined with negative freeboard conditions.

The crest elevation of embankments has historically been set by examination of local records or design formulae determined from physical models. For wave overtopping and run-up on embankments with positive freeboard the formulae for predicting wave-overtopping rates are usually based on empirical equations based on hydraulic model data. For wave overtopping there exists extensive model data, (eg. van der Meer 2009), against which to validate models and for surge overflow of a wide defence without waves the situation can be modelled as a broad crested weir. However, for combined discharge considerably less work has been conducted. Schuttrumpf (2001) developed equations for wave overtopping at zero freeboard based on experimental laboratory data. A method developed to evaluate combined discharge is to sum the wave component derived using the equation developed by Schuttrumpf along with the surge component calculated using weir equations. More recently overtopping discharge formulae have been derived that allows the combined discharge to be calculated directly. This work was conducted by Reeve et al. (2008) and was carried out in a numerical wave flume using a Reynolds-averaged Navier-Stokes based wave model and a Volume of Fluid surface capturing scheme (RANS-VOF). The formulae produced were tested against the results predicted by Schuttrumpf combined with the weir equations. At that point no hydraulic physical model data existed for combined wave and storm surge overtopping. More recently still, Hughes and Nadal (2009) reported the results of a laboratory study of overtopping caused by combined wave and storm surge and produced design equations that predicted more modest overtopping than Reeve et al. (2008) had predicted.

<sup>1</sup> Britannia Royal Naval College, College Way, Dartmouth, Devon, UK. TQ6 0HJ

<sup>2</sup> Coastal Engineering Research Group, University of Plymouth, Plymouth Devon PL4 8AA UK.

<sup>3</sup> Coastal Engineering Research Group, University of Plymouth, Plymouth Devon PL4 8AA UK

This paper assesses the ability of a modified version of the RANS-VOF numerical model used by Reeve et al. (2008) to directly reproduce on a wave by wave basis the tests conducted by Hughes and Nadal (2009). This is achieved by using an alternative wave absorbing boundary condition that allows a wave time history as input but without the usual wave absorbing sponge layer required to allow the outgoing waves to leave the computational domain without reflection. The validated model is then used to determine combined discharge rates and the results are compared with design formulae and differences between design formulae are investigated.

### Empirical Formulae

In this section some commonly used design formulae that are employed to estimate discharge rates for wave overtopping of embankments are presented. Schuttrumpf developed Equations (1) to determine overtopping discharge caused by waves overtopping at zero freeboard. These equations are based on model studies for uniform smooth slopes between 1:3 and 1:6. To estimate the combined discharge these equations are summed with the equation for flow over a broad crested weir, with the surge component being calculated with the weir equation and the wave component being calculated with Equation (1). Clearly this simple addition of the two components is a coarse approximation to reality and does not fully describe the complex hydrodynamic situation; it might however be expected to provide a reasonable first approximation to the problem.

$$\frac{q}{\sqrt{g \cdot H_{m0}^3}} = 0.0537 \cdot \xi_{m-1,0} \quad \text{for } \xi_{m-1,0} < 2.0 \text{ Breaking waves} \quad (1)$$

$$\frac{q}{\sqrt{g \cdot H_{m0}^3}} = 0.136 - \frac{0.226}{\xi_{m-1,0}^3} \quad \text{for } \xi_{m-1,0} \geq 2.0 \text{ Non breaking waves}$$

There are a number of different equations used to determine flow over broad crested weirs. Possibly the simplest equation for ideal flow is given in Chadwick and Morfett (1998) as:

$$q = C_d \times 1.705bh^{3/2} \quad (2)$$

where  $b$  is the weir breadth and  $h$  is the upstream depth above the weir crest and  $C_d$  is 1.0 for ideal fluids. For real fluids  $C_d$  has been derived empirically by Ackers et al (1978). For  $0.45 < h/L < 0.8$  and  $0.35 < h/(h+h_1) < 0.6$   $C_d$  has been given by Chadwick & Morfett (1998) as:

$$C_d = 0.848 \left[ 0.91 + 0.21 \frac{h}{L} + 0.24 \left( \frac{h}{h+h_1} - 0.35 \right) \right] \quad (3)$$

where  $L$  is the length of the weir crest and  $h_1$  is the water depth to the crest of the weir. Pullen et al. (2007) presented Equation (4) as a suitable formula for use with Equation (1) when determining combined wave and surge overtopping, where  $-R_c$  is the overflow depth measured at the weir and  $q$  is the discharge per metre length of defence. The key difference between Equation (4) and Equation (2) is the location the depth of flow is measured at. The flow depth recorded at the weir crest is subject to the draw down that occurs near broad crested weirs.

$$q = 0.6 \cdot \sqrt{g \cdot | -R_c^3 |} \quad (4)$$

The equation for combined wave overtopping and storm surge developed by Reeve et al. are given in Equation (5). The equations are based on regression analysis of validated numerical flume tests for irregular breaking and non breaking waves on seawalls with slopes 1:3, 1:4 and 1:6 and small negative dimensionless freeboards in the region  $0.0 > R \geq -0.8$ .

$$Q = \frac{q}{\sqrt{g \cdot H_s^3}} \cdot \frac{\sqrt{\tan \alpha}}{\xi_p} = 0.051 \exp \left( -1.98 \frac{R_c}{H_s \xi_p} \right) \quad \text{for } \xi_p < 2.0 \quad (5)$$

$$Q = \frac{q}{\sqrt{g \cdot H_s^3}} = 0.233 \exp \left( -1.29 \frac{R_c}{H_s} \right) \quad \text{for } \xi_p \geq 2.0$$

The laboratory experiments of combined wave and surge overtopping conducted by Hughes and Nadal (2009) allowed the following best-fit equation, Equation (6), to be developed. These tests were conducted for irregular breaking and non-breaking waves on a seawall slope of 1:4.25 and for negative freeboards,  $R_c$  of 0.29, 0.81 and 1.3m, at a scale of 1:25.

$$\frac{q}{\sqrt{g \cdot H_{m0}^3}} = 0.034 + 0.53 \left( \frac{-R_c}{H_{m0}} \right)^{1.58} \quad \text{for } R_c < 0 \quad (6)$$

It should be noted that although well-established this range of predictors for discharge indicates a degree of uncertainty. For example, relationships inferred from computer models will be influenced by

the assumptions inherent in the numerical model, while relationships derived from laboratory experiments will be subject to experimental error, scaling effects and so on.

In this paper a comparison is made between the overtopping discharge calculated with the above formulae and that estimated with the RANS-VOF model.

### Numerical modelling

The RANS-VOF model is used in this study to calculate the free surface and general turbulent flow. It has been coupled with a second-order  $k$ - $\epsilon$  turbulence closure model, where  $k$  is the turbulent kinetic energy and  $\epsilon$  is the turbulence dissipation. The model uses a set of equations for the mean flow containing contributions from the fluctuating turbulent flow. The RANS-VOF model uses the two step projection finite difference method (Chorin, 1968) to solve the Reynolds equations. The calculation of mean flow has been based on an earlier Navier-Stokes equation solver RIPPLE that was developed at Los Alamos Laboratory (Kothe et al., 1991). A fuller description of the model can be found in Lin & Liu (1998).

The usual boundary conditions are applied within the model. That is, if the mesh is small enough to resolve the viscous boundary layer then the no slip boundary condition would be applied. However for these tests, to be computationally efficient, the mesh is not fine enough to resolve the boundary layer. If the viscous boundary layer is not resolved then a free-slip condition is more appropriate at a solid boundary. In this case the turbulent field near the solid boundary is described using the log-law to find the distribution of mean tangential velocities within the boundary layer. This allows values of  $k$  and  $\epsilon$  to be expressed as a function of distance from the solid boundary.

The wave generation in the model uses a wave time history defined at the seaward boundary, as developed by Torres-Freyermuth (2007). This is sometimes used in preference to a source function, (eg Lin & Liu 1999), because the absorbing sponge layer is not required at absorbing boundaries and leads to a more efficient reduction in computational domain. In this study, wave generation using a wave time history is used to directly simulate the physical model tests conducted by Hughes and Nadal (2009). The assumptions used within this wave generating procedure are that the high frequency energy is dissipated by the breaking waves at the embankment and the long wave components reflected from the shore propagate as non-dispersive waves according to linear shallow water wave theory; so that at the boundary linear superposition between incident and reflected waves is valid. In order to reproduce the required waves at the boundary, as well as wave height data, the model also requires the velocity components at the boundary. This was derived from the wave height data using linear theory.

With a wave overtopping model a system has to be devised to ensure that the discharge is recycled back into the flume. This ensures the conservation of mass failure to do this would result in a lowering of water level within the flume over time. To implement this in the model the depth and velocity information at the crest of the embankment is used to determine the discharge. The discharge is used as an input back into the model as a depth averaged velocity at the seaward boundary. This velocity is combined with the velocity determined for wave generation. If the instantaneous discharge is directly fed back into the wave generating boundary, it effectively generates a false wave at the boundary. To overcome this problem, whilst still maintaining a conservation of mass, a running average discharge is used to feed the seaward boundary. It was found that a running mean over a twenty second period successfully produced the required wave profiles. It will later be shown that the degree of success of the wave generating procedure is satisfactory.

The next section briefly describes the physical model laboratory study of combined discharge conducted by Hughes and Nadal (2009), a more detail description of the tests can be found in the original paper. A number of the test conducted by Hughes and Nadal were simulated with the RANS-VOF model and comparisons between various recorded and predicted parameters are made.

### Experimental data

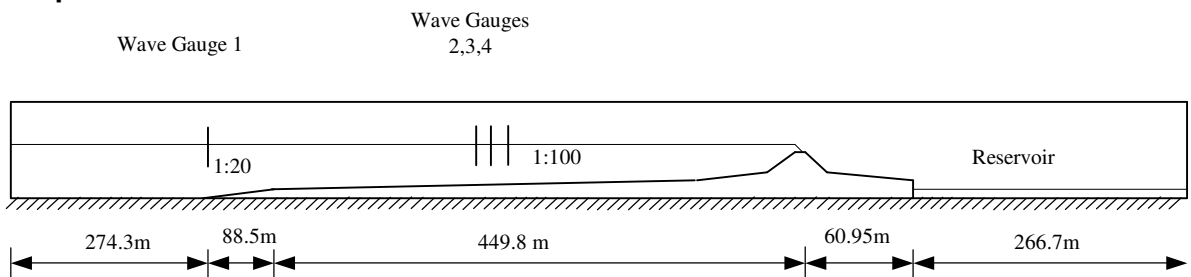


Fig. 1 General set-up of flume with the prototype embankment.

Hughes and Nadal (2009) conducted a series of physical model flume tests of combined discharge over an embankment, a brief description of the model tests is given here. The tests were conducted at a scale of 1:25. Fig. 1 shows the general flume setup and Fig. 2 shows the detail of a cross section through

the embankment. Recirculation of the discharge over the crest was achieved in the physical model by pumping the water from the reservoir to near the wave generator. Adjusting the flow rate in the pump set the surge level tested in the model.

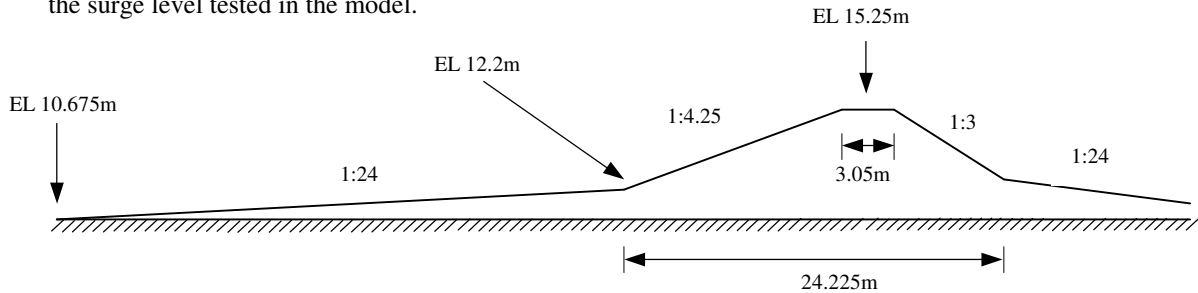


Fig. 2 Detail of the prototype embankment cross section.

The flume model used four resistance type wave gauges, one near the wave generator and a three-gauge array on the 1:100 slope. Flow depth over the embankment was recorded with pressure cells. The location of the pressure cells is given in Fig. 3. The horizontal flow velocity directly above pressure gauge 2 (P2) was recorded with a Laser Doppler Velocimeter (LDV). The location of the LDV was adjusted for each test so that the velocity was always recorded at half of the flow depth.

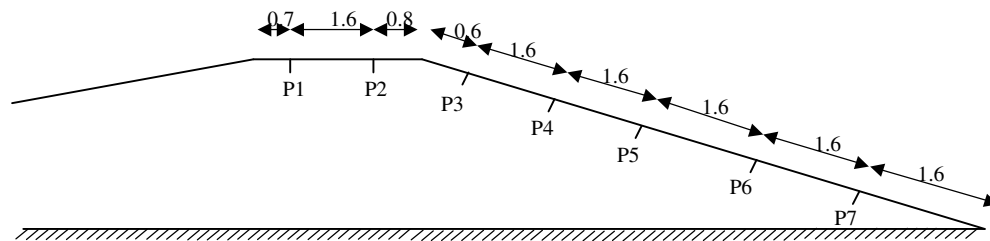


Fig. 3 Location of pressure cell on the prototype embankment, dimensions in m.

The test programme investigated storm surge levels of 0.29, 0.81 and 1.3m above the embankment crest. Each storm surge level was tested for three wave heights and three wave periods. This gave a total of 27 tests.

Wide embankments, when subjected to surge overflow, act as a broad crested weir, with flow at the crest progressing from sub critical flow near the seaward boundary to critical and then supercritical flow on the lee side. This means the flow depth on the embankment crest will vary with location across the crest. In order to determine an appropriate surge level the model was run without waves for an initial period at the start of each test. The steady discharge for this period was determined with the flow depth and velocity information at P2. The surge level was then determined from the equation for flow over a broad crested weir, Equation (2) with a  $C_d$  value of 1.0. This allowed the upstream surge level to be estimated from the measured discharge. This surge level would be more useful to designers than a depth at the weir because it corresponds to the surge level calculated from tide and meteorological conditions. A surge level recorded at the embankment crest would be subject to the draw down that occurs near weirs.

The pressure and velocity data for the tests were collected at 50Hz and a total of 15000 data points was collected for each channel, giving an equivalent of 1500s of prototype scale data. The first 500 data points from each test was used to determine the steady discharge conditions, with waves beginning to reach the embankment shortly after this. To determine combined discharge when the embankment was subject to waves and steady discharge the discharge average over the prototype time period 100 to 1500s was used.

As already stated the discharge was determined at P2 with reference to the flow depth and velocity recorded at half depth. However, when the embankment was subjected to waves the water level would periodically drop below the level of the LDV. The LDV was set so that when this occurred the velocity recorded would remain at the last value recorded. This is more likely to occur on the tests with the lower surge levels. As a consequence the average discharges would be higher than expected. To determine the range of this error a second calculation was done with the LDV set to zero when the water level dropped below the laser level. These two sets of reading effectively gave the maximum range of the error. Hughes and Nadal (2009) determined that the maximum difference caused by this problem was 13% for a test at the lower surge level. On average it caused a 4% error. For tests at the highest surge level the LDV mostly remained submerged and so the problem was less apparent.

For this paper the RANS-VOF model has been used to simulate the tests conducted at the larger 1.3m surge level. The table below give a list of wave conditions tested.

Test Number	$H_{m0}$	$T_p$	$\xi_p$
1	0.64	6.07	2.1
2	1.17	6.07	1.6
3	2.3	6.07	1.2
4	0.86	10.12	3.3
5	1.79	10.12	2.4
6	2.74	10.12	1.8
7	0.74	14.37	5.0
8	1.5	14.37	3.5
9	2.31	14.37	2.8

Table 1 Wave conditions tested and Iribarren number.

### Description of the numerical model

For computational efficiency only part of the physical model flume was reproduced in the RANS-VOF model. The wave input signal for the RANS-VOF model was taken from wave gauge 2, G2, in the physical model and so the seaward boundary of the model was the G2 location. This allowed waves generated within the RANS-VOF model to be compared with those measured at G3 and G4 in the physical model. The landward boundary of the RANS-VOF model was defined as being on the 1:3 slope on the lee side of the embankment. This boundary was defined as being an open boundary, so allowing waves to exit the flume without reflection. The boundary condition used at the bottom was a rigid free slip condition, which is used when the mesh size is thicker than the viscous boundary layer and so the  $k-\epsilon$  turbulence model is used. The vertical extent of the computational mesh was determined by the largest wave, so that the wave did not touch the top of the flume. Reducing the height where possible ensured computational efficiency. Fig. 4 shows the model set-up along with a snapshot of the wave surface elevation and flow field velocity vectors.

The defining criterion for the mesh size was that the mesh had to be small enough to resolve the supercritical flow on the landward side of the embankment. To achieve this a mesh size for all 1.3m surge tests was 0.4m in the horizontal direction and 0.1m in the vertical direction. This gave a total of up to 58600 node points. The mesh size was required to adequately define the flow over the crest of the embankment and to define the waves whilst still being computationally efficient. To confirm that the results were not dependent on mesh size, a test was conducted with mesh size of 0.2m in the horizontal direction and 0.05m in the vertical direction, 234432 node points. Results for the more refined mesh were near identical to the coarser mesh and provided no advantage.

The time step used for all tests was 0.01s. The test duration of the RANS-VOF model was 250s. This allowed approximately 100s of steady flow with no waves followed by 150s of steady surge with waves. The initial period allowed the surge level in the model to be calculated by using Equation (2). The discharge in the model was also calculated at the location of P2. However, unlike the physical model that only recorded the velocity at half of the average depth at P2, in the RANS-VOF model the velocities are evaluated at each node allowing a depth integrated discharge to be calculated.

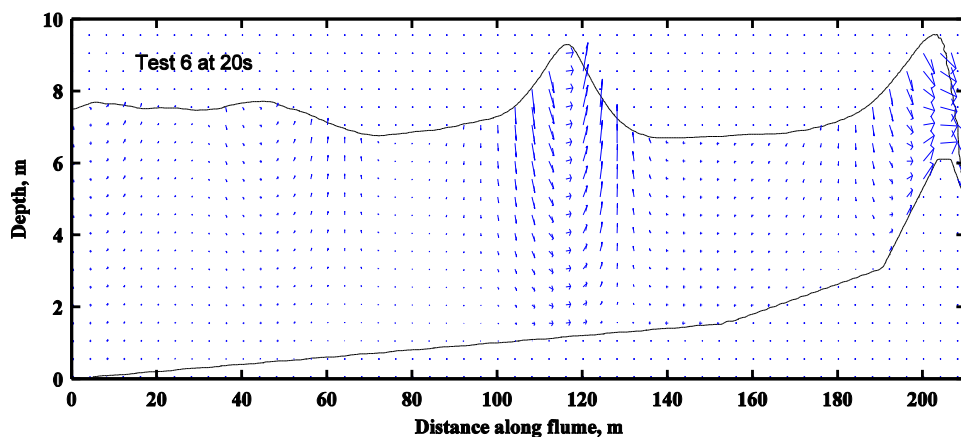


Fig. 4 A snap shot showing wave surface elevation, embankment detail and flow field velocity vectors plotted at every fifth node vertically and every tenth node horizontally.

## Comparison between RANS-VOF model and physical model results

### Wave generation

As already mentioned waves generated in the RANS-VOF model used the waves recorded at wave G2 in the physical model. For verification purposes it is useful to compare waves recorded at wave G4 in the physical model with those in the equivalent position in the RANS-VOF model. As the wave gauge is only 14.922m away from the wave-generating boundary and little wave transformation will have occurred, this is a good test of the wave generating boundary condition. This comparison is shown in Figure 5 for a representative sample of tests. The tests shown were selected to show each of the wave periods and wave heights. There is good agreement throughout the test and demonstrates that the assumption that breaking waves dissipated high frequency energy is valid and that there is no build-up of unwanted long wave reflections.

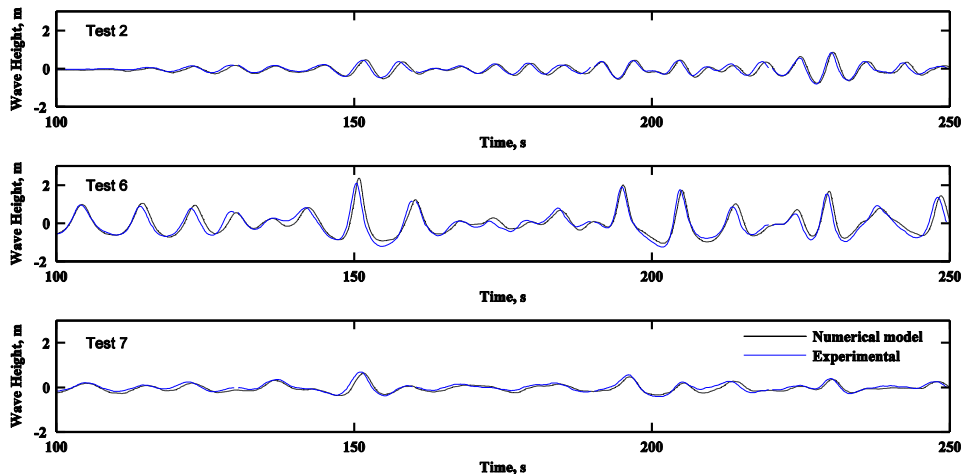


Fig. 5 Comparison of wave generated at G4.

### Discharge comparison

The discharge in both the physical model and the RANS-VOF model was calculated at the crest of the embankment using the flow depth and velocity information. In the RANS-VOF model, the discharge through partially filled cells was calculated with reference to the VOF function. The calculated discharge with steady overflow and no waves ( $q_s$ ) and the discharge with combined wave overtopping and overflow ( $q_{ws}$ ) were averaged over the same time period in physical model and the RANS-VOF test to ensure equivalence. The start time for the averaging period for  $q_{ws}$  began when the waves had reached the embankment and were established. Table 2 gives discharge rates and the discrepancy between the laboratory and numerical models in terms of the relative error (the numerical model predicted relative to the laboratory results). It can be seen that generally the models compare well, however there is an increase in relative error for the tests with larger wave heights. The average relative error for the lower wave heights tested (Tests 1, 4, and 7) is  $-0.5\%$ . At the larger wave heights (Tests 3, 6 and 9) the average relative error is  $+7.8\%$ .

Test	Physical Model		RANS-VOF		$q_s$ relative error (%)	$q_{ws}$ relative error (%)
	$q_s$ ( $m^3/s/m$ )	$q_{ws}$ ( $m^3/s/m$ )	$q_s$ ( $m^3/s/m$ )	$q_{ws}$ ( $m^3/s/m$ )		
1	2.53	2.62	2.56	2.68	1.27	2.06
2	2.46	2.59	2.49	2.63	1.26	1.82
3	2.40	2.72	2.47	2.89	2.70	6.55
4	2.63	2.68	2.53	2.62	-3.99	-2.13
5	2.53	2.67	2.53	2.78	-0.24	4.20
6	2.70	2.71	2.56	2.98	-5.07	9.96
7	2.57	2.66	2.54	2.63	-0.93	-1.43
8	2.51	2.57	2.40	2.73	-4.23	6.43
9	2.53	2.75	2.50	2.94	-1.30	6.83

Table 2 Comparison of discharge rates.

In order to determine why the tests with larger wave heights record higher discharge peaks in the RANS-VOF model than the physical model it is useful to plot the time histories of discharge. These are shown below for the same sample tests.

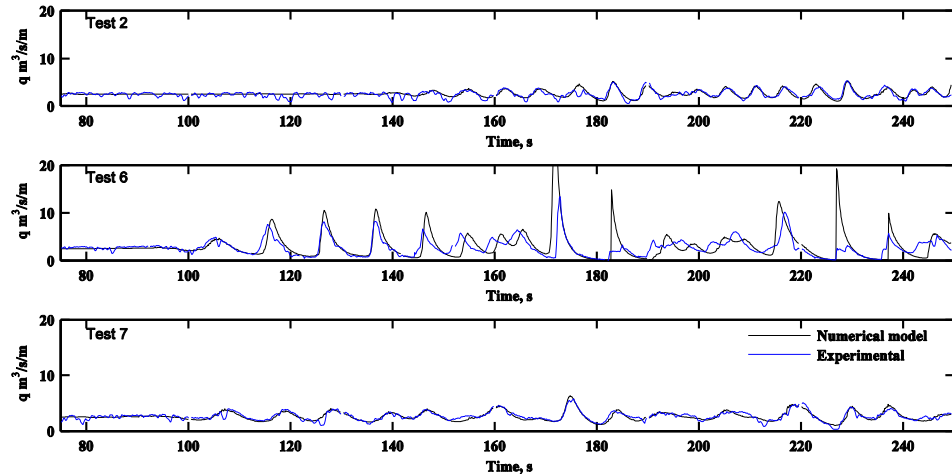


Fig. 6 Comparison of discharge at P2.

Although the general agreement is very good the RANS-VOF model has slightly larger peaks, particularly at the larger wave height (Test 6). It also shows a slight phase shift for some of the peaks and a couple of peaks showing substantial differences. This could be a result of differences in either the surge depth or velocity measurement or both. To investigate this further a comparison of time histories of surge depth and velocity in each model has been performed.

### Flow depth comparison

The time histories of water depth at the embankment crest for Test 2, 6 and 7 are shown in Fig. 7. Again the comparison is very good for the smaller wave heights but for some of the waves in the larger wave test (Test 6) the peaks in the RANS-VOF model are over represented. The phase shift is limited to just two of the larger peaks and the two discharge peaks at about 185 and 230s show a more favourable comparison of water depth but with the RANS-VOF model peaks still being larger than that from the laboratory.

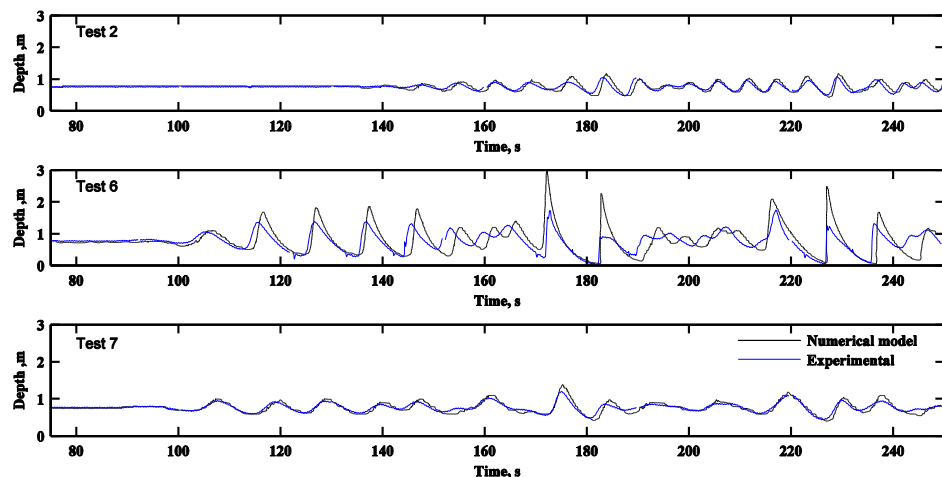


Fig. 7 Comparison of flow depth at P2.

### Velocity comparison

Figure 8 shows the time histories of flow velocities at the crest of the embankment, the velocities for the RANS-VOF model are depth averaged whilst the physical model velocities are recorded at mid-depth. It is evident that the velocity time history from the physical model is quite spiky, this is particularly true of the velocities recorded during the steady surge period of Test 2. The variation in the discharges shown for Test 2 result from the variable nature of the velocity signal for this period.

For all tests the peak velocities recorded in the physical model are generally larger than those recorded in the RANS-VOF model. In Test 6, it can be seen that when the water level fell below the level of the LDV in the physical model the recorded velocities remained uniform during this period. This has affected the two largest velocity peaks at approximately 185s and 230s in the record. Each of these results has flat periods that extend onto the next peak and have significantly reduced the following peaks. These

under predictions of velocities correspond to an under prediction of discharge and are the two peaks that appear as over predictions in the RANS-VOF model in Figure 6.

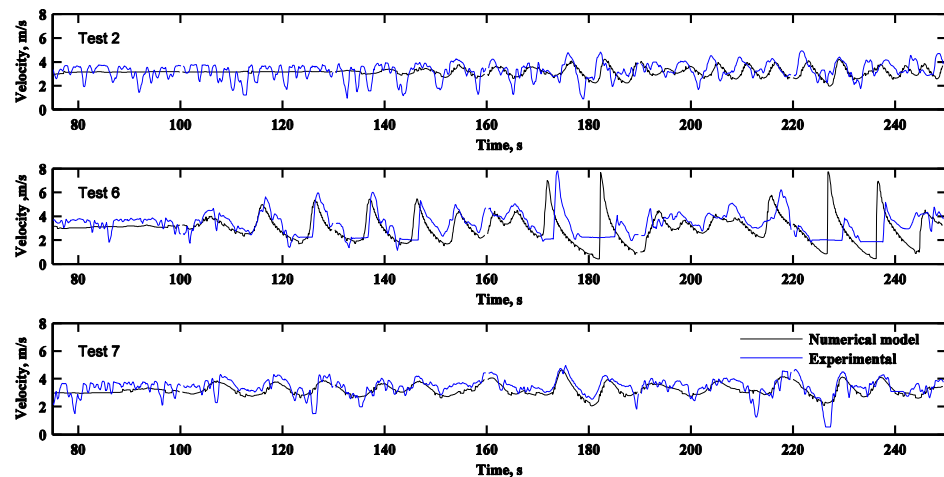


Fig. 8 Comparison of velocities under combined discharge conditions at P2.

### Discussion of results

The prediction of discharge using the RANS-VOF model is generally very good, however for larger wave heights the discrepancy between the predictions made by RANS-VOF and physical model tend to increase. These discrepancies could be due to the assumptions made within the RANS-VOF model or could be due to scale effect or modelling methodology within the physical model or possibly a combination of both. In this section the variation between the computational and physical model results are considered.

In the physical model it has been shown that the velocity record shows a time delay between the time the water level rising above the LDV and when the LDV begins to record data. This has occasionally resulted in the next peak not being recorded and subsequently the next discharge peak being underrepresented.

A comparison of flow depth at the embankment crest shows good agreement between the RANS-VOF model and physical model for all but the peaks of the largest waves. However the peaks are larger in the RANS-VOF model than in the physical model. This difference could be due to RANS-VOF model not correctly describing the flow conditions during wave peaks at the embankment crest. The free surface profile of a typical peak wave is shown in Fig. 9 and shows that, for some tests, the wave is clearly breaking at the embankment crest.

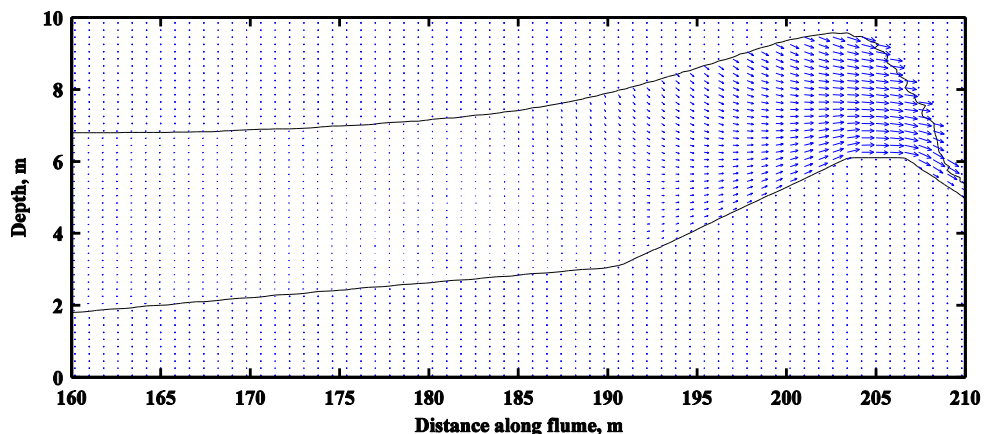


Fig. 9 Free surface profile for Test 6 at 172s showing a breaking wave and the velocity vectors plotted at alternate nodes.

Lin and Liu (1998) validated the RANS-VOF model for a cnoidal wave breaking on a sloping beach against numerical and laboratory data. Although the hydrodynamics of a wave breaking on a sloping beach will be different to a wave breaking on the top of an embankment with combined overflow, it is useful to consider how the RANS-VOF model performs near a breaking wave. In these tests a comparison was made for mean quantities such as wave elevation, velocities and turbulence at points in a breaking wave. The mean quantities were obtained by phase averaging after waves had reached a quasi-steady state. Four locations were investigated on the landward side of the breaking point, with the nearest point being about a quarter of a wavelength from the breaker point. For these tests it was found that, at the point

nearest to the breaking point, the crests measured in the model were lower than the laboratory data and the velocities were higher. This is the opposite of that found in the current study. In the Lin and Liu study it was found that nearer to the breaking point turbulence intensity was overestimated and quite different to the measurements. The lower crest elevations were a result of the excessive estimated turbulence intensity. Further from the breaker point the RANS-VOF model more accurately represented the turbulence intensity and consequently the water surface elevation was also better represented. The poorer representation of the turbulence intensity near the breaker point was caused by the model not accurately predicting the initiation of turbulence in the initial stages of wave breaking where a rapidly distorted shear flow region exists. These uncertainties in the initial turbulence conditions at the initiation of breaking present difficulties in predicting the location of the breaking point. As stated above the turbulence closure model used in the RANS-VOF model describes the velocity profile in a steady, uniform, turbulent boundary layer, which is not the situation in a breaking wave.

The comparison between calculated and measured values in the current series of tests differs from the study by Lin and Liu (1998) in that it is not the phase averaged quantities being compared but the instantaneous measurements. Also the instantaneous measurements at P2 are at the breaking point, where the phase-averaged measurements were at about a quarter of a wavelength from the breaking point.

To determine the type of wave at the crest of the embankment the Iribarren number,  $\zeta$ , has been calculated for each test. These values are shown in Table 1. Where  $\zeta$  is less than two, indicating plunging breakers, generally a worse comparison was found for combined discharge. For tests where  $\zeta$  is greater than two, surging waves, the RANS-VOF model generally provided a better representation of wave overtopping discharge. This is because the turbulence regime under a wave depends on the nature of the wave and whether it is breaking. Our results indicate that the present RANS-VOF model is not fully able to reproduce the surface profile and breaking point for a plunging wave. These predictions can be affected by turbulent closure model as well as the temporal and spatial numerical scheme as suggested by Wang et al (2009).

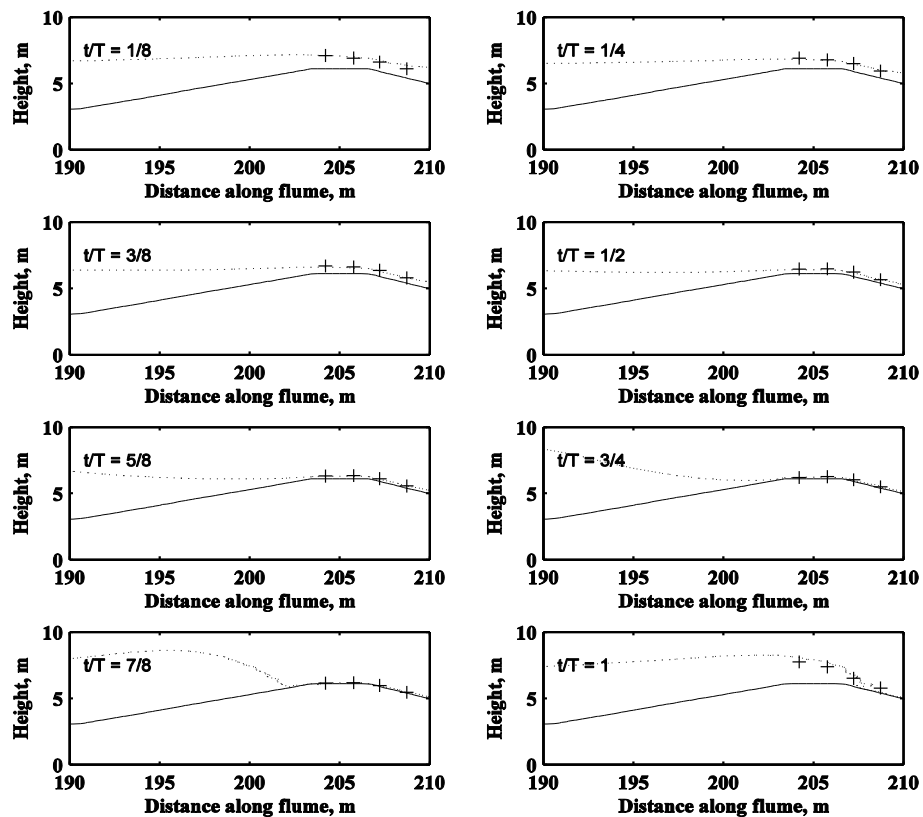


Fig. 10 Embankment profile(solid line), RANS-VOF calculated free surface (dotted line) and measured free surface at P1, P2, P3 and P4 (crosses) for Test 6.

As already discussed, Fig. 9 shows that location of the breaking point occurs at the crest of the embankment. The actual breaking point occurs near the rear edge of the crest. This is near P2, which is the point at which the velocities and depths were recorded in the physical model. This is clearly a region of great flux and small changes in the computed location of the breaker point will significantly alter the calculated depth at this point. Although it is not possible to compare discharge at locations other than P2,

it is possible to compare the flow depths. The free surface profiles of measured and calculated data are shown in Fig. 10 for intervals through a breaking wave, at locations P1, P2, P3 and P4. This is for one of the larger waves in Test 6 and demonstrates that the embankment crest will dry for short periods. The figure shows good agreement between RANS-VOF results and the physical model data, however at the point when the wave breaks the agreement is not as good. This is in agreement with the depth time histories shown in Fig. 7, with the depths at the highest waves being over predicted in the RANS-VOF model. Figure 10 confirms that the over prediction is not localised to P2. However in the RANS-VOF model the wave is breaking very near to the location of P2 and small errors in the calculation of this location will have a large effect on the depth of flow at the breaker location.

### Model comparison against design formulae

In this section the discharge calculated with the RANS-VOF model is compared with available design formulae for combined overtopping.

To compare the RANS-VOF results with the equation presented in Schuttrumpf(2001) summed with a broad crested weir equation, the most appropriate weir equation must be selected. Pullen (2007) suggested Equation (4) could be used to calculate the weir discharge, which can be calculated directly from the depth of flow over the weir, this is the equivalent to the negative freeboard  $R_c$ . However, the flow over a broad crested weir can vary from sub critical to critical and then super critical so the flow depth will vary with location. Consequently the value of  $q$  calculated in Equation (4) is dependent on where  $R_c$  is recorded. For broad crested weirs it is usual to use the upstream head measured at a distance sufficiently upstream to be relatively free from the draw down in water surface elevation near the weir. In terms of water level above a seawall, this corresponds to the still water level plus the surge component. Equation (2) uses the upstream head and is based on ideal flow conditions with the value of  $C_d$  found from empirical formulae and is 1.0 for ideal flow. Reeve et al. (2008) used Equation (2) for comparison purposes with the value of  $C_d$  is given by Equation (3) which has a range of validity of  $0.45 < h/L < 0.8$  and  $0.35 < h/(h+h_1) < 0.6$ . For the tests conducted in this study  $h/L$  have a range from 0.1 to 0.44 and  $h/(h+h_1)$  has a range of 0.09 to 0.30, therefore the value of  $C_d$  calculated with Equation (3) will be outside the acceptable range for the formula. The approach adopted by Hughes and Nadal was to calculate the equivalent upstream head above the weir crest from the measured steady discharge at the start of each test using Equation (2) with a  $C_d$  value of 1.0. For the purposes of comparison the value of  $R_c$  calculated from the steady discharge part of the RANS-VOF tests using the same procedure as adopted by Hughes and Nadal was used to predict dimensionless discharge for each of the design formulae. The comparison is shown in Fig.11 and this figure is comparable with Figure 7 in Hughes and Nadal (2009).

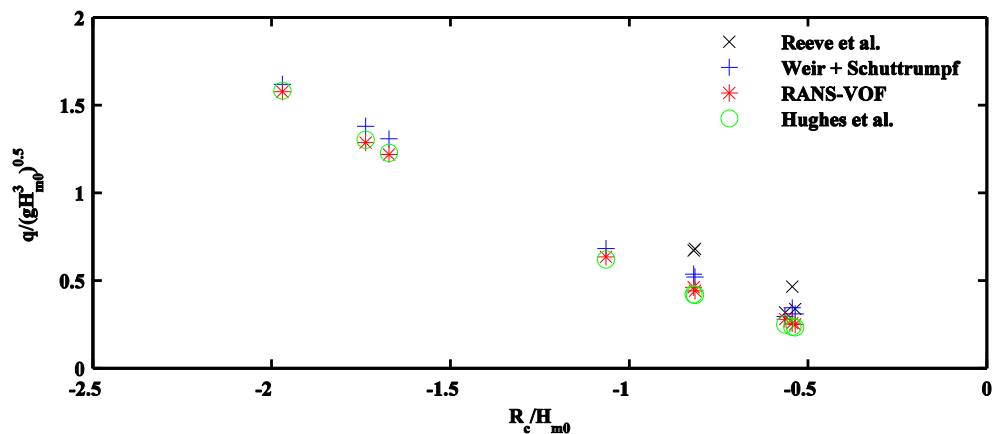


Fig. 11 Dimensionless discharge and dimensionless negative freeboard for the RANS-VOF test and calculated values based on  $R_c$  calculated from Equation 2.

The dimensionless discharge calculated with the RANS-VOF model generally compares well with that predicted by Equations (1) and (2) and Equation (6). The dimensionless discharge calculated using Equations (1) and (2) is slightly larger than that found with the RANS-VOF model and that found with Equation (6) is generally slightly less. It is noted that better agreement is found for more negative values of  $R_c/H_{m0}$ . The range of applicability of Equation (5) is for negative freeboards in the region  $0 > R_c/H_s > -1.0$ , a number of the tests conducted in this series of tests were outside of this range of applicability and this data has been excluded from Fig. 11. The remaining data shows an overestimation of the dimensionless discharge when compared with the other results.

A problem with this analysis is that the steady discharge at the start of the test has been used to calculate  $R_c$  rather than a direct measurement. Also using Equation (2) for this calculation with a value of  $C_d$  set to 1.0 assumes ideal flow. This method of calculating  $R_c$  values may well produce different values to  $R_c$  determined from meteorological and surge calculations.

ISO 3846:2008 is the international standard for flow over a broad crested weirs and recommends that the upstream head readings should be recorded between 3 and 4 times the maximum level upstream from the upstream face of the weir. This allows a measurement of head which is a sufficient distance upstream to avoid the draw down near the weir and is close enough to the weir for the energy loss between the measurement location and the weir to be negligible. The equation given in the standard is equivalent to Equation (2), with tables and graphs that allow  $C_d$  to be evaluated, with  $C_d$  being dependent on the ratios of the surge level to crest width and surge level to height of weir. To determine the value of  $R_c$  for the RANS-VOF tests in accordance with ISO 3846:2008 the average depth was determined during the steady surge part of the test for the period 30-80 seconds at a location near 3.5 times the nominal surge depth from the seaward edge of the embankment. The value of  $R_c$  found using this method was on average 6.0% less than using the steady discharge and Equation (2) to calculate  $R_c$ .

The geometry of the broad crested weir for which Equation (2) is applicable is a rectangular weir where the upstream face forms a sharp right angle corner at its intersection with the crest. The embankment used in this study is significantly different to this design and this difference is a likely source of error. The ISO 3846:2008 states that if this edge is slightly rounded the discharge coefficient may increase significantly. For the embankment used in this study the upstream face has a 1:4.25 slope which is likely to increase discharge in a similar way to having a rounded edge. To demonstrate this the values of  $R_c$  determined from the RANS-VOF results was used to calculate the discharge over the embankment using the Equation (2) and values of  $C_d$  given in ISO 3846:2008. This gave an average discharge that was 21% lower than the RANS-VOF measured discharge. The higher discharge found with the RANS-VOF model is due to the upstream face of the embankment not being perpendicular to the crest. When a non-standard broad crested weir is used in the field a calibration exercise is usually carried out either in the field or a scale model study is used to determine the characteristics of the weir. As no discharge characteristics exist for this type of weir the characteristics could be derived from the physical model study data, unfortunately the depth of flow information at the specified location is not available. However this information is available for all the combined overtopping tests conducted with the RANS-VOF model. To determine the weir characteristics a graph of measured values of  $q_{ws}$  and  $R_c^{3/2}$  is given in Figure 12. The data is well correlated and the linear regression line has a coefficient of determination,  $r^2$  of 0.9987. The equation of the regression line is Equation (2) with the value of  $C_d$  calculated to be 1.126.

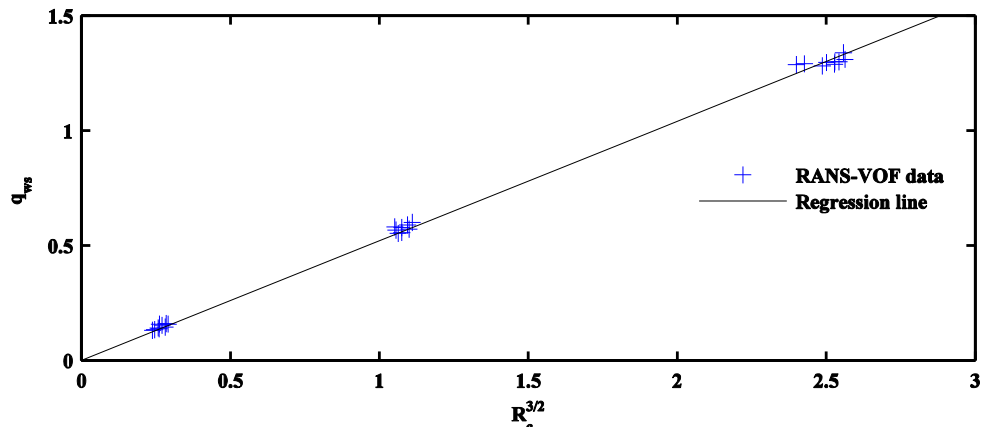


Fig. 12 Embankment steady discharge,  $q_{ws}$  and  $R_c$  calculated with the RANS-VOF model discharge, measured in accordance with ISO 3846.

Equation (5) and (6) were used to recalculate the combined overtopping discharge over the embankment with  $R_c$  measured in accordance with ISO 3846:2008. The combined overtopping discharge was also calculated using Schuttrumpf (2001) combined with Equation (2) with the value of  $C_d$  of 1.126. Figure 13 shows the dimensionless discharge and dimensionless freeboard for these equations along with the RANS-VOF measured values.

Comparing Fig. 11 and Fig 13 shows that the dimensionless discharge is sensitive to the method of evaluating  $R_c$ . Although the dimensionless discharge calculated with the RANS-VOF model has not changed, the measured value of  $R_c$  has reduced. This caused the RANS-VOF data points on Figure 13 to move the right. The dimensionless discharge calculated from Hughes et al., Equation (6), gives lower values than recorded with the RANS-VOF model. This is because using a value of  $R_c$  measured in this way gives on average a 6.0% lower value for  $R_c$ . As the only parameters in Equation (6) are  $R_c$  and  $H_{m0}$ , and  $H_{m0}$  remains the same, a lower value of  $R_c$  results in a lower dimensionless discharge. Similarly as  $R_c$  is the only parameter to change within Equation (5) gives a lower dimensionless discharge. Although the wave component of the overtopping discharge calculated with Equation (1) has remained the same, the weir flow component calculated with Equation (2) has increased significantly. This has increased the combined total and given a combined total marginally above the RANS-VOF results. Overall the VANS-

VOF results fall somewhere between the results expected from the equations provided by Reeve et al. and Hughes and Nadal and are marginally lower than the dimensionless discharge found by combining the modified weir equation and the equation provided by Schuttrumpf.

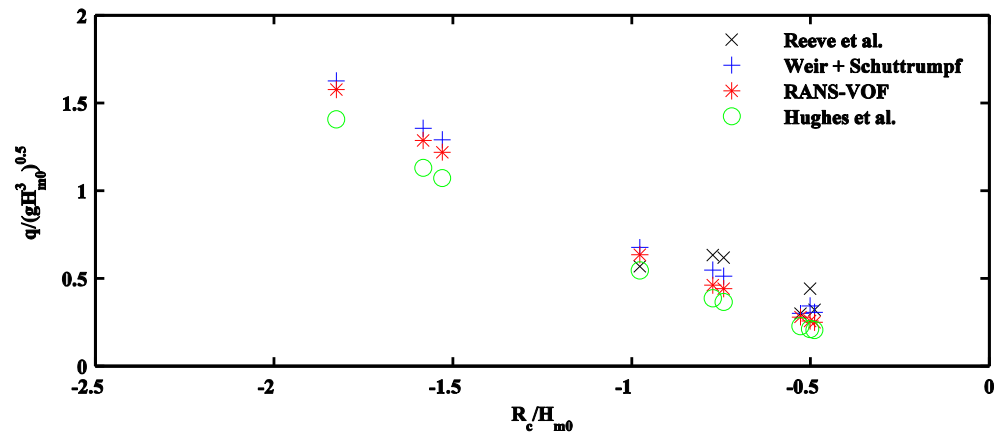


Fig. 13 Dimensionless discharge and dimensionless negative freeboard for the RANS-VOF test and calculated values based on  $R_c$  evaluated in accordance with BS3846 and a  $C_d$  value of 1.1126.

Perhaps one of the key differences between the combined wave overtopping study reported by Reeve et al. (2008) and the other studies on combined wave overtopping is the model set up. Reeve et al. used a sloping foreshore retained by a thin wall of approximately 0.5m thickness. The crest of this wall would act more like a thin plate weir than a broad crested weir. The discharge over a thin wall weir is given by Douglas (1979) as;

$$q = \frac{2}{3} B \sqrt{(2g)} h^{3/2} \quad (7)$$

A comparison between Equation (7) and Equation (2) shows that a thin wall would be expected to show an increase in measured discharge. This may explain why the dimensionless discharge predicted by Equation (5) is greater than recorded in the current study.

It should also be noted that as the ratio  $R_c/H_{m0}$  increases, i.e. as the wave height reduces, the discharge prediction should tend towards that predicted by the equation for broad crested weir. Clearly this will be true for Schuttrumpf combined with the weir equation, but it is also true for both the RANS-VOF model results but Figure 13 show this is less so for the formula derived by Hughes and Nadal.

## Conclusion

The tests conducted as part of the study have demonstrated that the RANS-VOF model is able to successfully predict, on a wave-by-wave basis, wave overtopping discharge of seawalls with negative freeboards. It was found that for smaller and mid sized waves the model provided good predictions of discharge when compared with that measured in a physical model study. For larger waves the RANS-VOF model over predicted the overtopping discharge by on average 8%. This is caused by a poorer representation of turbulence intensity at the breaker point leading to small errors in calculating the location the breaker point. This causes errors in the depth of flow and calculated discharge.

Much of the difference between the RANS-VOF and physical model discharges were as a result of differences in the recorded velocities. The RANS-VOF model used a depth-averaged velocity whilst a mid-depth velocity was recorded in the physical model, which then had to infer the velocity when the water level dropped below the ADV. On occasion the ADV did not respond immediately when the water level had increased beyond mid-depth, causing the velocity from some waves to be missed. To overcome uncertainties, there is a continued need for more physical model tests with depth integrated velocity information.

For comparative purposes, the flow depth over the seawall has been determined from steady overflow conditions using equation (2), which is the equation for discharge over a broad crested weir. However this equation assumes ideal flow and a rectangular weir configuration, a better estimate of flow depth would be found using a value of  $C_d$  determined for real flow.

In this study a comparison was made between the output from the RANS-VOF model and existing design formulae for combined discharge over embankments. It was found that very good agreement exists between the RANS-VOF output and Equations (1) and (2) and Equation (6). Equation (1) and (2) predict slightly higher discharge than the RANS-VOF model and Equation (6) predict very marginally lower. Some of the tests conducted for this paper were outside the range of applicability of Equation (5). Those tests within the range showed that Equation (5) predicted higher discharge rates. This can be accounted for by differences in the embankment shape used in the model by Reeve et al.

The design equations considered in this paper for combined discharge are based on studies for embankments of simple design and for a limited range of slopes. For a fuller understanding a range of different design configuration needs to be investigated. Within the constraints noted earlier, the validated model is a useful and efficient design tool which can be used to investigate different embankment and sea wall design variations such as the slope of the seaward and lee face and berm configurations.

This paper has investigated the capability of the RANS-VOF model in simulating the combined storm wave and surge overtopping at a 1.3m negative freeboard. The RANS-VOF model is currently being used to investigate the 0.29 and 0.81m negative freeboard situations.

## LIST OF SYMBOLS

b	Weir crest width [m]
$C_d$	Coefficient [-]
g	acceleration due to gravity [ $m^2/s$ ]
h	Upstream depth of flow above weir [m]
$h_1$	Water depth to crest of weir [m]
$H_{m0}$	Mean energy wave height [m]
$H_s$	Significant Wave Height [m]
k	turbulent kinetic energy [Nm]
L	Weir crest length [m]
q	Overtopping discharge [ $m^3/s$ ]
R	Dimensionless Freeboard [-] $R = R_c / (H_s \xi_p)$
$R_c$	Crest Freeboard [m]
$\alpha$	Sea wall slope angle [ $^\circ$ ]
$\varepsilon$	turbulence dissipation [Nm]
$\xi_{m-1,0}$	Surf similarity parameter (Iribarren number) defined as $\xi_{m-1,0} = \frac{\tan \alpha}{\sqrt{H_{m0}/L_{om-1,0}}}$
$\xi_p$	Surf similarity parameter (Iribarren number) defined as $\xi_p = \frac{\tan \alpha}{\sqrt{H_s/L_p}}$

Other symbols are defined in the text.

## ACKNOWLEDGEMENTS

We wish to thank Professor Pengzhi Lin of Sichuan University, China for providing the original version of the RANS-VOF model and Dr Alec Torres Freyermuth for providing the modified version of the wave generator subroutine. We also wish to thank Professor Steven Hughes of the US Army Corps of Engineers for providing the data from the Levee overtopping study. David Jones acknowledges the support of a scholarship provided by Britannia Royal Naval College and Plymouth University. Dr Qingping Zou and Prof Dominic Reeve acknowledge support from the Flood Risk from Extreme Events (FREE) Programme of the UK Natural Environmental Research Council (NERC) (NE/E0002129/1), and the Flood Risk Management Research Consortium (GR/576304/01).

## REFERENCES

- Ackers, P., White, W. R., Perkins, J. A., and Harrison, A. J. M. 1978. Weirs and Flumes for flow Measurement, Wiley, Chichester.
- Chadwick, A., Morfett, J., 1998. Hydraulics in Civil and Environmental Engineering Second Edition. E & FN SPON, London.
- Chorin, A.J., 1968. Numerical solution of the Navier–Stokes equations. Mathematics and Computation 22, 745–762.
- Hirt, C. W. & Nichols, B. D. 1981. Volume of fluid (VOF) method for dynamics of free boundaries. J. Comput. Phys. 39, 201-225.
- Hu, K., Mingham, C.G., Causon, D.M., 2000. Numerical simulation of wave overtopping of coastal structure using the non-linear shallow water equation. Coastal Engineering 41, 433–465.
- Hughes, S.A., Nadal, N.C., 2009. Laboratory study of combined wave overtopping and storm surge over low of a levee. Coastal Engineering 56, 244–259.
- Kobayashi, N., Wurjanto, A., 1989. Wave Overtopping on Coastal Structures. J. Waterway, Port, Coastal, and Ocean Engineering 115 (2), 235–251.
- Kothe, D.B., Mjolsness, R.C., Torrey, M.D., 1991. RIPPLE: a computer program for incompressible flows with free surfaces. Report LA-12007-MS, Los Alamos Scientific Report, Los Alamos, NM, USA

- Lin, P., Liu, P.L.-F., 1998. A numerical study of breaking waves in the surf zone. *Journal of Fluid Mechanics* 359, 239–264.
- Lin, P., Liu, P.L.-F., 1999. Internal wave-maker for Navier–Stokes equations models. *Waterway, Port, Coastal, and Ocean Engineering* 125 (4), 207–215.
- Lv, X., Zou, Q., Reeve, D., 2009. A Hybrid LS and VOF Method for 3-D Simulation of Wave Breaking and Overtopping. *Intl. J. Offshore and Polar Engineering* Vol. 4 No. 4, 1-9.
- Nielsen, P., 1992. *Coastal Bottom Boundary Layers and Sediment Transport*. Advanced Series on Ocean Engineering Volume 4, World Scientific, London.
- Pullen, T., Allsop, N.W.H., Bruce, T., Kortenhaus, A., Schüttrumpf, H., van der Meer, J.W., 2007. *EurOtop: Wave overtopping of sea defences and related structures: Assessment Manual*. [www.overtopping-manual.com](http://www.overtopping-manual.com).
- Reeve, D.E., Soliman, A., Lin, P.Z., 2008. Numerical study of combined overflow and wave overtopping over a smooth impermeable seawall. *Coastal Engineering* 55, 155–166.
- Schüttrumpf, H., 2001. *Wellenüberlaufströmung bei Seedeichen – Experimentelle und Theoretische Untersuchungen*. PhD-Thesis,
- Shih, T.-H., Zhu, J., Lumley, J. L. 1996. Calculation of wall-bounded complex flows and free shear flows. *Intl. J. Numer. Meth. Fluids* 23, 1133-1144..
- Torres-Freyermuth, A. 2007. *Estudio de la Hidrodinámica de la Zona de Rompientes mediante ecuaciones tipo RANS*, PhD-Thesis, Cantabria, Spain
- Wang, Z., Zou, Q., Reeve, D., 2009. Simulation of spilling breaking waves using a two phase CFD model. *Computers & Fluids* 38, 1995-2005.

**Computational modelling of coastal flooding caused by combined surge overflow and wave overtopping on embankments.**

*David K. Jones<sup>a</sup>, Qingping Zou<sup>b</sup>, Dominic E. Reeve<sup>c</sup>*

<sup>a</sup> *Britannia Royal Naval College, College Way, Dartmouth, Devon, UK. TQ6 0HJ E-mail brnc-dkj@nrta.mod.uk*

<sup>b</sup> *Department of Civil and Environmental Engineering, University of Maine, Orono, ME 04469, USA*

*Email: qingping.zou@maine.edu*

<sup>c</sup> *Coastal Engineering Research Group, College of Engineering, Talbot Building, Swansea University, Singleton Park, Swansea, SA2 8PP, UK. Email: d.e.reeve@swansea.ac.uk<sup>1</sup>*

**Abstract**

In this paper we investigate the process of embankment wave overtopping combined with overflow due to extreme surge levels that are above the embankment crest. A Reynolds Averaged Navier-Stokes (RANS-VOF) model is employed to simulate the hydrodynamics. To investigate the success of the model at reproducing the hydrodynamic processes, the model is compared with experimental laboratory measurements. Comparisons are performed for quantities including discharge, depth and velocity. The overtopping discharge predicted by the model is compared against empirical design methods. Specific conditions under which discrepancies occur between the model, laboratory measurements and design formulae are identified and explained and design guidance is provided.

This study has demonstrated that the RANS model can adequately represent the complex hydrodynamics encountered in extreme storms where combined overflow and wave overtopping occurs. A tendency was found for the model to somewhat over-predict the overtopping volume as wave heights increase and has been hypothesised as being due to shortcomings of the representation of turbulence within the model.

**Introduction**

Coastal flooding can be caused by overflow (when the still water level rises above the defence crest level) and by wave overtopping (when the incident waves break and run up over the crest of the defence). In very extreme conditions overtopping may be combined with overflow. While there are well tested empirical formulae to predict overtopping, combined overflow and overtopping has received much less attention. It is of practical interest because coastal defences have life times of the order of 50 years or more. Defences constructed before the relatively recent understanding of climate change and sea level rise are potentially providing a reduced level of service. The decision on how to respond to this, perhaps by raising the crest or accepting an increase in discharge during storms, requires accurate estimation of the volumes of water likely to pass the crest of the defences.

Protection of low-lying areas against coastal flooding is often in the form of armoured earthen embankments or levees. Defining the geometry of these structures is key to their successful performance. In practice a balance must be met between the cost of increasing crest elevation and the consequences of overtopping or breach.

High coastal water levels can be caused by combinations of tides, waves and surge driven by storms. During extreme storm events, embankments may experience situations where the freeboard, (the difference in the level between the defence crest and the undisturbed water level), is very small or even negative, leading to a combination of pure overflow (weir flow) and wave overtopping. At these times, as well as the obvious

danger presented by the volume of water flowing over the crest there is also the potential for the overflow to remove lee side protection, erode the back face and possibly breach the embankment. It is this worst situation caused by overflow combined with wave overtopping that is investigated in this paper.

In what follows, to avoid confusion, we use ‘overtopping’ to refer to wave overtopping a defence with positive freeboard, ‘overflow’ to refer to the flow of water over a crest (negative freeboard) in the absence of waves and ‘combined discharge’ to refer to the flow of water over the crest when waves are combined with negative freeboard conditions. These terms are clarified below.

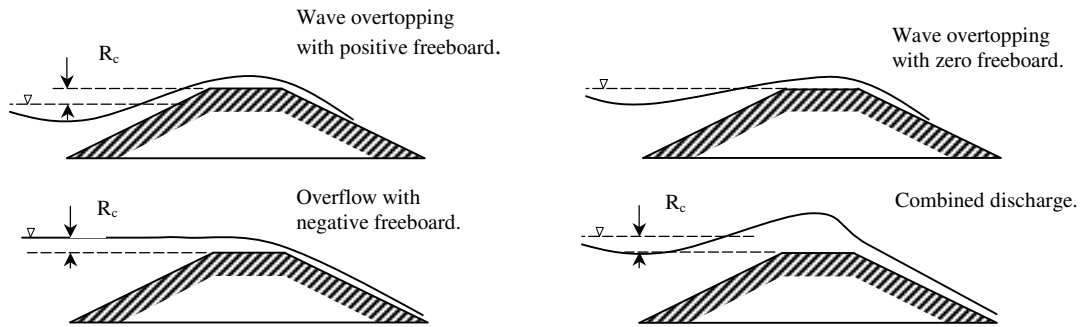


Fig. 1 Overflow (negative freeboard) and wave overtopping of embankments.

The crest elevation of embankments has historically been set by examination of local records or design formulae determined from physical models. For wave overtopping and run up on embankments with positive freeboard the formulae for predicting wave-overtopping rates are usually based on empirical equations based on hydraulic model data. For wave overtopping there exists extensive model data, (e.g. van der Meer, 2005), against which to validate models and for surge overflow of a wide defence without waves the situation can be well modelled as a broad crested weir. However, for combined discharge considerably less work has been conducted. Schuttrumpf and Oumeraci, (2005) developed equations to describe the flow during wave overtopping at zero freeboard, based on experimental laboratory data. One method developed to evaluate combined discharge is to sum the wave component derived using the equation developed by Schuttrumpf (2001) along with the surge component calculated using weir equations. More recently formulae have been derived that allow the combined discharge to be calculated directly. This work was conducted by Reeve et al., (2008) and was carried out in a numerical wave flume using a Reynolds-averaged Navier-Stokes based wave model (RANS). The formulae produced were tested against the results predicted by Schuttrumpf combined with the weir equations. At that point no hydraulic physical model data existed for combined wave and storm surge overtopping. More recently still, Hughes and Nadal, (2009) reported the results of a laboratory study of combined discharge over a broad-crested levee and produced design equations that predicted more modest overtopping than Reeve et al., (2008) had predicted.

As a validation exercise, this paper assesses the ability of a RANS model to directly reproduce, on a wave-by-wave basis, the tests conducted by Hughes and Nadal, (2009). The validated model is then used to determine combined discharge rates and the results are compared with that found with design formulae. The differences between the combined discharge rates found with the design formulae are investigated with view to providing design guidance. A validated numerical model for this situation will prove to be advantageous when compared to physical models because alternative embankment configurations, wave conditions and negative freeboards can be investigated more economically.

### Empirical Formulae

Currently, there are few design equations available for estimating combined discharge over embankments, and in this section some commonly used design formulae are presented.

$$Q = \frac{q_w}{\sqrt{g \cdot H_s^3}} = 0.038 \cdot \xi_{om} \quad \text{for } \xi_{om} < 2.0 \text{ Breaking waves}$$

$$Q = \frac{q_w}{\sqrt{g \cdot H_s^3}} = 0.096 - \frac{0.160}{\xi_{om}^3} \quad \text{for } \xi_{om} \geq 2.0 \text{ Non breaking waves}$$
(1)

Equations (1) were developed by Schuttrumpf, (2001) to determine overtopping discharge caused by waves overtopping at zero freeboard, where  $q_w$  is the mean overtopping discharge,  $H_s$  is the significant wave height and  $\xi$  is the Iribarren number. The equations are based on physical model studies for uniform smooth slopes between 1:3 and 1:6. To estimate the combined discharge, Pullen, (2007) superimposed the overtopping discharge for zero freeboard, with the overflow component caused by negative freeboard. The equations developed by Schuttrumpf were used to calculate the wave component, and the overflow component was calculated as a flow over a broad crested weir. Clearly this simple addition of the two components is a coarse approximation to reality and does not fully describe the complex hydrodynamic situation; it might however be expected to provide a reasonable first approximation to the problem. The equation used to determine mean flow over broad crested weirs is given in Chadwick and Morfett, (1998) as:

$$q = C_d \times 1.705bh^{3/2} \quad (2)$$

where  $b$  is the weir breadth,  $h$  is the upstream depth relative to the weir crest and the coefficient  $C_d$  is 1.0 for ideal fluids. For real fluids,  $C_d$  depends on the weir configuration and flow depth. Methods for determining  $C_d$  can be found in Ackers et al., (1978).

Mean combined discharge,  $q_{ws}$  can be directly calculated using Equations (3), which were developed by Reeve et al., (2008), where  $g$  is the acceleration due to gravity and  $\alpha$  is the slope of the embankment seaward face. The equations are based on regression analysis of validated numerical flume tests for irregular breaking and non breaking waves on seawalls with slopes 1:3, 1:4 and 1:6 and for the dimensionless parameter  $R_c / (H_s \xi_p)$  in the region  $0.0 > R_c / (H_s \xi_p) \geq -0.8$ .

$$Q = \frac{q_{ws}}{\sqrt{g \cdot H_s^3}} \cdot \frac{\sqrt{\tan \alpha}}{\xi_p} = 0.051 \exp\left(-1.98 \frac{R_c}{H_s \xi_p}\right) \quad \text{for } \xi_p < 2.0$$

$$Q = \frac{q_{ws}}{\sqrt{g \cdot H_s^3}} = 0.233 \exp\left(-1.29 \frac{R_c}{H_s}\right) \quad \text{for } \xi_p \geq 2.0$$
(3)

Hughes and Nadal, (2009) conducted physical model experiments on seawalls with a slope of 1:4.25 subjected to combined discharge. The tests were performed at a scale of 1:25 for negative freeboards,  $R_c$  of 0.29, 0.81 and 1.3m. Equation (4) is the given best-

fit equation, for irregular breaking and non-breaking waves and is determined from  $H_{m0}$ , the energy based significant wave height.

$$\frac{q_{ws}}{\sqrt{g.H_{m0}^3}} = 0.034 + 0.53 \left( \frac{-R_c}{H_{m0}} \right)^{1.58} \quad \text{for } R_c < 0 \quad (4)$$

It should be noted that although well established this range of predictors for discharge indicates a degree of uncertainty. For example, relationships inferred from computer models will be influenced by the assumptions inherent in the numerical model, while relationships derived from laboratory experiments will be subject to experimental error, scaling effects and so on.

Later in this paper, the mean overtopping discharge calculated with the RANS model is compared with that calculated with equations (3), (4) and the sum of the discharge calculated with Equations (1) and (2).

### **Numerical modelling**

There have been many attempts at numerical modelling of wave overtopping of coastal structures. The success of a numerical model depends on the equation and solution techniques used and how the model computes features such as turbulence and the free surface. Often, models that offer a more complete description of the flow dynamics require greater computational effort.

Modelling wave overtopping of structures has been conducted with numerical models based on the non-dispersive non-linear shallow water equations (NLSWE). These models are derived by vertically integrating the Navier–Stokes equation and prove to be computationally efficient. However, in order to satisfy the shallow water limit, the boundary has to be placed near the structure. Additionally, these models use a semi-empirical approach to estimate the initiation of wave breaking. Kobayashi and Wurjanto, (1989) used such a model that was capable of representing wave shoaling and reflection effects to calculate wave overtopping. Also, more recently, Hu et al., (2000) and Hubbard and Dodd, (2002) have used NLSWE models to investigate wave run up and overtopping of seawalls. Tuan and Oumeraci, (2010) used a NLSWE with an energy dissipation additional term to simulate individual overtopping events. The NLSWE derivation assumes that vertical accelerations are small and near vertical walls the NLSWE may not be valid. However, Hu and Meyer (2000) modelled vertical walls as steep slopes and demonstrated that the NLSWE can reasonably represent reflections for small amplitude waves in shallow water.

To improve the ability of a model at describing the complexities of flow that occur during wave overtopping, a model should be used that make no assumptions of the vertical flow structure. This allows improved flow description during wave breaking when vertical flow becomes significant, Lin (2008). One such model is the Smoothed Particle Hydrodynamics (SPH) model, which is a mesh-free Lagrangian method that has been successfully applied to wave overtopping of structures. The method divides the flow into discrete elements or particles, and the fluid flow is computed as the trajectories of particles, which interact according to the Navier–Stokes equations. This has the advantage that it is possible to track large free surface deformations, as well as fragmentation and coalescence of water. However, the accuracy of the SPH method depends on the number of particles represented, and for increased number of particles

the method becomes less efficient. This method has been used by a number of researchers to investigate wave overtopping. Gómez-Gesteira et al., (2005) used a two-dimensional SPH scheme to examine the overtopping of a flat plate. Gotoh et al., (2004) investigated regular wave overtopping over partially immersed breakwaters and overtopping of a vertical seawall was investigated by Gotoh et al., (2005). Dalrymple and Rogers, (2006) used SPH methods to investigate breaking waves on a beach but included some work on green water overtopping, defined as when a continuous sheet of water passes over the crest. Shao et al., (2006) used an SPH model to investigate the wave overtopping of a seawall and Lv et al., (2009) revisited this problem using a 3-D hybrid level set model coupled with the Volume of Fluid (VOF) surface-capturing scheme. To the authors' knowledge the SPH models have yet to be applied to combined discharge.

An alternative to the SPH model is the fixed mesh, Eulerian approach, based on the Navier–Stokes equations. This provides a more efficient alternative to the SPH model, although it remains computationally expensive in comparison with NLSWE methods. It has the advantage of providing a more complete description of flow and overcomes the limitations associated with using a particular wave theory. This type of model has the ability to calculate wave breaking by including a turbulence model and by considering the RANS equations. RANS models are often combined with a VOF surface-capturing scheme that allows the model to treat large free surface deformations. Numerous researchers have been working with this type of model, with applications that include wave breaking and overtopping. Lin and Liu, (1998) developed a two-dimensional RANS model based on a previous model called RIPPLE, Kothe et al., (1991). Numerous researchers have subsequently used this model or its variants to investigate surf zone dynamics. For example, Hsiao and Lin, (2009) used this model to investigate solitary waves overtopping of trapezoidal seawalls. However, there are a number of other RANS based models. Lara et al., (2008) and Losada et al., (2008) used an alternative RANS model to investigate wave run-up, transmission, wave overtopping and breaking on low-mound breakwaters. In this study a variant of the RANS-VOF model developed by Lin and Liu, (1998) is used and is briefly described below. Peng & Zou (2011) used a similar model to investigate the spatial distribution of wave overtopping water behind coastal structures

### **The present numerical model**

This study uses the RANS-VOF model to calculate the mean flow parameters such as free surface and general turbulent flow. The model has been coupled with a second-order  $k-\varepsilon$  turbulence closure model, where  $k$  is the turbulent kinetic energy and  $\varepsilon$  is the turbulence dissipation. The turbulent velocity and pressure is split into two parts the mean (ensemble averaged) velocity  $\langle u_i \rangle$  and pressure  $\langle p \rangle$  and the turbulent fluctuation components of velocity and pressure  $u_i'$  and  $p'$ . So that  $u_i = \langle u_i \rangle + u_i'$  and  $p = \langle p \rangle + p'$ . If these are substituted into the Navier-Stokes equations:

$$\frac{\partial u_i}{\partial x_i} = 0 \quad (5)$$

$$\frac{\partial u_i}{\partial t} + u_j \frac{\partial u_i}{\partial x_j} = -\frac{1}{\rho} \frac{\partial p}{\partial x_i} + g_i + \frac{1}{\rho} \frac{\partial \tau_{ij}}{\partial x_j} \quad (6)$$

and if the fluid is assumed to be incompressible then the Reynolds Averaged Navier-Stokes equations become:

$$\frac{\partial \langle u_i \rangle}{\partial x_i} = 0 \quad (7)$$

$$\frac{\partial \langle u_i \rangle}{\partial t} + \langle u_j \rangle \frac{\partial \langle u_i \rangle}{\partial x_j} = -\frac{1}{\rho} \frac{\partial \langle p \rangle}{\partial x_i} + g_i + \frac{1}{\rho} \frac{\partial \langle \tau_{ij} \rangle}{\partial x_j} - \frac{\partial \langle u_i' u_j' \rangle}{\partial x_j} \quad (8)$$

where the Reynolds stress is the product of the density and the correlation of the velocity fluctuation,  $\rho \langle u_i' u_j' \rangle$ ,  $\rho$  is the density and  $\tau_{ij}$  is the viscous stress.

Within the model the mean flow is governed by the Reynolds equations with a non-linear Reynolds stress model described in Shih et al., (1996). Further turbulence closure assumptions lead to a set of transport equations for  $k$  and  $\varepsilon$ . A detailed description of the turbulence closure model is given in Lin and Liu, (1998).

The usual boundary conditions are applied within the model. That is, if the mesh were small enough to resolve the viscous boundary layer then the no slip boundary condition would be applied. However, for these tests to be computationally efficient, the mesh used is not fine enough to resolve the boundary layer. In this case, a free-slip condition is more appropriate at a solid boundary and the turbulent field near the solid boundary is described using the log-law to find the distribution of mean tangential velocities within the boundary layer. This allows values of  $k$  and  $\varepsilon$  to be expressed as a function of distance from the solid boundary. Application of this condition is discussed later in this paper.

The wave surface profile is tracked using the volume of fluid method (VOF). The method was originally developed by Hirt and Nichols, (1981) and later modified by Kothe et al., (1991). This method defines a function  $F(x,y,t)$  that represents the fractional volume of fluid in a cell. When  $F$  is 1 the cell is completely filled with fluid and there is no water surface. When  $F$  is 0 the cell is empty and again there is no water surface. At values of  $F$  between 0 and 1 a free surface exists.

The original code developed by Lin and Liu, (1998) allowed a wave time history to be used to generate waves at the inflow boundary. However, in this study a version of the RANS model developed by Torres-Freyermuth, (2007) has been used. This improved the wave generating procedure by ensuring mass conservation and the absorption of reflected long waves. This wave generating procedure made this version of the RANS model particular suitable for this study because it allowed the wave records from physical model records to be successfully reproduced. It assumes that the high frequency energy is dissipated by the breaking waves at the embankment and the long wave components reflected from the shore propagate as non-dispersive waves, according to linear shallow water wave theory. At the inflow boundary it is assumed that linear superposition between incident and reflected waves is valid. In order to reproduce the required incident waves at the boundary, the model requires a time history file of surface elevations and velocity components at the boundary. The velocity component was derived from the surface elevations using linear theory. Further details of this wave generating procedure can be found in Torres-Freyermuth, (2007).

With a wave-overtopping model a system has to be devised to ensure that the overtopping discharge is recycled back into the flume, this ensures a constant mean water level. In physical models this is achieved with a pump that recirculates the

overtopping discharge back to the wave maker. To implement a similar result in the numerical model, the depth and velocity information at the crest of the embankment is used to determine the overtopping discharge. The discharge is then used as an input back into the model as a depth averaged velocity at the seaward boundary. This velocity is combined with the velocity determined for wave generation. However, if the instantaneous discharge is directly fed back into the wave-generating boundary, it effectively generates a false wave at the boundary. To overcome this problem, whilst still maintaining a conservation of mass, a moving average of the discharge at the crest of the embankment is calculated. This average discharge at the embankment crest is fed back in at the seaward boundary using a depth-averaged velocity. It will later be shown that the degree of success of the wave generating procedure is quite satisfactory.

The next section briefly describes the physical model laboratory study of combined discharge conducted by Hughes and Nadal, (2009). A number of these tests were reproduced with the RANS-VOF model and comparisons between various recorded and predicted parameters are made.

### Numerical and physical model set-up

#### Experimental data

The design equation for combined discharge over an embankment, developed by Hughes and Nadal, (2009), and is based on a series of physical model tests described by Hughes (2008). In this study the results from the physical model are compared with the RANS-VOF model simulations of the same tests. In this section the Hughes and Nadal physical model tests are briefly described.

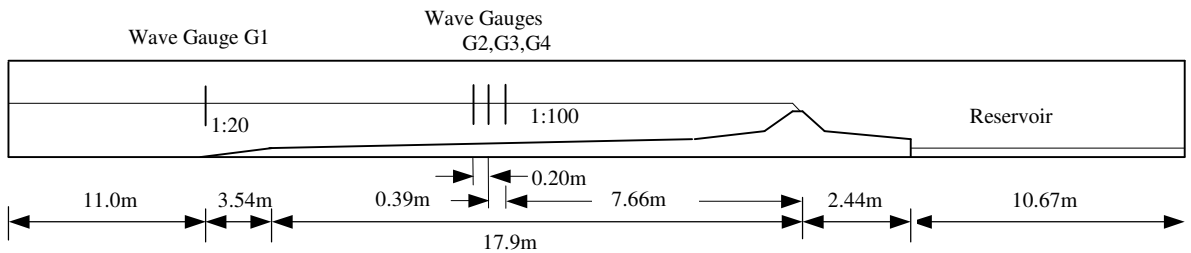


Fig. 2 General set-up of the embankment within the physical model flume, with model scale dimensions.

The tests were conducted at a scale of 1:25. Fig. 2 shows the general flume set-up and Fig. 3 gives the detail of a cross section through the embankment. Recirculation of the discharge over the crest was achieved in the physical model by pumping the water from the reservoir to a position near the wave generator. Adjusting the flow rate in the pump set the water depth in the model.

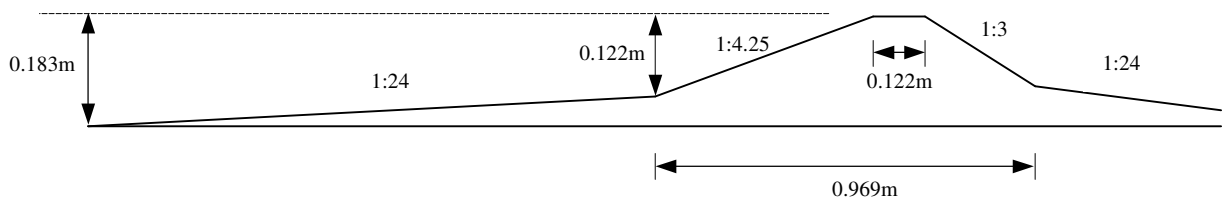


Fig. 3 Detail of the physical model embankment cross-section.

The model used four resistance type wave gauges, one near the wave generator, G1, and a three-gauge array G2, G3 and G4 on the 1:100 slope. Flow depths over the embankment crest and lee slope were recorded with pressure cells. The location of the pressure cells is given in Fig. 4. The horizontal flow velocity directly above P2 was

recorded with a laser Doppler velocimeter (LDV). The location of the LDV was adjusted for each test so that the velocity was always recorded at half of the flow depth. In order to determine an appropriate flow depth level the model was run without waves for an initial period at the start of each test.

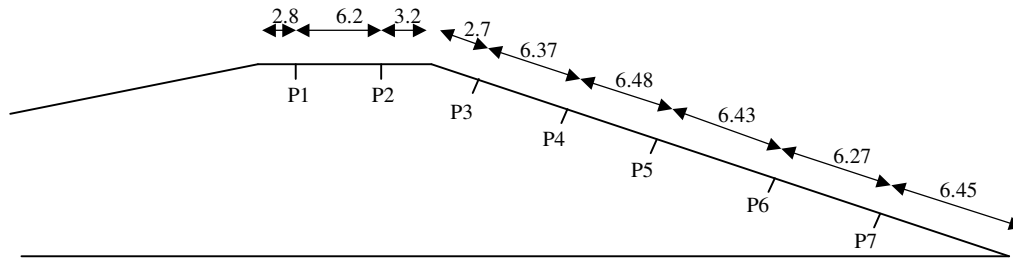


Fig. 4 Location of pressure cell on the physical model embankment, dimensions in cm.

The test programme investigated storm surge levels of 0.29, 0.81 and 1.3m above the embankment crest. Each storm surge level was tested for three wave heights and three wave periods. This gave a total of 27 tests.

Wide embankments, when subjected to overflow, act similarly to a broad crested weir, with flow at the crest progressing from sub critical flow near the seaward boundary to critical and then supercritical flow on the lee side. Consequently, the flow depth on the embankment crest will vary with location across the crest. The steady discharge for this period was determined during the initial period of the test without waves, with the flow depth and velocity information at being recorded at P2. The surge level was then determined from the broad crested weir equation, Equation (2) with  $C_d = 1.0$  and the flow depth being equivalent to  $h$ . This allowed the upstream surge level to be estimated from the measured discharge. This surge level would be more useful to designers than a depth at the weir because it corresponds to the surge level calculated from tide and meteorological conditions. A surge level recorded at the embankment crest would be subject to the drawdown that occurs near weirs.

### Numerical model set-up

For this paper the RANS-VOF model has been used to simulate the tests conducted at the 1.3m surge level by Hughes and Nadal, (2009). The table below give a list of the wave conditions tested.

<i>Test Number</i>	$H_{m0}$ <i>m</i>	$T_p$ <i>s</i>	$\xi_p$
1	0.64	6.07	2.1
2	1.17	6.07	1.6
3	2.30	6.07	1.2
4	0.86	10.12	3.3
5	1.79	10.12	2.4
6	2.74	10.12	1.8
7	0.74	14.37	5.0
8	1.50	14.37	3.5
9	2.31	14.37	2.8

Table 1 Wave conditions tested and Iribarren number, prototype units

To be computationally efficient, the numerical model represented only part of the physical model flume. The seaward limit was defined as being at the wave gauge 2, G2, location, as shown in Fig. 2. This allowed the input signal for the RANS-VOF model to be taken from the physical model wave gauge, G2. The landward boundary of the numerical model was defined on the lee side slope of the embankment. This boundary was defined as being an open boundary, so allowing waves to exit the flume without reflection. Fig. 5 shows the extent of the numerical model.

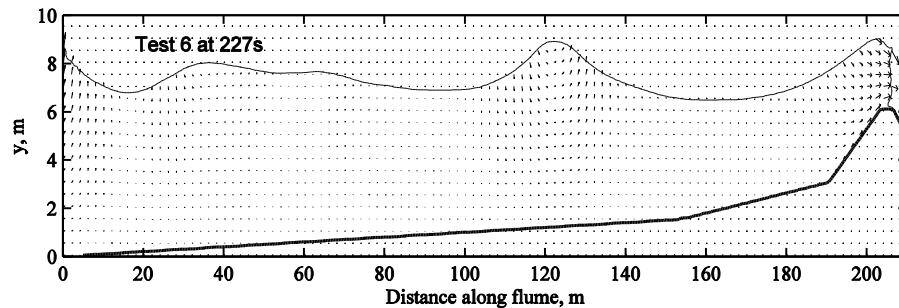


Fig. 5 A snap shot showing wave surface elevation, embankment detail and flow field velocity vectors plotted at every fifth node vertically and every tenth node horizontally, prototype dimensions.

The mesh size had to be small enough to resolve the supercritical flow on the landward side of the embankment and define flow during wave breaking. To achieve this a mesh size for all tests was 0.4m in the horizontal direction and 0.1m in the vertical direction. This gave a total of 58600 grid points. To ensure the mesh size was small enough to adequately define the flow, a test was conducted to verify the calculated flow was independent of the mesh size. Test 2 was repeated with a 50% reduction in mesh size in both directions. This causes a four-fold increase in the number of nodes points and a similar increase in run time. The average combined discharge recorded for the finer mesh was 3.4% lower than with the coarse mesh. The coarser mesh was accepted as giving sufficient resolution whilst providing satisfactory computational efficiency. The duration of the RANS-VOF model tests was 250s, with approximately 100s of steady overflow with no waves, followed by 150s of combined discharge. To be consistent with the physical model, the overflow discharge calculated for this initial period was used to determine the upstream head above the weir level using Equation (2). When waves had established at the embankment, the combined discharge was calculated at P2 from the calculated velocity and depth information. The time step used for all tests was 0.01s.

## Comparison between RANS-VOF model and physical model results

### Wave generation

In order to verify that the waves generated within the numerical model are comparable with the physical model, it is useful to compare waves recorded at wave gauge G4 in the physical model with those in the equivalent position in the RANS-VOF model. As G4 is only 14.9m away from the numerical model wave-generating boundary, and little wave transformation will have occurred, this is a good test of the wave-generating boundary condition. Time histories of wave generated in the numerical and physical model are shown in Fig. 6 for a representative sample of tests. The tests shown were selected to show each of the wave periods and wave heights. The average absolute difference between the wave elevation found with the numerical and physical model, for all tests, was 0.070m. This demonstrates that there is no build-up of unwanted long wave

reflections, and that the assumption inherent within wave generating boundary, that breaking waves dissipated high frequency energy, is valid.

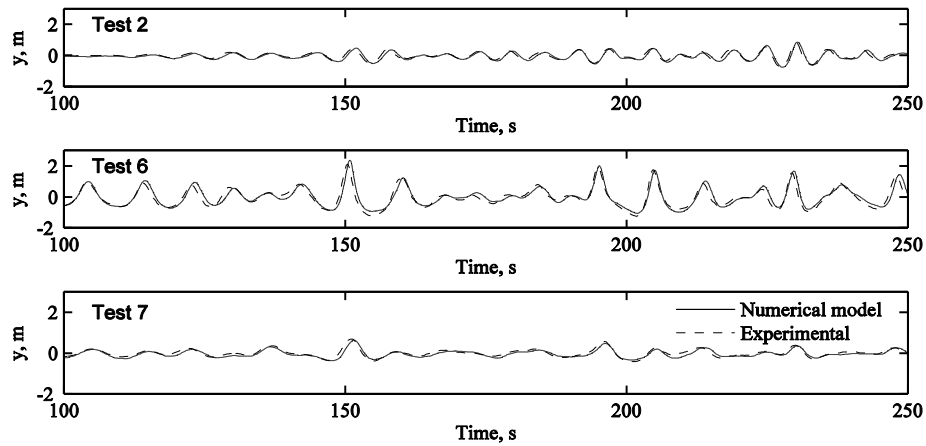


Fig. 6 Wave time histories at G4, prototype dimensions.

### Discharge

The discharge at the crest of the embankment was determined from the flow depth and velocity. In the physical model the LDV recorded the velocity at half depth. Whilst in the numerical model, the velocity information is available at each cell node, this allows the discharge through each cell to be determined. The total flow over the crest was calculated as the sum of the flow through the cells above the location of P2. The calculated average discharge during the steady overflow ( $q_s$ ) and combined discharge ( $q_{ws}$ ) parts of the tests were averaged over the same time period in the physical model and RANS-VOF tests to ensure equivalence. The start time for the averaging period for  $q_{ws}$  began when the waves had reached the embankment and were established.

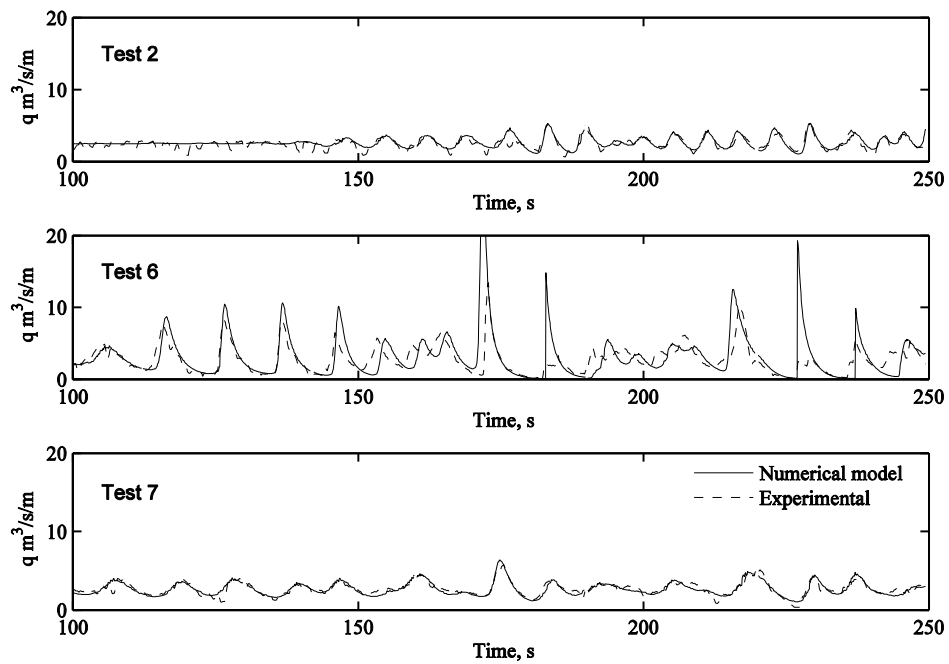


Fig. 7 Discharge time histories at P2, prototype dimensions.

The time histories of discharge measured in the physical and numerical model is shown in Fig. 7. As a measure of the agreement or difference between the models the relative error is used, this is defined as  $(q_{\text{prot}} - q_{\text{model}})/q_{\text{proto}}$ . Table 2 gives the test details, average discharge rates and relative errors. It can be seen that generally the models compare well, however there is an increase in  $q_{ws}$  relative error for the tests with larger wave heights. The average absolute value of the  $q_{ws}$  relative error for the lower wave heights tested (Tests 1,4, and 7) is 1.87%. At the larger wave heights (Tests 3, 6 and 9) the average  $q_{ws}$  relative error is +8.3%.

Test	$H_{m0}$	$T_p$	$\xi_p$	Physical Model		RANS-VOF		$q_s$ relative error (%)	$q_{ws}$ relative error (%)
	m	s		$q_s$ ( $m^3/s/m$ )	$q_{ws}$ ( $m^3/s/m$ )	$q_s$ ( $m^3/s/m$ )	$q_{ws}$ ( $m^3/s/m$ )		
1	0.64	6.07	2.1	2.53	2.62	2.56	2.68	1.27	2.06
2	1.17	6.07	1.6	2.46	2.59	2.49	2.63	1.26	1.82
3	2.30	6.07	1.2	2.40	2.72	2.43	2.94	0.96	8.25
4	0.86	10.12	3.3	2.63	2.68	2.53	2.62	-3.99	-2.13
5	1.79	10.12	2.4	2.53	2.67	2.53	2.78	-0.24	4.20
6	2.74	10.12	1.8	2.70	2.71	2.56	2.98	-5.07	9.96
7	0.74	14.37	5.0	2.57	2.66	2.54	2.63	-0.93	-1.43
8	1.50	14.37	3.5	2.51	2.57	2.40	2.73	-4.23	6.43
9	2.31	14.37	2.8	2.53	2.75	2.50	2.94	-1.30	6.83

Table 2 Comparison of numerical model and physical model average discharge rates.

It might also be thought that the  $q_{ws}$  relative error would depend on the nature of the wave breaking. The average  $q_{ws}$  relative error for Iribarren numbers,  $\xi_p$ , less than two, indicating plunging waves, was 6.8% and for  $\xi_p$  greater than two, surging waves, the  $q_{ws}$  average relative error was 3.8%. However, the strongest trend was shown to be between wave height and  $q_{ws}$  relative error. This can be seen in Fig. 8, which shows strong positive correlation, between wave height and  $q_{ws}$  relative error, and poor correlation between  $\xi_p$  and  $q_{ws}$  relative error.

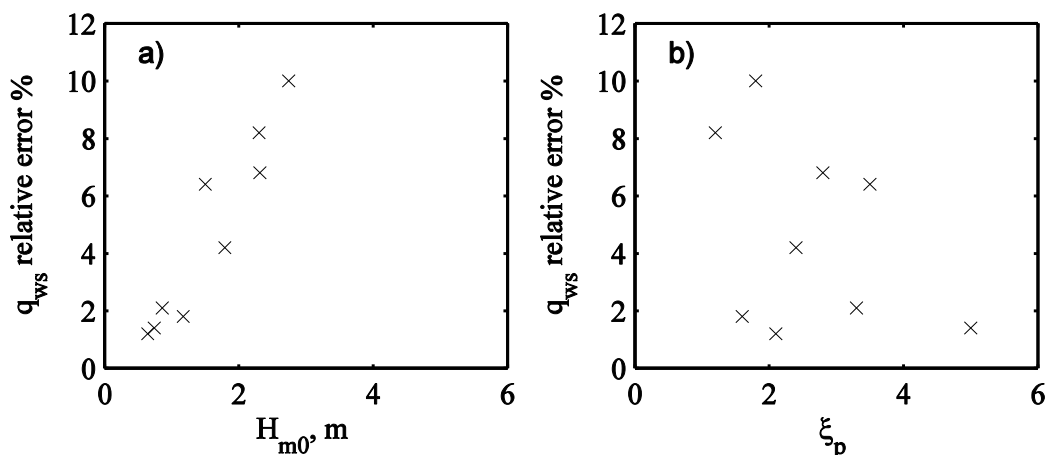


Fig. 8 Correlation between a) wave height and absolute relative error and b) Iribarren number and absolute relative error.

Fig. 7 shows that generally the agreement between the physical and numerical model is satisfactory, but the numerical model has slightly larger peaks, particularly at the larger wave height (Test 6). It also shows a slight phase shift for some of the peaks and a couple of peaks where the numerical model grossly over-predicts relative to the

measured experimental values. This could be a result of differences in either the surge depth or velocity measurement or both. To investigate this further a comparison of time histories of surge depth and velocity in each model has been performed.

### Flow depth

The time histories of water depth at P2 on the embankment crest for Test 2,6 and 7 are shown in Fig. 9. The agreement is very good for the smaller wave heights but, for some of the waves in the larger wave test, (Test 6) the peaks in the RANS-VOF model are too high. The phase shift is limited to a few of the larger peaks. The two discharge peaks at about 185 and 230s in Fig. 7, which were too high in the RANS-VOF model, show a more favourable agreement for water depth, but with the RANS-VOF model peak still being higher than those in the physical model.

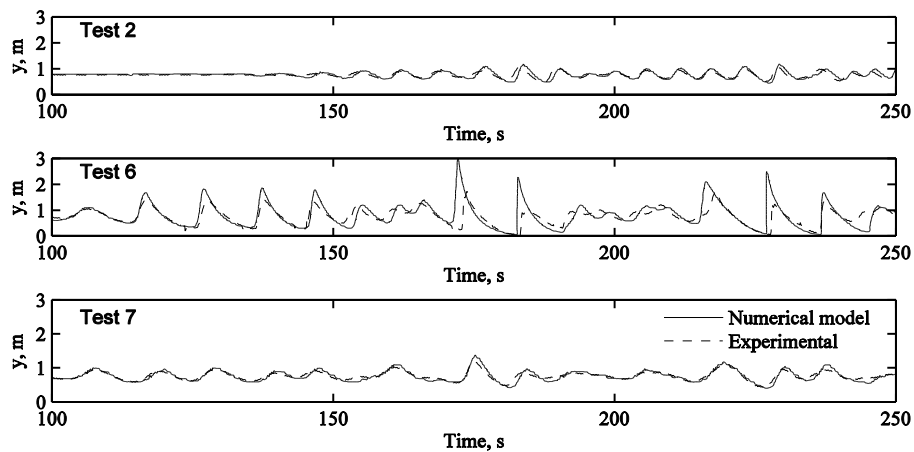


Fig. 9 Flow depth time histories at P2, prototype dimensions.

### Velocity

The time histories of velocities at the crest of the embankment are shown in Fig. 10 and show the physical model velocity time history contains some spikes. This caused the variability in the discharges shown in Fig. 7, particularly for Test 2.

For all tests, the peak velocities recorded in the physical model are generally higher than those recorded in the RANS-VOF model. The velocity record for Test 6 shows that when the water level fell below the level of the LDV in the physical model the recorded velocities remained uniform during this period. On occasion, there appears to be a time lag between the water level rising above the LDV and the LDV correctly recording velocities. This has affected the two largest velocity peaks at approximately 185s and 230s in the record. Each of these peaks has flat periods that extend onto the next peak and have significantly reduced the following peaks. These under-predictions of velocities correspond to the under-prediction of discharge, and are the two peaks that appear as over-predictions in the RANS-VOF model in Fig. 7.

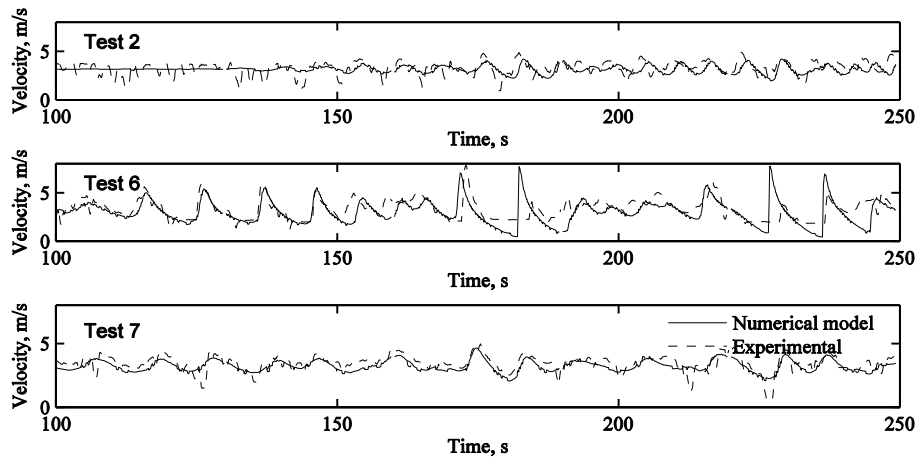


Fig. 10 Velocity time histories at P2, prototype dimensions.

### Discussions

The average combined discharge relative error is 5.9% and is considered to be acceptable. However, for larger wave heights the discrepancies between the predictions tend to increase. The discrepancies could be due to the assumptions made within the RANS-VOF model or physical model scale effects and modelling methodology or possibly a combination of both. In this section the differences between the computational and physical model results are discussed.

Consideration of the physical model velocity record has shown that some significant peaks have been missed following the water level falling below the LDV. During this time the LDV records a uniform value of the last value recorded, the LDV should begin to record again when the water level rises above the instrument. An analysis of the depth and velocity record shows a time delay from the water level rising above the LDV and when the LDV begins to record data. This has occasionally resulted in the next peak not being recorded and subsequently the next discharge peak being under-represented.

A comparison of flow depth at the embankment crest shows good agreement between the RANS-VOF model and physical model for all but the peaks of the largest waves. However the peaks are larger in the RANS-VOF model than in the physical model. This difference could be due to RANS-VOF model not correctly describing the flow conditions during wave peaks at the embankment crest. The free surface profile of a typical peak wave is shown in Fig. 11 and shows that, for some tests, the wave is clearly breaking at the embankment crest.

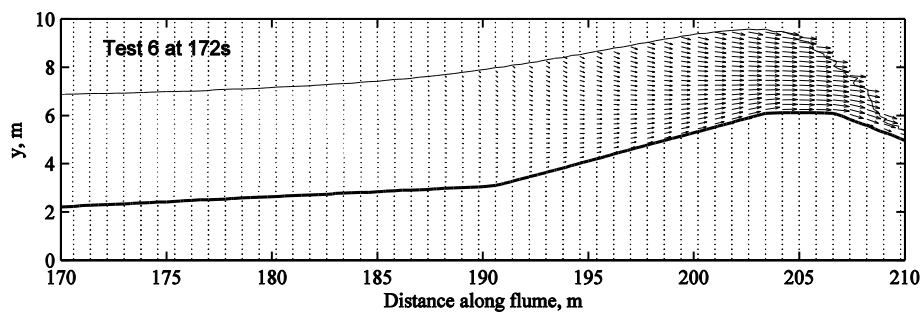


Fig. 11 Free surface profile, embankment profile and velocity vectors plotted at alternate nodes.

Lin and Liu, (1998) validated the RANS-VOF model against laboratory data, for a cnoidal wave breaking on a sloping beach. Although the hydrodynamics of a wave breaking on a sloping beach will be different to a wave breaking on the top of an embankment with combined overflow, it is useful to consider how the RANS-VOF model performs near a breaking wave. For these tests it was found that nearer to the breaking point, the crests measured in the numerical model were lower than the laboratory data and the velocities were higher. This is the opposite of that found in the current study. It was found that nearer to the breaking point turbulence intensity was over-estimated and quite different to the measurements. The lower crest elevations were a result of the excessive estimated turbulence intensity. Further from the breaker point the RANS-VOF model more accurately represented the turbulence intensity and consequently the water surface elevation was also better represented. The poorer representation of the turbulence intensity near the breaker point was caused by the model not accurately predicting the initiation of turbulence in the initial stages of wave breaking, where a rapidly distorted shear flow region exists. The uncertainties in the initial turbulent conditions, at the initiation of breaking, make it difficult to predict the location of the breaking point. As already stated, the turbulence closure model used in the RANS-VOF model describes the velocity profile in a steady, uniform, turbulent boundary layer, which is clearly not the situation in a breaking wave.

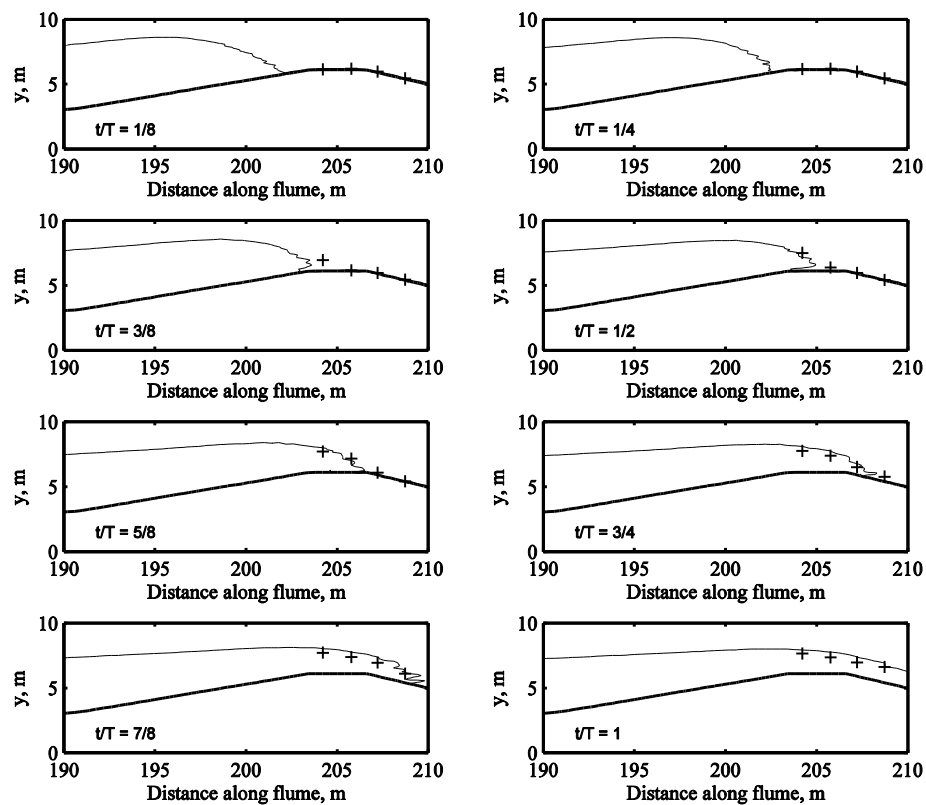


Fig. 12 Embankment profile, RANS-VOF calculated free surface (dotted line) and measured free surface at P1, P2, P3 and P4 (crosses) for Test 6, during one wave period starting at 236s.

Wave breaking was seen to occur at the crest of the embankment at or near to P2. This is the point at which the velocities and depths were recorded in the physical model and this location is clearly a region of great flux. Small changes in the computed location of the breaker point will significantly alter the calculated depth at P2. Although it is not possible to compare discharges or velocities at locations other than P2, it is possible to compare the flow depths because pressure gauges were provided at the locations shown

in Fig. 4. The measured and calculated free surface profiles are shown in Fig. 12 for various stages during wave breaking. This is for one of the larger waves in Test 6 and demonstrates that the embankment crest dries for short periods. The figure shows acceptable agreement between the RANS-VOF model and physical model. However, at the point when the wave breaks the agreement is not as favourable. This is in agreement with the depth time histories shown in Fig. 9, with the depths for the highest waves being over-predicted within the RANS-VOF model. Fig. 12 confirms that the over prediction is not localised to P2. However, as the wave is breaking very near P2 and small errors in the calculation of the breaker location will have a large effect on the depth of flow at this point in the numerical model.

### Model comparison against design formulae

In this section the discharge calculated with the RANS-VOF model is compared with three different design formulae. To determine the negative freeboard,  $R_c$  to use in the design equations, the procedure was the same as that adopted by Hughes and Nadal, (2009). This determined the overflow discharge at the start of each test and used Equation (2) with a  $C_d$  of 1.0 to calculate the equivalent upstream head above the weir crest. This value of  $R_c$  was then used to estimate combined discharge using the available design equations. The comparison is shown in Fig. 13 and this figure is comparable with Fig. 7 in Hughes and Nadal, (2009).

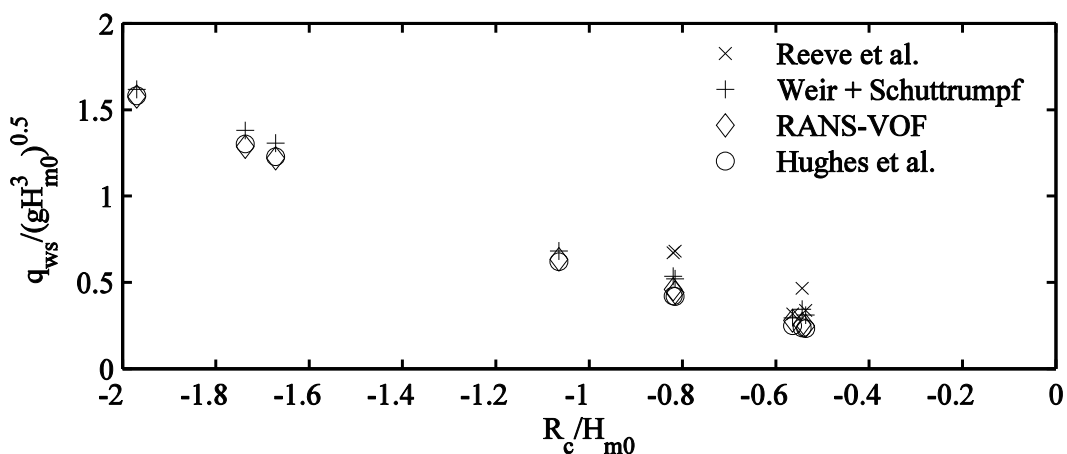


Fig. 13 Dimensionless discharge and dimensionless negative freeboard from the design formulae and the RANS-VOF model.

Fig. 13 compares the dimensionless combined discharge calculated with each of the design formulae and with the RANS-VOF model. The dimensionless combined discharge calculated with the RANS-VOF model compares very well with that predicted by Equations (1) and (2) and Equation (4). Which on average differ from the RANS-VOF results by +9.2% and -1.7% respectively. The range of applicability of Equation (3) is for small negative freeboards in the region  $0 > R_c / H_s > -1.0$ . A number of the tests conducted in this series of tests were outside of this range of applicability and this data has been excluded from Fig. 13. The remaining data shows an average 46% overestimation of the dimensionless combined discharge when compared with the RANS-VOF results.

However, this analysis presents some difficulties. The steady discharge at the start of the test has been used to calculate an estimate of  $R_c$  rather than a direct measurement. Additionally, Equation (2) is used to calculate the combined discharge with Equation

(1). However, Equation (2) is for a broad crested weir defined with rectangular cross-section and sharp edges and using a value of  $C_d$  of 1.0 assumes ideal flow.

ISO 3846:2008 is the international standard for flow over broad crested weirs. It recommends that the upstream head readings should be recorded at a distance of between 3 and 4 times the maximum head on the weir. This allows a measurement of head that is a sufficient distance upstream to avoid the draw down that occurs near the weir and is close enough to the weir for the energy loss between the measurement location and the weir to be negligible. The flow depth at this location can readily be determined from the data provided in the RANS-VOF model tests. The value of  $R_c$  determined this way was on average 6.0% lower.

The equation for discharge over a broad crested weir, Equation (2), is applicable to a particular geometry. That is a rectangular weir, where the upstream face forms a sharp right angle corner at its intersection with the crest. Any rounding of the edges causes the discharge coefficient,  $C_d$ , to increase significantly. For the embankment used in this study the upstream face has a 1:4.25 slope and is likely to increase discharge in a similar way to having a rounded edge. Non-standard weirs require a calibration exercise, and this has been conducted using the RANS-VOF model. To determine the weir characteristics a graph of measured values of  $q_s$  and  $R_c^{3/2}$  is given in Fig. 14. The regression line has a coefficient of determination,  $r^2$  of 0.999, and the equation of the regression line is the same as Equation (2) with the value of  $C_d$  calculated to be 1.126.

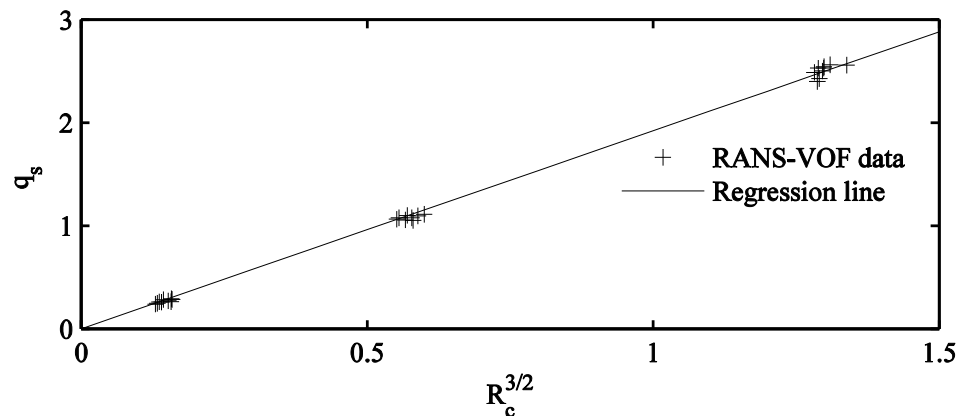


Fig. 14 Embankment steady discharge,  $q_s$  and  $R_c$  calculated at a location in accordance with ISO 3846:2008.

The value of  $R_c$  calculated in accordance with ISO 3846:2008, was used to recalculate the combined discharge over the embankment from Equations (3) and (4). The combined discharge was also calculated using Equation (1) combined with Equation (2) with the value of  $C_d$  of 1.126. Fig. 15 shows the dimensionless discharge and dimensionless freeboard for these equations along with the values calculated with the RANS-VOF model.

Fig. 13 and Fig. 15 show that the dimensionless combined discharge is sensitive to the method of evaluating  $R_c$ . Although the combined discharge calculated with the RANS-VOF model has not changed, the method used to calculate  $R_c$  has changed. The dimensionless combined discharge calculated from Hughes and Nadal, (2009), Equations (4), gives 13.3% lower values than computed with the RANS-VOF model because of the lower value of  $R_c$ . Also, the over estimation in dimensionless discharge found with Equation (3) was found to be 24.1% higher than that determined with the RANS-VOF model. Although the wave component of the overtopping discharge calculated with Equations (1) has remained the same, the weir overflow component

calculated with Equation (2) has increased significantly as a result of the different value for  $C_d$ . This has increased the combined total and given a combined discharge that is 8.6% above the RANS-VOF results. Overall the results calculated with the RANS-VOF model fall between the results expected from the equations provided by Reeve et al., (2008) and Hughes and Nadal, (2009) and are marginally lower than the dimensionless combined discharge found by combining the modified weir equation and the equation provided by Schuttrumpf, (2001).

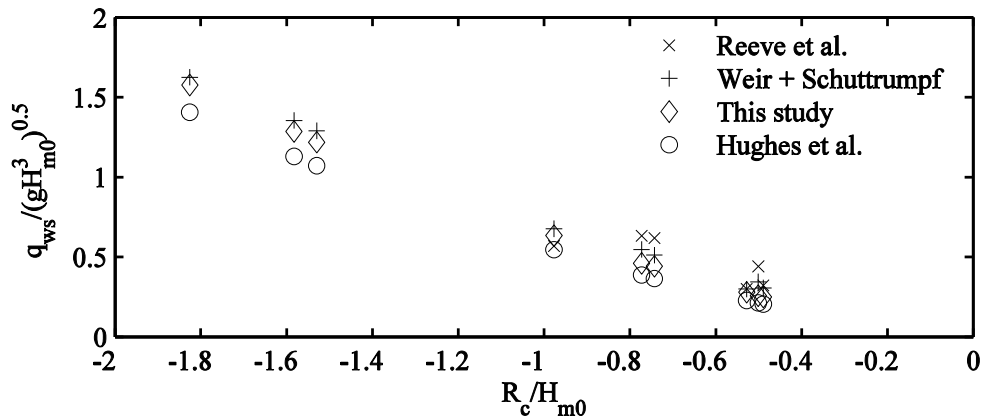


Fig. 15 Dimensionless discharge and dimensionless negative freeboard for the RANS-VOF test and calculated values based on  $R_c$  evaluated in accordance with ISO 3846:2008 and a  $C_d$  value of 1.126.

The cause for the increase in combined discharge calculated with Equation (3) is most likely the model set up. Reeve et al., (2008) used a sloping embankment retained by a relatively thin crest width. The thin crest width would act more like a thin plate weir than a broad crested weir and would result in a greater predicted discharge.

### Conclusion

The RANS-VOF model has been used to directly reproduce the physical model tests of combined discharge over an embankment, conducted by Hughes and Nadal, (2009). The wave time histories recorded in the physical model were reproduced in the numerical model. This allowed a wave-by-wave comparison of values such as combined discharge. The combined discharge calculated with the RANS-VOF model, for smaller and mid-sized waves was found to be within 2% of that measured with the physical model. For larger waves the RANS-VOF model over-predicted the combined discharge, (on average by 8%).

The difference between the combined discharge found with the physical and numerical models can be partially accounted for by the differences in the recorded velocities. The RANS-VOF model provided velocity information at each node whilst the physical model recorded a mid-depth velocity, from which the velocity had to be inferred when the water level dropped below the LDV. Occasionally the LDV did not respond immediately when the water level had increased beyond mid-depth, causing the velocity from the following wave crest to be missed. Also, an increase in flow depth at the embankment crest found with the RANS-VOF model is hypothesised to be caused by a poorer representation of turbulence intensity near the breaking point, leading to errors calculating the location of the breaker point, causing inaccuracies in the calculated flow depth. The current RANS turbulence model describes flow in a steady, uniform, turbulent boundary layer, which is not the situation in a breaking wave. To improve the flow description during breaking will require the development of a better description of turbulence within the RANS model.

One of the objectives of this study was to investigate the differences in the combined discharge predicted with the current design equations, as identified by Hughes and Hadal, (2009). The combined discharge calculated with the RANS-VOF model was compared to that found with Equations (3) and (4) and Equation (1) combined with broad crested weir equation (2). The level of agreement was found to depend upon the method used to determine the negative freeboard,  $R_c$ . The most appropriate method was found to be in accordance with ISO3846:2008. Additionally, the overflow component found with Equation (2) was dependent upon the value of  $C_d$  used. A calibration exercise was conducted to determine a more appropriate value for  $C_d$  for the trapezoidal embankment studied, and was found to be 1.126. The comparison between the calculated combined discharge found with the RANS-VOF model and existing design formulae for combined discharge over embankments found that the combined discharge calculated with the numerical model fell between that found by Reeve et al., (2008) and Hughes and Nadal, (2009). The combined discharge found by combining the modified weir equation and the equation from Schuttrumpf, (2001) was marginally above that found with the numerical model. Some of the tests conducted in this study were outside the range of applicability of Equation (3). Those tests within the range showed that Equation (3) predicted higher discharge rates. It is most likely due to the different embankment shape used by Reeve et al. (2008).

This study has demonstrated the current design formulae for combined discharge should be used within the constraints of structure configuration, water level and wave conditions for which the equations were tested. In particular, the equation developed by Reeve et al., (2008) is applicable for a relatively thin seawall with a 1:4 seaward slope. The equation given by Hughes and Nadal, (2009) is for the embankment configuration shown in Fig. 3 but this equation predicts lower combined discharge than that found with either the RANS model or Equation (1) combined with broad crested weir Equation (2). Additionally, when using the above equations, the negative freeboard should be determined in accordance with ISO3846:2008. Also, for embankments, the value of  $C_d$  used in Equation 2 differs from the values given for broad crested weirs and needs to be determined for each embankment configuration experimentally.

The design equations considered in this paper for combined discharge are based on studies for embankments of simple design and for a limited range of slopes. For a fuller understanding a range of different design configuration needs to be investigated. Within the constraints noted earlier, the validated model is a useful and efficient design tool, which can be used to investigate different embankment and sea wall design variations such as the slope of the seaward and lee face and berm configurations. Further, it provides the means to estimate combined discharge rates and volumes that may occur over coastal flood defences. As suggested in the introduction, this situation is anticipated to become increasingly important should sea level rise predictions come to be. Existing defences designed without the benefit of the latest climate change predictions are likely to offer diminishing levels of service. Policy and engineering decisions will then have to be made to raise the standard of the defence or to accept a greater frequency and volume of inundation.

**List of symbols**

b	weir crest width [m]
$C_d$	coefficient [-]
g	acceleration due to gravity [m/s <sup>2</sup> ]
h	upstream head above weir [m]
$H_{m0}$	energy based significant wave height [m]
$H_s$	significant wave height [m]
k	turbulent kinetic energy [Nm]
L	weir crest length [m]
q	mean overtopping discharge [m <sup>3</sup> /s/m]
$q_s$	mean steady overflow discharge, surge component [m <sup>3</sup> /s/m]
$q_w$	mean wave overtopping discharge [m <sup>3</sup> /s/m]
$q_{ws}$	mean combined discharge, surge and wave component [m <sup>3</sup> /s/m]
p	pressure [Nm <sup>-2</sup> ]
r	roughness [m]
R	dimensionless freeboard [-] $R = R_c / H_{m0}$
$R_c$	crest freeboard [m]
t	time [s]
T	wave period [s]
u	velocity [ms <sup>-1</sup> ]
x	horizontal distance [m]
y	vertical distance [m]
z	vertical coordinate measure from the bed [m]
$\alpha$	slope of embankment seaward face [-]
$\varepsilon$	turbulence dissipation [Nm]
$\lambda_o$	deepwater wave length based on the peak spectral wave period [m]
$\lambda_{om}$	deepwater wave length based on the mean spectral wave period [m]
$\rho$	density [kg/m <sup>3</sup> ]
$\sigma$	coefficient
$\tau$	viscous stress
$\xi_{om}$	surf similarity parameter (Iribarren number) defined as $\xi_{om} = \frac{\tan \alpha}{\sqrt{H_{m0} \lambda_{om}}}$
$\xi_p$	surf similarity parameter (Iribarren number) defined as $\xi_p = \frac{\tan \alpha}{\sqrt{H_s \lambda_p}}$

Other symbols are defined in the text.

**Acknowledgements**

We wish to thank Professor Pengzhi Lin of Sichuan University, China for providing the original version of the RANS-VOF model and Dr Alec Torres Freyermuth for providing the modified version of the wave generator subroutine. We also wish to thank Professor Steven Hughes of the US Army Corps of Engineers for providing the data from the Levee overtopping study. David Jones acknowledges the support of a scholarship provided by Britannia Royal Naval College and Plymouth University. Dr Qingping Zou and Prof Dominic Reeve acknowledge support from the Flood Risk from Extreme Events (FREE) Programme of the UK Natural Environmental Research Council (NERC) (NE/E0002129/1). Prof Dominic reeve also acknowledges the support of the UK Engineering and physical Sciences Research Council through the Flood Risk Management Research Consortium (GR/576304/01). Dr. Zou would like to acknowledge the support of the start-up fund by University of Maine.

## References

- Ackers, P., White, W. R., Perkins, J. A., Harrison, A. J. M., 1978. Weirs and Flumes for flow Measurement, Wiley, Chichester.
- Chadwick, A., Morfett, J., 1998. Hydraulics in Civil and Environmental Engineering Second Edition. E & FN SPON, London.
- Dalrymple, R. A., Rogers, B.D., 2006. Numerical modeling of water waves with the SPH method. Coastal Engineering, 53, pp141-147.
- Gotoh, H., Ikari, H., Memita, T., Sakai, T., 2005. Lagrangian particle method for simulation of wave overtopping on a vertical seawall. Coastal Engineering Journal, 47, pp.157-181.
- Gotoh, H., Shao, S., Memita, T., 2004. SPH-LES Model for numerical investigation of wave interaction with partially immersed breakwater. Coastal Engineering Journal, 46, pp.39-63.
- Gómez-Gesteira, M., Cerqueiro, D., Crespo, C., Dalrymple, R.A., 2005. Green water overtopping analyzed with a SPH model. Ocean Engineering, 32, pp.223-238.
- Hirt, C. W., Nichols, B. D., 1981. Volume of fluid (VOF) method for dynamics of free boundaries. J. Comput. Phys. 39, pp.201-225.
- Hsiao, S., Lin, T., 2009. Tsunami-like solitary waves impinging and overtopping an impermeable seawall: Experiment and RANS modeling, Coastal Engineering 57, pp.-18.
- Hu, K., Meyer, D., 2005. The Validity of the Non-linear Shallow Water Equations for Modelling Wave Runup and Reflection. In, Coastlines, Structures and Breakwaters. Telford, Thomas Limited, London
- Hu, K., Mingham, C.G., Causon, D.M., 2000. Numerical simulation of wave overtopping of coastal structure using the non-linear shallow water equation. Coastal Engineering 41, pp.433-465.
- Hubbard, M., Dodd, N., 2002. A 2D numerical model of wave run-up and overtopping. Coastal Engineering 47, pp.1-26.
- Hughes, S. A. 2008. Combined wave and surge overtopping of levees: Flow hydrodynamics and articulated concrete mat stability. Technical Rep. No ERDC/CHL TR-08-10, U.S. Army Engineering Research and Development Center, Vicksburg, Miss.
- Hughes, S.A., Nadal, N.C., 2009. Laboratory study of combined wave overtopping and storm surge overflow of a levee. Coastal Engineering 56, pp.244-259.
- ISO 3846:2008 Hydrometry. Open channel flow measurement using rectangular broad-crested weirs.
- Kobayashi, N., Wurjanto, A., 1989. Wave Overtopping on Coastal Structures. J. Waterway, Port, Coastal, and Ocean Engineering 115 (2), pp.235-251.
- Kothe, D.B., Mjolsness, R.C., Torrey, M.D., 1991. RIPPLE: a computer program for incompressible flows with free surfaces. Report LA-12007-MS, Los Alamos Scientific Report, Los Alamos, NM, USA
- Lara, J.L., Losada, I.J., Guanche, R., 2008. Wave interaction with low-mound breakwaters using a RANS model. Ocean Engineering, 35, Issue 13, pp.1388-1400.
- Lin, P., 2008. Numerical modeling of water waves. Routledge. E & FN SPON.
- Lin, P., Liu, P.L.-F., 1998. A numerical study of breaking waves in the surf zone. J. Fluid Mechanics 359, pp.239-264.
- Lin, P., Liu, P.L.-F., 1999. Internal wave-maker for Navier-Stokes equations models. J. Waterway, Port, Coastal, and Ocean Engineering 125 (4), pp.207-215.
- Liu, Y., Guo, X., Wang, B., Liu, H., 2007. Numerical simulation of wave overtopping over seawalls using the RANS equations. J. Hydrodynamics 06.
- Losada, I.J., Lara, J.L., Guanche, R., Gonzalez-Ondina, J. M., 2008. Numerical analysis of wave overtopping of rubble mound breakwaters. Coastal Engineering, 55, pp.47-62.
- Lv, X., Zou, Q.-P., Reeve, D., 2009. A Hybrid LS and VOF Method for 3-D Simulation of Wave Breaking and Overtopping. Intl. J. Offshore and Polar Engineering Vol. 4 No. 4, pp.1-9.
- Peng, Z. & Q.-P. Zou, 2011: Spatial distribution of wave overtopping water behind coastal structures, Coastal Engineering, Vol 58, Issue 6, June 2011, Pages 489-498, (doi: 10.1016/j.coastaleng. 2011.01.010)
- Pullen, T., Allsop, N.W.H., Bruce, T., Kortenhaus, A., Schüttrumpf, H., van der Meer, J.W., 2007. EurOtop: Wave overtopping of sea defenses and related structures: Assessment Manual. [www.overtopping-manual.com](http://www.overtopping-manual.com).
- Reeve, D.E., Soliman, A., Lin, P.Z., 2008. Numerical study of combined overflow and wave overtopping over a smooth impermeable seawall. Coastal Engineering 55, 155-166.
- Schüttrumpf, H., 2001. Wellenüberlaufströmung bei Seedeichen – Experimentelle und Theoretische Untersuchungen. PhD-Thesis.
- Schüttrumpf, H., Oumeraci, H., 2005. Layer thicknesses and velocities of wave overtopping flow at seadikes. Coastal Eng. 52 (6), 473-495
- Shih, T.-H., Zhu, J., Lumley, J. L. 1996. Calculation of wall-bounded complex flows and free shear flows. Intl. J. Numer. Meth. Fluids 23, 1133-1144.
- Shao, S., Ji, C., Graham, D.I., Reeve, D.E., James, P.W., Chadwick, A.J., 2006. Simulation of wave overtopping by an incompressible SPH model. Coastal Engineering 53, pp.723-735.

## Appendix C Journal and conference papers - Journal of Flood Risk Management

- Tuan, T. Q., Oumeraci, H., 2010. A numerical model of wave overtopping on seadikes. *Coastal Engineering*, 57, pp.757-772.
- Torres-Freyermuth, A., 2007. Estudio de la Hidrodinámica de la Zona de Rompientes mediante ecuaciones tipo RANS, PhD-Thesis, Cantabria, Spain
- Torres-Freyermuth, A., Losada, I.J., Lara, J.L., 2007. Modelling of surf zone processes on a natural beach using Reynolds-Averaged Navier–Stokes equations. *J. Geophysical Research* 112 (L05601)
- van der Meer, J. W., Verhaeghe, H., Steendam, G. J., 2005. Database on Wave Overtopping at Coastal Structures, CLASH WP2 database. Infram, Marknesse, The Netherlands.

## REFERENCES

- Ackers, P., White, W. R., Perkins, J. A., and Harrison, A. J. M., 1978. Weirs and Flumes for flow Measurement, Wiley, Chichester.
- Ahrens, J. P., Heimbaugh, M. S., 1988. Seawall overtopping model. Proc. 21<sup>st</sup> International Conference on Coastal Eng. Malaga, Spain: pp. 795-806.
- Aminiti, P. and Franco, L., 1998. Wave overtopping on rubble mound breakwaters. Proc. 21<sup>st</sup> International Conference on Coastal Eng. Malaga, Spain.
- Baxter, P. J., 2005. The east coast Big Flood, 31 January–1 February 1953: a summary of the human disaster. Phil. Trans. R. Soc. Vol 360 no 1813 1293-1312
- Bagnold, R. A. 1954. Experiments on a gravity-free dispersion of large solid spheres in a Newtonian fluid under shear. Proc. Roy. Soc. London. A 225 pp. 49-63
- Bagnold, R.A., 1963. Mechanics of marine sedimentation. In: Hill, M.N. (Ed.), The Sea. Wiley-Interscience, New York, pp. 507–528.
- Bagnold, R.A., 1966. An Approach to the Sediment Transport Problem General Physics. US Geological Survey, Washington, DC, Paper 422.
- Barnes, M.P., Baldock, T.E., 2010. A Lagrangian model for boundary layer growth and bed shear stress in the swash zone, Coastal Eng. 57, pp. 385-396
- Bijker, E.W., Kalkwijk J.P.T., Pieters, T., 1974. Mass transport in gravity waves on a sloping bottom. Proc. 14th Int. Conf. on Coastal Eng.
- Bradbury, A. P. and Allsop, W., 1988. Hydraulic effects of breakwater crown halls. Proc. Conf. Design of Breakwaters, Institution of Civil Engineers, London. pp:385-396.
- Brebner, A., Askew, J.A., and Law, S.W., 1966. The Effect of Roughness on the Mass-Transport of Progressive Gravity Waves; Proc. 10<sup>th</sup> Conf. on Coastal Eng., pp. 175-184
- Brocchini, M., and Dodd, N., 2008. Nonlinear Shallow Water Equation Modeling for Coastal Eng. ASCE J. Waterw., Harbors Coastal Eng. 134, pp. 104-120.
- Burcharth H.F., Hughes, S.A., 2002. Coastal Eng. Manual, Part VI, Design of Coastal Project Elements, Chapter VI-5, Engineer Manual 1110-2-1100, U.S. Army Corps of Engineers, Washington, DC.
- Caligny, A. F. H., 1878. Experiences sur les mouvements des molecules liquides des ondes courantes, considerees dans leur mode d'action sur la marche des navires. C. R. Acad. Sci., Paris.

- Carter, T. G., Liu, L.-F., Mei, P., 1973. Mass transport by waves and offshore sand bedforms. *ASCE J. Waterw., Harbors Coastal Eng.* 99, pp. 165-184.
- Chadwick, A., Morfett, J., 1998. *Hydraulics in Civil and Environmental Eng.* Second Edition. E & FN SPON, London.
- Chen Q., Kirby J.T., Dalrymple R.A., Kennedy A.B., Chawla A., 2000. Boussinesq modeling of wave transformation breaking and run up. II: 2D. *ASCE J. Waterw., Harbors Coastal Eng.* Vol. 41, No. 6, pp. 48 - 56
- Chorin, A. J., 1968. Numerical solution of the Navier-Stokes equations. *Mathematics of Computation.* 22, pp. 745-762
- Collins, J.I. 1963. Inception of Turbulence at the Bed under Periodic Gravity Waves: *J. Geophys. Res.*, Vol. 68, pp. 6007-6014
- Cox, D.T., Hobensack, W., Sukumaran, A., 2000. Bottom stress in the inner surf and swash zone. In: B. Edge (Editor), 27th International Conference on Coastal Eng.. ASCE, Sidney, Australia, pp. 108-119.
- Dalrymple, R. A., Rogers, B.D., 2006. Numerical modeling of water waves with the SPH method. *Coastal Eng.* 53, pp. 141-147.
- Davies A.G., Villaret, C., 1999 Eulerian drift induced by progressive waves above rippled and very rough beds. *J. Geophys. Res.* Vol. 104, pp. 1465–1488.
- Dean, R. G., Darymple, R. A., 1991. *Water wave mechanics for engineers and scientists.* World Scientific.
- de Best, A., Bijker, E. W., Wichers, J. E. W., 1971. Scouring of sand in front of a vertical breakwater. In: *Proc. Conference on Port and Ocean Eng under Artic Conditions Vol 2* . The Norwegian Institute of Technology, Trondheim, Norway, pp. 1077-1086.
- de Gerloni M., Franco, L., Passoni, G., 1991. The safety of breakwaters against wave overtopping. *Proc. ICE Conf. on Breakwaters and Coastal Structures.* T. Telford, London.
- de Rouck, J., Geeraerts, J., Troch, P., Kortenhaus, A., Pullen, T., Franco, L., 2005. New results on scale effects for wave overtopping at coastal structures. *Coastal Structures and Breakwaters 2005.* Institution of Civil Engineers.
- Dore, B. D., 1982. On the second approximation to mass transport in the bottom boundary layer. *Coastal Eng.* 6, pp. 93-120
- Douglas, J. F., Gasiorek J. M., Swaffield J. A., 1979. *Fluid Mechanics.* Pitman. London.
- Endoh, K., Takahashi, S., 1994. Numerically Modelling Personnel Danger on a Promenade Breakwater due to Overtopping Waves, *Proc 241 ICCE*, Kobe, ASCE, New York.

- Einstein, H. A., 1950. The bed-load function for sediment transport in open channel flows. US Dept. of Agriculture, Techn. Bulletin No. 1026
- FEMA-1605-DR-AL, 2006. High Water Mark Collection for Hurricane Katrina in Alabama. FEMA Atlanta, GA, USA.
- FEMA photo, <<http://www.photolibrary.fema.gov/photodata/original/18177.jpg>>.
- Franco, L., de Gerloni, M., van der Meer, J. W., 1994. Wave overtopping on vertical and composite breakwaters. Proceedings of the 24<sup>th</sup> International Coastal Eng. Conference, American Society of Civil Engineers Vol. 1: pp. 1030-1045.
- Fredsoe, J., and Deigaard, R. 1992. Mechanics of Coastal Sediment Transport. Advanced Series on Ocean Eng. Vol. 3. World Scientific.
- Fukuda, N., Uno, T., Irie, I., 1974. Field observations of wave overtopping of wave absorbing revetment. Coastal Eng. in Japan.
- Garcia, N., Lara J.L., Losada I.J., 2004. 2-D numerical analysis of near-field flow at low-crested permeable breakwaters. Coastal Eng. 51, pp. 991-1020
- Gibson A. H., 1930. The Effect of Surface Waves on The Discharge over Weirs. The Institution of Civil Engineers. London.
- Gislason, K., Fredsøe, J., Sumer B. M., 2009. Flow under standing waves Part 2. Scour and deposition in front of breakwaters. Coastal Eng. 56: pp. 363-370.
- Goda, Y., 1970. Estimation of the rate of irregular wave overtopping of seawalls. Min. Transp. Japan, Report of the Port and Harbour Research Institute.
- Goda, Y., 2009. Derivation of unified wave overtopping formulas for seawalls with smooth, impermeable surfaces based on selected CLASH datasets. Coastal Eng. 56, pp. 385-399.
- Goda, Y., Suzuki, Y., 1976. Estimation of incident and reflected waves in random wave experiments. Proc. 15th International Coastal Eng. Conf., Vol.1. American Society of Civil Engineers, pp. 828–845
- Gómez-Gesteira, M., Cerqueiro, D., Crespo, C., Dalrymple, R.A., 2005. Green water overtopping analyzed with a SPH model. Ocean Eng. 32, pp. 223-238.
- Gotoh, H., Ikari, H., Memita, T., Sakai, T., 2005. Lagrangian particle method for simulation of wave overtopping on a vertical seawall. Coastal Eng. J., 47, pp. 157-181.
- Gotoh, H., Shao, S., Memita, T., 2004. SPH-LES Model for numerical investigation of wave interaction with partially immersed breakwater. Coastal Eng. J., 46, pp. 39-63.
- Hamill, L., 1995. Understanding Hydraulics. Macmillan, London.

- Hedges, T.S., 1987. Combinations of waves and currents: an introduction. Proc. ICE, Part 1, Vol. 82, pp. 567-585.
- Hedges, T. S., Reis M. T., 1998. Random wave overtopping of simple sea walls: a new regression model. Proc. ICE: Water, Maritime and Energy. Vol. 130 – 1: pp. 1-10.
- Hirt, C. W., Nichols, B. D., 1981. Volume of fluid (VOF) method for dynamics of free boundaries. J Comput. Phys. 39, pp. 201-225.
- Hooke, R., Jeeves T. A., 1961. Direct Search solution of numerical and statistical problems. J. Ass. Comput. Mach. 8: pp. 212- 229.
- Hsiao, S., Lin, T., 2009. Tsunami-like solitary waves impinging and overtopping an impermeable seawall: Experiment and RANS modelling, Coastal Eng. 57, pp. 1-18.
- Hsu, J. R. C., Silvester, R., 1989. Model test results of scour along breakwaters. J. Waterways, Port, Coastal and Ocean Eng., Vol. 115, pp. 66-85.
- Hu, K., Mingham, C.G., Causon, D.M., 2000. Numerical simulation of wave overtopping of coastal structure using the non-linear shallow water equation. Coastal Eng. 41, pp. 433–465.
- Hubbard, M., Dodd, N., 2002. A 2D numerical model of wave run-up and overtopping. Coastal Eng. 47, pp. 1–26.
- Hughes, S.A., Nadal, N.C., 2009. Laboratory study of combined wave overtopping and storm surge overflow of a levee. Coastal Eng. 56, pp. 244–259.
- Johns, B., 1970, On the mass transport induced by oscillatory flow in a turbulent boundary layer. J. Fluid Mech. 43, pp. 177–185.
- Klopman, G., 1994. Vertical structure of the flow due to waves and currents. Rep. H840.30, Part II, Delft Hydraulics, Delft.
- Kobayashi, N., Wurjanto, A., 1989. Wave Overtopping on Coastal Structures. J. Waterway, Port, Coastal, and Ocean Eng. 115 (2), pp. 235–251.
- Kothe, D.B., Mjolsness, R.C., Torrey, M.D., 1991. RIPPLE: a computer program for incompressible flows with free surfaces. Report LA-12007-MS, Los Alamos Scientific Report, Los Alamos, NM, USA
- Komar, P.D. 1976. Beach Processes and Sedimentation. Prentice Hall, New Jersey.
- Lara, J.L., Losada, I.J., Guanche, R., 2008. Wave interaction with low-mound breakwaters using a RANS model. Ocean Eng., 35, Issue 13, pp. 1388-1400.

- Lin, P. 1998. Numerical modelling of breaking waves. Ph.D thesis, Cornell University, USA.
- Lin, C., Jeng, D.S., Jeng, C.N. 2002. An experimental study on the flow characteristics of a standing wave: application of FLDV measurements. *Ocean Eng.* Vol. 29, pp. 1265–1282
- Lin, P. and Liu P. L –F. 1998a. A numerical study of breaking waves in the surf zone. *J. Fluid Mech.* 359, pp. 239-264.
- Lin, P. and Liu P. L –F. 1998b. Turbulence transport, vorticity dynamics, and solute mixing under plunging breaking waves in surf zone. *J Geophys. Res.* 103, pp. 15677-15694.
- Lin, P. and Liu P. L –F. 1999. Internal wave–maker for Navier-Stokes equations models. *J. ASCE J. Waterway, Port, Coastal Eng.* pp. 207-215.
- Lin, P. and Liu P. L –F. 2002. A user manual for a breaking wave model. School of Civil and Environmental Eng. Cornell University, Ithaca, NY 14853.
- Liu, P.L.-F., Lin, P., Chang, K.A., Sakakiyama, T., 1999. Numerical modelling of wave interaction with porous structures. *J. of Waterway, Port, Coastal and Ocean Eng.* 125, 322-330.
- Liu P. L -F. and Losada I. J. (2002) Wave Propagation modelling in coastal Engineering. *J. Hydr. Res.*, 40, 229-240.
- Longuet-Higgins, M.S., 1953. Mass transport in water waves. *Philos. Trans. R. Soc. London. A* 245 903 pp. 535–581.
- Longuet-Higgins, M.S., 1958. The mechanics of the boundary-layer near the bottom in a progressive wave. *Proc. 6th Int.Conf. on Coastal Eng.*, American Society of Civil Engineers, Miami, pp. 184–193.
- Losada, I.J., Lara, J.L., Guanche, R., Gonzalez-Ondina, J. M., 2008. Numerical analysis of wave overtopping of rubble mound breakwaters. *Coastal Eng.* 55, pp. 47-62.
- López de San Roman-Blanco, B., Coates, T.T., Holmes, P., Chadwick, A.J., Bradbury, A., Baldock, T.E., Pedrozo -Acuña, A., Lawrence, J. and Grüne, J., 2006. Large Wave Channel (GWK) experiments on gravel and mixed beaches: experimental procedure and data documentation. *Coastal Eng.*, 53, pp. 349-362.
- Lynett P. J., Melby J. A., Kim D. 2010, An application of Boussinesq modeling to Hurricane wave overtopping. *Ocean Eng.* 37 pp. 135-153.
- Lv, X., Zou, Q., Reeve, D., 2009. A Hybrid LS and VOF Method for 3-D Simulation of Wave Breaking and Overtopping. *Intl. J. Offshore and Polar Eng.* Vol. 4 No. 4, pp.1-9.

- Madsen, O.S., 1991. Mechanics of cohesionless sediment transport in coastal waters. Proceedings of Coastal Sediments '91, ASCE, pp. 15– 27.
- Madsen, P. A., Murray, R., and Sørensen, O. R. 1991 A new form of the Boussinesq equations with improved linear dispersion characteristics. Coastal Eng., 15, pp. 371–388
- Meyer-Peter, E., Müller, R., 1948. Formulas for bed load transport, 2nd Congress of the Int. Association of Hydraulics Structures Res., Stockholm, Sweden
- Marin, F., 2004. Eddy viscosity and Eulerian drift over rippled beds in waves. Coastal Eng., 50 pp. 139-159.
- Masselink, G., Hughes, M., G., 1998. Field investigation of sediment transport in the swash zone. Continental Shelf Research, 18: pp. 1179-1199.
- McKee Smith, J., 2002. Wave Pressure Gauge Analysis with Current, J. of Waterway, Port, Coastal, and Ocean Eng., Vol. 128, No. 6, pp. 271-275
- Menter, F.R., 1993. Zonal two equation  $k-\Omega$  turbulence models for aerodynamic flows. AIAA Paper 93-2906, AIAA 24th Fluid Dynamic Conference, Orlando, Florida.
- Nikuradse, J., (1933). Stromungsgesetze in glatten und rauhen rohren. V D I Forschungsheft 361, Berlin.
- Nielsen, P., 1992. Coastal Bottom Boundary Layers and Sediment Transport. Advanced Series on Ocean Eng.. Vol. 4, World Scientific, London.
- Nielsen, P., 2002. Shear stress and sediment transport calculations for swash zone modelling. Coastal Eng. 45 pp. 105-114.
- Noda, H., 1968. A study on mass transport in boundary layers in standing waves. Proceedings of XI conference on Coastal Eng., Chapter 15, pp. 227-247.
- Owen, M.W., 1980. Design of seawalls allowing for wave overtopping. Technical Report EX-924. H.R. Wallingford, United Kingdom
- Owen, M.W., 1982. The hydraulic design of seawall profiles. Proc. Conf. on Shoreline Protection. Institution of Civil Engineers, London. pp. 185-192.
- Pedersen, J., 1996. Experimental Study of Wave Forces and Wave Overtopping on Breakwater Crown Walls. Hydraulic and Coastal Eng. Laboratory, Department of Civil Eng., Aalborg, Denmark, Aalborg University.
- Pedersen, J., Burcharth, H. F., 1992. Wave Forces on Crown Walls. Proc. 23<sup>rd</sup> International Conf. on Coastal Eng., Venice, Italy.
- Pedrozo-Acuña, A., 2005. Concerning swash on steep beaches. PhD Thesis, University of Plymouth, Plymouth, UK, 225 pp.

- Pedrozo-Acuña, A., Simmonds, D.J., Otta, A.K., Chadwick, A.J., Silva, R., 2007. A numerical–empirical approach for evaluating morphodynamic processes on gravel and mixed sand–gravel beaches, *Marine Geology*, 241, pp.1-18
- Pedrozo-Acuña, A., Torres-Freyermuth, A. Zou Q., Hsu T., Reeve D. E., 2010. Diagnostic investigation of impulsive pressures induced by plunging breakers impinging on gravel beaches. *Coastal Eng.*, 57: pp. 252- 266.
- Peregrine, D.H., 1967. Long waves on a beach. *J. Fluid Mech.* 27, pp. 815–827.
- Powell, K.A., 1990. Predicting short term profile response for shingle beaches. SR Report 219, HR Wallingford, Wallingford.
- Puleo, J., Holland, T., 2001. Estimating swash zone friction coefficients on a sandy beach. *Coastal Eng.* 43 pp. 25-40.
- Puleo, J., Holland, T., Plant N. G., 2003. Fluid acceleration effects on suspended sediment transport in the swash zone. *J. Geophysical Research*,108. pp. 1-12
- Pullen, T., Allsop, N.W.H., Bruce, T., Kortenhaus, A., Schüttrumpf, H., van der Meer, J.W., 2007. *EurOtop: Wave Overtopping of Sea Defences and Related Structures: Assessment Manual*. Available at: [www.overtopping-manual.com](http://www.overtopping-manual.com).
- Rakha K.A., Deigaard R., Brprker I., 1997. A phase-resolving cross shore sediment transport model for beach profile evolution. *Coastal Eng.* 31, pp. 23 I-261
- Raubenheimer, B., Elgar, S., Guza, R.T., 2004. Observations of swash zone velocities: A note on friction coefficients. *J. Geophysical Research*,109.
- Reeve, D.E., Soliman, A., Lin, P.Z., 2008. Numerical study of combined overflow and wave overtopping over a smooth impermeable seawall. *Coastal Eng.* 55, pp. 155–166.
- Rodi, W., 1980. *Turbulence Models and Their Application in Hydraulics - A State-of-the-Art Review*. IAHR Publication.
- Russell, R. C. H., Osorio, J. D. C., 1958 An experimental investigation of drift profiles in a closed channel. *Hydraulics Research Station, Wallingford, England*.
- Sawaragi, T., Deguchi, I., Park, S., 1988. Reduction of Wave Overtopping Rate by the Use of Artificial Reefs. *Coastal Eng.*, pp. 335-349
- Schüttrumpf, H., 2001. *Wellenüberlaufströmung bei Seedeichen – Experimentelle und Theoretische Untersuchungen*. PhD Thesis.
- Shih, T.-H., Zhu, J., Lumley, J. L. 1996. Calculation of wall-bounded complex flows and free shear flows. *Intl J. Numer. Meth. Fluids* 23, pp. 1133-1144.

- Shao, S., Ji, C., Graham, D.I., Reeve, D.E., James, P.W., Chadwick, A.J., 2006. Simulation of wave overtopping by an incompressible SPH model. *Coastal Eng.* 53, pp. 723-735.
- Shields, A., 1936. Anwendung der Ahnlichkeits Mechanik und der Turbulenzforschung auf die Geschiebe Bewegung, 26. Mitteilungen Preuss. Versuchsanstalt fur Wasserbau and Schiffbau, Berlin, 26pp.
- Smith G..M, Seiffert, J. W. W., van der Meer, J. W., 1994. Erosion and overtopping of a grass dike: large scale model tests. Proc 24<sup>th</sup> ICCE, pp. 2639-2652, Kobe, ASCE.
- Soulsby, R.L., 1997. Dynamics of Marine Sands. Thomas Telford. HR Wallingford, London.
- Soulsby, R.L., Whitehouse, R. J. S. 1997. Threshold of Sediment Motion in Coastal Environments. Pacific Coasts and Ports 1997: Proceedings of the 13th Australasian Coastal and Ocean Eng. Conference and the 6th Australasian Port and Harbour Conference; Vol. 1. pp. 145-150.
- Stansby P.K., 2003. Solitary wave run up and overtopping by a semi-implicit finite-volume shallow-water Boussinesq model. *J. Hydraulic Research.* Vol. 41 Issue 6. pp.639 - 647
- Steendam, G. J., van der Meer. J. W., Hardeman, B., van Hoven, A., 2010. Destructive wave overtopping tests on grass covered landward slopes of dikes and transition to berms. Proc. of International Conference on Coastal Eng., Shanghai, China.
- Stokes, G.G. 1847. On the theory of oscillatory waves. *Trans. Camb. Phil. Soc.* 8, 441
- Sumer, B. M., and J. Fredsøe, 2000. Experimental study od 2-D scour and its protection at a rubble mound breakwater. *Coastal Eng.*, 40. pp. 59-87
- Tuan, T. Q., Oumeraci, H., 2010. A numerical model of wave overtopping on seadikes. *Coastal Eng.*, 57, pp. 757-772.
- Tirindelli M., Lamberti A., Paphitis D., Vidal C., Hawkins S., Morchella P., Sanchez-Arcilla A. 2000. Wave action on rubble mound breakwaters: the problem of scale effect. DELOS EVK3-CT-2000-00041 Amsterdam
- Torres-Freyermuth, A. 2007. Estudio de la Hidrodinámica de la Zona de Rompientes mediante ecuaciones tipo RANS, PhD Thesis, Cantabria, Spain
- Trowbridge, J., Madsen, O. S. 1984. Turbulent wave boundary layers 2. Second-order theory and mass transport. *J. Geophys. Res.*, 89, pp. 7999-8007
- Tsuruta, S., Goda, A., 1968. Expected discharge of irregular wave overtopping. Proc. Conf. on Coastal Eng., llth, pp. 833-852

- van Doorn, T. 1981. Experimental investigation of near-bottom velocities in water waves with and without currents, Rep. M1423, Delft Hydraulics Lab., Delft, Netherlands.
- van der Meer, J., 1988. Rock slopes and gravel beaches under wave attack. Delft University of Technology, Delft, The Netherlands
- van der Meer, J. W., Janssen J. P.F.M., 1995. Wave run-up and wave overtopping at dikes. In: Wave Forces on Inclined and vertical wall structures. American Society of Civil Engineers. pp. 1-27
- van der Meer, J. W., Verhaeghe, H., Steendam, G. J., 2005. Database on Wave Overtopping at Coastal Structures, CLASH WP2 database. Infram, Marknesse, The Netherlands.
- Verwaest T., Vanpoucke P., Willems M., De Mulder T., 2010. Waves Overtopping a Wide-Crested Dike. Proc. 32nd Int. Conf. on Coastal Eng., CERC and OES, Shanghai.
- Wang, Z., Zou, Q., Reeve, D., 2009. Simulation of spilling breaking waves using a two phase CFD model. Computers & Fluids 38, pp.1995-2005.
- Wei, G., Kirby, J.T., 1995. Time-dependent numerical code for extended Boussinesq equations. J. Waterway, Port, Coast. and Ocean Eng. 121, pp. 251–261.
- Wilcox, D.C. 1998. Turbulence modelling for CFD. DCW Industries Inc., Ca. USA.
- Xie, S.L. 1981. Scouring patterns in front of vertical breakwaters and their influence on the stability of the foundations of the breakwaters. Report. Department of Civil Eng., Delft University of Technology, Delft, The Netherlands, 61 pp.
- Xie, S. L. 1985. Scouring patterns in front of vertical breakwaters. Acta Oceanol. Sin. 4 (1), pp. 153-164